INFORMATION TO USERS

This manuscript has been reproduced from the microfilm master. UMI films the text directly from the original or copy submitted. Thus, some thesis and dissertation copies are in typewriter face, while others may be from any type of computer printer.

The quality of this reproduction is dependent upon the quality of the copy submitted. Broken or indistinct print, colored or poor quality illustrations and photographs, print bleedthrough, substandard margins, and improper alignment can adversely affect reproduction.

In the unlikely event that the author did not send UMI a complete manuscript and there are missing pages, these will be noted. Also, if unauthorized copyright material had to be removed, a note will indicate the deletion.

Oversize materials (e.g., maps, drawings, charts) are reproduced by sectioning the original, beginning at the upper left-hand corner and continuing from left to right in equal sections with small overlaps.

Photographs included in the original manuscript have been reproduced xerographically in this copy. Higher quality 6" x 9" black and white photographic prints are available for any photographs or illustrations appearing in this copy for an additional charge. Contact UMI directly to order.

Bell & Howell Information and Learning
300 North Zeeb Road, Ann Arbor, MI 48106-1346 USA
800-521-0600

Université d'Ottawa · University of Ottawa

A Mixed Lagrangian-Eulerian Approach for Numerical Simulation of Mixing Layers and Uniformly Sheared Flow

by

Reza Abdolhosseini

A dissertation submitted in partial fulfilment
of the requirements for the degree of
DOCTOR of PHILOSOPHY
in
MECHANICAL ENGINEERING

Ottawa-Carleton Institute for
Mechanical and Aerospace Engineering
University of Ottawa
Ottawa, Ontario, K1N5N6
September 1998

Acknowledgements

I wish to express my deepest gratitude to my advisor, Dr. Roger Milane, for his guidance and support during my graduate studies. His sincere relationship with me combined with his kindness will always be appreciated.

Special thanks to my mother and father for their support during my studies. My only regret is that my father is not alive to share this accomplishment with me.

I am grateful to my wife, Lida Ghavami, and my little daughter Nika for their patience during the past years.

Abstract

The vortex-in-cell (VIC) method is applied for the prediction of the turbulent characteristics and flow development of the two-dimensional spatially growing mixing layer, the two-dimensional uniformly sheared flow and the three-dimensional uniformly sheared flow. The VIC method has the advantage that it requires less computational time compared with the Lagrangian method.

In the first part of thesis, the two-dimensional VIC method is validated by simulating a spatially growing mixing layer. The results show that the VIC method is capable of predicting the characteristics of the spatially growing mixing layers as well as the grid-free Lagrangian method.

In the second part of thesis, the two-dimensional VIC method is used to simulate the uniformly sheared flow. In this new approach a combination of several adjacent mixing layers simulate the initial condition used to generate the uniformly sheared flow. Turbulent characteristics such as the mean velocity, the r.m.s. longitudinal and lateral velocity fluctuations and the Reynolds shear stress are predicted and compared with previous numerical and experimental works.

In the third part of this work, three-dimensional simulation of uniformly sheared flows is performed as an extension of the two-dimensional simulation in order to take into account the effect of stretching which is a major contributor to turbulence production. The methodology is based on a mixed Lagrangian-Eulerian three-dimensional vortex-in-cell method. Histograms and two-angle probability distribution of the inclination angle of the vorticity vectors at the grid points with the horizontal plane indicate the presence of vortical structures at a 35°-40° angle with horizontal plane which is consistent with the results of Rogers and Moin (1987). The time evolution of the component energy ratios K_{11}, K_{22} and K_{33} are calculated and compared with the previous works. Sensitivity to the numerical parameters is investigated and the results exhibited robustness to the numerical parameters.

Table of Contents

Chapter 3. Formulations and Mathematical Models

Chapter 4. Numerical Approximations and Solution Procedure

Chapter 5. Results of Two-Dimensional Simulation

Chapter 6. Results of Three-Dimensional Simulation

List of Figures

List of Tables

Nomenclature

English Symbols

A	Area of the cell
dx, dy, dz	Distances in a cell, as shown in figure 4.6.
G_p	Number of grid points
H	Half width of the computational domain as shown in figure 4.4.
H_{shear}	Width of the shear region in two-dimensional simulation.
H_x, H_y, H_z	Mesh size in x, y and z direction
K_s	Flow generator constant in two-dimensional uniformly sheared flow
L	Length of the computational domain
l	Initial distance between the neighbouring vortices
M_x, M_y	Number of mesh points in x and y directions
N	Number of vortices
p	Pressure
q, q_r	Turbulent kinetic energy, A reference Turbulent kinetic energy
r	Velocity ratio (U_1/U_2)
$R_{i,j}$	Residual defined in equation 4.5.
S	Shear rate
St	Non-dimensional time
t	Time
dt	Time step
u	Velocity vector
u, v, w	Cartesian velocity components
u', v', w'	Turbulent velocity fluctuations
u_n, v_n, w_n	Velocity components of the vortices
U	Mean velocity in streamwise direction
U_1, U_2	Velocities on the upper and lower side of splitter plate in mixing layer
U_{av}	Arithmetic average velocity above and below the splitter plate
U_c	Centerline mean velocity
V	Volume of the cell in vortex-in-cell method; Mean velocity in the lateral direction
x_v	Virtual origin
x, y, z	Cartesian coordinates
x_n, y_n, z_n	Coordinates of the vortex elements
Δx, Δy, Δz	Cell size in the vortex-in-cell method

Greek Symbols

α	Over relaxation factor; Angle of the projection of the filaments segments on xy-plane, with spanwise (y) direction as shown in figures 6.6 and 6.7.

β	Aspect ratio of the mesh cells (dx/dy)
Γ	Circulation
Γ_n	Circulation of the vortex element number n
$\Gamma_x, \Gamma_y, \Gamma_z$	Components of circulation vector of vortex elements
δw	Vorticity thickness
ϵ_{ijk}	Alternating tensor
η	Angle of the filaments segments with xy-plane shown in figure 6.6; Angle of the vorticity vectors with xy-plane shown in figure 6.7.
θ	Momentum thickness; Angle of the filaments segments with xy-plane shown in figure 6.6; Angle of the vorticity vectors with xy-plane shown in figure 6.7
κ	Coefficient of asymptotic growth rate of turbulent kinetic energy in uniform shear
λ	Aspect ratio of the mesh cells (dx/dz),
μ	Viscosity
ν	Kinematic viscosity
ρ	Density
σ	Core size radius
σ_0	Initial core size
τ	Non-dimensional time
ϕ	Velocity Vector Potential
Φ_x, Φ_y, Φ_z	Velocity vector potential components
χ	Trajectory of vortices
ψ	Stream function
$\underline{\omega}$	Mean vorticity
ω	Vorticity vector
$\omega_x, \omega_y, \omega_z$	Components of vorticity vector

Chapter 1

Introduction

1.1. Turbulent Mixing

Turbulence is, in essence, a problem in statistical dynamics. It is a superposition of an irregular eddying motion on a mean stream whose detailed configuration is neither reproducible from one experiment to the next nor predictable theoretically, but whose statistical properties are significant (Phillips, 1969). Turbulent flows have common characteristics. We can define a turbulent flow by a set of characteristics. Turbulent flows have disorder which is not reproducible in detail. They mix efficiently and they have vorticity fluctuations in three dimensions. Turbulent flows are three-dimensional, but something like turbulent motion can occur in two-dimensions. Large-scale weather systems have some of this character. However, in a two-dimensional flow, vorticity behaves as a scalar, and there is no vorticity production by vortex filament stretching. Another basic concept

in defining turbulence is " cascade". Turbulent flows are hierarchical and involve entities usually referred to as eddies of varying sizes. The largest eddies are produced by the forces driving the flow. The large eddies are unstable and produce eddies of a somewhat smaller size, which themselves become unstable and generate eddies of even smaller size. This process continues until eventually molecular viscosity suppresses further cascading and dissipates the eddies. Eddies are large groups of fluid particles which move laterally or longitudinally in the flow field. While undergoing these motions, an eddy can change its shape or stretch, and rotate or break into two or more eddies. The motion of a smoke ring released from a cigarette and moving in the air gives a realistic picture of an eddy. One of the main characteristics of the eddies in a turbulent flow is vorticity. Vorticity may be distributed throughout the entire fluid, but often the vorticity is very large only in a thin thread of fluid while the remaining fluid is virtually without vorticity. Therefore, our thinking can be simplified by lumping all the vorticity into a concentrated vortex filament around which the fluid spins. The vortex filaments are like tangled spaghetti. The mutually-induced velocities of these vortex filaments cause some of them to stretch, and this stretching produces turbulence with smaller eddies and higher vorticity. The processes of cascading and reducing the size of eddies is by break-up and reconnection of these filaments. In the numerical simulation presented in this work, the vorticity is lumped into concentrated vortex filaments similar to the above mentioned model. However, in the absence of a break-up and reconnection mechanism to generate smaller scale structures, the larger structures are unmergable and unbreakable throughout the simulation.

The significance of the turbulent mixing is well recognized due to the fact that most of the flows occurring naturally or in engineering applications are involved with it. Turbulent mixing dominates the initial flow pattern in jets and in wakes caused by bluff bodies. It governs the flow field

in combustion chambers and flow reactors whose size or efficiency depends on the rate of mixing. Often in combustion devices one works to increase the turbulence level of the flow to increase the mixing and therefore, to have more efficient burning. It is also recognized that most of the noise associated with jet propulsion originates in the turbulent mixing (Oster and Wygnanski, 1982). Since in any real fluid the action of the viscosity causes the dissipation of the kinetic energy, in the absence of any external source the turbulent motion will decay. One of the simplest ways of producing and maintaining turbulence is using mean shear flow. Shear flows are common and important to many industrial systems. The mixing layer where two initially separated parallel flows come into contact and mix, is one of the simplest conceivable free shear flows, and a generic mixing configuration for many practical applications.

The governing equations of turbulent flows are known, namely, those of conservation of mass, momentum and energy. Due to the complexity of turbulent flows most of the information about the characteristics of turbulent flows is obtained from experiments. Recent advances in computer technology have made feasible the numerical simulation of turbulent flows. What follows is a brief explanation of various methods of computing turbulent flows and an explanation of each.

1.2. Reynolds Averaged Equations

In this method, the Navier-Stokes equations are averaged over time or homogeneous directions in the flow. When the averaging is performed, the equations of motion contain averages of products of fluctuating velocities, and the number of unknowns is more than the number of equations. This is the well-known "closure problem", because the set of equations can never be closed by further averaging. To close the problem, empirical models must be constructed to relate the new

variables to the old ones. The Reynolds averaged Navier-Stokes (RANS) method is one of the most affordable methods of computing turbulent flows because velocity fluctuations are not calculated, and all turbulent scales are modelled. The weakness of RANS is that it is not an appropriate method for a Lagrangian type simulation of turbulent flows, because, when the velocity fluctuations are not calculated, a Lagrangian element cannot be traced at each time step. In other words, RANS methods may be applied for the numerical simulation of the shear flows using an Eulerian approach.

1.3. Large Eddy Simulation

In the large eddy simulation (LES) method, the equations are averaged over a small spatial region. The main idea in this approach originates from the experimental observation that the large-scale motions differ from one flow to another, but the small scale motions are almost universal. Therefore, the small eddies may be removed from the flow field and an equation for the large eddies can then be derived. A spatial filter function can be employed to filter a range of small scales (subgrid scales) in the momentum or vorticity equations. In these filtered equations, the terms representing the large scale structures are separated from those representing the small scale motions (Leonard, 1974). The effect of the small eddies is then introduced using subgrid scale models. As a result, large eddy motions of the resolved scales are simulated by solving the filtered Navier-Stokes equations.

This approach was first used by Smagorinsky (1963) followed by Lilly (1967) and Deardorff (1970). Leonard (1974) continued this method and used a Gaussian filter explicitly. Other examples can be found in Kwak et. al. (1975), Bardina et. al. (1980), Leslie and Quarini (1979), Schumann (1975), Lin and Pratt (1987) and Milane and Nourazar (1995, 1997). There are many reviews of large eddy simulation (LES) and subgrid scale modelling. Some of these reviews can be found in Shaanon

et al. (1975), Mansour et al. (1978), Cain et al. (1981), Antonopoulos (1981), Rogallo and Moin (1984) and Lesieur (1987).

1.4. Direct Numerical Simulation

A numerical simulation of the Navier-Stokes equations that resolves all scales of motion is called a direct numerical simulation (DNS). In this approach, rather than averaging the equations first, a time and space resolved flow field is computed, and then an ensemble average is taken. The only errors made in the DNS approach are numerical ones.

Among the three ways of computing turbulent flows (Reynolds averaged equations, LES and DNS), the DNS approach is the most attractive, because it dispenses with models and solves the unfiltered Navier-Stokes equations. In a DNS approach, since all turbulent time and length scales are resolved (from the largest down to the smallest scales, which increase rapidly with increasing Reynolds number), its application is limited to low Reynolds numbers. Direct numerical simulations are very useful, since they provide a case for the subgrid scale models required in large eddy simulations, as well as providing physical insight which can be used in developing proper subgrid scale models. The accuracy of DNS makes it a complement to (and perhaps in the future a replacement for) laboratory experiments. Examples of DNS calculations can be found in Orszag and Patterson (1972), Clark et al. (1979), Shirani et al. (1981), Feiereisen et al. (1981), Rogallo (1981), Corcos and Sherman (1984) and Riley et al. (1986).

1.5. Vortex Methods

There are several numerical techniques to solve the equations of turbulent flow. Most of these techniques employ an Eulerian approach, using finite difference, finite elements or spectral methods. Unlike these methods, in the Lagrangian description of the evolution of the discretized vorticity field, which is the basic nature of the vortex method, the motion of discrete vortices is traced step by step. Vortex methods have been used extensively to simulate incompressible flows, especially two-dimensional problems. In the pure Lagrangian approach, the basic idea is the application of the Biot-Savart law of interaction between vortices. The Biot-Savart law can be derived mathematically from the conservation of mass for a potential flow assuming an incompressible fluid. It determines kinematically the instantaneous velocity field related to a given vorticity field. In this technique only fluid particles with concentrated vorticity (vortex points or blobs) need to be tagged and traced. As time proceeds, the change of vorticity distribution within a blob is governed by the vorticity transport equation. This method was first introduced by Rosenhead in 1931, prior to the availability of digital computers. Aided by computers, Abernathy and Kronauer (1962) used the point vortex method to simulate vortex streets. Chorin (1973) solved the two-dimensional problem through the use of vortex blobs. He also introduced a three-dimensional solution using a filament method. Ashurst (1979) applied Chorin's method to a two-dimensional mixing layer, and his results were almost similar to Brown and Roshko's experiment (1974).

A description of direct numerical simulation using vortex methods can be found in many papers, such as Leonard (1980), Inoue (1985), Ng and Ghoneim (1985), Ghoneim and Ng (1986), Inoue and Leonard (1987). The large eddy simulation using vortex methods can be found in Lin and Pratt (1987) and Milane and Nourazar (1995, 1997), amongst others. Also the reviews of Clements

and Maull (1975), Fink and Soh (1974), Saffman (1981), Leonard (1980,1985), Aref (1983) and Sarpkaya (1994) give a complete description of the vortex methods.

Another approach which has been developed for calculating vortex problems is known as the vortex-in-cell(VIC) or the cloud-in-cell(CIC) method. This method combines some of the best features of both Lagrangian and Eulerian approaches. In the VIC method vortex markers are treated in a Lagrangian fashion, but these markers move through an Eulerian mesh system. In this method, the velocity field is calculated from Poisson's equation, and the vorticity distribution is obtained from the Laplacian of the stream function. In the VIC method the Eulerian scheme is used to calculate the velocity field and the Lagrangian scheme to track the vortices. This work makes extensive use of this methodology, which will be discussed in considerable detail throughout. Examples of calculations employing the VIC method can be found in Christiansen (1973), Christiansen and Zabusky (1973), Baker (1979), Aref and Siggia (1980,1981), Aref (1980) and Meng and Thomson (1978). In addition, the reviews of Leonard (1980), Aref (1983) and Sarpkaya (1994), provide a description of this technique.

Chapter 2

Literature Review

2.1. Scope of the Thesis

This work was originally focused on the two-dimensional simulation of the spatially growing mixing layers and uniformly sheared flows. The primary objective was to apply a two-dimensional vortex-in-cell (VIC) scheme to simulate a spatially growing mixing layer in order to validate the capability of the VIC method by comparing its results with the Lagrangian grid-free vortex method. Then, a new methodology to simulate a two-dimensional uniformly sheared flow was developed. This was done by assuming that a uniformly sheared flow is composed of several adjacent mixing layers. Insight gained during this investigation revealed that the uniformly sheared flow is structurally

different from the mixing layers, because the existence of the coherent structures in the uniformly sheared flow is not as evident as in the mixing layer. Therefore, the effect of three-dimensionality cannot be ignored and the vortex stretching, which is ignored in the two-dimensional simulation, should be taken into account. Hence, a three-dimensional simulation of the uniformly sheared flow was performed as an extension to the two-dimensional simulation of the uniformly sheared flow.

Based on the above description, the numerical simulation presented in this work is divided into three parts, namely, the two-dimensional spatially growing mixing layer, the two-dimensional uniformly sheared flow and the three-dimensional uniformly sheared flow.

The literature review on the mixing layer is limited to two-dimensional results of the grid-free Lagrangian vortex method because the objective here is to apply the VIC method and to validate its results by comparing with the grid-free Lagrangian vortex method results. The focus of the present study in the numerical simulation of the uniformly sheared flow is to predict the flow field and to compare the r.m.s. velocity fluctuations, the turbulent kinetic energy, the component energy ratios, the angles of the vortex filaments and the angles of the vorticity vectors with previous experimental and numerical results. The literature review on the uniformly sheared flow is limited to: a)- The most recent experimental works in which the Reynolds stresses and turbulent kinetic energy are reported, such as, Tavoularis and Karnik (1989), Harris et al (1977) and Rohr et al (1988); and b)- The numerical simulation in which the r.m.s. velocity fluctuations, the turbulent energy ratios, the component energy ratios and the vortical structures in the flow field are predicted, such as Rogers and Moin (1987) and Kida and Tanaka (1994). The numerical simulation of Roger and Moin (1987) predicted correctly the component energy ratios copmared to the experimental results of Tavoularis and Karnik (1989). The numerical simulation of Kida and Tanaka (1994) is more concentrated on the

prediction of the vortical structures without reporting the Reynolds stresses and turbulent kinetic energy which is discussed in section 2.3.2. The objective of this study is to extend the capabilities of the three-dimensional VIC method, to predict the component energy ratios, the turbulent kinetic energy and the vortex filaments, and to compare them with the results of Rogers and Moin (1987) and Kida and Tanaka (1994). It is expected that, since the three-dimensional VIC method is a mixed Eulerian-Lagrangian method, the numerical diffusion which exists in the purely Eulerian method (e.g., finite difference approximations) used by Rogers and Moin (1987) and Kida and Tanaka (1994) can be reduced.

2.2. Vortex-Methods Applied for the Numerical Simulation of Mixing Layers

An extensive review of mixing layer simulations and experimental results is discussed in Ho and Huerre (1984). In this section the literature concerned with the application of the vortex method to incompressible mixing layers is reviewed, specifically the two-dimensional formulations. Works by Ashurst (1979), Inoue (1985), Leonard (1980), Ng and Ghoneim (1985), Ghoneim and Ng (1986), Lin and Pratt (1987), Milane and Nourazar (1994) and Abdolhosseini and Milane (1998) are among the numerous computational simulations of two dimensional mixing layers that utilize the vortex method. Ashurst (1979) used blobs and the random walk technique (Chorin, 1973), to simulate the mixing layer and concluded that pairing is the primary growth mechanism of mixing layers and is responsible for the entrainment of the surrounding non-turbulent fluid. His first calculation was with constant core radius blobs at a low Reynolds number which did not give satisfactory results. The

r.m.s. longitudinal and lateral velocity fluctuations were in good agreement with the experiment, while the Reynolds shear stress was twice the experimental value. In order to improve the results, he used an exponentially spreading blob, which produced results, in good agreement with experiment. Inoue (1985) attributed the entrainment of the non-turbulent fluid into the mixing layer region partly to the vortex pairing and mostly to the vertical velocity induced by the Biot-Savart law. In the other simulation of the mixing layer reported by Leonard (1980), he used a Gaussian distribution of vorticity inside the vortex core to simulate the effect of viscosity, instead of using Chorin's random walk.

There has been increasing interest in the study of the effect of forcing on the structure of mixing layers. Inoue (1985) and Ng and Ghoneim (1985) simulated unforced layers, while Inoue and Leonard (1987) and Ghoneim and Ng (1986), reported the effect of harmonic forcing on the formation of large structures in mixing layers. Their results for the forced mixing layer were in excellent agreement with experiment, while the r.m.s. lateral velocity fluctuations for unforced mixing layer simulation was twice the experimental values. They concluded that the differences between the experimental and numerical results, were mainly due to the neglect of the effect of the third dimension in calculations. Since forcing has a suppressing effect on the third dimension, a forced mixing layer can be considered a two-dimensional flow, but the unforced mixing layer is three-dimensional (Oster and Wygnansky, 1982).

Inoue (1992) extended the work of Inoue and Leonard(1987) to study the effect of double frequency forcing on the development of the mixing layers. He examined the effect of amplitude and relative phase shift between the two forcing frequencies. His results showed that if the forcing frequency, the phase shift and the forcing amplitude are suitably selected, the growth of a mixing layer

and the number of merging vortices can be effectively controlled.

Aref and Siggia (1980) calculated the roll-up of a two-dimensional mixing layer by using the vortex-in-cell method. Their simulation was for a temporally growing mixing layer in which the velocities of the flows above and below the splitter plate are in opposite directions. Their results for the r.m.s. longitudinal and lateral velocity fluctuations and the Reynolds shear stress indicated much larger values than the experimental results. They attributed the differences to the effect of viscosity and vortex stretching which is due to the non-negligible effect of three-dimensionality. Inoue (1985) attributed the disagreement between Aref and Siggia's results and many experimental observations to their fourth order integral scheme rather than the other effects. He used a first order Euler scheme for time integration with larger time steps. His results showed that the r.m.s. lateral fluctuations are smaller than the r.m.s. longitudinal fluctuations which was in reasonably good agreement with the experiments. Mansour (1985) used a two-dimensional hybrid scheme for a spatially growing mixing layer. He divided the computational domain into two regions and solved the vorticity equation by different methods. He applied a two-dimensional vortex-in-cell method in the upstream region immediately after the splitter plate where the turbulent eddies are small relative to the size of grids and an Eulerian method (finite difference) in the downstream region where the eddies are larger than the grids. His results showed that the r.m.s. longitudinal velocity fluctuations was over-predicted whereas the r.m.s. lateral velocity fluctuations was about the same as the experimental values. In two-dimensional simulations, the r.m.s. lateral velocity component is expected to be greater than the experimental results, because the energy transfer from the streamwise component is only to the cross-stream component. Kuwahara and Takami (1983) investigated the amalgamation of two eddies by using first order and fourth order schemes for the time integration. They concluded that for the first

order scheme, there is a built-in eddy-viscosity modelling due to the larger numerical errors. They also concluded that introducing more viscosity has a suppressing effect on the roll-up and vortex pairing processes. In addition, results of Nakamura et al. (1982) showed that the effective viscosity for first order Euler scheme with small time steps is the same as fourth order Runge-Kutta with the larger time steps.

Lin and Pratt (1987) utilized a hybrid method for numerical simulation of the turbulent mixing layer. They applied LES to predict the turbulent scalar transport. They also used the Monte-Carlo technique to solve the time dependent scalar concentration field. Their results for statistical quantities such as the mean velocity, the growth rate, the r.m.s. velocity fluctuations and the Reynolds shear stress are quantitatively in agreement with experiments, except for the r.m.s. lateral velocity fluctuations which was over-predicted. The discrepancies between their results and experimental values were due to inadequate modelling of the eddy viscosity and the non-negligible three-dimensionality effect.

Recently, the numerical simulations of two-dimensional shear layers has been extended to three dimensions. Since the effect of small scales becomes more important for higher Reynolds numbers, the direct numerical simulation of a three-dimensional spatially growing mixing layer for high Reynold numbers is not possible in the foreseeable future. In the past few years there have been several numerical simulations of three-dimensional shear flows for low and moderate Reynold numbers, which have relied on various simplifying assumptions. Examples of these works are Couet et al. (1981), Ashurst and Meiburg (1988), Metcalf et al. (1987), Knio and Ghoniem (1988, 1990, 1991) and Fishelov (1990).

2.3 Uniformly Sheared Flow

2.3.1. Experimental Works in Uniformly Sheared Flows

Uniform-mean-gradient shear flow is of special interest due to its similarity to real physical situations such as turbulent boundary layers, mixing layers, jets and wakes. It is also a valuable tool for the verification of turbulence models and turbulent combustion models such as flame stretch.

There have been numerous experiments attempting to generate and investigate various aspects of uniformly sheared turbulent flows. The first attempt using a wind tunnel was made by Rose (1966). His results showed that the integral length scales and Taylor micro scales vary in the cross-stream direction due to the mean shear generator mechanism. This difficulty was overcome by Champagne et al. (1970), who used a setup consisting of a row of equally spaced channels with adjustable internal resistance. Harris et al. (1977) were the first to recognize that the value of the non-dimensional time (τ) determines whether or not the Reynolds stresses and turbulent kinetic energy are growing with the streamwise direction. The non-dimensional time τ is $K_s\, x$, where K_s is the flow generator constant defined as $1/U_c(dU/dy)$, where U_c is the centerline mean velocity, dU/dy is the shear rate and x is the streamwise coordinate. Tavoularis (1985) showed that the turbulent kinetic energy grows exponentially in the asymptotic development range as $e^{\kappa\tau}$ where κ was found to be about 0.1 for the high shear rate experiments by Tavoularis and Karnik (1989). Rohr et al. (1988) produced a uniformly sheared flow using a ten-layer closed loop water tunnel. The same Reynolds number with a much smaller mean velocity was obtained because the kinematic viscosity of water is approximately fifteen times smaller than air. In addition, the authors pointed out that the differences in the growth

rates between the experimental results can be reduced if the non-dimensional time (τ), is used instead of the streamwise coordinate (x). The above comment is in agreement with the findings of Harris et al. (1977), regarding the importance of the non-dimensional time.

Rose (1966), Champagne et al (1970) and Mulhearn and Luxton (1975) obtained non-growing downstream Reynolds stresses because of the small values of τ (τ<5), whereas Harris et al (1977), Tavoularis and Corrsin (1981), Rohr et al (1988) and Tavoularis and Karnik (1989) showed that given sufficient non-dimensional time (τ >8), the Reynolds stresses increase monotonically. In a more recent investigation, Souza (1993) conducted measurements in a high speed uniformly sheared turbulent flow with *dU/dy* ranging from 436 to 705 s^{-1} and Mach number below 0.2. Her measurements showed qualitatively the same results for downstream growth rate of the turbulent kinetic energy. However the Reynolds shear stress was lower than in experiments with a lower shear rates, e.g., 84 s^{-1} in Tavoularis and Karnik (1989).

2.3.2. Direct Numerical Simulation of Uniformly Sheared Flow

Currently available computational capabilities have made the numerical investigation of shear flows using the DNS method feasible. In a DNS method, all scales of motion should be resolved, which needs a very small grid size and time step. the simulation presented in this work is not a real DNS of the shear flow, for two reasons. Firstly, the grid size is not as small as the smallest eddies. Secondly, the mechanism of generation of small scale structures is not provided in the simulation.

However, the current simulation contains some features of a DNS work, because velocity fluctuations are resolved in time and space and the motions of all vortices are traced in time and then an ensemble average is taken. Therefore, a review of the previous works using the DNS of uniformly sheared turbulent flows is discussed in this section.

Shirani et al. (1981) used the spectral method and concentrated on the case where the mean scalar gradient was imposed in the same direction as the mean shear. Since their computation used a relatively coarse grid, no effort was made to search for organized turbulent structure. Feiereisen et al. (1981) applied the spectral method to simulate incompressible and compressible sheared flows. They did not report the streamwise variation of the Reynolds stresses, but they compared the pressure-strain terms with the predictions of turbulence models. Rogers and Moin (1987) simulated the structure of the vorticity field in uniformly sheared turbulent flows. They used the DNS of a three-dimensional, incompressible, time-dependent Navier-Stokes equation using Rogallo's (1981) computer code. The initial velocity field was random, subject to the constraint of continuity and a specified isotropic energy spectrum. The streamwise variation of the component energy ratios were in agreement with the experimental results of Tavoularis and Corrsin (1981) in the range $8<\tau<12$. They found in all cases, the presence of coherent vortical structures. The results for three different flow fields showed that the vorticity tends to be aligned with the direction of positive strain. Their results also show that in the early development of the flow, the angle of inclination of most of the vortical structures lies near 45°, which after the flow develops, decreases to between 35° and 40°. Lee et al (1990) investigated the structure of highly sheared homogeneous turbulent flows using the pseudo-spectral code developed by Rogallo (1981). They applied a combination of DNS and the rapid distortion theory (RDT) to calculate the instantaneous flow fields. The initial velocity field was

isotropic as in Rogers and Moin (1987). Their results showed that turbulent kinetic energy is increasingly concentrated in the streamwise component with increasing downstream position, suggesting that a prolonged shear ($\tau \to \infty$) would produce asymptotically a one component turbulence, i.e., the streamwise component of turbulent kinetic energy becomes much higher than the other components. Higher order finite difference methods have also been used by Rai and Moin (1989). They simulated a fully developed turbulent shear flow using fifth order upwind differences for the convective term and sixth order central difference for the viscous term. Their results showed good agreement between the finite difference results and the spectral calculations. The numerical simulation of uniformly sheared flow by Kida and Tanaka (1994) indicates that, at an earlier time, the peak of the angle of the vortical structures with the horizontal plane appears at 45°. However, as times goes on, the peaks become sharper, representing longitudinal vortices that are being generated. The angle of the filaments with the horizontal plane moves toward 0° and the fluctuating vorticity inclines more toward the streamwise direction. This movement, however, decelerates at later times and the position of the peaks eventually stays around 20° with the xy-plane. Jacobitz et al (1997) used a spectral method to simulate the evolution of turbulence in a uniformly sheared stratified flow. They found an exponential growth rate for the evolution of the turbulent kinetic energy. Their results showed that larger shear rates do not necessarily lead to larger values of the asymptotic growth rate of turbulent kinetic energy.

To the author's knowledge, the vortex method has not yet been used to simulate uniformly sheared flow and the present work is the first attempt to apply a mixed Lagrangian- Eulerian approach to this problem.

2.4. Validity of Two-Dimensional Vortex Method

It is well known that vortex stretching in mixing layers and uniformly sheared flow is a major contributor to turbulence production. It is, therefore, somewhat surprising that the two-dimensional vortex method predicts some of the physics of mixing layers and uniformly sheared flow. A tentative explanation based on what has been reported in the literature is given in the next three subsections.

2.4.1. Phenomenological Description of Turbulence Production in a Uniformly Sheared Flow

In a uniformly sheared flow, the initially straight and parallel vortex filaments (see figure 2.1), are shown to be unstable against some disturbances (Hinze, 1975). The disturbances deform (stretch and bend) the straight vortex filaments. Self-induction effects and nonuniform mean-velocity distribution further deform the vortex farther downstream. This process leads to the formation of horseshoe vortices which are also called hairpin vortices (see the last stage in figure 2.1). The upper part of the horseshoe vortex is transported into a higher velocity region and the lower part of it is transported into a lower velocity region. This movement further stretches and bends the vortex filaments in the streamwise direction and forms pairs of opposite signs streamwise vorticity. Unlike the initial filaments which have only the spanwise component, the deformed vortex filaments have components in the streamwise, cross-stream and spanwise directions. The streamwise and cross-stream components of the vorticity contribute to the velocity fluctuations in the spanwise direction. Therefore, the generations of streamwise and cross-stream vorticity is attributable to the three-

dimensional deformation of the vortex filaments. Evidence for the phenomenon described above, is provided experimentally for mixing layers and numerically for uniformly sheared flows. Bernal and Roshko (1986) showed experimentally that unforced mixing layers exhibit hairpin vorticity structures (figure 2.2). Rogers and Moin (1987) reported hairpin structures in the numerical prediction of uniformly sheared flows (figure 2.3). Some experimentalists (Muller and Gyr 1986; Kiya 1989) have reported the existence of hairpin vortices in the backward facing step flow as another example of a mixing layer. Figure 2.4 shows a vertical cross-section of the longitudinal vortices in a backward facing step (Neto et al, 1993). The hairpin counter-rotating vortices are shown in this figure.

2.4.2. Stretching in Two-Dimensional Flows

Knio and Ghoniem (1989) reported that a two-dimensional mixing layer develops by the migration of vortices and accumulation of them in clusters of vortices. These clusters of vortices expand in the cross-stream direction and then collapse toward the streamwise direction. This process stretches and flattens the initially circular clusters into elliptical structures whose shearing action results in further thinning of the regions between the clusters (usually called braid regions). The word "stretch" is used here to signify the deformation and flattening of collections or cores of vortices which is different from the stretch of a vortex filament used in three-dimensional simulations. Therefore, in a two-dimensional simulation vortex stretching is reproduced by stretching the collection of the vortices. This also corresponds to the description of Sarpkaya (1994) who argued that a similarity exists between three-dimensional vortex stretching and stretching vorticity gradient in two-dimensional simulations.

2.4.3. Energy Transfer in a Two-Dimensional Uniformly Sheared Flow

The turbulent kinetic energy is defined by $K=1/2\ \overline{u_i u_i}$. For a uniformly sheared flow with $dU/dy = constant$, the balance of the instantaneous kinetic energy of each component can be written as (Tennekes and Lumley, 1977):

$$1/2D\overline{u^{'2}}/Dt = -\overline{u'v'}\,\partial U/\partial y + \overline{p'/\rho\,\partial u'/\partial x} - \partial/\partial y\,(\overline{1/2\,u'^2 v'}) - 1/3\epsilon \qquad (2.1)$$

$$1/2D\overline{v^{'2}}/Dt = 0 + \overline{p'/\rho\,\partial v'/\partial y} - \partial/\partial y\,(\overline{p'/\rho + 1/2\,v'^2)\,v'} - 1/3\epsilon \qquad (2.2)$$

$$1/2D\overline{w^{'2}}/Dt = 0 + \overline{p'/\rho\,\partial w'/\partial z} - \partial/\partial y\,(\overline{1/2\,w'^2 v'}) - 1/3\epsilon \qquad (2.3)$$

These equations show that for a shear flow in the streamwise direction with $dU/dy = constant$, the production of the turbulent kinetic energy contributes to u'^2 only (the first equation), and there is no production term in the equations for v'^2 and w'^2. Energy has to be transferred to v'^2 and w'^2 by the terms associated with pressure-velocity correlations because the incompressibility condition implies that the sum of the pressure terms is equal to zero:

$$\overline{p'\partial u'/\partial x} + \overline{p'\partial v'/\partial y} + \overline{p'\partial w'/\partial z} = 0. \qquad (2.4)$$

Therefore the pressure-strain terms exchange energy between components, without changing the total amount of energy (Tennekes and Lumley, 1977). In two-dimensional flows the spanwise component, w', disappears, but the production of the turbulent kinetic energy exists and contributes to u'^2 only,

as in the three-dimensional situation. By definition, a two-dimensional flow is a flow in which there is no mean velocity in the third dimension ($W=0$). This means that although the instantaneous velocity vectors may have the spanwise component ($w\neq 0$), the time average of the velocity in the third-dimension must be zero at any point. In a two-dimensional numerical simulation, the assumption is different from the above, and both the mean and the fluctuating velocity components in the third dimension are zero ($W=w=0$). Based on this assumption, in a two-dimensional simulation, the energy is transferred from u' to v' component only, following the incompressibility condition as

$$\overline{p'\partial u'/\partial x} + \overline{p'\partial v'/\partial y} = 0. \qquad (2.5)$$

Therefore v', in a two-dimensional simulation, is expected to be larger than the experimental values, as reported in two-dimensional vortex method. It is noteworthy that, in reality, there are no two-dimensional turbulent flows, but a two-dimensional simulation may predict some physics of turbulent flows, specially when the flow field is dominated by two-dimensional large structures, as in the mixing layers.

2.5. Green's Function Method versus Vortex-in-Cell Method

The solution of a Poisson equation, which satisfies the convection part of the vorticity transport equation is governed by the Green's function or the Biot-Savart law of interaction (Batchelor, 1967). In this approach, vortices are tracked in a Lagrangian frame, and the velocity field is calculated by the Boit-Savart formula. For more details see, e.g., Sarpkaya (1994).

There are some difficulties using a Green's function approach. First, the singularities that each vortex has, creates large velocities in their neighbourhood, which causes numerical as well as theoretical instabilities. To overcome this difficulty, finite core size vortices or blob vortices, may be used instead of point vortices (e.g., Chorin, 1973). With this approach, inside the core, the velocity is smooth and is finite at the centre of the core. Although this trick creates some errors, it is very effective in removing the singularities from the flow field. By using this technique the velocity field induced by each vortex is quantitatively correct, away from the centre of the vortices. The second difficulty in the Green's function method is the computational cost. With N discrete vortices involved in computation, the total number of calculations required in each time step is proportional to N× N. Therefore, for a large number of vortices the computational time increases significantly.

In order to dispense with the errors and difficulties generated by the application of the Green's function method, an alternative method can be constructed which is independent of the vortex core size. This method is neither pure Lagrangian nor pure Eulerian, but a hybrid of these two methods, because the pure Eulerian method is unable to resolve sharp interfaces and pure Lagrangian method is computationally expensive and generates acceptable results only when the core size is non-zero. The alternative is a mixed Lagrangian-Eulerian method called the vortex-in-cell (VIC) or cloud-in-cell(CIC) method. A VIC method can be a DNS type, provided that the grid size is as small as the smallest eddy in the flow (which depends on the Reynolds number), and a proper mechanism for break-up and reconnection of the vortex filaments is employed. There is a built-in eddy-viscosity model inherent in the VIC method which makes it appropriate for the simulation of turbulent flows only. This built-in viscosity is larger, if a first-order Euler scheme is used for displacement of the vortices (Nakamura et al, 1982). The VIC method, in general, is a vortex method and vortex methods

are numerical tools for the simulation of flows with vorticity. Since vorticity is important in turbulent flows and it is one of the main features in characterization of turbulent flows, therefore a VIC method is an appropriate tool for the numerical simulation of turbulent flows and its use for a laminar flows is not considerable. One of the main advantages of the VIC method is that the solution of the velocity field can be performed by solving the Poisson equation using a finite difference method. If M_x and M_y are the number of mesh points in the x and y directions, for $M_x \times M_y$ mesh points the order of computations for a Poisson solver is usually $M_x M_y \log(M_x M_y)$ which is independent of the number of vortices N. (see, e.g., Sarpkaya, 1994). However, the number of grid points $M_x M_y$ in a typical two dimensional problem are usually of the same order of magnitude as the number of the vortices. Thus, the velocity field calculations don't increase as N×N as in the Green's function method, and also using larger number of vortices does not increase the computational effort as quickly.

2.6. Objectives

This thesis is concerned with a mixed Lagrangian-Eulerian description of the evolution of a discretized vorticity field. As discussed in section 2.1, the primary objective of this work was to apply a two-dimensional vortex-in-cell (VIC) method to reduce the computational time in the numerical simulation of spatially growing mixing layers, and after validating the results of the mixing layers, to apply the VIC method, to the numerical simulation of two-dimensional uniformly sheared flows. The objectives of the thesis were extended to include the three-dimensional simulation of uniformly sheared flows, due to the fact that the uniformly sheared flow is structurally different from mixing layers and ignoring the three-dimensionality of the flow in a uniformly sheared flow introduces more errors in

the calculations than in a mixing layer simulation. Therefore, this work consists of three parts, namely, the two-dimensional spatially growing mixing layers, the two-dimensional uniformly sheared flow and the three-dimensional uniformly sheared flow.

In the first part of this thesis, a spatially growing mixing layer is simulated using the vortex-in-cell method. The vortex-in-cell method is chosen to avoid the large amount of computer time required in the pure Lagrangian method. The formation of the coherent structures is investigated and the root-mean-square longitudinal and lateral velocity fluctuations and negative average cross-stream correlation($-\overline{u'v'}$) are calculated. The effect of numerical parameters such as number of vortices and averaging time on the evolution of the vorticity field is investigated, and the results of the simulation are validated through comparison with the results of the grid-free Lagrangian method and experiments.

The second part of this thesis is the numerical simulation of a two-dimensional uniformly sheared flow. This is the first time that the numerical simulation of a uniformly sheared turbulent flow is accomplished using a vortex-in-cell method. The vortex-in-cell method seems to be an appropriate technique to handle this problem, rather than the Lagrangian grid-free vortex method, because a large number of vortices are required for the calculations. In reporting the results of the simulation of uniformly sheared flow, special importance is given to the dimensionless time (τ), which is used in most previous work, e.g. Tavoularis and Karnik (1989), and has a fundamental role in characterizing the development of the uniformly sheared flows. The effect of the flow generator constant (K_s) on the evolution of the streaklines of the vortices, on the downstream growth rate of the root-mean-square longitudinal and lateral velocity fluctuations and negative average cross-stream correlation($-\overline{u'v'}$), and on the turbulent kinetic energy is investigated.

In the third part of this work, a three-dimensional simulation of the uniformly sheared flow

is performed as an extension of the two-dimensional simulation. The effect of stretching which is a fundamental feature of the three-dimensional turbulence, is taken into account in this part of the thesis. The methodology is based on a three-dimensional mixed Lagrangian-Eulerian method, with a vortex-in-cell scheme. The objectives are to study the evolution of the three-dimensional vortex filaments. The present three-dimensional simulation may not provide a complete view of the turbulent structures because generation of small scale structures by break-up of the filaments is not modelled in this work. Therefore, the ability of the simulation is confined to the early development of the flow field where filaments have not yet broken-up.

Chapter 3

Formulations and Mathematical Models

3.1 Vorticity equation

Vorticity is not a primary variable in flow calculations, but it has a vital importance in fluid mechanics. When performing a numerical calculation of a viscous and incompressible flow by vortex methods, one should start the calculations by writing the governing equations in a vorticity transport equation form. Turbulence is rotational and contains high levels of fluctuating vorticity. Therefore, vorticity is one of the main features that characterizes the level of turbulence in the fluid.

Vorticity is defined as the curl of the velocity vector,

$$\boldsymbol{\omega} = curl\, \boldsymbol{u} = \nabla \times \boldsymbol{u} \qquad (3.1)$$

or using index notation,

$$\omega_i = \varepsilon_{ijk} \frac{\partial u_k}{\partial x_j} \qquad (3.2)$$

where ε_{ijk} is the alternating tensor. The divergence of vorticity is zero, because the divergence of a curl vector is zero

$$div\omega = div\ curl\ \boldsymbol{u} = 0 \tag{3.3}$$

Therefore, in mathematics, the vorticity vector is called solenoidal.

The vorticity transport equation can be derived from the momentum equation. Starting with the Navier-Stokes equation (Schlichting, 1968),

$$\rho\left(\frac{\partial u_i}{\partial t}+u_j\frac{\partial u_i}{\partial x_j}\right) = -\frac{\partial P}{\partial x_i} + \frac{\partial}{\partial x_i}\left[\ \mu\left(\frac{\partial u_i}{\partial x_j}+\frac{\partial u_j}{\partial x_i}-\frac{2}{3}\delta_{ij}\frac{\partial u_k}{\partial x_k}\right)\ \right] \qquad i,j,k=1,2,3 \tag{3.4}$$

for an incompressible Newtonian fluid with constant viscosity the momentum equation becomes

$$\frac{\partial u_i}{\partial t}+u_j\frac{\partial u_i}{\partial x_j} = -\frac{1}{\rho}\frac{\partial P}{\partial x_i} + \nu\frac{\partial u_i^2}{\partial x_j \partial x_j} \tag{3.5}$$

By some manipulations the convective and the viscous terms in eq.(3.5) can be expressed as, (Tennekes and Lumley, 1977),

$$u_j\frac{\partial u_i}{\partial x_j} = -\varepsilon_{ijk}u_j\omega_k + \frac{\partial}{\partial x_i}\left(\frac{1}{2}u_j\ u_j\ \right) \tag{3.6}$$

$$\nu\frac{\partial u_i^2}{\partial x_j \partial x_j} = -\nu\ \varepsilon_{ijk}\frac{\partial \omega}{\partial x_j} \tag{3.7}$$

Substituting eq.(3.6) and eq.(3.7) into eq.(3.5) results in another form of the incompressible, constant viscosity Navier-Stokes equations

$$\frac{\partial u_i}{\partial t} = \frac{\partial}{\partial x_i}\left[\frac{P}{\rho} + \frac{1}{2}(u_j u_j)\right] + \varepsilon_{ijk} u_j \omega_k - \nu \varepsilon_{ijk} \frac{\partial \omega_k}{\partial x_j} \qquad (3.8)$$

The vorticity transport equation can be obtained by taking the curl of eq.(3.8),

$$\frac{\partial \omega_p}{\partial t} = -\varepsilon_{pqi} \frac{\partial^2}{\partial x_i \partial x_q}\left[\frac{P}{\rho} + \frac{1}{2}(u_j u_j)\right] + \varepsilon_{pqi}\varepsilon_{ijk}\left[\frac{\partial}{\partial x_q}(u_j \omega_k) - \nu \frac{\partial^2 \omega_k}{\partial x_q \partial x_j}\right] \qquad (3.9)$$

and using the tensor identity, $\varepsilon_{pqi}\varepsilon_{ijk} = \delta_{pj}\delta_{qk} - \delta_{pk}\delta_{qj}$, to obtain

$$\frac{\partial \omega_p}{\partial t} = -\varepsilon_{pqi} \frac{\partial^2}{\partial x_i \partial x_q}\left[\frac{P}{\rho} + \frac{1}{2}(u_j u_j)\right] + (\delta_{pj}\delta_{qk} - \delta_{pk}\delta_{qj})\left[\frac{\partial}{\partial x_q}(u_j \omega_k) - \nu \frac{\partial^2 \omega_k}{\partial x_q \partial x_j}\right] \qquad (3.10)$$

The first term on the right-hand side of equation 3.10 (i.e., the pressure term) is zero because it involves the product of the skew-symmetric tensor ε_{pqi} and the symmetric tensor operator $\partial^2/\partial x_i \partial x_q$ (see Tennekes and Lumley, 1977). The second term on the right-hand side can be reduced when accounting for all of the Kronecker deltas in equation (3.10). The Kronecker delta (δ_{ij}) is equal to one if $i=j$ and is equal to zero otherwise. Therefore, equation (3.10) reduces to

$$\frac{\partial \omega_p}{\partial t} = \omega_k \frac{\partial u_p}{\partial x_k} - u_k \frac{\partial \omega_p}{\partial x_k} - \nu \frac{\partial}{\partial x_p}\left(\frac{\partial \omega_k}{\partial x_k}\right) + \nu \frac{\partial^2 \omega_p}{\partial x_k \partial x_k} \qquad (3.11)$$

The third term on the right-hand side of this equation is zero because as noted earlier in this section,

the divergence of a curl vector is zero (see equation (3.3)). Thus, the three dimensional vorticity transport equation is:

$$\frac{\partial \omega_i}{\partial t} + u_j \frac{\partial \omega_i}{\partial x_j} = \omega_j \frac{\partial u_i}{\partial x_j} + \nu \frac{\partial^2 \omega_i}{\partial x_j \partial x_j} \qquad (3.12)$$

This equation is also known as the Helmholtz equation of hydrodynamics. Another common form of this equation is:

$$D\omega/Dt = (\omega . \nabla)u + \nu \nabla^2 \omega \qquad (3.13)$$

where ω is the vorticity vector. The left-hand side (L.H.S.) of this equation includes the local and convective terms. The first term on the right-hand side (R.H.S.) of the equation is called the vortex stretching term which is derived from the convective derivative, and is zero for two-dimensional cases. The second term on the R.H.S. shows the viscous diffusion.

There are some useful results obtained by neglecting the viscous term. In this case, eq.(3.13) reduces to the equation of motion for an ideal fluid:

$$D\omega/Dt = (\omega . \nabla)u \qquad (3.13\text{-}a)$$

The term $(\omega . \nabla)u$ is constant for an ideal fluid (see e.g. Karamcheti, 1976). This leads to Helmholtz' theorem, that the vorticity of a fluid element remains a constant for an ideal fluid. Furthermore, the term $(\omega . \nabla)u$ is zero in two-dimensional and axisymmetrical flows. Therefore, for a two-dimensional flow of an ideal fluid, equation (3.13-a) reduces to

$$D\omega/Dt=0 \qquad (3.14)$$

The other result is Kelvin's theorem which states that the circulation around a closed curve moving with the fluid is constant. This is the theorem of conservation of circulation (see e.g. Karamcheti, 1976):

$$D\Gamma/Dt=0 \qquad (3.15)$$

where Γ is the circulation. In this work we have used the theorem of conservation of circulation in both the two-dimensional and the three-dimensional simulations. Based on this theorem, when a vortex element (in the two-dimensional simulation) or a vortex filament (in the three-dimensional simulation) is introduced into the flow field, it's circulation remains constant throughout the simulation. Another aspect of Helmholtz theorem that we have used in the three-dimensional simulation is that vortex filaments never end in the fluid. They either form closed loops or end at a fluid boundary.

3.2. Two-Dimensional Formulation

As mentioned in the last section, the stretching term (the first term on the R.H.S. of equation (3.13)) vanishes in two-dimensional cases, because the vorticity vector, ω is perpendicular to the gradient of **u**. Thus, the vorticity transport equation reduces to

$$D\omega/Dt = \nu\nabla^2\omega \qquad (3.16)$$

and since **u**=**u**(x,y,t) only, the vorticity vector reduces to one component in the z direction perpendicular to the xy-plane (the plane of the motion),

$$\omega = \frac{\partial v}{\partial x} - \frac{\partial u}{\partial y} \qquad (3.17)$$

From vector calculus, if the divergence of a vector is zero, that vector can be expressed as the gradient of a scalar. By using the continuity equation:

$$\frac{\partial u}{\partial x} + \frac{\partial v}{\partial y} = 0 \qquad or \qquad \nabla . \boldsymbol{u} = 0 \qquad (3.18)$$

the velocity **u** can be expressed in terms of a stream-function ψ such that:

$$u = \frac{\partial \psi}{\partial y} \quad , \quad v = -\frac{\partial \psi}{\partial x} \qquad (3.19)$$

Combining equations(3.19) and (3.17), Poisson's equation is obtained:

$$\nabla^2 \psi = -\omega_z \qquad (3.20)$$

Equations (3.19) and (3.20) can be used to determine the velocity field, in which the vorticity

distribution is given by the R.H.S. of equation (3.20).

3.2.1. Fractional Step Method

In this work the method of fractional steps is used to solve the vorticity equation (3.16). This method is helpful for multidimensional problems and higher order partial differential equations, because it usually reduces the dimensions and order of the equations to a series of steps, each of which involves only one part of the equation. An extensive description of this method may be found in Yanenko(1971).

In the vortex method, equation (3.16) is split in two fractional steps,

$$\frac{\partial \omega_z}{\partial t} + u\frac{\partial \omega_z}{\partial x} + v\frac{\partial \omega_z}{\partial y} = 0 \qquad (3.21)$$

$$\frac{\partial \omega_z}{\partial t} = \nu \left(\frac{\partial^2 \omega_z}{\partial x^2} + \frac{\partial^2 \omega_z}{\partial y^2}\right) \qquad (3.22)$$

In the first fractional step (eq. 3.21), the convection due to the action of the vortices is considered. Further details about this step will be discussed in sections 3.2.2. and 4.1.3. The second fractional step is the diffusion of vorticity, which will be discussed in section 3.2.4.

The essence of applying the fractional step in the vorticity transport equation is that, in one fractional step the flow is considered non-viscous, so that the theorem of conservation of vorticity and circulation could be applied. Using the second fractional step, the viscosity effect is handled. This technique is well suited for slightly viscous flows.

3.2.2. Convection due to Vortex Action

The first fractional equation, (3.21), which is for two-dimensional motion of an incompressible, invicid fluid governs the evolution of vorticity (a conservative scalar in a two-dimensional simulation), that is transported solely by the convection of the fluid. In a vorticity-stream function formulation, the solution of equation (3.21) is equivalent to the solution of the Poisson equation (3.20). Therefore, the stream function is calculated by solving the Poisson equation and then, using equation (3.19) the velocity components are obtained. In the first fractional step, since vorticity is conserved, then

$$\omega(\chi(x,y,t),t))=\omega(\chi(x,y,0),0) \qquad (3.23)$$

where χ is the trajectory of the vortices governed by

$$d\chi/dt= \boldsymbol{u}(\chi(x,y,t)) \qquad (3.24)$$

In order to calculate the velocity of the vortices and to convect them, a vortex-in-cell (VIC) method is used in this work. Details of the numerical scheme using the VIC method is discussed in chapter 4.

3.2.3. Diffusion Equation

The second fractional equation, eq.(3.22), governs the effect of diffusion on the transport of

vorticity. Disregarding eq. (3.22) is an approximation of the vorticity equation for infinite Reynolds number, or zero viscosity. In the vortex method the effect of viscosity has been incorporated in two ways as follows.

3.2.3.1. Core Spreading Method

Core spreading is giving the vortices a rotational core and expanding the core of each vortex while keeping the total circulation constant. The size of each vortex in this method is a function of viscosity and age. It is usually assumed that the cores of the vortices have a Gaussian vorticity distribution and the size of their core increases according to

$$\sigma^2=\sigma_0^2+4\nu t \qquad (3.25)$$

where σ is the core radius, σ_0 is the initial core radius, ν is kinematic viscosity and t is time. Using this method, gives acceptable results for the effect of diffusion of vorticity. However, Greengard (1985), showed that the core spreading method approximates the wrong equation.

3.2.3.2. Constant Core Method: Random-Walk

The second method for treatment of the diffusion equation is to assume each vortex has a finite and constant vorticity, and apply the random-walk method (Chorin, 1973). This technique is used in this work, and a brief description of it is presented in this section.

The random-walk process in vortex method was first introduced by Chorin (1973) to model

the diffusion effect. He showed that, for the slightly viscous flow, the random-walk solution is an approximation to the solution of the diffusion equation. According to this method, the diffusion equation governs the probability of the existence of particles moving randomly, like Brownian motion. Therefore, the random-walk process is a statistical method of reproducing the viscous effect. The step length in the random-walk with a Gaussian probability distribution is proportional to $(\nu\Delta t)^{1/2}$, where ν is the kinematic viscosity and Δt is the time step used in the simulation. So, the solution of the diffusion equation by the random-walk may be superimposed on the motion due to the convection of the particles obtained from the first fractional step, according to

$$x_n(t+\Delta t) = x_n(t) + u_n\Delta t + \eta_1 \qquad (3.26\text{-}a)$$

$$y_n(t+\Delta t) = y_n(t) + v_n\Delta t + \eta_2 \qquad (3.26\text{-}b)$$

where x_n and y_n are the coordinates of the vortex element n, and η_1 and η_2 are Gaussian distributed random variables with zero mean and standard deviation $(\nu\Delta t)^{1/2}$.

3.3. Three-Dimensional Formulation

3.3.1. The Vorticity-Stream function Formulation

In the majority of previous investigations, the formulation of incompressible viscous flows using a mixed Eulerian-Lagrangian vortex-in-cell (VIC) method is based on the vorticity-stream function formulation. For two-dimensional flows the vorticity-stream function formulation was

discussed in detail in previous sections. There are several reasons for the popularity of the vorticity-stream function formulation as a basis for Eulerian or mixed Eulerian-Lagrangian methods. Firstly, storage in a computer program has to be provided for only two variables, namely the vorticity (ω) and the stream function (ψ). Therefore, only two-dimensional arrays are required. In comparison, in the primitive variable (u,v) formulation additional arrays for the velocity components should also be provided. The storage requirements are frequently a decisive aspect, especially for problems where high resolution and many grid points are necessary. Secondly, direct use of vorticity as a dependent variable allows better observation and control of vorticity which is an important quantity for viscous flow simulations. Thirdly, plots of streamlines as ψ=constant lines are readily produced. Such plots often provide an excellent survey of the entire flow field and allow insight into a given flow problem. Obvious disadvantages of the vorticity-stream function formulation exist when for unsteady flows, the velocity components u and v are of major interest. In these cases additional calculations are required to determine u and v. The velocity components are necessary, for example to compute the streaklines, which for unsteady flows have more meaning than streamlines, and to compute the Reynolds stresses in turbulent regimes.

The three-dimensional formulation based on a vorticity-stream function is as follows. Using equation (3.13), the expanded form of the vorticity transport equation for three-dimensional flows can be written as (Batchelor, 1967):

$$\frac{\partial \omega_x}{\partial t} + \nabla.(\boldsymbol{u}\ \omega_x) - \boldsymbol{\omega} \cdot \nabla u = \nu \Delta \omega_x \qquad (3.27)$$

$$\frac{\partial \omega_y}{\partial t} + \nabla.(\boldsymbol{u}\ \omega_y) - \boldsymbol{\omega} \cdot \nabla v = \nu \Delta \omega_y \qquad (3.28)$$

$$\frac{\partial \omega_z}{\partial t} + \nabla.(\boldsymbol{u}\ \omega_z) - \boldsymbol{\omega}\ .\nabla w = \nu \Delta \omega_z \qquad (3.29)$$

with the velocity $\boldsymbol{u} = (u, v, w)$ and vorticity vector $\boldsymbol{\omega} = (\omega_x, \omega_y, \omega_z)$. The vorticity vector is defined as

$$\boldsymbol{\omega} = \nabla \times \boldsymbol{u} \qquad (3.30)$$

thus

$$\omega_x = \frac{\partial w}{\partial y} - \frac{\partial v}{\partial z} \qquad (3.31\text{-}a)$$

$$\omega_y = \frac{\partial u}{\partial z} - \frac{\partial w}{\partial x} \qquad (3.31\text{-}b)$$

$$\omega_z = \frac{\partial u}{\partial y} - \frac{\partial v}{\partial x} \qquad (3.31\text{-}c)$$

With the introduction of a vector potential $\boldsymbol{\Phi} = (\phi_x, \phi_y, \phi_z)$ such that

$$\boldsymbol{u} = \nabla \times \boldsymbol{\Phi} \qquad (3.32)$$

and using the definition of the vorticity vector (eq. 3.30), the curl of equation (3.32) results in the

vorticity (ω), being expressed as

$$\boldsymbol{\omega} = \nabla \times (\nabla \times \boldsymbol{\Phi}) = \nabla (\nabla . \boldsymbol{\Phi}) - \nabla^2 \boldsymbol{\Phi} \qquad (3.33)$$

Due to the incompressibility condition

$$\nabla . \boldsymbol{\Phi} = 0 \qquad (3.34)$$

so, the Poisson equation for the vector potential $\boldsymbol{\Phi}$ can be written as

$$\nabla^2 \boldsymbol{\Phi} = -\boldsymbol{\omega} \qquad (3.35)$$

or explicitly for the x, y and z components

$$\partial^2 \phi_x / \partial x^2 + \partial^2 \phi_x / \partial y^2 + \partial^2 \phi_x / \partial z^2 = -\omega_x \qquad (3.36)$$

$$\partial^2 \phi_y / \partial x^2 + \partial^2 \phi_y / \partial y^2 + \partial^2 \phi_y / \partial z^2 = -\omega_y \qquad (3.37)$$

$$\partial^2 \phi_z / \partial x^2 + \partial^2 \phi_z / \partial y^2 + \partial^2 \phi_z / \partial z^2 = -\omega_z \qquad (3.38)$$

These equations, in which the vorticity distributions are given by the right-hand side of the equations, can be used to determine the velocity vector-potential field. Then, using equation (3.32) the components of velocity can be calculated as

$$u = \frac{\partial \phi_z}{\partial y} - \frac{\partial \phi_y}{\partial z} \qquad (3.39\text{-}a)$$

$$v = \frac{\partial \phi_x}{\partial z} - \frac{\partial \phi_z}{\partial x} \qquad (3.39\text{-}b)$$

$$w = \frac{\partial \phi_y}{\partial x} - \frac{\partial \phi_x}{\partial y} \qquad (3.39\text{-}c)$$

It is remarkable that in two-dimensional simulations, this technique is identical to the stream function-based formulation (described in previous sections), because the velocity-vector potential is reduced to the stream-function.

3.3.2. The Vorticity-Velocity Formulation

As noted earlier, disadvantages of the vorticity-stream function systems are obvious when for unsteady flows the velocity components are of major interest. In this case additional numerical operations are necessary to determine the velocity components. Another disadvantage of the vorticity-stream function formulation is that the accuracy of the entire solution is dependent on the accurate calculation of the vorticity on the boundaries. In the other words, implementation of boundary conditions for the three-dimensional case appears to be far more complicated for the vorticity-stream function formulation than for the primitive variable formulation. Finally, the advantage of the vorticity-stream function formulation in requiring less storage due to fewer dependent variables in comparison to other formulations does not extend to the three-dimensional

case, because the scalar stream function and vorticity, transform to the vector-stream-function and vector-vorticity. For these reasons the primitive-variable formulation retains its attraction as a basis for the Eulerian and mixed Eulerian-Lagrangian methods for three-dimensional problems. The formulation for a vorticity-velocity method is as follows:

The governing equations are equations (3.27) to (3.29). The vorticity vector is as described in equation (3.30). Taking the curl of equation (3.30), gives

$$\nabla \times \boldsymbol{\omega} = \nabla \times (\nabla \times \boldsymbol{u}) \tag{3.40}$$

or

$$\nabla \times \boldsymbol{\omega} = \nabla (\nabla . \boldsymbol{u}) - \nabla^2 \boldsymbol{u} \tag{3.41}$$

Using the continuity equation

$$\nabla . \boldsymbol{u} = 0 \tag{3.42}$$

the Poisson equation for the velocity components is obtained as:

$$\nabla^2 \boldsymbol{u} = -\nabla \times \boldsymbol{\omega} \tag{3.43}$$

thus

$$\frac{\partial^2 u}{\partial x^2}+\frac{\partial^2 u}{\partial y^2}+\frac{\partial^2 u}{\partial z^2}=\frac{\partial \omega_y}{\partial z}-\frac{\partial \omega_z}{\partial y} \qquad (3.44)$$

$$\frac{\partial^2 v}{\partial x^2}+\frac{\partial^2 v}{\partial y^2}+\frac{\partial^2 v}{\partial z^2}=\frac{\partial \omega_z}{\partial x}-\frac{\partial \omega_x}{\partial z} \qquad (3.45)$$

$$\frac{\partial^2 w}{\partial x^2}+\frac{\partial^2 w}{\partial y^2}+\frac{\partial^2 w}{\partial z^2}=\frac{\partial \omega_x}{\partial y}-\frac{\partial \omega_y}{\partial x} \qquad (3.46)$$

A definite merit of this formulation, is that boundary conditions for the Poisson equation for the velocity components can be more easily provided as Dirichlet type conditions. On the other hand, finding proper boundary conditions for the governing equations in the vorticity-stream function form is often not as straightforward. Equations (3.44) to (3.46) can be used to determine the velocity field, in which the curl of the vorticity distribution is given by the right-hand side of the equations. The present simulation uses the vorticity-velocity formulation and is based on a fractional step method, which is discussed in the following section.

3.3.3. Fractional Step Method

Similar to what was discussed in section 3.2.1, for the two-dimensional simulation, the method of fractional steps is used for the three-dimensional simulation. In the fractional step method the three-dimensional vorticity equation (3.13) is split into three fractional steps. For the first

fractional step, the convection due to the action of vortices is solved using equations (3.44) to (3.46). Once u, v and w are calculated at the nodes, the velocity components of each vortex in the cell are calculated using a trilinear interpolation. This step will be discussed in section 3.3.3.1. In the second fractional step, a 3-D random walk method is used to handle the diffusion term (i.e., the second term in the right-hand side of equation 3.13). The solution of the diffusion equation by the random-walk is added to the motion resulting from the convection of the vortex elements obtained from the first fractional step. This step will be discussed in section 3.3.3.2. For the third fractional step the vortex stretching term (the first term on the right-hand side of equation 3.13) is computed by applying a finite difference scheme on the nodal points. The third fractional step will be discussed in section 3.3.3.3.

3.3.3.1. Convection due to Vortex Action

The point vortex method is one of the most popular applications of vortex methods. Nevertheless, it cannot describe the three-dimensional flows. In order to simulate the evolution of a three-dimensional turbulent structure, it is natural to represent the vorticity field as a collection of vortex filaments. Therefore, the shear layer is discretized into a set of vortex filaments whose motion is traced in time. As discussed in section 2.4, using the direct summation scheme (Biot-Savart) is applicable only for a small number of vortex elements because it requires the summation of all interactions among all the elements in all the filaments. In this work, as in two-dimensional problems, we employ the vortex-in-cell (VIC) method which creates a mesh record of the vorticity field. The

VIC method speeds up the calculation of the interactions and allows the three-dimensional vortex tracing method to be applied to a space densely filled with vortex filaments. In our model, each vortex filament is described by a succession of closely spaced vortex elements. The computation of convection due to vortex action, as the first fractional step, is by solving the left-hand side of equation (3.13), which is for the three-dimensional motion of an incompressible, invicid fluid. In a Lagrangian scheme, since vorticity is conserved, then

$$\omega\,(\chi(x,y,z,t),t)) = \omega\,(\chi(x,y,z,0),0) \qquad (3.47)$$

where χ is the trajectory of the vortices governed by

$$d\chi/dt = \boldsymbol{u}\,(\chi(x,y,z,t)) \qquad (3.48)$$

3.3.3.2. Diffusion Equation: Three-Dimensional Random Walk

The second fractional equation, governs the effect of diffusion on the transport of vorticity (second term on the right-hand side of equation 3.13). The method is similar to what was discussed for the two-dimensional formulation in section 3.2.3.2. In a three-dimensional simulation, three random numbers with zero mean and standard deviation $(\nu\Delta t)^{1/2}$ are generated every time step, and the motion of each vortex element by the random-walk is added on the motion due to the convection of the vortex elements obtained from the first fractional step. Therefore, the new location of each

vortex element is calculated as

$$x_n(t+\Delta t) = x_n(t) + u_n \Delta t + \eta_1 \qquad (3.49\text{-}a)$$

$$y_n(t+\Delta t) = y_n(t) + v_n \Delta t + \eta_2 \qquad (3.49\text{-}b)$$

$$z_n(t+\Delta t) = z_n(t) + w_n \Delta t + \eta_3 \qquad (3.49\text{-}c)$$

where x_n, y_n and z_n are the coordinates of the vortex element n, and η_1 ,η_2 and η_3 are Gaussian distributed random variables with zero mean and standard deviation $(\nu\Delta t)^{1/2}$. In these equations u_n, v_n and w_n are the velocity components of the vortex elements obtained from the first fractional step.

3.3.3.3. Vortex Stretching

For the third fractional step, the vortex stretching term (the first term on the right-hand side of equation 3.13) is computed by solving,

$$\partial\omega/\partial t = \omega . \nabla u \qquad (3.50)$$

or explicitly for x, y and z components

$$\partial\omega_x/\partial t = \omega_x \partial u/\partial x + \omega_y \partial u/\partial y + \omega_z \partial u/\partial z \qquad (3.51)$$

$$\partial\omega_y/\partial t = \omega_x \partial v/\partial x + \omega_y \partial v/\partial y + \omega_z \partial v/\partial z \qquad (3.52)$$

$$\partial\omega_z/\partial t = \omega_x \partial w/\partial x + \omega_y \partial w/\partial y + \omega_z \partial w/\partial z \qquad (3.53)$$

The effect of stretching terms is to modify the values of the components of vorticity at the grid points. Details of the numerical scheme used to solve the above equations will be discussed in chapter four.

Chapter 4

Numerical Approximations and Solution Procedure

4.1. Two-Dimensional Mixing Layer

4.1.1. Description of the Problem

The geometry of the problem to be simulated in the first part of the present study is described as two parallel flows with uniform mean velocities separated by a thin splitter plate. Usually, in the actual mixing layers, a thin boundary layer exists on both sides of the splitter plate, which has not been considered in the present simulation. Therefore, the uniform mean velocities above and below the splitter plate are U_1 and U_2, respectively (fig. 4.1-a). In combustion applications, U_1 and U_2 could be fuel and oxidant. As a result of the velocity discontinuity, a vortex sheet is formed at the interface of the two streams, which rolls up at downstream locations due to the Helmholtz instability. In any shear layer generated at the trailing edge of an aerofoil or at the edge of a splitter plate, the circulation generated across the shear layer should be just enough to make the flow leave the splitter plate or the aerofoil smoothly at the trailing edge (Karamcheti, 1976). Therefore, there is a unique value of

circulation for a flow with velocity discontinuity and consequently a unique solution for that flow. This condition was suggested by Kutta in 1902 and independently by Joukowski in 1906, and is usually called the Kutta condition. In numerical simulations, the velocity difference $\Delta U\ (=U_1 - U_2)$ defines the vorticity density of the vortex sheet. If the circulation of each vortex is indicated by Γ, and d is the initial distance between the neighbouring vortices, the circulation of each vortex to satisfy the Kutta condition is

$$\Gamma = \Delta U \,.\, d \qquad (4.1)$$

and the total circulation of the vortex sheet is

$$\Gamma_{total} = \Delta U \,.\, L \qquad (4.2)$$

where L is the length of the computational domain (see e.g. Sarpkaya, 1994 for details).

4.1.2. Discrete Two-Dimensional Poisson Equation

As discussed in section 3.2, a Poisson equation (eq. 3.20) satisfies the convection part of the vorticity transport equation. The schematic configuration of the flow field is depicted in figure 4.2, which is a rectangular region with a uniform mesh system. Using a central difference scheme for the second derivatives, the Poisson equation is discretized as:

$$\nabla^2 \psi(x_i, y_j) = \frac{\psi(i+1,j) - 2\psi(i,j) + \psi(i-1,j)}{\Delta x^2} + \frac{\psi(i,j+1) - 2\psi(i,j) + \psi(i,j-1)}{\Delta y^2} = -\omega(x_i, y_j) \qquad (4.3)$$

where Δx and Δy are the distances between two neighbouring mesh points in the x and y directions.

For each nodal point, equation (4.3) can be rewritten as:

$$\psi(i,j)=\frac{1}{2(\beta^2+1)}\left[\psi(i+1,j)+\psi(i-1,j)+\beta^2(\psi(i,j+1)+\psi(i,j-1))+\Delta x^2\omega(i,j)\right] \qquad (4.4)$$

where $\beta=\Delta x/\Delta y$. The large number of mesh points suggests that iterative methods are more appropriate compared to the matrix solution. There are several methods of iteration. The iterative solution of equation (4.4), when it is written for all of the nodal points with estimated initial values for internal nodes and given values at the boundaries, is called Liebmann's method. This method is suitable for the computer but the convergence is slow. The iterative method, which converges faster than Liebmann's method, is the relaxation method. The essence of this method is to obtain an initial estimate for each nodal point and then calculate the residuals, $R_{i,j}$, for each point using the following equation:

$$\frac{1}{4}R(i,j)=\left(\frac{1}{2(\beta^2+1)}\left[\psi(i+1,j)+\psi(i-1,j)+\beta^2(\psi(i,j+1)+\psi(i,j-1))+\Delta x^2\omega(i,j)\right]\right)-\psi(i,j) \qquad (4.5)$$

The largest residual is chosen for the next iteration and calculation continues until the residuals are sufficiently small. Although this method converges quickly, it is not appropriate for computer programming because choosing the largest residual is computationally expensive.

4.1.2.1 Successive Over-Relaxation Method

An accelerated convergence scheme is attainable by combining the advantages of the

relaxation method with the systematic iteration scheme. Liebmann's equation for the Poisson equation is

$$\psi(i,j)^{n+1}=\frac{1}{2(\beta^2+1)}\,[\psi(i+1,j)^n+\psi(i-1,j)^n+\beta^2(\psi(i,j+1)^n+\psi(i,j-1)^n)+\Delta x^2\omega(i,j)^n] \qquad (4.6)$$

where the superscripts show that the $n+1^{th}$ iteration utilizes the n^{th} set of values for calculation. The residual of the relaxation is

$$\frac{1}{4}R(i,j)^n=(\frac{1}{2(\beta^2+1)}\,[\psi(i+1,j)^{n+1}+\psi(i-1,j)^{n+1}+\beta^2(\psi(i,j+1)^{n+1}+\psi(i,j-1)^n$$

$$+\Delta x^2\omega(i,j)^{n+1}]\;)-\psi(i,j)^n \qquad (4.7)$$

Substituting the value of $\psi(i,j)^{n+1}$ from the eq. (4.6) into the eq. (4.7) and rearranging gives

$$\psi_{i,j}^{n+1}=\psi_{i,j}^{n}+1/4R_{i,j}^{n} \qquad (4.8)$$

It can be seen from eq. (4.8) that this pattern is more systematic than choosing the largest values of the residual, and also by using the relaxation procedure, the residuals are brought exactly to zero.

It can be shown that the rate of convergence is faster if, in eq. (4.8) we use a residual factor larger than 1/4. If we write the eq. (4.8) as

$$\psi_{i,j}^{n+1}=\psi_{i,j}^{n}+\alpha R_{i,j}^{n}$$

$$=\psi_{i,j}^{n}+\alpha\{2/(\beta^2+1)(\psi_{i+1,j}^{n}+\psi_{i-1,j}^{n}+\beta^2(\psi_{i,j+1}^{n}+\psi_{i,j-1}^{n})+\Delta x^2\omega_{i,j}))-4\psi_{i,j}^{n})\}$$

$$=\alpha\{2/(\beta^2+1)(\psi_{i+1,j}^{n}+\psi_{i-1,j}^{n}+\beta^2(\psi_{i,j+1}^{n}+\psi_{i,j-1}^{n})+\Delta x^2\times\omega_{i,j}^{n})-(4-1/\alpha)\psi_{i,j}^{n}\} \qquad (4.9)$$

For a rectangular region with M and N mesh in the x and y direction, the optimum value of α is the smaller root of

$$(Cos\ \pi/M + Cos\ \pi/N)^2\ \alpha^2 - 4\alpha + 1 = 0. \qquad (4.10)$$

for different values of M and N, α is between 1/4 to 1/2. For this reason the described method, which is used in this thesis, is called successive-over-relaxation (SOR) or extrapolated Liebmann method.

4.1.3. Two-Dimensional Vortex-In-Cell Method

The two-dimensional vortex-in-cell formulation is as follows:

The total circulation is discretized by introducing N vortices such that,

$$\sum_{n=1}^{N}\Gamma_n = \int_A \omega\, dA \qquad (4.11)$$

where Γ_n is the circulation of the vortex element n, and A is the mesh area. In this method, the vorticity from the point vortex (i.e., the Lagrangian element) is distributed to the four neighbouring nodes surrounding each vortex using the area-weighting scheme (Baker, 1979) as,

$$\omega(k) = \Gamma\, A_k/(\Delta x \Delta y)^2 \qquad k=1,2,3,4 \qquad (4.12)$$

where A_i's are the areas shown in Figure 4.2-a, Γ is the circulation of each vortex (see section 4.1.1), and Δx and Δy are the grid sizes. The total vorticity at each node is obtained by summing the contributions of all the vortices which are within the four neighbouring grids surrounding that vortex. Therefore, the vorticity is distributed to the four neighbouring nodal points as:

$$\omega_{i,j} = (\Delta x - dx)(\Delta y - dy)\Gamma_n / (\Delta x \Delta y)^2 = A_1 / A^2 \Gamma_n \qquad (4.13\text{-}a)$$

$$\omega_{i+1,j} = dx(\Delta y - dy)\Gamma_n / (\Delta x \Delta y)^2 = A_2 / A^2 \Gamma_n \qquad (4.13\text{-}b)$$

$$\omega_{i,j+1} = (\Delta x - dx)dy\Gamma_n / (\Delta x \Delta y)^2 = A_3 / A^2 \Gamma_n \qquad (4.13\text{-}c)$$

$$\omega_{i+1,j+1} = dxdy\Gamma_n / (\Delta x \Delta y)^2 = A_4 / A^2 \Gamma_n \qquad (4.13\text{-}d)$$

where dx and dy are as shown in figure (4.2-a). The total vorticity at each nodal point is obtained by summing the contributions of all the surrounding vortices. Then, the Poisson equation (equation 3.20) is solved in order to obtain the streamfunction $\psi(i,j)$ at each node (i,j) of the computational domain (Figure 4.2-b) using the extrapolated Liebmann's method, as discussed in section 4.1.2.1. The components of the velocity at the nodes are determined using a central difference scheme as,

$$u(i,j) = \{\psi(i,j+1) - \psi(i,j-1)\} / 2\Delta y \qquad (4.14\text{-}a)$$

$$v(i,j) = -\{\psi(i+1,j) - \psi(i-1,j)\} / 2\Delta x \qquad (4.14\text{-}b)$$

The velocity $u_n = (u_n, v_n)$ acting on the n^{th} vortex within a grid is calculated using the velocities of the neighbouring nodes employing a bilinear interpolation (Baker, 1979) as:

$$u_n = \left(\sum_{k=1}^{4} u(k)\, A_k \right) / \Delta x \Delta y \qquad (4.15\text{-}a)$$

$$v_n = \left(\sum_{k=1}^{4} v(k)\, A_k \right) / \Delta x \Delta y \qquad (4.15\text{-}b)$$

The notation of Figure 4.2-a has been used in equations (4.15-a) and (4.15-b). The position $\chi=(x_n,y_n)$ of the n^{th} vortex is calculated by integrating

$$d\chi/dt = u_n(\chi(x,y,t)) \qquad (4.16)$$

using the first-order Euler scheme to yield

$$x_n(t+\Delta t) = x_n(t) + u_n \Delta t \qquad (4.17\text{-}a)$$

$$y_n(t+\Delta t) = y_n(t) + v_n \Delta t \qquad (4.17\text{-}b)$$

where Δt is the time-step, and x_n and y_n are the coordinates of the nth vortex. Thus, the above-mentioned interpolation and area-weighting schemes is applied back and forth between the Lagrangian particles and the Eulerian mesh system.

Distributing the vorticity from the vortices on the rectangular grids and interpolating to obtain the velocity of each vortex introduces errors into the vortex-in-cell calculations. This causes fine-scale behaviour dependent on the grid spacing, on the number of vortices, on the boundary conditions and on the time step (Sarpkaya, 1994). Baker (1979) demonstrated that the distribution and interpolation errors introduce instabilities in the vortex sheet on the order of mesh spacing. These fine scale instabilities do not significantly affect the large scale vortex structure. A simple bilinear interpolation

provides satisfactory results for both the vorticity-allotment and velocity-interpolation schemes. The interpolation and distribution errors can be reduced by employing higher order interpolation and distribution schemes, at the cost of losing the natural simplicity of the method. A few examples of these techniques are: using higher order vorticity distribution around the vortices, e.g. the Gaussian distribution, using higher order interpolation schemes, using higher order integration schemes for the convection of vortices and smoothing schemes. There are several methods that can be used for the area/volume weighting schemes. In the weighting scheme adopted in the thesis, it is assumed that the vortex cores have a uniform vorticity. More complicated schemes such as, a Gaussian distribution core, can be found in some of the previous investigations using the VIC method, e.g., Meng and Thomson (1978). The interpolation scheme used in the thesis for calculation of the velocity of the vortices in the cell, is a bilinear scheme for the 2-D simulation, and a tri-linear scheme (discussed in section 4.3.2), for the 3-D simulation. Higher order interpolation schemes can be used in the VIC method (see e.g, Wang, 1977). It is noteworthy that, although the above mentioned techniques are expected to create fewer errors, using higher order schemes does not necessarily improve the results. The errors involved with the simpler VIC methods are sometimes beneficial because these errors create an artificial viscosity in the flow which stabilizes the simulation (see e.g., Sarpkaya, 1994). On the other hand, using higher order schemes increases the complexity of the method and decreases the speed of the method compared to the pure Lagrangian simulation. In the present study these techniques are not used and further study is required to incorporate these techniques in the simulation and to investigate their effects on the results. Furthermore, the stability condition states that the convection of a single vortex, during each time step, should not exceed one mesh size (Baker, 1979), that is:

$$\Delta t < Min(\Delta x/u_n, \Delta y/v_n) \qquad (4.18)$$

4.1.4 Boundaries and Initial Conditions

The lower left corner of the grid system is located at $x=1$ and $y=1$ (figure 4.2). The Neumann conditions apply to the inflow and outflow boundaries. At the inflow, a stepwise uniform velocity results in a linear distribution of the stream function with slope equal to the local velocity as

$$(\partial\psi/\partial y)_{1,j} = U \qquad U = U_1 \text{ for } y > y_{sp} \qquad (4.19)$$
$$U = U_2 \text{ for } y \le y_{sp}$$

where subscript j corresponds to the grids in the y-direction, U_1 and U_2 are the velocities of the high-speed side and the low-speed side, respectively, and $\psi=0$ at $y=0$. The outflow boundary corresponds to a hyperbolic tangent velocity profile (Monkewitz and Huerre, 1982) as

$$(\partial\psi/\partial y)_{N,j} = (\Delta U/2) \tanh \{2(y-y_0)/\delta_w\} + U_c \qquad (4.20)$$

where $\Delta U=U_2-U_1$ is the velocity difference across the layer, $U_c=(U_1+U_2)/2$ is the average velocity, $\delta_w = 0.181 (x-x_v) \Delta U/U_c$ is an experimental expression for the vorticity thickness, x_v is the virtual origin, and $\psi=0$ at $y=0$. The numerical experiments can be performed using the reflection outflow boundary condition, rather than specifying an outflow boundary condition for the streamfunction.

Results have shown that the momentum thickness growth rate is faster when the reflection boundary condition is used. The tanh outflow boundary condition has been adopted in this study because it constrains the growth rate of the momentum thickness, and yields a slope for the linear growth region (i.e., 0.25<x/H<0.85) in close agreement with the experiment. Therefore it is concluded that the need to prescribe the outflow boundary condition when the VIC method is used, highly restricts the prediction of the general flows where an outflow boundary condition is not a priori known.

Slip conditions are assumed for the top and bottom boundaries. The Dirichlet condition is used for the bottom boundary at $y=1$, consistent with $\psi_{i,0}=0$ at $y=0$, as

$$\psi_{i,1} = U_2 \tag{4.21}$$

and for the top boundary

$$\psi_{i,N} = U_2 y_{sp} + U_1 (y_{i,N} - y_{sp}) \tag{4.22}$$

The velocity discontinuity across the splitter plate is simulated using a vortex sheet discretized into a row of point vortices (figure 4.2). Initially, the point vortices are equidistant, and separated by a distance d. At time $t=0$, the vortex closest to the edge of the splitter plate is moved vertically a small distance $0.5d$ to initialize the Helmholtz instability. At the end of each time step, a vortex element with circulation $\Gamma = d.\Delta U$, is generated at the trailing edge of the splitter plate at the inflow boundary with $x=1$ and $y=y_{sp}$, and the vortex with the largest residence time is discarded. The time step is $\Delta t = d/U_c$, and the strength of vortices doesn't decay with time. Therefore, in the present simulation, by keeping the total number and strength of vortices constant throughout the simulation, we satisfy the conservation of circulation and vorticity. Furthermore, the vortices can move freely in

and out through the outflow boundary to avoid the collection of vortices at the end of the computational domain, and their effect is disregarded when they are outside the domain.

4.1.5 Summary of the Solution Procedure

The solution procedure consists of the following steps:

a. Initializing by distributing the vortices at the level of the splitter plate, with circulation values defined in equation (4.1), and assuming initial values for ψ at grid points (the initial value for ψ is arbitrary and can be set equal to zero) together with the boundary conditions (eqns. 4.19-22).

b. Distributing the vorticity to the four neighbouring grids using the area-weighting scheme.

c. Solving the Poisson's equation for ψ, using a successive-over-relaxation (SOR) method, with a left-to-right sweep of the grid points and bottom-to-top sweep of the lines. The iterations are conducted until the difference between consecutive values of ψ is less than 0.1%.

d. Computing the velocities u and v at the grids using equation 4.14.

e. Calculating the velocities at the location of each vortex (u_n,v_n) using a bilinear interpolation (equation 4.15).

f. Applying a two-dimensional random-walk on each vortex, as described in section 3.2.3.2.

g. Updating the coordinates of the vortices using equations 3.26-a and b.

h. Introducing a new vortex at the edge of the splitter plate, and discarding the oldest.

I. Marching in time by repeating the calculations from step b through h.

4.2. Two-Dimensional Uniformly Sheared Flow

4.2.1. Description of the problem

The second part of this study deals with the numerical simulation of the uniformly sheared flow. A schematic configuration of one of the simplest ways of generating uniformly sheared flows is shown in figure 4.3. Several adjacent splitter plates generating mixing layers, are used to simulate the initial condition of the uniformly sheared flow. Co-flowing streams with uniform but different stream velocities are discharged from the splitter plates. This method is similar to the production of the uniformly sheared flows experimentally. The velocity difference ΔU between the streams defines the circulation of the vortices, similar to what was discussed in section 4.1, for the mixing layers. At the edge of each splitter plate a vortex is introduced at different time intervals $\boldsymbol{d}/U_i$ where U_i is the arithmetic average of the velocities above and below the splitter plate i.

4.2.2 Boundary and Initial Conditions

The computational domain consists of a rectangular region covered by a uniform mesh system (Fig. 4.4). Slip wall boundaries are assumed for the top and bottom boundaries. The inflow (left) boundary condition is of Neuman type. At this boundary, a combination of stepwise uniform velocity profiles between splitter plates give linearly distributed stream-functions with gradients equal to the local velocity as

$$\partial\psi/\partial y\,|_{1j} = U_{1j} \qquad (4.23)$$

The outflow boundary condition is similar to the inflow boundary condition. A boundary condition of Dirichlet type is used for the top and bottom boundary conditions. Since the stream function can take an arbitrary additive constant, the bottom boundary value of ψ is

$$\psi_{i,1} = 1U_{bottom} \qquad (4.24)$$

and the top boundary value of ψ representing the flow rate passing between $y=1$ and $y_{1,N}$ is

$$\psi_{1N} = U_{bottom} \cdot y_{bottom} + \Sigma U_k \cdot S + U_{top}(y_{1,N} - y_{top}) \qquad (4.25)$$

where S is the distance between splitter plates, U_{bottom} and U_{top} are the velocities below the bottom splitter plate and above the upper splitter plate, respectively, y_{bottom} and y_{top} are the coordinates of the bottom splitter plate and the top splitter plate, respectively, and U_k is the velocity between splitter plate k and $k+1$.

4.2.3. Summary of the Solution Procedure

The solution procedure consists of the following steps:

a. Initializing by distributing the vortices at the level of each splitter plate, with circulation values defined in equation (4.1), and assuming initial values for ψ at grid points (initial values for ψ are arbitrary and can be set equal to zero) together with the boundary conditions (eqns. 4.23-25).

b. Distributing the vorticity to the four neighbouring grids using the area-weighting scheme.

c. Solving the Poisson's equation for ψ, using the SOR method, with a left-to-right sweep of the grid points and bottom-to-top sweep of the lines. The iterations are conducted until the difference between consecutive values of ψ is less than 0.1%.

d. Computing the velocities u and v at the grids using equation 4.14.

e. Calculating the velocities at the location of each vortex (u_n,v_n) using a bilinear interpolation (equation 4.15).

f. Applying a two-dimensional random-walk on each vortex, as described in section 3.2.3.2.

g. Updating the coordinates of the vortices using equations 3.26-a and b.

h. Introducing a new vortex at the edge of each splitter plate, and discarding the oldest.

I. Marching in time by repeating the calculations from step b through h.

4.3. Three-Dimensional Uniformly Sheared Flow

4.3.1. Discretized Three-Dimensional Poisson Equation

Based on what was discussed for the two-dimensional Poisson equation, the three-dimensional central difference approximation of the Poisson equation is straightforward. Following is the solution of the 3-D Poisson equation based on the velocity-vorticity formulation.

$$\nabla^2 u = \frac{\partial^2 u}{\partial x^2} + \frac{\partial^2 u}{\partial y^2} + \frac{\partial^2 u}{\partial z^2} = -curl\omega_x \qquad (4.26)$$

$$\nabla^2 v=\frac{\partial^2 v}{\partial x^2}+\frac{\partial^2 v}{\partial y^2}+\frac{\partial^2 v}{\partial z^2}=-curl\omega_y \tag{4.27}$$

$$\nabla^2 w=\frac{\partial^2 w}{\partial x^2}+\frac{\partial^2 w}{\partial y^2}+\frac{\partial^2 w}{\partial z^2}=-curl\omega_z \tag{4.28}$$

These equations are similar to equations (3.44) to (3.46) in which *curl* ω_x, *curl* ω_y and *curl* ω_z are now on the right-hand side of the equations, respectively. Before solving the x, y and z components of the Poisson equation, *curl* ω_x, *curl* ω_y and *curl* ω_z which are defined as

$$curl\omega_x=\frac{\partial \omega_z}{\partial y}-\frac{\partial \omega_y}{\partial z} \qquad curl\omega_y=\frac{\partial \omega_x}{\partial z}-\frac{\partial \omega_z}{\partial x} \qquad curl\omega_z=\frac{\partial \omega_y}{\partial x}-\frac{\partial \omega_x}{\partial y} \tag{4.29}$$

are discretized using a central difference approximation as follows

$$curl\omega_x(i,j,k)=\frac{\omega_z(i,j+1,k)-\omega_z(i,j-1,k)}{2\Delta y}-\frac{\omega_y(i,j,k+1)-\omega_y(i,j,k-1)}{2\Delta z} \tag{4.30}$$

$$curl\omega_y(i,j,k)=\frac{\omega_x(i,j,k+1)-\omega_x(i,j,k-1)}{2\Delta z}-\frac{\omega_z(i+1,j,k)-\omega_z(i-1,j,k)}{2\Delta x} \tag{4.31}$$

$$curl\omega_z(i,j,k)=\frac{\omega_y(i+1,j,k)-\omega_y(i-1,j,k)}{2\Delta x}-\frac{\omega_x(i,j+1,k)-\omega_x(i,j-1,k)}{2\Delta y} \tag{4.32}$$

Then the Poisson equations are solved for x, y and z components

$$\nabla^2 u = \frac{u(i+1,j,k)-2u(i,j,k)+u(i-1,j,k)}{(\Delta x)^2}$$

$$+\frac{u(i,j+1,k)-2u(i,j,k)+u(i,j-1,k)}{(\Delta y)^2}$$

$$+\frac{u(i,j,k+1)-2u(i,j,k)+u(i,j,k-1)}{(\Delta z)^2} = -curl\omega_x(i,j,k) \qquad (4.33)$$

$$\nabla^2 v = \frac{v(i+1,j,k)-2v(i,j,k)+v(i-1,j,k)}{(\Delta x)^2}$$

$$+\frac{v(i,j+1,k)-2v(i,j,k)+v(i,j-1,k)}{(\Delta y)^2}$$

$$+\frac{v(i,j,k+1)-2v(i,j,k)+v(i,j,k-1)}{(\Delta z)^2} = -curl\omega_y(i,j,k) \qquad (4.34)$$

$$\nabla^2 w = \frac{w(i+1,j,k)-2w(i,j,k)+w(i-1,j,k)}{(\Delta x)^2}$$

$$+\frac{w(i,j+1,k)-2w(i,j,k)+w(i,j-1,k)}{(\Delta y)^2}$$

$$+\frac{w(i,j,k+1)-2w(i,j,k)+w(i,j,k-1)}{(\Delta z)^2} = -curl\omega_z(i,j,k) \qquad (4.35)$$

By some manipulations and using $\beta=\Delta x/\Delta y$ and $\lambda=\Delta x/\Delta z$, equations (4.33) to (4.35) lead to the following forms

$$u(i,j,k)^{n+1}=\{u(i+1,j,k)^n+u(i-1,j,k)^n+\beta^2[u(i,j+1,k)^n+u(i,j-1,k)^n] \\ +\lambda^2[u(i,j,k+1)^n+u(i,j,k-1)^n]+(\Delta x)^2 curl\omega_x\} \;/\; 2(\beta^2+\lambda^2+1) \tag{4.36}$$

$$v(i,j,k)^{n+1}=\{v(i+1,j,k)^n+v(i-1,j,k)^n+\beta^2[v(i,j+1,k)^n+v(i,j-1,k)^n] \\ +\lambda^2[v(i,j,k+1)^n+v(i,j,k-1)^n]+(\Delta x)^2 curl\omega_y\} \;/\; 2(\beta^2+\lambda^2+1 \tag{4.37}$$

$$w(i,j,k)^{n+1}=\{w(i+1,j,k)^n+w(i-1,j,k)^n+\beta^2[w(i,j+1,k)^n+w(i,j-1,k)^n] \\ +\lambda^2[w(i,j,k+1)^n+w(i,j,k-1)^n]+(\Delta x)^2 curl\omega_z\} \;/\; 2(\beta^2+\lambda^2+1 \tag{4.38}$$

Based on the discussion of the 2-D approximation, an accelerated convergence is attained using the successive over-relaxation (SOR) method. Calculating the residuals $R(i,j,k)$, for each nodal point and using the following form:

$$u(i,j,k)^{n+1}=u(i,j,k)^n+\alpha\ R(i,j,k)^n \tag{4.39}$$

$$v(i,j,k)^{n+1}=v(i,j,k)^n+\alpha\ R(i,j,k)^n \tag{4.40}$$

$$w(i,j,k)^{n+1}=w(i,j,k)^n+\alpha\ R(i,j,k)^n \tag{4.41}$$

leads to the final form of three-dimensional Poisson equations:

$$u(i,j,k)^{n+1} = \alpha \left(\frac{6}{2(\beta^2+\lambda^2+1)} \{u(i+1,j,k)^n + u(i-1,j,k)^n \right.$$

$$+\beta^2[u(i,j+1,k)^n + u(i,j-1,k)^n] + \lambda^2[u(i,j,k+1)^n$$

$$\left. +u(i,j,k-1)^n] + (\Delta x)^2 curl\omega_x(i,j,k)\} - (6-\frac{1}{\alpha})u(i,j,k)^n \right) \qquad (4.42)$$

$$v(i,j,k)^{n+1} = \alpha \left(\frac{6}{2(\beta^2+\lambda^2+1)} \{v(i+1,j,k)^n + v(i-1,j,k)^n \right.$$

$$+\beta^2[v(i,j+1,k)^n + v(i,j-1,k)^n] + \lambda^2[v(i,j,k+1)^n$$

$$\left. +v(i,j,k-1)^n] + (\Delta x)^2 curl\omega_y(i,j,k)\} - (6-\frac{1}{\alpha})v(i,j,k)^n \right) \qquad (4.43)$$

$$w(i,j,k)^{n+1} = \alpha \left(\frac{6}{2(\beta^2+\lambda^2+1)} \{w(i+1,j,k)^n + w(i-1,j,k)^n \right.$$

$$+\beta^2[w(i,j+1,k)^n + w(i,j-1,k)^n] + \lambda^2[w(i,j,k+1)^n$$

$$\left. +w(i,j,k-1)^n] + (\Delta x)^2 curl\omega_z(i,j,k)\} - (6-\frac{1}{\alpha})w(i,j,k)^n \right) \qquad (4.44)$$

4.3.2. Three-Dimensional Vortex-in-Cell Method

The methodology used for the development of a three-dimensional vortex-in-cell (VIC) method is an extension to Baker's (1979) approximation scheme for the two-dimensional formulation, discussed in section 4.1.3. What follows is details of the three-dimensional VIC method, which deals with vortex filaments instead of vortex elements. In a two-dimensional model the vorticity vectors have only one component perpendicular to the plane of motion. However, in a three-dimensional simulation, the vorticity vectors at the nodes and the circulation vectors of the elements of each filament may have components in the x, y and z directions. As shown schematically in figure 4.5, when a filament bends and stretches, directions of the circulation vectors which are tangent to the filament, vary along the filament. The bending and stretching procedure of the filaments is similar to the bending and stretching of a vortex filament in a shear flow which was discussed in detail in section 2.4.1. In our model, the direction of the circulation vector of each element is determined using the locations of its two neighbouring vortex elements. Since the direction of the circulation vector at any location of a filament is always tangent to the filament, therefore, the circulation vector of any element has approximately the same direction cosines as the line connecting its two neighbouring elements (see figure 4.5). Therefore, the vorticity allocation to the eight nodal points surrounding each vortex element is performed using the three components of the circulation of each element. In the three-dimensional VIC method, the following volume-weighting scheme may be employed, which is conceptually similar to the two-dimensional area-weighting scheme of Baker (1979),

$$\omega(k) = \Gamma_n V_k/(\Delta x \Delta y \Delta z)^2 \qquad k=1,2,...8 \qquad (4.45)$$

where $\omega(k)=(\omega(k)_x, \omega(k)_y, \omega(k)_z)$, $\Gamma_n=(\Gamma_{nx}, \Gamma_{ny}, \Gamma_{nz})$ are the vorticity vector and the circulation vector of the nth element, respectively. V_k's are the volumes shown in figure (4.6) and Δx, Δy and Δz are the mesh sizes. Therefore, the vorticity distribution to the eight neighbouring nodes are:

$$\omega(1) = (\Delta x-dx)(\Delta y-dy)(\Delta y-dz)\,\Gamma_n/(\Delta x\Delta y\Delta y)^2 = V_1/V^2\,\Gamma_n \qquad (4.46\text{-}a)$$

$$\omega(2) = dx(\Delta y-dy)(\Delta y-dz)\,\Gamma_n/(\Delta x\Delta y\Delta y)^2 = V_2/V^2\,\Gamma_n \qquad (4.46\text{-}b)$$

$$\omega(3) = (\Delta x-dx)dy(\Delta y-dz)\,\Gamma_n/(\Delta x\Delta y\Delta y)^2 = V_3/V^2\,\Gamma_n \qquad (4.46\text{-}c)$$

$$\omega(4) = (\Delta x-dx)(\Delta y-dy)dz\,\Gamma_n/(\Delta x\Delta y\Delta y)^2 = V_4/V^2\,\Gamma_n \qquad (4.46\text{-}d)$$

$$\omega(5) = dxdy(\Delta y-dz)\,\Gamma_n/(\Delta x\Delta y\Delta y)^2 = V_5/V^2\,\Gamma_n \qquad (4.46\text{-}e)$$

$$\omega(6) = dx(\Delta y-dy)dz\,\Gamma_n/(\Delta x\Delta y\Delta y)^2 = V_6/V^2\,\Gamma_n \qquad (4.46\text{-}f)$$

$$\omega(7) = (\Delta x-dx)dydz\,\Gamma_n/(\Delta x\Delta y\Delta y)^2 = V_7/V^2\,\Gamma_n \qquad (4.46\text{-}g)$$

$$\omega(8) = dxdydz\,\Gamma_n/(\Delta x\Delta y\Delta y)^2 = V_8/V^2\,\Gamma_n \qquad (4.46\text{-}h)$$

where dx, dy and dz are as shown in figure (4.6). The total vorticity at each nodal point is obtained by summing the vorticity contributions of all the vortex elements. Next, the Poisson equations are solved to obtain the velocity components at the nodes by a finite difference approximation (equations (3.42) to (3.44)). The velocity $u_n=(u_n, v_n, w_n)$ acting on the nth vortex within a grid is calculated using the velocities of the eight neighbouring nodes employing a trilinear interpolation similar to the bilinear interpolation of Baker (1979), as:

$$u_n = \left(\sum_{k=1}^{8} u(k)\, V_k\right) / \Delta x \Delta y \Delta z \qquad (4.47\text{-}a)$$

$$v_n = \left(\sum_{k=1}^{8} v(k)\, V_k\right) / \Delta x \Delta y \Delta z \qquad (4.47\text{-}b)$$

$$w_n = \left(\sum_{k=1}^{8} w(k)\, V_k\right) / \Delta x \Delta y \Delta z \qquad (4.47\text{-}c)$$

The notation of Figure 4.6 has been used in equations (4.47-a), (4.47-b) and (4.47-c). The position $\chi=(x_n, y_n, z_n)$ of the n^{th} vortex is calculated by integrating, using the first order Euler scheme to yield

$$\chi_n(t+\Delta t) = \chi_n(t) + u_n \Delta t \qquad (4.48)$$

Equation (4.48) can be written explicitly for each of the coordinates as,

$$x_n(t+\Delta t) = x_n(t) + u_n \Delta t \qquad (4.49\text{-}a)$$

$$y_n(t+\Delta t) = y_n(t) + v_n \Delta t \qquad (4.49\text{-}b)$$

$$z_n(t+\Delta t) = z_n(t) + v_n \Delta t \qquad (4.49\text{-}c)$$

Then, three random numbers with zero mean and standard deviation $(\nu\Delta t)^{1/2}$ are generated (see sections 3.2.3.2 and 3.3.3.2 for details), and the motion of each vortex element by the random-walk is added on the motion due to the convection of the vortex elements. Therefore, the new location of each vortex element is calculated as

$$x_n(t+\Delta t) = x_n(t) + u_n \Delta t + \eta_1 \qquad (4.50\text{-}a)$$

$$y_n(t+\Delta t)= y_n(t) + v_n\Delta t + \eta_2 \qquad (4.50\text{-}b)$$

$$z_n(t+\Delta t)= z_n(t) + w_n\Delta t + \eta_3 \qquad (4.50\text{-}c)$$

where η_1, η_2 and η_3 are Gaussian distributed random variables with zero mean and standard deviation $(\nu\Delta t)^{1/2}$. Thus the above mentioned interpolation and area-weighting scheme must be applied back and forth between Lagrangian particles and Eulerian mesh system.

4.3.3 Numerical Approximation for the Stretching Terms

The effect of the stretching terms is to alter the value of the vorticity of filaments. In our model which was used previously by other investigators, e.g. Doorly and Liu (1994), the vortex stretching terms are solved at the grid point. The numerical solution is based on a central-difference approximation to solve equations (3.50) as

$$\omega_x(t+\Delta t)=\omega_x(t)+\omega_x(t)[u(i+1)-u(i-1)/\Delta x] + \omega_y(t)[u(j+1)-u(j-1)/\Delta y] + \omega_z(t)[u(k+1)-u(k-1)/\Delta z] \qquad (4.51\text{-}a)$$

$$\omega_y(t+\Delta t)=\omega_y(t)+\omega_x(t)[v(i+1)-v(i-1)/\Delta x] + \omega_y(t)[v(j+1)-v(j-1)/\Delta y] + \omega_z(t)[v(k+1)-v(k-1)/\Delta z] \qquad (4.51\text{-}b)$$

$$\omega_z(t+\Delta t)=\omega_z(t)+\omega_x(t)[w(i+1)-w(i-1)/\Delta x] + \omega_y(t)[w(j+1)-w(j-1)/\Delta y] + \omega_z(t)[w(k+1)-w(k-1)/\Delta z] \qquad (4.51\text{-}c)$$

4.3.4. Boundary and Initial Conditions

The boundary conditions used for the three-dimensional simulations, are Dirichlet type velocity components, because, as discussed in section 3.3.2, in a vorticity-velocity formulation, the boundary conditions for the Poisson equation can be more easily provided using the velocity components.

The geometry that we consider in this problem is a rectangular cubic region covered by a uniform mesh system with grid size Δx, Δy and Δz in the x, y and z directions, respectively. In the present formulation, the boundary condition associated with the three-dimensional velocity Poisson equations (3.44 to 3.46), is implemented by the velocity vector components assigned on the imaginary slip-walls surrounding the computational domain. In the next two subsections, the boundary conditions used for the numerical simulation of a spatially growing uniformly sheared flow with non-periodic free-slip-walls and the boundary conditions for the quasi-temporally developing uniformly sheared flow with free-slip-walls and periodic boundary conditions in the streamwise direction are discussed.

4.3.4.1 Boundary and Initial Conditions for Spatially Growing Uniformly Sheared Flow

Inflow and Outflow Boundary Conditions

A set of five parallel splitter plates produces channels of flow with stepwise uniform velocities.

The boundary condition is of the Dirichlet type. The velocity components for $y \leq y_{s1}$ are

$$u(x, y, z)=U_{Bottom} \qquad v(x, y, z)= 0 \qquad w(x, y, z)= 0 \tag{4.52}$$

where y_{s1} indicates the location at the first splitter plate. A stepwise velocity profile is used where the velocity changes at the level of each splitter plate, that is at $y= y_{s1}$, y_{s2} , y_{s3} , y_{s4} and y_{s5} the velocity components are:

$$u(x, y, z)= U_{Bottom} +(y- y_{s1})\times \Delta U \qquad v(x, y, z)= 0 \qquad w(x, y, z)=0 \tag{4.53}$$

In between the splitter plates where $y_{si} \prec y \preceq y_{si+1}$, the velocity components are:

$$u(x, y, z)= u(x, y_{si}, z) \qquad v(x, y, z)= 0 \qquad w(x, y, z)=0 \tag{4.54}$$

and the velocity components for $y \succ y_{s5}$

$$u(x, y, z)= U_{top} \qquad v(x, y, z)= 0 \qquad w(x, y, z)= 0 \tag{4.55}$$

The components of the vorticity-vector ω_x, ω_y and ω_z are zero everywhere except at the level of the splitter plates where

$$\omega_x =0 \qquad \omega_y =0 \qquad \omega_z = \Delta U\times\Delta x/(\Delta x\times\Delta y\times\Delta z) =\Delta U/\Delta y\times\Delta z \tag{4.56}$$

The outflow boundary condition is similar to the inflow boundary condition.

Top and Bottom Boundary Conditions

Since the top and bottom boundaries are parallel to the free stream where there is no shear, therefore they are simply introduced as

$$u(x, y_{Top}, z) = U_{Top} \qquad u(x, y_{Bottom}, z) = U_{bottom} \tag{4.57}$$

The cross-stream velocity component (v) and the spanwise velocity component (w) are assumed zero for the top and bottom boundaries. The values of the vorticity-vector components ω_x, ω_y and ω_z are zero every where on the top and bottom boundaries.

Boundary Condition on the Side Faces

The vortex filaments are always attached to the side boundaries following the Helmholtz's vortex laws, that vortex filaments can never end in the fluid. They either form closed loops, as vortex rings, or end at the fluid boundary (Karamcheti, 1976).

The values of the velocity components on the side boundaries are the same as the inflow boundary condition, described by equations (4.52) to (4.55). This implies that, on the side boundaries where dU/dy is constant, the combined effect of the circulation vectors of all vortex elements inside the cubic grids attached to a boundary node, should be perpendicular to the side boundaries. Satisfying this condition shows the compatibility of the Eulerian (grid) information with the Lagrangian (vortex elements) information. However, there is no easy way to enforce such a constraint

on the vortex elements, because the vortex filaments should be able to move freely in the computational domain, and the effect of applying any constraint on their movement can propagate inside the domain. In the present study, the above compatibility on the side boundaries is not enforced, and there might be some local deviations from a fully compatible boundary condition. Furthermore, as a first approximation in this model, the direction and the value of the circulation vector of the elements attached to the boundaries do not influence any of the circulations of the elements inside the computational domain. This is due to the fact that, the direction of the circulation vector of each vortex element inside the computational domain, is determined using the locations of its two neighbouring vortex elements only, irrespective of the circulation vector of the neighbouring vortex elements (see section 4.3.2 for details).

Another approach that may be considered for the side boundaries is to apply an open boundary on the side, whose grid values are updated every time step. In this approach, the compatibility of the filament-information and the grid-information is a part of the solution. However, using such boundary conditions, the velocity vectors at the grid points on the side boundaries may have three components, and the trilinear interpolation to the location of the vortex elements would create a spanwise component of velocity for the vortex elements on the side boundaries. The spanwise velocity component moves the elements inside or outside the computational domain, and detaches the filaments from the side boundaries, which is against the Helmholtz's law which states that the vortex filaments can never end in the fluid.

Initial Distribution of Vortex filaments

The velocity discontinuity across the splitter plates is simulated using shear layers. Each shear

layer is discretized into a row of equidistant vortex filaments. As discussed in section 4.1.1, the velocity difference ΔU between the streams defines the circulation of the vortex filaments, $\Gamma=\Delta U.d$, where d is the initial distance between neighbouring filaments. At the edge of each splitter plate, a vortex filament is introduced at different time interval d/U_i where U_i is the arithmetic average of the velocities above and below the splitter plate i. The filaments are introduced in this fashion because the lower layers have smaller convective velocities.

4.3.4.2 Boundary and Initial Conditions used for Quasi-Temporally Growing Uniformly Sheared Flow

The second set of numerical investigations performed in this work, is a three-dimensional simulation of a quasi-temporally developing uniformly sheared flow with periodic boundary conditions in the streamwise direction. The periodic boundary condition is a mathematical trick used to mimic an infinite domain, and is in that sense, not physical. In general, periodic boundaries are very useful if the computational domain is short and has something (like Lagrangian particles) moving in it. In the numerical simulation of uniformly sheared flow with periodic boundary conditions, the initially straight vortex filaments, deform and stretch when they reach the end of the computational box. At the end of each time step, filaments which have some of their vortex elements crossing the outflow boundary, are frozen and transferred to the inflow boundary. This is done by deducting the length of the computational domain (L) from the streamwise coordinate of each vortex element of the crossing filaments as $x_1 = x_n - L$, $y_1 = y_n$ and $z_1 = z_n$. A periodic boundary condition in this work is

only applied in the streamwise direction while in the other directions, a slip-wall boundary is adopted. The flow parameters used for this section are the same as those used for the spatially growing uniformly sheared flow. The computational box is replaced with a shorter box which consists of a uniform mesh system with 64×64×32 grid points in the streamwise, the spanwise and the cross-stream direction, respectively. The grid size is $\Delta x = \Delta y = \Delta z = 0.25cm$. Initially, the vortex sheets of each one of the five co-flowing layers are discretized into 240 equidistant filaments and each filament consists of sixty five vortex segments (i.e., one segment per grid). Circulation of each vortex filament is $\Gamma = \Delta U.d$, similar to what is described for the spatially growing uniformly sheared flow.

Inflow and Outflow Boundary Conditions

For the first time step, the inflow boundary condition is the same as the spatially growing shear as described by equations (4.52) to (4.56). For subsequent time steps, the periodic boundary condition is used and the velocities at the grid points just upstream of the outflow boundary are inserted at the corresponding grid points at the inflow boundary.

The filaments are stretched and skewed as time increases, because the mean shear moves the filaments at large cross-stream (y) locations further downstream than those at small cross-stream locations. The filaments are stretched increasingly with time and their lengths tend to exceed the extent of the computational domain. Therefore, it is necessary to reshape the filaments at regular intervals in such a way that the angle of the vortex filaments is about 45 degree with the horizontal plane, as reported in uniformly sheared flow. The approach followed is analogous to the one described in Rogallo (1977) for Eulerian calculations with periodic boundary conditions, and used by Rogers and Moin (1987) and Kida and Tanaka (1994) for the calculation of the temporally

growing shear flow. In their approach the grid system becomes increasingly skewed with time and has to be remeshed at regular intervals, i.e., every 2St (see Rogers and Moin, 1987 for more details). In the present study, the filaments are reshaped as they re-enter the inflow boundary. Several reshaping techniques were tested, and the one that gave results in closest agreement with the previous experimental and numerical results is adopted in this work. In this reshaping, *the vortex elements of a filament that are outside the computational domain* at inflow (in section 4.3.4.2, it is explained, why some parts of the filaments at the inflow boundary are outside the grid system), are reshaped by being convected inside the domain using

$$u(x, y, z) = u(1, y, z) + u(1, 2H-y, z)$$

$$v(x, y, z) = v(1, y, z)$$

$$w(x, y, z) = w(1, y, z) \qquad (4.58\text{-}a)$$

where $2H$ is the height of the computational domain (see figure 4.4). Equation (4.58-a) implies that, an additional streamwise velocity is added to the convection velocity of the vortex elements at each time step, as long as they are not inside the computational domain. As illustrated schematically in figure 4.7, this additional convective velocity increases the angle of the filaments, because the lower parts of the filaments are convected faster than the upper parts.

Three other reshaping techniques have been tested. In the first one, *the whole filament* was reshaped at each time step, i.e. the parts that are inside and outside the computational domain, if some of its vortex elements are outside the computational domain at inflow. This was done by convecting all of the vortex elements of the filaments into the computational domain as:

$$u(x, y, z) = u(1, y, z) + u(1, 2H-y, z)$$

$$v(x, y, z) = v(1, y, z)$$

$$w(x, y, z) = w(1, y, z) \qquad (4.58\text{-}b)$$

Reshaping the filaments in this fashion controls the stretching of the filaments but components energy ratios does not show agreement with the previous numerical and experimental results. In the second approach, *the vortex elements of a filament that are outside the computational domain* at inflow, are reshaped by being convected inside the domain using a constant velocity as:

$$u(x, y, z) = u(1, y, z) + Constant.$$

$$v(x, y, z) = v(1, y, z)$$

$$w(x, y, z) = w(1, y, z) \qquad (4.58\text{-}c)$$

The simulation in this case was tested for several values of the constant velocity, such as the centerline mean velocity, the velocity of the top layer and the velocity of the bottom layer. The results of the simulation in this case is similar to the first approach. In the third approach, *all the filaments in the computational domain* are reshaped at regular time intervals, i.e., t=St, 2St,...nSt. The time interval St is the residence time of each filament in the computational domain, which is approximately the time interval that a filament is convected from the inflow to the outflow boundary. Therefore, the equations for this case become:

$$u(x, y, z) = u(x, y, z) + u(x, St(H-y), z)$$

$$v(x, y, z) = v(x, y, z)$$

$$w(x, y, z) = w(x, y, z) \qquad (4.58\text{-}d)$$

Equation (4.58-d) implies that an additional streamwise velocity is added to the convection velocity of all vortex filaments in the computational domain. This will rotate the filaments around the centerline. The elements above the centerline will move backward, and the elements below the centerline will move forward. The results in this case shows that not only the component energy ratios are not in agreement with previous experimental and numerical results, but also the filaments do not show any organised form with an angle with horizontal plane.

At the outflow boundary the velocity components are:

for $y \leq y_{s1}$

$$u(x, y, z) = U_{Bottom} \qquad v(x, y, z) = 0. \qquad w(x, y, z) = 0. \qquad (4.59)$$

for $y_{s1} < y \leq y_{s5}$

$$u(x, y, z) = U_{Bottom} + (y - y_{s1}) \times \Delta U \qquad v(x, y, z) = 0. \qquad w(x, y, z) = 0. \qquad (4.60)$$

and for $y > y_{s5}$

$$u(x, y, z) = U_{top} \qquad v(x, y, z) = 0. \qquad w(x, y, z) = 0. \qquad (4.61)$$

The values of the vorticity-vector components ω_x, ω_y and ω_z are zero everywhere except at the level of the splitter plates, as specified in equation (4.56).

Top and Bottom Boundary Conditions

Since the periodic boundary condition is only applied in the streamwise direction, the top and bottom boundaries, are slip-wall boundaries similar to the spatially growing uniform shear, described in equation (4.57). The values of vorticity-vector components ω_x, ω_y and ω_z are zero everywhere on the top and bottom boundaries.

Boundary Condition on the Side Faces

The values of the velocity components on the side boundaries are assumed to be the same as the outflow boundary condition, described in equations (4.59) to (4.61). On the side boundaries where the filaments are attached, the circulation of the elements are assumed to be zero. However, these elements are convected downstream with the corresponding filaments.

4.3.5. Summary of the Solution Procedure

The solution procedure consists of the following steps:

a. Initializing by assuming distributions of **u** and ω together with the boundary conditions.

b. Solving the Poisson equation (equations 3.44-46), for components of **u** by sweeping all nodes left to right and line by line, and using the SOR method with a second order central difference scheme.

c. Calculating the effect of stretching terms (equations 3.51-53) and updating the values of the vorticity components at the nodal points.

d. Calculating the velocities of the vortices in the cell using the trilinear interpolation.

e. Applying a three-dimensional random walk at the location of each vortex marker.

f. Advancing the vortices in time by integrating using the first order Euler scheme (equations 3.49).

g. Applying the volume weighting scheme (equation 4.46), to update the components of the vorticities at the nodal points.

h. In the spatially growing uniformly sheared case: introducing a filament at the splitter plates and discarding the oldest one. In the quasi-temporally growing uniformly sheared case: checking the location of the filaments and moving the filaments which have passed the outflow boundary to the inflow boundary and updating the inflow velocity using the velocities of the grid points just before the outflow boundary.

The unsteady solution is obtained by repeating the calculations from step b to step h.

Chapter 5

Results of Two-Dimensional Simulations

5.1. Mixing Layer

Results of the simulation with a velocity ratio r=0.6, where r is U_2/U_1 (velocity ratio of the lower velocity side of the splitter plate to the higher velocity side) are reported in this work. The uniform velocities used for the present simulation are U_1= 1350 cm/s and U_2 = 810 cm/s, similar to the parameters used in the experiment of Oster and Wygnanski (1982) and in the numerical simulation of Inoue and Leonard (1987). Therefore the velocity difference is $\Delta U = U_1 - U_2$ = 540 cm/s and the average velocity is U_c= 945 cm/s. The reported results are for a viscous flow condition with $\nu = 14.5\times10^{-2}$ cm^2/s (the kinematic viscosity of air at 18 °C). A numerical investigation was conducted to find out the effect of number of vortices, the effect of time averaging and the effect of grid size on the evolution of the spatially growing mixing layers and on downstream growth of the Reynolds stresses. The statistical results for the mean velocity, the root-mean-square (r.m.s.) longitudinal and

lateral velocity fluctuations, and the Reynolds shear stress are obtained by averaging the unsteady solution over a period of time. The results are reported at four downstream locations, x/H= 0.5, 0.6, 0.7, 0.8 where H (which is 32cm in our simulation) is the length of the computational domain.

For the presentation of the results, the velocities are made dimensionless by ΔU which is the velocity difference between the upper side and the lower side of the splitter plate. In the plots of turbulent statistics, the similarity profiles obtained experimentally by Oster and Wygnanski (1982) for the same velocity ratio, r=0.6, and the numerical results based on a pure Lagrangian grid-free method, obtained by Inoue and Leonard (1987) are also presented for the purposes of comparison.

5.1.1. Numerical Parameters

A base run with 19200 vortex elements throughout a computational domain using a 256×256 grid system with $\Delta x = \Delta y = 0.125$ cm is what has been chosen in this work. On the centerline, the shear layer is discretized into a layer of equidistant vortex elements. Therefore, by using eq. 4.1 the circulation of each vortex is $\Gamma = \Delta U.\ d = 9.0\times10^{-5}$ m^2/s, where d is the initial spacing between the vortices. The time step used for the simulation is calculated as $\Delta t = d/U_{av}$, where $U_{av} = (U_1 + U_2)/2$. Accordingly for the simulation using 19200 vortex elements the time step is 1.076×10^{-6} sec. The computer program was run for 200,000 time-steps (Δt) to obtain 200,000 velocity-samples. Turbulent characteristics are obtained by averaging the last 185000 velocity-samples. Here the results with 19200 vortices are presented

5.1.2. Streaklines and Vorticity Contours

The streaklines of the vortices and the vorticity contours are shown in figure 5.1-a and b, respectively, as a function of x/H, where H is the downstream length of the computational domain. The vorticity contours in figure 5.1-b show that the roll-up of the vortices starts at x/H≈0.15, followed by the formation of a separate cluster at x/H≈0.25. An interaction of the clusters is shown at x/H≈0.4, and a rotation and amalgamation at x/H≈0.55. The above results are in qualitative agreement with the results of the simulation of Inoue and Leonard (1987), and the experiment of Oster and Wygnanski (1982). It is noteworthy that a time period equal to the residence time of one vortex, i.e., 19200Δt is required for the development of the flow field.

5.1.3. Momentum Thickness

The time-average momentum thickness θ is evaluated as,

$$\theta = \frac{\sum_{m=1}^{m=M} \int_{-\infty}^{\infty} \{\frac{1}{4} - (\frac{u-U_c}{\Delta U})^2\} dy}{M} \qquad (5.1)$$

where M is the number of time steps, and u is the instantaneous velocity (see e.g., Schlichting, 1968 for details). Figures 5.2-a and b show the momentum thickness θ and the streamwise growth rate dθ/dx as a function of x/H. The growth rate dθ/dx in figure 5.2-b is calculated using the central difference approximation. Convergence is achieved using 5000 velocity-samples. The presented

results are for two runs; the base run, for which the numerical parameters are described in section 5.1.1, and the second run, where a longer computational domain, i.e., 1.5 times longer than the base run, is used. In the second run the grid sizes are the same as the base run ($\Delta x = \Delta y = 0.125$ cm), but the number of vortices is 1.5 times more than the base run (i.e., 19200×1.5) to keep the same vortex density per grid. Four regions are noted in figure 5.2-a and b. In the first region, when $x/H<0.25$ in the base run and when $x/H<0.30$ in the longer computational domain, the flow is in the developing regime. In the second region, when $0.25<x/H<0.85$ in the base run and when $0.30<x/H<1.25$ in the longer computational domain, the momentum thickness grows linearly. This is in agreement with the simulation in Inoue and Leonard (1987), and the experiment in Oster and Wygnanski (1982) as shown in figure 5.2-b. In the third region, when $0.85<x/H<0.95$ in the base run and when $1.25<x/H<1.45$ in the longer computational domain, the growth rate is nonlinear, and greater than the experimental results. It is noted that the trend of the third region in the base run, i.e., $0.85<x/H<0.95$, has been moved further downstream to $1.25<x/H<1.45$ with the longer computational domain. This is an indication that the behaviour in the third region is due to the experimentally prescribed outflow boundary condition rather than to any other physical phenomena such as the onset of three-dimensional effects. In the fourth region, when $x>0.95$ in the base run and when $x/H>1.45$ in the longer computational domain, the growth rate is adjusted by the experimentally prescribed outflow boundary condition (see section 4.1.4 for the effect of outflow boundary condition on the growth rate of the momentum thickness). It is noticeable in figures 5.2-a and b, that for the base run the symbols are shown for $0.03<x/H<1.03$. This is due to the fact that the first node, at the edge of the splitter plate, is specified as node number one, located at x =1cm, and accordingly the last grid point is specified as node number 257 located at x= 33cm. Since the length of the computational domain is

32 cm, therefore, the location of the first grid point is specified as x/H= 1/32≈ 0.03 and accordingly the last grid point is specified as x/H= 33/32≈ 1.03

5.1.4. Streamwise mean velocity profile

The streamwise mean velocity normalized as $U_{av}= (U- U_2)/\Delta U$ is shown in figure 5.3-a as a function of the similarity variable η at x/H=0.5, 0.6, 0.7 and 0.8, where U is the mean velocity, $\eta=(y-y_0)/\theta$, and y_0 is the ordinate of the centerline at x. The mean velocity in figure 5.3-a is in agreement with the simulation in Inoue and Leonard (1987), and with the experiment in Oster and Wygnanski (1982). Self-similar profiles are obtained for 0.5≤x/H≤0.9. Convergence is achieved using 5000 or more velocity-samples similar to the momentum thickness. The centerline, defined as the locus of locations with the average velocity U_c, is tilted toward the low-speed side. Its slope, obtained from a linear curve-fit of the streamwise centerline points, is equal to -0.007 which is in agreement with the value of -0.006 reported by Inoue and Leonard (1987). The virtual origin, defined as the intersection of the centerline with the horizontal line at the level of the splitter plate (y_{sp}), is $x_v = 2.9$ cm, i.e., 1.9 cm from the edge of the splitter plate.

5.1.5. Reynolds Stresses

The r.m.s. longitudinal (r.m.s. u') and lateral (r.m.s. v') fluctuation velocities normalized with ΔU are shown in figure 5.3-b and c. As shown in these figures, the results obtained by the VIC method are in agreement with the results of the pure Lagrangian simulation reported by Inoue and Leonard (1987). Self-similar profiles are obtained for 0.5≤x/H≤0.9 and convergence is achieved using

30000 or more velocity-samples. Table 1 shows the peak values of the Reynolds stresses obtained in the present study and the results that have been reported previously. Comparing these results indicates that the peak value of the r.m.s. u' is close to the experimental results of Oster and Wygnanski (1982) and to the numerical results of Inoue and Leonard (1987). The peak value of the r.m.s. v'/ΔU is in agreement with the value (0.25) obtained in the simulation of Inoue and Leonard (1987) and about twice the experimental value (0.153) obtained by Oster and Wygnanski (1982), because the three-dimensional effect has not been included in this study. The discrepancy with the experiment can be explained by noting that the production of the turbulent kinetic energy in a mixing layer with velocity gradient dU/dy, contributes to the longitudinal turbulent kinetic energy only (see section 2.4.3 for details). Then, the turbulent kinetic energy is transferred to the lateral and the spanwise components by the terms associated with pressure-velocity correlations (Tennekes and Lumley, 1977). In a two dimensional simulation, the spanwise velocity fluctuations disappear, and the energy is transferred from the longitudinal component to the lateral component only. Therefore, the lateral component is expected to be higher than the experimental values. It is also noted that the predicted two-dimensional total kinetic energy $[(r.m.s.u'/\Delta U)^2+ (r.m.s.v'/\Delta U)^2]/2 =0.0518$ is close to the experimental value $[(r.m.s.u'/\Delta U)^2 + (r.m.s.v'/\Delta U)^2 + (r.m.s.w'/\Delta U)^2]/2=0.04$. This indicates that the predicted two-dimensional kinetic energy is distributed among the three dimensions in the experiment as noted by Ghoneim and Ng (1987).

The Reynolds shear stress $(\overline{-u'v'})$, normalized with ΔU is shown in figure 5.3-d. The calculations are performed over 200000 time-steps using the last 185000 velocity-samples. Calculations performed over a shorter time interval, consisting of 165000 time-steps using the last 150000 velocity-samples indicated that the shorter time interval is adequate. The Reynolds shear

stress $(\overline{-u'v'})$ requires more velocity-samples because it includes the contributions from pairs of clusters of vortices of various stages of rotation and amalgamation, as discussed in Aref and Siggia (1981). The maximum values in Inoue and Leonard (1987), obtained using the Lagrangian method, are in the range 0.11 to 0.13 when $0.16 \le x/H \le 0.48$ (see Inoue and Leonard (1987-b) for numerical parameters). This is in close agreement with the maximum values 0.11 to 0.135 of the present study, when $0.5 \le x/H \le 0.7$. However, the Lagrangian method has a longer region with similar profiles than the VIC method. The average maximum value of the similar profiles shown in Table (5.1) is in close agreement with the experimental value (0.013) of Oster and Wygnanski (1982) and the value (0.012) from the numerical simulation of Inoue and Leonard (1987). The negative cross-stream correlation $(-u'v'/\Delta U2)$ is expected to be in close agreement with the experiment because it is linked to the mean flow by the mean momentum and the mean flow is well predicted as indicated by Figure 5.3-a

The computational time of the present run using the VIC method is 117 hours on the IBM Risc System 6000 model 390. A comparison with the Lagrangian method cannot be made due to unavailability of the computational time for the Lagrangian method. Consequently, only an estimate is presented. In the Lagrangian calculations, the number of operations per time-step is proportional to N^2, where N is the number of vortices. Therefore, results reported in Inoue and Leonard (1987) for 110000 time steps and 2600 vortices will require 7436×10^8 operations; it is also mentioned in Inoue and Leonard (1987-b) that adequate results for $(-u'v')$ are obtained with 14000 time-steps; i.e., 946×10^8 operations. In the VIC method, the number of operations per time-step is proportional to $\{G_p \text{ Ln } G_p + 8N\}$, where G_p is the number of grid points, and 8N is the number of operations required for the area-weighting scheme and for the bilinear interpolation. Therefore, the number of operations is 1761×10^8 for the data reported in figure 5.3-d using a 256×256 grid system. However, the results in

figure 5.3-d are close to those obtained using a smaller number of grid points with a 128×128 grid system, with a shorter time interval, 100000 time-steps, and a smaller number of vortices, 9600 vortices which require 236×10^8 operations. Based on the above estimates, the VIC method requires a smaller number of operations in comparison with the Lagrangian method. Finally based on what is reported in the literature, e.g., Sarpkaya (1994), it is a presumption in this study that the VIC method needs less computational time compared to the pure Lagrangian methods, and it is not one of the objectives of the present study to prove that the VIC method is faster than the pure Lagrangian methods.

TABLE 5.1. Maximum values of Reynolds stresses

Authors	r	r.m.s. $u'/\Delta U$	r.m.s. $v'/\Delta U$	$u'v'/\Delta U^2$
Present study (VIC)	0.6	0.21	0.26	0.012
Inoue and Leonard (Lagrangian)	0.6	0.20	0.25	0.012
Oster and Wygnanski (Exp.)	0.6	0.18	0.153	0.013

5.1.6. Effect of Grid Size

The sensitivity of the results to grid sizes has been investigated using 128×128 and 256×256 grid systems, with grid sizes of 0.25 cm and 0.125 cm, respectively. Due to the mixed Eulerian-Lagrangian nature of the VIC method, one cannot simply check the grid-sensitivity by reducing the size of the grids and keeping the other numerical parameters constant. As discussed in Sarpkaya (1994), the VIC method is sensitive to the numerical parameters. One aspect of this comment is, for

example, reducing the size of the grids and keeping the number of vortices constant, reduces the density of the vortices per grid. Therefore, the sensitivity of the results to the grid size is performed by halving the size of the grids and doubling the number of vortices.

Figures 5.4-a to c show the results of the r.m.s. u', the r.m.s. v' and the Reynolds shear stress for the simulations using grid sizes of 0.25 cm (128×128 grid system), with 9600 vortices and the results of the base run (grid sizes of 0.125 cm, 256×256 grid systems and 19200 vortices). As shown in figures 5.4-a and b, the values of the r.m.s. longitudinal and lateral velocity fluctuations are very close in both cases. Figure 5.4-c shows that using smaller number of vortices creates negative values in -u'v' correlation on the low-speed side, in the vicinity of the centerline of the mixing layers. The author believes that, the occurrence of the negative -u'v'correlation has some similarities with the phenomena described by the experimental investigation of Oster and Wygnanski (1980). Their investigation has indicated that the Reynolds shear stress is very sensitive to an imposed lateral velocity. Therefore, a small mean lateral velocity may cause negative values in -u'v' correlation. They have shown that for ratios of $V/(U_2-U_1)>0.0185$, where V is the mean lateral velocity, the correlation -u'v' starts having negative values which are accentuated as the ratio increases. The results of our simulation have indicated that, there is a small lateral mean velocity (V), which increases when using fewer number of vortices. This manifests itself by a downward deflection of the centerline of the mixing layers (see the schematic figure 4.1-b). In the present study, the magnitude of the ratio $V/(U_2-U_1)$ is in the range 0 to 0.015 when $x/H<0.56$. The negative values of -u'v' start to appear when the ratio $V/(U_2-U_1)>0.012$ at $x/H=0.56$. This result is compatible with the experiments of Oster and Wygnanski (1980), and provides an evidence which is probably connected to the negative values of -u'v' on the low speed side of the mixing layers. The results of the simulation using 32000 vortices

give approximately the same results as 19200 vortices, which is in agreement with the above explanation.

5.1.7 Effect of the Number of Vortices

The sensitivity of the results to the number of vortices has been investigated using different numbers of vortices. The results of simulations using 640, 1920, 3200, 9600, 19200 and 32000 vortices are reported in this work. Figures 5.5-a to f show the streaklines of the vortices for 640, 1920, 3200, 9600, 19200 and 32000 vortices, respectively. Downstream development of the streakline of vortices shows that the flow field starts to develop earlier for the simulations using a smaller number of vortices. The delay in the development of the flow is less visible in figures 5.5-a to c because the differences in the number of vortices are not significant. However, it becomes clearly noticeable in figures 5.5-d to f that the development of the streaklines of vortices is affected by the number of vortices and the roll-up of the vortices starts at locations farther downstream. Magnified graphs of the streakline of vortices are plotted in figures 5.6-a to f. In these graphs it is easier to distinguish the downstream location of the onset of roll-up and amalgamation of the vortices. The reason for the delay in the development of the flow is not investigated in the present work, and further studies to explain this phenomenon is necessary. Figures 5.7-a to f and 5.8-a to f show the contour-plot of the evolution of the vorticity field and the magnified contour-plot of the vorticity field, in the same order as in figures 5.5-a to f. The contour-plots of the downstream evolution of vortices show that the vortex pairing and amalgamation is qualitatively the same for all of the cases regardless of the number of vortices. The only difference is the delay in the development of the flow field. It is hard to distinguish the precise downstream location where the mixing layer starts to develop, but three

major stages in the development of the flow field can be observed in figures 5.5 and 5.6. The first stage is immediately after the splitter plate where the streaklines of the vortices show small perturbations of individual vortices. In the second stage, the small perturbations suddenly transform to considerably higher amplitude perturbations. These, after a short while, cause the break up of the streaklines of the vortices followed by roll-up, pairing and amalgamation of the vortices in the third stage.

Downstream growth of the momentum thickness for the simulations using 640, 1920, 3200, 9600, 19200 and 32000 vortices is plotted in figure 5.9. The numerical values of the momentum thickness have indicated that, for all of the above cases, the maximum difference between the highest and the lowest value is about 0.06 cm. This difference is considerably smaller than the size of the grids and there is no systematic increase or decrease in the size of the momentum thickness with the variation of the number of vortices.

5.1.8. Effect of Averaging Time

The effect of averaging time is shown for four different averaging times (30000Δt, 50000Δt, 70000Δt and 100000Δt) in figures 5.10-a to c. Figures 5.10-a and b show that the averaging time has a minimal effect on the longitudinal and the lateral velocity fluctuations. These graphs show that the similarity is achieved within a shorter averaging time for the longitudinal and the lateral velocity fluctuations. Figure 5.10-a indicates that, the longitudinal velocity fluctuations exhibit a noticeable double peak when using a shorter averaging time. The effect of time averaging is clearly noticeable in the graph of the Reynolds shear stress (figure 5.10-c). The graph shows that the Reynolds shear stress obtains similar profiles after 70000 time steps and further averaging (100000 time steps) does

not affect the outcome. Aref and Siggia (1981) attributed the larger averaging time necessary for the Reynolds shear stress to the large statistical fluctuations of the Reynolds shear stress. They pointed out that, since the Reynolds shear stress is a sum of contributions from pairs of vortex clusters in various stages of relative rotation or amalgamation, a much longer ensemble averaging is necessary to produce smooth averages. Figure 5.10-c shows that the simulation with $70000\Delta t$ generates not only similar profiles, but also the peak value of the Reynolds shear stress (≈ 0.013) is in excellent agreement with the experimental results of Oster and Wygnanski (1982) and with the grid-free numerical simulation of Inoue and Leonard (1987).

5.2 Uniformly Sheared Flow

A schematic of the velocity field is shown in fig. 4.3. As shown in the figure, the flow field is initially generated by a set of splitter plates which makes a stepwise linear velocity profile. This velocity profile gradually transforms to a uniformly sheared flow through turbulent mixing of the adjacent layers. Since the mean shear is a dimensional quantity and the main purpose is to have a longer dimensionless time (τ) for the same downstream distance(x) from the splitter plates, therefore

$$\tau = (x / U_c).(dU/dy) \qquad (5.2)$$

where U_c is the centerline velocity and dU/dy is the rate of the shear in the lateral direction, is used as the non-dimensional downstream distance. As discussed in section 2.3.1, the dimensionless time (τ), which was first introduced by Harris et al. (1977), has a special importance in characterizing the uniformly sheared flow, and its value determines whether or not the Reynolds stresses and the

turbulent kinetic energy are growing with the streamwise direction (see e.g., Rohr et. al., 1988 for more details).

5.2.1. Results and Discussions

The two-dimensional simulation of uniformly sheared flows are performed for several cases. The flow parameters are selected as close as possible to the previous experimental and numerical studies, to facilitate the comparison of the results. The flow field is calculated for various combination of shear rates and centerline mean velocities. The results are reported for a viscous flow with $\nu = 14.5\times10^{-2}$ cm^2/s (the kinematic viscosity of air at 18°C). The results of the runs with dU/dy=75 s^{-1} and U_c =237.5 cm/s, and dU/dy = 60 s^{-1} and U_c =200 cm/s are tabulated in table 5.2, and some representative plots for the case with dU/dy=75 s^{-1} are presented in this thesis. A uniform mesh system with 80×16 grid points in which the grid size is $\Delta x=\Delta y$=1cm is used. Initially the vortex sheet of each one of five co-flowing mixing layers is discretized into 2400 equidistant vortices. Therefore, a total of 12000 vortices are tracked in each time step. For the case with dU/dy=75 s^{-1} and U_c=237.5 cm/s, the circulation of each vortex is $\Gamma=2.5\times10^{-2}$ m^2/s. A time step of 8.71×10^{-5} sec., calculated as $\Delta t=d/U_{up}$ is used, where d is the initial spacing between the vortices and U_{up} is the arithmetic average of the velocities below and above the upper splitter plate. In the definition of the time step it is preferable to use the highest velocity (U_{up}), because the time steps become shorter. For the case with dU/dy=60 s^{-1} and U_c=200 cm/s, the circulation of each vortex is $\Gamma=2.0\times10^{-2}$ m^2/s, and a time step of 1.04×10^{-4} sec. is used. Initially the vortex sheets are perturbed by moving the first vortex on each sheet a short distance, 0.3d in the lateral direction. The total number of time steps used are 45000,

with the last 30000 time steps used to calculate the mean velocity and the Reynolds stresses.

5.2.1.1. Flow Field

Streaklines of the vortices are shown in fig. 5.11 from τ=0 (edge of the splitter plates) to 22. The roll-up of the vortex sheet, vortex pairing and amalgamation are responsible for the initial flow development. The lower layers develop earlier than the upper layers due to their lower velocities. A magnified instantaneous spatial distribution of the vortices is shown in figure 5.11-b which indicates a directional concentration of vortices. As noted by Sarpkaya (1994), the gradient of the vorticity field, which can be inferred from the directional stretching of the clusters of the vortices (illustrated in figure 5.11-b), can be a manifestation of the vortex stretching in two-dimensional simulations. See section 2.4.2 for more details.

5.2.1.2. Mean Velocity Profile

Normalized mean velocity profiles (U/U_{up}) at several downstream stations are illustrated in figure 5.12. The normalized mean velocity is plotted versus $2(y-y_0)/H_{shear}$, where y_0 is the ordinate of the third splitter plate from the bottom splitter plate and H_{shear} is the width of the shear region. Therefore $2(y-y_0)/H_{shear}$ =-1 corresponds to the first splitter plate (bottom), $2(y-y_0)/H_{shear}$ =1 corresponds to fifth splitter plate (top) and $2(y-y_0)/H_{shear}$ =0. corresponds to the centerline. The mean velocity profiles are homogeneous in the streamwise positions and vary linearly with the cross stream positions.

5.2.1.3. Reynolds Stresses

The r.m.s. velocity fluctuations and the Reynolds shear stress profiles, normalized by the centerline velocity at several downstream stations are shown in figures 5.13 to 5.15. Figures 5.13 and 5.14 show that the r.m.s. u' and the r.m.s. v' are nearly homogeneous in the cross-stream direction. The non-homogeneity in the range $0. \leq 2(y-y_0)/H_{shear} \leq 1.5$ is due to the late development of the upper layers as shown by the streaklines in figure 5.11. The homogeneity of the Reynolds shear stress in figure 5.15 is better than the r.m.s. u' and the r.m.s. v'. The growth of the Reynolds stresses with the downstream positions is evident and its trend will be discussed later in this section.

Figures 5.16(a) to 5.18(a) show the downstream growth of the Reynolds stresses at the centerline layer and figures 5.16(b) to 5.18(b) show the downstream growth of the Reynolds stresses at the level of each layer. Also shown in these graphs are the experiments of Tavoularis and Karnik (1989) with K_s=0.064cm^{-1} (in a wind tunnel), Harris et al. (1977) with K_s = 0.035cm $^{-1}$(in a wind tunnel), and Rohr (1988) with K_s=0.047, 0.48 and 0.61 cm^{-1} (in a water tunnel) at the centerline where the Reynolds stresses are almost maximum (see section 2.3.1 for the definition of K_s). The experimental results show that the growth rate of the Reynolds stresses is insensitive to the value of K_s when plotted versus τ. The value of K_s=0.315 cm^{-1} used in the simulation is about five times the reported experimental values. This is done to lower the computational cost by reducing the computational domain in the streamwise direction. However, the value of the non-dimensional time τ, which plays a fundamental role in characterizing the uniformly sheared flow (Rohr et al 1988), is in the range of the experimental data reported. The r.m.s. longitudinal velocity fluctuations (u'/U_c) in figures 5.16-a and b exhibit two regions for the growth rate. An undeveloped region (closer to the splitter plates), where the growth rate is faster than the experiments, and a developed region ($\tau \geq 10$),

where the growth rate reaches an asymptotic state, and is in good agreement with the experiment. All of the layers are showing almost the same growth trend in figure 5.16-b and their asymptotic values are getting close to each other. Table 5.2 shows that the simulated slope is close to the experiments in particular to the experiment of Tavoularis and Karnik (1989). The offset between the numerical and the experimental results in the developed region is probably due to the difference in the inflow conditions. In the numerical simulations the inflow boundary condition has no turbulence, while in the experimental cases the shear flow is generated by a set of splitter plates with grids of various resistance which are inherently turbulence generators.

Table 5.2. Slopes of the streamwise growth rate of Reynolds stresses and turbulent kinetic energy

	Uc (cm/s)	dU/dy (1/s)	K_s (1/cm)	Slope r.m.s. u'/Uc	Slope r.m.s. v'/Uc	Slope $(q/Uc)^2$
Exp. Tavoularis&Karnik (1989)	1300	84	0.064	0.05	0.041	0.094
Exp. Harris et al. (1977)	1240	46.8	0.037	0.07	0.061	———
Exp. Rohr et al. (1988)	20.1 20.2 26.4	1.23 0.96 1.29	0.061 0.047 0.048	0.062	0.068	———
Present Simulation	237.5 200	75 60	0.315 0.3	0.05 0.05	0.038 0.04	0.094 0.094

The grid-generated turbulence dominates the inlet region and decays after a while, depending on the type of generators. As explained in detail by Rohr et al (1988), the grid generated turbulence

has a continuing effect on the downstream growth of the turbulence, depending on the grid size, the distance between the grids and the inlet flow condition. The grid generated turbulence introduces an offset in the Reynolds stresses profiles. In the asymptotic region (developed region), the magnitudes of the Reynolds stresses are directly related to the initial conditions but their growth rate is independent of the initial conditions when plotted versus τ.

Downstream growth rates of the r.m.s. lateral velocity fluctuations (v'/U_c) are shown in figure 5.17-a for the centerline layer and in figure 5.17-b for all of the layers. The conclusions are similar to those presented for the growth rate of the r.m.s. longitudinal velocity fluctuation, except that in 2-D simulations the r.m.s. lateral velocity component is expected to be greater than the experimental results, because the energy-transfer from the streamwise component is only to the cross-stream component.

Downstream growth rates of the Reynolds shear stress ($-u'v'$) are shown in figure 5.18-a for the centerline layer, and in figure 5.18-b for all of the layers. It is noticeable that the downstream growth of the Reynolds shear stress is not smooth and monotonic in some of the layers, and the lowest layer (marked in the figure 5.18-b as N=1), exhibits a large decrease in the downstream regions. The average cross-stream correlation $u'v'$ is sum of contributions from pairs in various stages of relative rotation and amalgamation of vortices. Aref and Siggia (1980), studied the variation in the sign of the Reynolds shear stress in a simple shear layer containing two pair of vortical structures. They have reported that the value of the Reynolds shear stress changes sign during pairing, and depending on the relative location of the eddies, it can be negative or positive. They have concluded that the cause of this observation is the cancellations due to fluctuations in sign of the Reynolds shear stress, and they have suggested that better statistics is necessary on this quantity than the longitudinal

and the lateral velocity fluctuations which are definitely positive quantities.

5.2.1.4. Turbulent Kinetic Energy

The downstream growth of turbulent kinetic energy $q^2=((r.m.s.u')^2+(r.m.s.\ v')^2)/2$ is plotted in figure 5.19-a for the centerline layer and in figure 5.19-b for all of the layers. The asymptotic growth rate of turbulence kinetic energy is in good agreement with the experimental results. The experimental and numerical values are 0.094 (see table 5.2.), which are close to the value $\kappa \approx 0.1$ obtained for the high shear rate experiments (Tavoularis and Karnik, 1989). Similar to what was described for the other Reynolds stresses, the downstream growth of the turbulent kinetic energy exhibits two regions for the growth rate. An undeveloped region (closer to the splitter plates), where the growth rate is faster than the experiments, and a developed region ($\tau \geq 10$), where the growth rate reaches an asymptotic state. All of the layers are showing almost the same growth trend in figure 5.19-b and their asymptotic values are getting close to each other. As discussed for the other Reynolds stresses, the offset is probably due to the grid generated turbulence in the experimental cases.

5.2.1.5. Component Energy Ratios

The component energy ratios $K_{11} = (r.m.s.\ u'/q)^2$, $K_{22} = (r.m.s.\ v'/q)^2$ and $K_{12} = (-u'v'/q)^2$ are shown in figure 5.20. The numerical value of $K_{11} = 0.32$ is about *37%* less than the experimental value of $K_{11} = 0.51 \pm 0.04$. This result is comparable to the mixing layers result using a two-dimensional vortex method, where K_{11} has a value of *0.4* and is *25%* less than the experimental value of $K_{11} = 0.5$

(see Ghoniem and Ng, 1987). The numerical value of K_{22} =*0.68* is about three times larger than the experimental value of K_{22} =*0.22±0.02*. In a two-dimensional simulation, the predicted value of K_{22} is expected to be higher than the experimental value, because in the absence of the third dimension, the transfer of energy from the longitudinal component (K_{11}) is to the lateral component only. Based on the above explanation, in a two-dimensional simulation of uniformly sheared flows, although it is expected that the predicted value of K_{22} will be higher than the experimental value, this value is not expected to be more than 100% of the experimental value. The discrepancy between the results of two-dimensional simulation of mixing layer and the uniformly sheared flow may be attributed to their structural difference. The large coherent structures, which are clearly visible in the mixing layers, are not observed in uniformly sheared flows. The large structures in the mixing layers behave more two-dimensionally than the small-structures-dominated uniformly sheared flows.

Chapter 6

Results of Three-Dimensional Simulation

A three-dimensional simulation is performed to examine the dynamics of filaments in a uniformly sheared turbulent flow. In this section, some representative plots produced by the simulations, are presented. The three-dimensional simulation described in this section is divided into two main categories, namely, the spatially developing uniformly sheared flow with non-periodic free-slip-wall boundary conditions and the quasi-temporally developing uniform shear flow with periodic boundary conditions in the streamwise direction.

6.1. Description of the Problem

A schematic of the velocity field was to be similar to what was described for the two

dimensional simulation of uniformly sheared flows, in figure 4.3. The flow field is initially generated by a set of splitter plates which make a stepwise linear velocity profile. The vorticity in the shear region, at the level of the splitter plates, is assumed to be represented by a set of discretized vortex filaments. Circulation of each one of the discretized filaments is constant along the filaments and stretching the filaments does not affect their strength. This is according to the Kelvin's theorem, that in an ideal fluid the total circulation is conserved (see equation 3.15). The straight filaments are also discretized into equidistant vortex elements, that are merely point vortices or markers. The vortex elements are characterized by a circulation vector whose direction is tangent to the filament. The tangent vector of each element is approximated as the difference between the position vectors of its neighbouring vortex elements (see section 4.3.2 and figure 4.5 for details). Therefore, the directions of the circulation vectors of the filaments are characterized by the directions of the circulation vectors of their elements.

The components of the vorticity vector are obtained at the nodal points only, and are calculated by distributing the components of the circulation vectors of the vortex elements to the surrounding nodes (four nodes in a 2-D simulation and eight nodes in a 3-D simulation). In the absence of dissipation, the circulation of a filament is constant and stretching of the filament changes the direction of the circulation only. However, the vorticity depends on the size of the cell and is higher for finer grids. In a 2-D simulation the vortex filaments not only do not stretch, but also they do not bend or tilt and their direction is always perpendicular to the plane of motion. Therefore, a vortex filament is simply assumed to be a vortex element whose vorticity is always perpendicular to the plane of motion. In both spatially developing uniformly sheared flow and quasi-temporally developing uniform shear flow, five splitter plates are used to generate the flow field. The flow

parameters used for the simulations are: the bottom velocity U_{bottom} =50.0 cm/s, the top velocity U_{top} = 80.0 cm/s, the velocity difference across the splitter plates ΔU = 6 cm/s, the mean centerline velocity U_c= 65 cm/s and the kinematic viscosity ν =0 .14 cm/s^2.

6.2. Spatially Developing Three-Dimensional Uniformly Sheared Flow

For the spatially developing shear flow, initially the vortex sheets of each one of the five co-flowing layers are discretized into 3840 equidistant filaments and each filament consists of seventeen vortex elements. Thus a total of 3840×17×5 vortex elements are tracked in each time step. The circulation of each vortex filament is calculated as $\Gamma_{filament}$= $\Delta U.L/N$, where ΔU is the velocity difference across each splitter plate, L is the length of the computational domain and N is the number of vortex filaments per splitter plate (the value of circulation obtained in this fashion is equal to the value of circulation using equation 4.1, because L/N=d, where d is the initial distance between the neighbouring vortex filaments). Therefore the circulation of each one of the vortex filaments is $\Gamma_{filament}$= 1.25×10^{-5} m^2/s. A uniform mesh system of 80×16×8 in the streamwise, spanwise and cross-stream direction, respectively, is used for the simulation with a grid size equal to 1cm. The time step is calculated as Δt= d/U_{up}, where d is the initial spacing between the vortex filaments and U_{up} is the arithmetic average of the velocities above and below the upper splitter plate. Thus a time step of Δt=2.59 ×10^{-4} sec is used in the calculations. In order to accelerate the time development of the flow field, a three-dimensional sinusoidal disturbance is applied to the vortex filaments introduced at the

edge of the splitter plates with an amplitude of 0.5d and 0.25d in the streamwise and cross-stream directions, respectively. The initial disturbance of the vortex filaments has a negligible effect on the distribution of the vorticity at the grid points, because the maximum amplitude is at least two orders of magnitude smaller than the grid size.

In the following sections, instantaneous flow fields are investigated with the help of plots of streaklines of the vortex elements, plots of circulation vectors of vortex elements, plots of locations of filaments in the computational box along the streamwise direction, contour-plots of the magnitude of vorticity at the grid points, histograms of the angle of filament segments, iso-surfaces of vorticity at the grid points and two-angle distribution of the vorticity vectors.

6.2.1. Streaklines and Circulation Vectors of Vortex Elements

A perspective view of the distribution of vortex elements in the uniformly sheared flow is presented in figure 6.1(a). The top view and the side view of the same graph is shown in figure 6.1(b) and (c). Unlike the two-dimensional simulation of the uniformly sheared flow, it is difficult to visualize any organized structures in the graph of the streaklines of the vortices. In a 2-D simulation, the vorticity vectors are always perpendicular to the plane of motion (xy-plane), but in a 3-D simulation, the vorticity vectors are initially perpendicular to the xy-plane, and the other components of the vorticity vectors are gradually produced due to the deformation of the vortex filaments. Vector-plots of the circulation of selected vortex elements are shown in figure 6.2(a-c). The circulation direction is determined using the locations of two adjacent vortex elements. A vector-plot of the circulation of the elements gives valuable information about the concentration of vortex

elements as well as the direction of their circulation vectors which is the same as the direction of the vorticity vectors. Figure 6.2(a-c) shows that the unidirectional vortex elements in the upstream region of the flow (x near 1.), with single component circulation vectors in the spanwise direction, gradually deform to have components of circulation vectors in all three directions in the downstream regions.

6.2.2. Evolution of Vortex Filaments

Clearer visualization of the streamwise development of the flow field is made possible by selecting some of the filaments on each shear layer. Figures 6.3(a-c) show the perspective, the top view and the side view of the development of vortex filaments at twenty selected downstream stations. Figures 6.4(a-c) show the perspective, top view and the side view of the development of the vortex filaments at the centerline layer. The straight and parallel vortex filaments close to the splitter plates (i.e., at x=1), are stretched and deformed due to the three-dimensional sinusoidal disturbance. The presence of the shear further deforms and bends the vortex filaments in the downstream regions. The filaments are then lifted upward as shown in figure 6.4(c). Several line patterns are used in figures 6.4(a-c) to facilitate the visualization of the filaments. Magnified views of a selected vortex filament in figure 6.4(c), are plotted in figure 6.5. It is readily seen in this graph that the filament segments have a positive angle with the xy-plane. Filaments of this shape are called horse-shoe vortices or hairpin vortices. Those segments of the deformed filaments that are moved in the positive z-direction are transported to a higher velocity region while the parts moved in the negative z-direction, are transported into the lower velocity regions. Similar to the description given by Hinze (1975), this movement further stretches and bends the vortex filaments in the streamwise direction,

and forms pairs with opposite signs of streamwise vorticity and circulation. The segments of the deformed vortex filaments have components in the streamwise, cross-stream and spanwise directions, unlike the initial filaments close to the splitter plates which have spanwise component only. Therefore the generation of streamwise and cross-stream components is due to the three-dimensional deformation of the vortex filaments. Figure 6.5 indicates that although the segments of a filament bend and stretch in different directions, the front view of the filament shows that most of the segments have a preferred angular direction with respect to the xy-plane. This angle is measured quantitatively in the following section.

6.2.3. Histograms of the Angle of Filament Segments

The angle of a filament segment with xy-plane (η), the angle of the xz-plane-projection of the segment with xy-plane (θ) and the angle of the xy-plane-projection of that segment with yz-plane (α) is shown in figure 6.6. Using the coordinate system and sign convention shown in figure 6.6, if l_x, l_y and l_z are the components of the length of each segment in the x, y and z directions respectively, the angles α, η and θ are calculated as

$$\alpha = \cos^{-1} (l_y / (l_x^2 + l_y^2)^{1/2}) \quad (6.1)$$

$$\theta = \cos^{-1} (l_x / (l_x^2 + l_z^2)^{1/2}) \quad (6.2)$$

$$\eta = \cos^{-1} ((l_x^2 + l_y^2)^{1/2} / l) \quad (6.3)$$

Histograms of the angles θ and α of all of the filament segments are shown in figures 6.8(a-c) and

figures 6.9(a-c), respectively. The angles of filaments are calculated using the segments which have a length equal to the distance between neighbouring vortex elements. The histograms of the angles θ and α of the filament are weighted by the length of their corresponding segments. The peak of the weighted histogram is higher than the peak of the unweighted histogram. The fact that the peak of the weighted histogram is higher than the peak of the unweighted histogram, implies that the segments with higher angle, are longer or more stretched. A simplified graph illustrating the effect of the length of the elements on the histogram is shown in figure 6.10. As shown in this figure, for two elements with the same angle, the histogram shows a higher peak for the element with longer length. Therefore, longer segments contribute more to the histogram. The instantaneous angle of the filaments throughout the computational domain is analysed by dividing the computational domain into ten equal sections and the angles of all filaments in every section, are calculated. Figures 6.8(a) shows that in the first region where $0<x/L<0.1$, the angles θ of the segments have no preference in any direction. Beginning with $x/L>0.1$, the angles θ gradually incline towards the positive angle (i.e., towards the positive z-direction) and the peak gets sharper farther downstream. The histogram in figure 6.8(b) shows that at $0.4<x/L<0.5$, the angle of the filaments have a peak value at about 30 degrees. The peak value of the angle of the filaments remains between 25 to 30 degrees until $x/L<0.7$, but further downstream at $0.8<x/L<0.9$, figure 6.8(c), the maxima reduces to 20 degrees. Histograms of the unweighted angle of the filaments shows that the maxima of angle θ is between 10-15 degrees. The fact that the weighted histogram demonstrates substantially higher peak angles, indicates that the segments of the filaments with higher angles are more stretched along the streamwise direction. This is expected because a vortex filament with a higher angle is subject to maximum stretching by the mean strain. This result illustrates the importance of vortex filament stretching by mean shear in the

dynamics of shear flow. It also indicates that planes with the angle near the maxima of the histogram (≈20°-25°) are likely to contain more vortical structures because the presence of vortex filaments on a plane indicates the presence of the vorticity in that region.

The weighted histograms of the angle of the xy-plane-projection of the segments of the filaments with yz-plane (α) are shown in figures 6.9(a-c). In the region closer to the splitter plate ($x/L<0.1$), figure 6.9(a) shows that the peak angle is about $\alpha=0$ (i.e., the segments are at right angle to the streamwise direction). Farther downstream, the angles of the segments of the filaments are distributed towards the streamwise direction ($\alpha \rightarrow \pm 90°$). In the section $0.8<x/L<0.9$, figure 6.9(c), the histogram illustrates that, the angles of the filaments are mostly inclined towards the streamwise direction ($\alpha = \pm 90$).

The above results for α and θ indicate that the filaments have a hairpin shape, because initially straight filaments with $(\theta, \alpha) = (0, 0)$ become deformed in such a way that the peak angle α has nearly even distribution for both positive and negative angles, figure 6.9(c), and the peak angle θ is lifted 20 degrees from the horizontal plane, figure 6.8(c). Although the magnified view of a vortex filament in figure 6.5 suggests that the vortex filaments display a hairpin-like structure, the tip of the hairpins does not have a Ω shape. Rogers and Moin (1986) obtained the same behaviour in their numerical investigation of uniformly sheared flow. They explained that the pronounced Ω-shape at the tip of the hairpin vortices, observed in channel flow, is due to self-induction effects. However, in a shear flow, uniform shear dominates the self-induction effect and inhibits the progressive deformation of the filaments into a pronounced Ω-shape, and ultimately into the ring vortices. The ring vortices are usually generated by the break-up and reconnection of the vortex filaments. The numerical simulation presented in this work does not provide a mechanism for the break-up and

reconnection (merging) of the filaments. The vortex elements that form a filament, are always considered as a part of that filament throughout the simulation. In a real flow, when some sections of the filaments get close together, they may break-up and form a vortex ring or they may reconnect to the other filaments. This is one of the limitations of the 3-D simulation presented in this work and further improvement of the model is remained for the future studies. Due to this limitation, it is believed that the results of the simulation are comparable to the experimental results for early development of the flow when the break-up and reconnection of the filaments have not dominated the flow field.

6.2.4. Two-Angle Distribution of the Vorticity Vectors

The two-angle distribution of the vorticity vectors shown in figures 6.11 (a-c), provide more directional information about the vorticity vectors at the grid points. In these graphs, η and α are the orientation angles defined in figure 6.6. Similar to the approach taken by Rogers and Moin (1987) to obtain the two-angle distribution of the vorticity vectors, the angles α and η are weighted by the magnitude of their corresponding the vorticity vectors. If ω_x, ω_y and ω_z are the components of the length of each segment in x, y and z directions, respectively, the angles α and η of the vorticity vectors are calculated as

$$\alpha = \cos^{-1}\left(\omega_y / (\omega_x^2 + \omega_y^2)^{1/2}\right) \tag{6.4}$$

$$\eta = \cos^{-1}\left((\omega_x^2 + \omega_y^2)^{1/2} / |\omega|\right) \tag{6.5}$$

The angle of the vorticity vectors throughout the computational domain is analysed by dividing the computational domain into ten equal sections. Figure 6.11(a) shows that in the section closest to the splitter plates, $0.0< x/L <0.1$, η and α are small. This indicates that most of the vorticity vectors are aligned in the spanwise (y) direction. This is expected, because in the present simulation the vortex filaments closer to the splitter plates are less developed and are mostly in the spanwise direction, as illustrated in figure 6.2. Farther downstream sections $x/L>0.1$, the contours become stretched in the positive and negative angles of α and η. The distribution of the contours is almost symmetric with respect to the origin, which indicate the invariance of the flow configuration by 180° rotation around y-axis. In downstream regions, i.e., $x/L>0.8$, figure 6.11(c) illustrates that the values of (η,α) range from (-25°,-60°) to (+25°,+60°).

6.2.5. Discussion

The results presented so far relate to the first part of the numerical simulation of the three-dimensional uniformly sheared flow. As described above, the angle θ of the filaments in the most developed parts of the flow shows that the filament segments have a positive angle with the xy-plane with a peak value around 20-25 degrees. Histograms of the angle α, figures 6.9(a-c), show that in the region closer to the splitter plate ($x/L<0.1$), the segments are perpendicular to the streamwise direction. In regions farther downstream, $0.8<x/L<0.9$, the angles of the segments of the filaments are distributed toward the streamwise direction ($\alpha \rightarrow \pm 90°$). The above results for α and θ suggests the presence of the hairpin shape structures in the downstream regions of the flow.

Two-angle distributions of the vorticity vector's angles α and η, figures 6.11(a-c) show that,

in the section closest to the splitter plates, $0.0< x/L <0.1$, η and α are small. This indicates that most of the vorticity vectors are aligned in the spanwise (y) direction. In sections farther downstream, $x/L>0.1$, the contours become stretched toward the positive and negative angles of α and η. For $x/L>0.8$, figure 6.11(c) illustrates that the values of (η,α) range from $(-25°,-60°)$ to $(+25°,+60°)$. Results of the direct numerical simulation of a three-dimensional uniformly sheared flow by Rogers and Moin (1987) show that, in the early development of the flow, the angle η of most of the vorticity vectors is near 45 degrees. After the flow develops, this angle lies between 35-40 degrees. In the more recent investigation by Kida and Tanaka (1994), they have distinguished between the angle of the vorticity vectors and that of the vortex tubes. They reported that the angle η of the vorticity vectors with the xy-plane is 40-42 degrees, which is steeper than the angle of vortex tubes.

In the present simulation the maxima of the segments' angle does not reach to 45 degrees throughout the simulation. This indicates that the flow field is still developing. In order to accelerate the development of the flow field with a reasonable computational cost, an alternative approach is implemented using a quasi-temporally growing uniformly sheared flow with periodic boundary conditions. Details of the simulation using periodic boundary conditions are discussed in the following section.

6.3. Quasi-Temporally Developing Three-Dimensional Uniformly Sheared Flow

The second set of the numerical investigations performed in this section, is a three-dimensional simulation of a quasi-temporally developing uniformly sheared flow with periodic boundary

conditions in the streamwise direction (see section 4.3.3.2 for more details).The flow parameters used for this section are the same as those used for the spatially growing uniformly sheared flow. The computational box is replaced with a shorter box which consists of a uniform mesh system with 64×64×32 grid points in the streamwise, the spanwise and the cross-stream direction, respectively, in which the grid size is $\Delta x = \Delta y = \Delta z = 0.25$cm. In the numerical simulation of a uniformly sheared flow that evolves in time, the time scale suggested for the mean flow is, 1/S, where S is the shear rate. This provides a convenient way to non-dimensionalize the time variable t, leading to a dimensionless time, St. It should be noted that the dimensionless time St of the numerical simulations can be related to the downstream distance in the experiments or in the spatially developing uniformly sheared flows. The dimensionless time St, is what has been used in most of the previous simulations of uniformly sheared flow and is adopted in the present study.

6.3.1. Development of the Vortex Elements with Time

Results of the instantaneous flow field are presented in this section for dimensionless times, St=0, 6 and 10. Plots of the streaklines of the vortices, the vector plot of the circulation vectors, and the iso-surfaces of magnitude of the vorticity will be discussed in this section. Figures 6.12(a-c) show the side views (at 10 degrees angle with the y-axis) of the flow field at St= 0, 6 and 10. The initial field (St=0) consists of undisturbed filaments throughout the domain which gradually develop in time (St= 6, 10). Since a structural pattern can not be distinguished in these plots, the side view (at 10 degrees angle with the y-axis) of circulation vectors of some of the vortex elements are plotted in figures 6.13(a,b) at St=0 and 10. These figures give better insight into the concentration and the

direction of the circulation vectors of the vortex elements. Figure 6.13(a) shows that, at St=0, straight vortex filaments are aligned in spanwise (y) direction and appear as vortex sheets in the xy-plane. Then, as shown in figures 6.13 (b,c), the circulation vectors of most of the elements align in the streamwise direction at a positive angle with the horizontal plane (xy-plane). This behaviour is expected in the uniformly sheared flows and will be discussed quantitatively, using histograms of the angle of segments, in section 6.3.3.

6.3.2. Characteristics of Vortex Elements and Filaments at St=10.

In this section, the discussion will focus on a description of the characteristics of the vortex elements and filaments at St=10, where the flow field is in the developed stage. Figures 6.14(a-c) show the perspective, side view and top view of the vector-plots of the circulation of the vortex elements at St=10. The side view of the vector-plot, figure 6.14(b), shows a directional preference in the vorticity vectors, which are mostly aligned towards the streamwise direction with a positive angle with xy-plane. Figures 6.15(a-c) illustrates the streamwise development of a few vortex filaments selected from the centerline shear layer. The presence of shear and a non-uniform velocity distribution deform, bend and stretch the vortex filaments to form the so-called hairpin or horse-shoe vortex filaments. The side view of the filaments shown in figure 6.15(b) indicates that the filaments are stretched and lifted from xy-plane. The magnitude of the angles of the filaments is discussed in the next section.

6.3.3. Histograms of the Angle of Segments

The angle of a filament segment with the xy-plane (η), the angle of the xz-plane-projection of the segment with the xy-plane (θ), and the angle of the xy-plane-projection of that segment with yz-plane (α) are shown in figure 6.6. The angles θ and α of the filaments, are calculated using equations (6.1) and (6.2) and the histograms of these angles are plotted in figures 6.16(a-f) and 6.17(a-f), respectively. The angles of filaments are calculated using segments which have a length equal to the distance between neighbouring vortex elements. The histograms of the angles θ and α are weighted by the length of their corresponding segments. The instantaneous angle of the filaments throughout the computational domain is calculated and the results of the calculations at dimensionless times St= 0, 1, 2, 4, 6, and 10 are plotted. Figure 6.16(a) shows that at St=0 the segments of the filaments are initially straight and in the spanwise (y) direction. Therefore, the histogram shows θ = 0 degree for all of the filaments. Figures 6.16(b,c) for St=1 and 2, show that the histograms of the angle θ of the segments become inclined towards a positive angle. At St=4, figure 6.16(d), the peak value of the angle of filament segments is θ=35-45 degrees. Figure 6.16(e) shows that the maxima of the histogram decreases slightly at St=6. After this stage, until St=10, figure 6.16(f), the histograms do not show any significant change, and the maxima remains between 35 and 40 degrees. The plot of unweighted histogram (not presented in the thesis) indicates a smaller peak value compared to the weighted histogram. This implies that the segments of the filaments with higher angles, are longer or more stretched (see section 6.2.3 for more details).

Distribution of the xy-plane-projection of the angle of segments of the filaments with yz-plane

(α), for St=0, 1, 2, 4, 6 and 10 are shown in figures 6.17(a-f). The histograms show that, initially at St=0, the filaments are parallel to y-axis (i.e., the segments are perpendicular to the streamwise direction). As time increases (St>0), the angle of the segments become more inclined towards the streamwise direction ($\alpha \rightarrow \pm 90$). The above results for α and θ imply that the filaments have a hairpin shape, because initially straight filaments with $(\theta, \alpha) = (0, 0)$ become deformed in such a way that the peak angle α has nearly even distribution in both the positive and negative angles, and the peak angle θ is lifted 35-40 degrees from the horizontal plane

The two-angle probability distribution of the angles η and α of the segments of the filaments are shown in figures 6.18(a-f). As defined in equations (6.1) and (6.3), η is the angle between the vorticity vectors and the xy-plane, while α is the angle between the projected length of the segments on xy-plane and spanwise direction (y-direction). In the calculation of the two-angle probability distribution of the angle of the segments, α and η are weighted by the magnitude of the length of their corresponding segments. Figure 6.18(a) shows that at St=0, η and α are small, which indicates that all of the filaments are aligned in the spanwise (y) direction. At St=1, not only the central peak of the contours does extend to larger angles of η and α, but also, two other peaks appear at $\eta \approx \pm 30°$. As time goes on, the peak of the angle η increases to 35°-40° and more segments appear in this region. Figures 6.18(e,f), show more developed stages at St=6 and St=10, respectively. Three regions containing the peak values of the angles η and α are visible in these graphs. Two peak angles appear at $(\eta,\alpha) \approx \pm(30°,90°)$ and a central peak at $(\eta,\alpha) \approx (0°,0°)$. This indicates that the high the vorticity structures are being formed in the streamwise direction with a 30° angle with the xy-plane. It is noticeable that although the location of the early-times central-peak at $(\eta,\alpha) = (0°,0°)$ moves toward $(\eta,\alpha)=\pm(30°,90°)$, at St=10 there is still a central peak at $(\eta,\alpha)= (0°,0°)$. Assuming that the

structures contributing to the behaviour of the peak values are hairpin vortices, the central peak values at $(\eta,\alpha)=\pm(30°,90°)$ may correspond to hairpin legs and the central peak value that appears at $(\eta,\alpha)=(0°,0°)$ can be attributed to the tip of the hairpins which are in the spanwise (y) direction.

6.3.4. Iso-Surfaces of the Vorticity Field

The plots presented so far were based on tracking the vortex filaments through the computational domain. Since the vortex-in-cell simulation produces both Lagrangian and Eulerian information about the vorticity field, this method enables us to study the structure of the vorticity field on the nodal points. Figures 6.19(a-d) show the iso-surfaces of the magnitude of the vorticity at dimensionless times St=1 and 10, respectively. In order to observe the vorticity structures more conveniently, the iso-surfaces of the vorticity are viewed from two different angles. At St=1, figures 6.19(a,b) show that the vorticity is concentrated at the level of the splitter plates where the vortex filaments are initially distributed as discretized vortex sheets. It is clearly visible that at this stage the flow is still developing and the layers are not mixed. These figures indicate that the vortex sheets gradually transform into clusters of the vorticity and start mixing with the neighbouring layers. Figures 6.19(c,d) for St=10 show the developed stages of the flow field. These figures illustrate that, as time elapses, the vorticity structures are formed in a direction inclined with the xy-plane.

6.3.5. Vector-Plot of the Vorticity Field

Figure 6.20 shows a perspective of the vector-plot of the vorticity field at dimensionless time

St=10. Hairpin vortices are distinguishable by viewing selected planes. Figure 6.21 is the top view of the vorticity vectors on a horizontal plane, at z=5 cm, extracted from the box shown in figure 6.20. Figure 6.22 shows a plane at a 26.6 degree angle with the xy-plane. Using hand drawing to connect the vorticity vectors that have hairpin shapes in figure 6.22, shows a more pronounced view of the hairpin vortices in this plane. Hairpin vortices are identified by two regions (legs) with opposite vorticity direction, connected at the top. Comparing figures 6.21 and 6.22 indicates that hairpin-shaped structures are formed on the plane with a positive angle with the xy-plane. These results are in agreement with the results obtained by the Eulerian simulation of Rogers and Moin (1987).

6.3.6. Two-Angle Distribution of the Vorticity Vectors

The two-angle probability distribution of the total vorticity vectors shown in figures 6.23(a-c), provides directional information about vorticity vectors on the nodal points. In these graphs η is the angle between the vorticity vectors and the xy-plane, and α is the angle between the projected vorticity vectors on the xy-plane and the spanwise direction (y-direction), as shown in figure 6.7. In the calculation of the two-angle probability distribution function (PDF) of the vorticity vectors, α and η are weighted by the magnitude of their corresponding vorticity vectors. Figure 6.23(a) shows that at St=0, η and α are small, which indicates that all of the vorticity vectors are aligned in the spanwise (y) direction. This is expected, because in the present simulation, the vortex filaments are initially distributed in the spanwise direction as illustrated in figure 6.12(a). As time goes on, St>1, the contours become stretched towards larger values (positive and negative) for α and η. The distribution

of the contours is almost symmetric with respect to the origin, which indicates the invariance of the flow configuration to 180 degree rotation around the y axis. At more developed stages, St>6, figures 6.23(e,f), show that the central peaks of the contours form at the location $(\eta,\alpha)=\pm(30°,60°)$. This indicates that the high vorticity structures are being formed in the streamwise direction with 30° angle with the xy-plane. It is noticeable that, although the location of the early-times central-peak at $(\eta,\alpha) = (0°,0°)$ moves to $(\eta,\alpha)=\pm(30°,60°)$, at St=10 there is still a central peak at $(\eta,\alpha)= (0°,0°)$. Assuming that the structures contributing to the behaviour of the peak values are hairpin vortices, the central peak values at $(\eta,\alpha)=\pm(30°,60°)$ may correspond to hairpin legs and the central peak value that appears at $(\eta,\alpha)= (0°,0°)$ can be attributed to the tip of the hairpins which are in the spanwise (y) direction.

The instantaneous vorticity ω can be decomposed into a mean vorticity (ω) and vorticity fluctuations ω', such that $\omega=\omega+\omega'$. The two-angle probability distribution of the fluctuating vorticities are presented in figures 6.24(a-f). In order to calculate the fluctuating vorticity, the mean values of the components of the vorticity at every cross-stream location are calculated using spatial averaging. Then, fluctuating vorticities are computed by deducting the calculated mean values from the instantaneous vorticities. The two-angle probability distribution function (PDF) of the fluctuating vorticities is weighted by the magnitude of fluctuating vorticities. Figure 6.24(a) shows that at St=0, the fluctuating vorticity vectors have small angles with the xy-plane and the spanwise direction (i.e. η and α are small). At St=1, figure 6.24(b), the peak values of the contours appear at about $(\eta,\alpha)=\pm(25°,35°)$, which represent the generation of streamwise vorticity. The trend of generation of streamwise vorticity continues with time and at St=6, shown in figure 6.24(e), more contours appear at about $(\eta,\alpha)=\pm(35°,60°)$. This manifests that the angle of the segments of the filaments with the

xy-plane and the yz-plane increases with time. Figure 6.24(f) shows that at St=10, besides increasing the angle of the segments with the xy-plane to $\eta=\pm 40$ degree, a central peak forms at the location corresponding to the mean vorticity ($\eta=0$, $\alpha=0$).

6.3.7. Turbulent Kinetic Energy

The time evolution of the turbulent kinetic energy, q,

$$q=((r.m.s.u')^2+(r.m.s.\ v')^2+(r.m.s.\ w')^2)^{1/2} \tag{6.6}$$

is computed for the three-dimensional quasi-temporally growing uniformly sheared flow, and the result of the simulation using 1200 vortex filaments with $\Delta x = \Delta y = \Delta z = 0.25$cm is presented in figure 6.25. In this figure, semilogarithmic coordinates are used for better comparison with the two-dimensional result and with the growth law prediction of Tavoularis (1985). As shown in this figure, unlike the two-dimensional simulation, the turbulent kinetic energy maintains almost a constant value, and does not grow with time. The growth of turbulent kinetic energy will be discussed in more details in chapter seven and a general comparison will be made between two-dimensional and three-dimensional results.

6.3.8. Component Energy Ratios

Profiles of the mean velocity at several dimensionless times are shown in figures 6.26(a-f). These figures illustrate that the mean velocity profile is linear and as St increases the mean remains linear. Therefore, the shear is uniform. In order to compare turbulent intensities from the present simulation with previous Eulerian simulations and experimental results, time evolution of the

component energy ratios are calculated and compared with the numerical simulation of Rogers and Moin (RM), 1987 and experimental results of Tavoularis and Karnik (TK), 1989. The details of the calculations are as follows. At each time step, the mean values of the velocity components are calculated using spatial averaging. Then, fluctuating velocities are computed by deducting the calculated mean values from the instantaneous velocities. The root mean square of the fluctuating velocity components is then calculated using all of the fluctuating velocity samples in the homogeneous turbulent computational box. Next, turbulent kinetic energy and component energy ratios are calculated. The component energy ratios are defined as $K_{11}=(r.m.s.\ u'/q)^2$, $K_{22}=(r.m.s.\ v'/q)^2$ and $K_{33}=(r.m.s.\ w'/q)^2$. Figure 6.27-a shows the time evolution of the component energy ratios K_{11}, K_{22} and K_{33} for the base run with $\Delta x = \Delta y = \Delta z = .25$cm and 1200 vortex filaments. In order to compare the results of the present simulation with previous experimental and numerical results, a curve fit of the component energy ratios is compared to the experimental results of Tavoularis and Karnik (1989) and the numerical simulation of Rogers and Moin (1987). This figure illustrates that, the values of K_{11} are close to the experimental and the DNS values. The curve-fit in figure 6.27-a shows that the value of K_{11} is around 0.57, while the previous experimental and numerical results are about 0.57 and 0.53, respectively. The ratio of K_{22} is 0.12, while the previous experimental result is 0.19 and the numerical result is 0.16. The ratio of K_{33} in figure 6.27-a shows that the values of K_{33} is around 0.31, while the previous experimental and numerical results are about 0.24 and 0.31, respectively. In order to make easier, the comparison between the results of the present simulation with previous numerical and experimental results, the above results are tabulated and presented in table 6.1.

The results of a simulation with a finer grid system using 128×128×64 grids with $\Delta x = \Delta y =$

Δz= 0.125 cm and 2400 filaments (figure 6.27-b), shows closer agreement with the experimental values of Tavoularis and Karnik(1989) and the numerical values of Rogers and Moin(1987). The curve-fit in figure 6.27(b) shows that the value of K_{11} is around 0.56, while the previous experimental and numerical results are about 0.57 and 0.53, respectively. The ratio of K_{22} is 0.13 while the previous experimental result is about 0.19 and the numerical result is 0.16. The ratio of K_{33} in figure

Table 6.1. Components energy ratios (K11, K22 and K33)

	dU/dy (1/s)	K_s (1/cm)	K_{11}	K_{22}	K_{33}
Exp. Tavoularis&Karnik (1989)	84	0.064	0.57	0.19	0.24
Simulation Rogers and Moin (1986)	12	0.0 Pure shear	0.53	0.16	0.31
Present simulation using grid size 0.25 cm	6	0.092	0.57	0.12	0.31
Present simulation using grid size 0.125 cm	6	0.092	0.56	0.13	0.31

6.27(b) shows very close agreement with the numerical value of Rogers and Moin(1987). The curve-fit in figure 6.27(b) shows that the value of K_{33} is around 0.31, while the previous experimental and numerical results are about 0.24 and 0.31, respectively. Furthermore, the results of the numerical simulation by Rogers and Moin (1987) show good agreement with the experimental results of Tavoularis and Karnik (1989) for 8<St<12 only, while in the present simulation the results are comparable over a longer range. It is also note-worthy that, the shear rate used for the present simulation is different from the shear rate used in previous works. Although the value of the flow generator constant (K_s), which is the main parameter in characterizing the flow field rather than the

shear rate (see section 5.2), in the present simulation is close to the K_s used in previous works (see table 6.1), however, the author speculates that the value of the shear rate may also affect the results.

The results (Figures 6.27-a,b) show that, $K_{22} < K_{33} < K_{11}$, which is in agreement with the results of the numerical simulation by Rogers and Moin (1987) and the experimental results of Tavoularis and Karnik (1989). Table 6.1, shows that, the value of K_{33} obtained from the present simulation, is the same as the result of the numerical simulation of Rogers and Moin (1987), and that the results are higher than the experimental results. On the other hand, the value of K_{11} predicted in this work is close to the experimental result of Tavoularis and Karnik (1989), while the numerical simulation of Rogers and Moin (1987) shows a lower value for K_{11}. Since $K_{11} + K_{22} + K_{33}$ is equal to one, therefore, the results of the present simulation and the results of the numerical simulation of Rogers and Moin (1987), compensate the discrepancy in an over-prediction of K_{33}, with an under-prediction of K_{22} and K_{11}, respectively. The present VIC simulation does not provide a clear answer to such a behaviour, but the author speculates that, besides the value of the flow generator constant (K_s), the shear rate (dU/dy), may also affect the values of the component energy ratios. Table 6.1 shows that although the value of the flow generator constants are close in all cases, but the shear rates used in the numerical simulations are lower than the experiment. Further investigation on this problem is left for future studies.

6.3.9. Sensitivity of the Simulation to Numerical Parameters

The investigation of the sensitivity of the simulation to the numerical parameters, indicate that the method is robust to the numerical parameters such as grid size, number of the filaments and

number of segments per filament.

6.3.9.1. Effect of Grid Size

The effect of grid size on the time evolution of the component energy ratios is presented in figures 6.27(a,b). In order to perform this test, the simulation using 1200 vortex filaments with a uniform grid size of 0.25 cm is chosen as the base case. The effect of grid size is studied by a simulation using 2400 filaments with a uniform grid system of 0.125 cm. As shown in the figures, the simulations show that the component energy ratios are qualitatively the same when different grid sizes are used. It is remarkable that in all of the test cases, the order of values of component energy ratios are the same as the base run which is $K_{11} > K_{33} > K_{22}$.

6.3.9.2. Effect of Number of Filaments

The sensitivity of the results to the number of vortex filaments has been investigated using different numbers of filaments in the streamwise direction. Figures 6.28(a-c) show the component energy ratios for simulations using 640, 1200 and 2400 filaments, respectively. It can be readily seen from the graphs that the time evolution of the component energy ratios are qualitatively close to each other and to the previous experimental and numerical results. The trend of the time evolution of the component energy ratios K_{11} ,K_{22} and K_{33} is also shown using a polynomial curve-fit in these figures.

Figures 6.29(a-c) show the side views of some of the vortex filaments at St=10 for the simulations using 640, 1200 and 2400 filaments, respectively. These graphs illustrate that vortex filaments have large angles with the xy-plane and the general configuration of the filaments and the direction of circulation vectors of the vortex elements are similar, regardless of the number of

filaments.

Figures 6.30(a-c), 6.31(a-c) and 6.32(a-c) show the histogram of the angle of the segments of the filaments for the simulations using 640, 1200 and 2400 filaments, respectively. At St=1, figures 6.30(a), 6.31(a) and 6.32(a) show that the histogram of the angle of the filaments with the xy-plane become gradually tilted toward a positive angle. At St=6, figures 6.30(b), 6.31(b) and 6.32(b) show that the peak value of the angle of filaments segments is θ=35°-40°. These figures show that the simulation is not sensitive to the number of filaments.

6.3.9.3. Effect of Number of Segments

A test of the sensitivity of the simulation to the number of segments of each filament is shown in figure 6.33(a,b). In order to perform this test, the simulation using 1200 vortex filament with 33 segments per filament and a uniform grid size of 0.5 cm is chosen as the base run. The effect of the number of segments is studied using the same number of filaments with a uniform grid system of 0.5 cm and 65 vortex segments for each filament. Figure 6.33(b) shows that, using 65 segments (two segments per grid) increases K_{33} making it closer to K_{11} . K_{22} remains unchanged with an increase in the number of segments. As shown in the figures, the simulations show that the component energy ratios are qualitatively the same when different number of segments are used. In both test cases, the order of the values of the component energy ratios is $K_{11} > K_{33} > K_{22}$.

The results have indicated that, increasing the number of segments of a filament increases the wrinkles of the filament, and bends it differently. However, the effect of the number of segments per filament, on the inclination angle of the filaments with the horizontal plane is not significant.

6.3.10. Discussion

A three-dimensional simulation of uniformly sheared flows is performed as an extension of the two-dimensional simulation in order to take into account the effect of stretching, which is a major contributor to turbulence production. As described above, in a quasi-temporally growing uniformly sheared flow the histogram of the angle θ of the segments of the filaments demonstrates a maxima around 35°-40° with horizontal plane. Two-angle distributions of the angles η and α of the segments of the filaments also indicates that the maxima of the angle of the segments of the filaments is about 35°-40° with the horizontal plane. These results (which are Lagrangian) are compared with the angle of the vorticity vectors at the grid points. The results of the two-angle probability distribution of the angles η and α of the vorticity vectors demonstrate good agreement with the two-angle probability distribution of the angle of the segments of the filaments. The results shown in figure 6.18 for the angle of the segments of the filaments and the results shown in figure 6.23 for the angle of the vorticity vectors indicate peak regions at about 35°, which corresponds to hairpin legs, and another peak region at about 0°, which can be attributed to the flat tip of the hairpin structures. Results of the direct numerical simulation of a three-dimensional uniformly sheared flow by Rogers and Moin (1987) show that in the early development of the flow, the angle of inclination of most of the vortical structures is near 45°; after the flow develops, this angle lies between 35°-40°. The numerical simulation of uniformly sheared flow by Kida and Tanaka (1994) distinguished between the angle of the vorticity vectors and of the vortex tubes. They reported that the angle η of the vorticity vectors with the xy-plane is 40°-42° and the angle of the vortex tubes is 14°-15°, which is much less than the vorticity vectors.

The time evolution of the component energy ratios K_{11}, K_{22} and K_{33} are calculated and compared with the numerical simulation of Roger and Moin (1987) and with the closest comparable case of the experimental results of Tavoularis and Karnik (1989). The results of the simulation with a fine grid size (0.125 cm), using a 128×128×64 grid system (figure 6.27-b), shows that the values of K_{11} ,K_{22} and K_{33} are close to the experimental values of Tavoularis and Karnik(1989) and the numerical values of Rogers and Moin(1987).

Chapter 7

Comparison Between 2-D and 3-D Simulation of Uniformly Sheared Flows

This chapter is devoted to a general discussion and comparison between the results of two-dimensional and three-dimensional simulations of uniformly sheared flows. The results of two-dimensional and three-dimensional simulations are processed and presented in two different fashions. In the numerical simulation of the two-dimensional uniformly sheared flow, the post-processing approach of Tavoularis and Karnik (1989) is followed, and the flow parameters are selected as close as possible to their experiments. For the three-dimensional uniformly sheared flow, since, in addition to turbulence statistics, the focus of the study is the investigation of the evolution of three-dimensional vortical structures (hairpin vortices), and their angles with the streamwise direction, the

post-processing method of Rogers and Moin (1987) is adopted. In this chapter a summary of some of the results of two-dimensional and three-dimensional simulations of the uniformly sheared flows is presented and comparisons are made to interpret the successes and failures of the computations in each case.

7.1. Turbulent Kinetic Energy

As discussed in section 5.2.1.4, the downstream growth of turbulent kinetic energy in figure 5.19-a shows that the asymptotic growth rate of turbulence kinetic energy is in good agreement with the experimental results. According to the exponential growth law, derived by Tavoularis (1985),

$$q^2/q_r^2 = e^{k\tau} \qquad (7.1)$$

the coefficient k of the exponent should be close to 0.1 for the high shear experiments (Tavoularis and Karnik, 1989). The result of the two-dimensional simulation in figure 5.19-a, which is tabulated in table 5.2, shows that the coefficient k of the exponential growth of turbulent kinetic energy is 0.094. This value is close to 0.1, and it is in agreement with the experimental results. In a two-dimensional simulation of the uniformly sheared flow, where the stretching term is absent, it is not expected that the growth of turbulent kinetic energy, which depends on a balance between dissipation (ϵ) and production (p), will be predicted correctly. Following the exponential growth law, equation 7.1, the coefficient k of the exponent depends on the ratio of dissipation to production (ϵ/p). If the value of ϵ/p is less than one, the turbulent kinetic energy grows in the streamwise direction, and if ϵ/p

is about one, the turbulent kinetic energy may maintain a nearly constant value. Therefore, it is somewhat surprising that the growth of turbulent kinetic energy is in agreement with the growth law presented by Tavoularis (1985). From the other side, the results of simulations using several different shear rates and centerline velocities have also indicated that the non-dimensionalized growth rates of the Reynolds stresses and turbulent kinetic energy, are in agreement with the experimental results. The author speculates that the reason why a two-dimensional simulation is able to generate growth rates which are in agreement with real flow experiments, lies in the fact that, since the production of turbulence,

$$P=-\overline{u'v'}\,dU/dy \qquad (7.2)$$

depends on the mean shear (dU/dy), and the Reynolds shear stress ($\overline{u'v'}$), and the value of Reynolds shear stress is linked to the mean flow by the mean momentum equation (see section 2.4.3 for more details), therefore, a simulation that correctly predicts the mean flow, may be able to predict the correct value of the production of turbulence either. Consequently, it is plausible that the production of turbulence is more affected by the mean flow rather than the three-dimensionality of the flow.

The growth rate of turbulent kinetic energy in the three-dimensional simulation is plotted in figure 6.25. This figure shows that, unlike the two-dimensional simulation, the turbulent kinetic energy maintains almost a constant value with time. The following explanation justifies the non-growing behaviour of turbulent kinetic energy in the three-dimensional simulation.

As mentioned earlier in this chapter, for the three-dimensional simulation we have followed the post-processing method of Rogers and Moin (1987). Therefore, the flow parameters are close to their numerical simulation, rather than the high shear experiments of Tavoularis and Karnik (1989).

Uniformly sheared turbulent flows can be divided in two subclasses, namely flows with growing Reynolds stresses and flows in which the Reynolds stresses are roughly constant. Existence of the third subclass of shear flows, where the Reynolds stresses are decaying, is only for the extremely weak turbulent flows. The experimental confirmation of the third subclass is inconclusive (Tavoularis and Karnik, 1989). The growth rate of the turbulent kinetic energy depends on the flow parameters, and is affected by the balance between production and dissipation. One of the main parameters that affect the growth of turbulent kinetic energy is the mean shear. The effect of this parameter is obvious, because by keeping all of the parameters constant and increasing the mean shear, a non-growing turbulent kinetic energy flow becomes a growing turbulent kinetic energy flow. However, the value of the mean shear is not sufficient to determine the growth rate of the turbulent kinetic energy. Tavoularis and Karnik (1989) reported that the asymptotic growth rate of turbulent kinetic energy depends on the flow generator constant (k_s), defined as

$$k_s = (1/U_c).(dU/dy) \qquad (7.3)$$

Their experimental results have shown that for small values of the flow generator constant, turbulent kinetic energy does not grow, while for a large k_s, it grows exponentially. Definition of the flow generator constant in equation 7.3 shows that, either by increasing the shear rate or by decreasing the centerline mean velocity, the value of k_s can be increased, and consequently, a flow with non-growing Reynolds stresses can become a growing Reynolds stresses flow. Based on the above description, since in this work, the shear rate used for the three-dimensional simulation is low, it is plausible that the non-growing behaviour of turbulent kinetic energy is due to the shear rate, and it may show a

growing behaviour by increasing the shear rate.

7.2. Component Energy Ratios

The component energy ratios $K_{11} = (r.m.s.\ u'/q)^2$, $K_{22} = (r.m.s.\ v'/q)^2$ and $K_{12} = (\overline{-u'v'}/q)^2$, for the two-dimensional simulation of uniformly sheared flow, are shown in figure 5.20. As discussed in section 5.2.1.5, while the predicted value of K_{11} is about *37%* less than the experimental value, the value of K_{22} is about three times larger than the experimental value. In a two-dimensional simulation, although it is expected that the predicted value of K_{22} be higher than the experimental value, this value is not usually more than 100% of the experimental value. This shows that the absence of the third dimension causes more error in the numerical prediction of the uniformly sheared flow than the mixing layers. The discrepancy between the results of two-dimensional simulation of mixing layers and the uniformly sheared flows is probably due to their structural differences. In the numerical simulation of mixing layers, the existence of large coherent structures, which behave more two-dimensionally than the small scale structures, reduces the effect of third dimension. But in the uniformly sheared flow the small scale structures dominate the flow field and the effect of third dimension is less negligible.

The component energy ratios for the three-dimensional simulation are shown in figure 6.27-a. As shown in this figure, the prediction of the component energy ratios is in agreement with the previous numerical and experimental results. The numerical values of the component energy ratios obtained from the three-dimensional simulation are discussed in detail in section 6.3.8. The results indicate that the three-dimensional simulation of uniformly sheared flows by the VIC method is able

to predict the component energy ratios as close as the previous direct numerical simulation (DNS) of Rogers and Moin (1987), and the results are in agreement with the experimental investigation of Tavoularis and Karnik (1989). It is also noteworthy that the predicted results by the VIC method show robustness to numerical parameters such as the grid size and the number of vortex elements.

Chapter 8

Summary and Conclusions

The vortex-in-cell (VIC) method is applied for the prediction of turbulent characteristics and the flow development of the two-dimensional spatially growing mixing layer, the two-dimensional uniformly sheared flow and the three-dimensional uniformly sheared flow. The numerical simulation of uniformly sheared flow by the vortex method is an approach which tries to provide a new understanding and insight into the dynamics of shear flows by tracking the fluid elements in a Lagrangian fashion. The previous numerical studies have not dealt directly with the vortical structures, due to their Eulerian nature, and instead, they have resorted to indirect methods in distinguishing the vortical structures by analysing the grid information. Moreover, none of the available experimental studies on the uniformly sheared flows has attempted to visualize of coherent

vortical structures either (such studies are in progress in a water tunnel by Tavoularis et al, 1999). Therefore, the necessity to investigate the presence of coherent vortical-structures, makes important the application of a Lagrangian method in tracking and studying the dynamics of vortical structures represented by the vortex filaments .

Summaries of the main contributions of this work are presented in the next three sections.

8.1. Two-Dimensional Mixing Layer

The vortex-in-cell method is used to predict the characteristics of a spatially growing mixing layer. The results are validated by comparing with the results of the grid-free Lagrangian vortex method in Inoue and Leonard (1987), and with the experiment in Oster and Wygnanski (1982). The predicted results of the mean flow and the Reynolds stresses are found to be close to the grid-free Lagrangian vortex method. The results demonstrate that the VIC method is an appropriate method for the numerical simulation of shear flows.

8.2. Two-Dimensional Uniformly Sheared Flow

One of the contributions of the methodology developed in the present work is the numerical simulation of uniformly sheared turbulent flows by vortex method. In this new application a combination of several adjacent mixing layers simulates the initial condition used to generate the uniformly sheared flow as is done in some wind tunnel experiments. The vortex-in-cell method is used to predict the flow field, and the growth rates of the Reynolds stresses and the turbulent kinetic energy of the uniformly sheared flows. The simulations are performed for various combination of

shear rates and centerline mean velocities, using the flow parameters close to the previous experimental and numerical studies, to facilitate the comparison of the results. The results of the simulation are presented for a representative case with dU/dy=75 s^{-1} and U_c=237.5 cm/s. Two regions of growth rate are predicted: regions closer to the splitter plates where the growth rate is greater than the experiment, followed by the asymptotic regions where the growth rate is in agreement with experiment. In the asymptotic regions the predicted growth rate of turbulent kinetic energy follow an exponential function as $e^{\kappa\tau}$ with κ =0.094 which is similar to the asymptotic growth rate of turbulent kinetic energy deduced by Tavoularis (1985). The absolute values of the Reynolds stresses and turbulent kinetic energy differ from the experiment by an offset due to existing grid generated turbulence in experiments. This is probably the reason why the region closer to the splitter plates indicates a growth rate greater than experiment. In a two-dimensional simulation of the uniformly sheared flow, where the stretching term is absent, it is not expected that the growth of turbulent kinetic energy, which depends on a sensitive balance between dissipation and production, to be predicted correctly. It has been suggested that, since the production of turbulence depends on the mean shear (dU/dy), and the Reynolds shear stress ($\overline{u'v'}$), and the value of Reynolds shear stress is linked to the mean flow by the mean momentum equation, therefore, the production of turbulence is more affected by the mean flow rather than the three-dimensionality of the flow.

8.3. Three-Dimensional Uniformly Sheared Flows

Three-dimensional simulation of uniformly sheared flows is performed as an extension of the two-dimensional simulation in order to take into account the effect of vortex stretching. The study in this part is focused on the evolution of the three-dimensional vortex filaments in the flow field. The

methodology is based on a mixed Lagrangian-Eulerian three-dimensional vortex-in-cell method. Summaries of some of the main results are as follows:

(a)- In quasi-temporally growing uniformly sheared flow the histograms of the angle of the segments of the filaments (θ) demonstrate a maxima around 35°-40° with the horizontal plane.

(b)- The two-angle distributions of the angles η and α of the segments of the filaments indicate that the maxima of the angle of the segments of the filaments is about η=35°-40° with the horizontal plane.

(c)- The results of two-angle probability distribution of the vorticity vectors (η,α) at the nodes, are in a good agreement with the two-angle probability distribution of the angle of the segments of the filaments. Results of the angle of segments and the angle of the vorticity vectors indicate a peak region at about $\eta = \theta = 35°$ which corresponds to hairpin legs, and another peak region at about $\eta = \theta = 0°$ which can be attributed to the flat tip of the hairpin structures. Results of the direct numerical simulation of a three-dimensional uniformly sheared flow by Rogers and Moin (1987) show that in the developed stages of the flow, the angles of inclination of most of the vortical structures lie between θ=35°-40°.

(d)- The time evolution of the component energy ratios K_{11}, K_{22} and K_{33} are calculated and compared with similar studies, i.e. the numerical simulation of Roger and Moin (1987) and the experimental results of Tavoularis and Karnik (1989). The value of K_{11} is around 0.56, while the previous experimental and numerical results are about 0.57 and 0.53, respectively. The value of K_{22} is 0.13 while the previous experimental result is about 0.19 and the numerical result is 0.16. The value of K_{33} is around 0.31, while the previous experimental and numerical results are about 0.24 and 0.31, respectively. Unlike the two-dimensional simulation, the growth rate of the turbulent kinetic energy

exhibits a non-growing behaviour and maintains almost a constant value with time.

(e)- The sensitivity of the simulation to the numerical parameters is also investigated and the results of the simulation exhibited robustness to numerical parameters such as grid size, number of filaments and number of segments per filament.

8.4. Recommendations for Future Studies

The three-dimensional simulation of shear flows is a challenging field and the methodology presented in this thesis is the first attempt in the numerical simulation of uniformly sheared flow by the VIC method. The results of the three-dimensional simulation presented in this study do not provide a complete view of the turbulent structures and scales in the flow field, and there are limitations, simplifying assumptions and shortcomings in the three-dimensional code. However, the main focus of the thesis is to trace and to study the dynamics of three-dimensional vortical structures or more specifically the vortex filaments. The following issues are recommended for future studies:

a)- In the uniformly sheared turbulent flow, the largest scale structures are produced at the edge of the splitter plates. The large structures are unstable and produce eddies of a somewhat smaller size, which themselves become unstable and generate eddies of even smaller size. This process continues until molecular viscosity suppresses further cascading. The process of producing smaller scale structures is by break-up and reconnection of the vortex filaments. In the present simulation the energy cascade and generation of small scale structures are not predicted and the ability of the simulation is confined to the early development of the flow field. Thus, to handle the energy cascade, it is recommended that a break-up and reconnection mechanism be developed.

b)- According to Helmholtz's vortex law, on a vortex filament of fixed identity (a vortex filament

which does not break-up or reconnect to the other filaments), the ratio of vorticity to the product of the fluid density with the length of the filament remains constant as time proceeds ($\omega/\rho L$= const.). Thus, if the vortex filament is stretched, the vorticity increases. In the VIC simulation, the size of the core of each vortex is assumed to be constant and equal to the cell size. Therefore, vorticities of stretched sections and unstretched sections of a filament are the same. It may be possible to develop a modified VIC scheme, in which the filaments have variable cross-section with variable vorticity. This may improve the performance of the simulation, by making the numerical model more realistic.

c)- The results of the VIC method in the numerical simulation of spatially growing mixing layers and uniformly sheared flows suggest that the VIC method can be applied for the three-dimensional simulation of other shear flows such as temporally growing mixing layers and backward-facing steps.

References

[1] - Abdolhosseini, R. and Milane, R., 1998, Vortex-in-Cell Simulation of Spatially Growing Mixing Layer, Mechanics Research Communications, v. 25, No. 3, pp. 237-244.

[2] - Abernathy, F. H. and Kronauer, R. E., 1962, The Formation of Vortex Sheets, J. Fluid Mech., v.13, pp. 1-20.

[3] - Antonopoulos-Domis, M., 1981 Large-Eddy Simulation of a Passive Scalar in Isotropic Turbulence, J. Fluid Mech. v. 104, pp. 55-79.

[4] -Aref, H. and Siggia, E. D., 1980 Vortex Dynamics of the Two Dimensional Turbulent Shear Layer, J. Fluid Mech. 100, pp.705-737.

[5]- Aref, H., 1983 Integrable, Chaotic and Turbulent Vortex Motion in Two Dimensional Flows, Ann. Rev. Fluid Mech., v.15, pp. 345-389.

[6] - Ashurst, W. T., 1979 Numerical simulation of Turbulent Mixing Layer Via Vortex Dynamics, Turbulent Shear Flows I, (Ed.) Durst et al., Springer-Verlag, New York, 402-413.

[7] - Ashurst, W. T. and Meiburg, E., 1988 Three Dimensional Shear Layer Via Vortex Dynamics, SAND 85-8772 Sandia National Laboratories, Livermore, California.

[8] - Baker, G. R., 1979 The Cloud-in-Cell Technique Applied to the Roll-Up of the Vortex Sheets, J. Comput. Phys., v.31, pp. 76-95.

[9] - Bardina, J., Ferziger, J. H. and Reynolds, W. C., 1980 Improved Subgrid-Scale Model for Large Eddy Simulation, AIAA Pap. 80- 1357.

[10] - Batchelor, G, K., 1967 An Introduction to Fluid Dynamics, Cambridge University Press.

[11]- Bernal, L. P. and Roshko, A., 1986, J. Fluid Mech., v.170, pp. 499-525.

[12]- Bradley, D., 1992 How Fast One Can Burn, 24th Symposium (International) on Combustion, pp. 247-262.

[13]- Brown, G. L. and Roshko, A., 1974 On Density Effects and Large Structure in Turbulent Mixing Layers, J. Fluid Mech., 57, pp. 785-796.

[14]- Cain, A. B., Reynolds, W. C. and Ferziger, J. H., 1981 A Three Dimensional Simulation of Transition and Early Turbulence in a Time Developing Mixing Layer, Rep. TF-15, Thermophysics Div. Dept. Mech. Engng., Stanford University, Stanford, California.

[15]- Champagne, F. H., Harris, V. G. and Corrsin, S., 1970 Experiments on Nearly Homogeneous Turbulent Shear Flows, J. Fluid Mech., v.41, pp. 81-140.

[16]- Chorin, A. J., 1973 Numerical Study of Slightly Viscous Flow, J. Fluid Mech., vol. 57, pp.785-796.

[17]- Christianson, J. P., 1973 Numerical Simulation of Hydromechanics by the Method of Point Vortices, J. Comput. Phys., v.13, pp. 363-379.

[18]- Christianson, J. P. and Zabusky, N. J., 1973 Instability, Coalescence and Fission of Finite Area Vortex Structures, J. Fluid Mech., v.61, pp. 219-243.

[19]- Clark, R. A., Ferziger, J. H. and Reynolds, W. C., 1979 Evaluation of Subgrid Scale Turbulence Models Using a Fully simulated Turbulent Flow, J. Fluid Mech., v.91, pp. 1-16.

[20]- Clements, R. R. and Maull, D. J., 1975 The Representation of Sheets of Vorticity by Discrete Vortices, Prog. Aerospace Sci., v.16, pp. 129-146.

[21]- Corcos, G. M. and Sherman, F. S., 1984 The Mixing Layer: Deterministic Model of a Turbulent flow, J. Fluid Mech., v.139, pp. 29-65.

[22] - Couet, B., Buneman, O. And Leonard, A., 1981, Simulation of Three-Dimensional Incompressible Flows with a Vortex-in-Cell Method, J. Computational Physics, v. 39.

[23]- Deardorff, J. W., 1970 A Numerical Study of Three Dimensional Turbulent Channel Flow at Large Reynolds Numbers, J. Fluid Mech, v.41, pp. 453-480.

[24]- Doorly, D. J. and Liu, C. H., 1994 Application of a 3-D Vortex Particle in Cell Computational Method to Free and Wall Bounded Shear Flows, Boundary Layer and Free Shear Flows, v.184, pp.163-172.

[25]- Feiereisen, W. J., Reynolds, W. C. and Ferziger, J. H., 1981 Numerical Simulation of a Compressible, Homogeneous, Turbulent Shear Flow. Department of Mech. Engng. Rep. TF-13, Stanford University, Stanford, California.

[26]- Felici, H. M., 1995 Eulerian/Lagrangian Coupling Procedure for Three-Dimensional Vortical Flows, AIAA journal, v.33, No. 1, pp. 48-55.

[27]- Fink, P. T. and Soh, W. K., 1974 Calculation of Vortex Sheet in Unsteady Flow and Application in Ship Hydrodynamics, Proc. 10th symp. on Naval Hydro., Cambridge, Mass., pp. 463-488.

[28] - Fishelov, D., 1989, A New Vortex Scheme for Viscous Flows, J. Of Computational Physics, v. 86, No. 1.

[29]- Galperin, B. and Orszag, S. A., 1993 Large Eddy Simulation of Complex Engineering and Geophysical Flows, Cambridge University Press.

[30]- Ghoniem, A. F. and Ng, K. K., 1986 Effect of Harmonic Modulation on Rates of Entrainment in a Confined Shear Layer, AIAA Pap. 86-0056.

[31]- Greengard, C., 1985 The Core Spreading Vortex Method Approximates the Wrong

Equation, J. Comput. Phys., v.61, p. 345.

[32]- Harris, V. G., Graham, A. H. and Corrsin, S., 1977 Further Experiments in Nearly Homogeneous Turbulent Shear Flow, J. Fluid Mech., v.81, pp. 657-687.

[33]- Hinze, J. O., 1975 Turbulence, Second edition, McGraw-Hill Inc.

[34]- Ho, C. M. and Huerre, P., 1984 Perturbed Free Shear Layers, Ann. Rev. Fluid Mech., v.16, pp. 365-424.

[35]- Hwang, W. S., 1971 Experimental Investigations of Turbulent Shear Flows, Ph.D. Dissertation, Univ. of Virginia.

[36]- Inoue, O., 1985 Vortex Simulation of a Turbulent Mixing Layer, AIAA J., vol. 23(3), p. 367.

[37]- Inoue, O., 1992 Double Frequency Forcing on Spatially growing mixing layers, J. Fluid Mech., v.234, pp. 553-581.

[38]- Inoue, O. and Leonard, A., 1987 Vortex Simulation of Forced/Unforced Mixing Layers, AIAA J. vol. 26(11), p.1417.

[39] - Jacobitz, F., Sarkar, S. And Van Atta, C., 1997, Direct Numerical Simulation of the Turbulence Evolution in a Uniformly Sheared and Stably Stratified Flow, J. Fluid Mechanics, v. 342, pp. 231-261.

[40] - Karamcheti, K., 1976, Principles of Ideal Flow Aerodynamics, John Wiley and Sons Inc.

[41]- Karnik, U. and Tavoularis, S., 1987 Generation and Manipulation of Uniform Shear with the Use of Screens, Exper. Fluids, v.5, pp. 247-254.

[42] - Kida, S. and Tanaka, M., 1994, Dynamics of Vortical Structures in a Homogeneous Shear Flow, J. Fluid Mechanics, v. 274, pp. 43-68.

[43]- Kim, J. and Moin, P., 1979 Large Eddy Simulation of Turbulent Channel Flow, AGARD Conf. Proc. No. 271, 14.

[44]- Kim, J. and Moin, P., 1986 The Structure of the Vorticity Field in Turbulent Channel Flow. J. Fluid Mech., v. 162, pp. 339-363.

[45]- Kim, J. and Moin, P., 1989 Transport of Passive Scalar in a Turbulent Channel Flow. Turbulent Shear Flow 6, Springer-Verlag, Berlin, Heidelberg.

[46]- Kiya, M., 1989 Theoretical and Applied Mech.(eds. P. Germain et al) Elsevier, pp.173-191.

[47]- Knio, O. M. and Ghoniem, A. F., 1989, AIAA Paper, 89- 0574.

[48]- Knio, O. M. and Ghoniem, A. F., 1988 On the Formation of Streamwise Vorticity in Turbulent Shear Flows, AIAA Pap. 88-0728.

[49]- Knio, O. M. and Ghoniem, A. F., 1990 Vortex Simulation of Three Dimensional Reacting Shear Layers, AIAA Pap. 90-0150.

[50]- Knio, O. M. and Ghoniem, A. F., 1991 Three Dimensional Vortex Simulation of Rollup and Entrainment in a Shear Layer, J. Computational Physics, v.79.

[51]- Kotake, S. and Hijikata, K., 1993 Numerical Simulation of Heat Transfer and Fluid Flow on a Personal Computer, Elsevier Science Publishers B.V.

[52]- Kuwahara, K. and Takami, H., 1983 Study of Turbulent Wake Behind Bluff Body by Vortex Method, Proceeding of IUTAM Symposium on Turbulence and Chaotic Phenomena in Fluids, Edited by T. Tatsumi, North Holland Publishing Corp., Amsterdam.

[53]- Kwak, D., Reynolds, W. C. and Ferziger, J. H., 1975 Three Dimensional, Time Dependent Computation of Turbulent Flow, Report TF-5 Dept. of Mech. Engng. , Stanford university.

[54]- Lee, M. J., Kim, J. and Moin, P., 1990 Structure of Turbulence in High Shear Rate, J. Fluid

Mech., v.216, pp. 561-583.

[55]- Leonard, A.,1974 Energy Cascade in Large Eddy Simulation of Turbulent Fluid Flows, Advances in Geophys., 18A, pp. 237-248.

[56]- Leonard, A., 1980 Vortex Methods for flow Simulations, J. Comput. Phys., vol. 37(3), p.289.

[57]- Leonard, A., 1985 Computing Three Dimensional Incompressible Flows with Vortex Elements, Ann. Rev. Fluid Mech., v.17, pp. 523-559.

[58]- Lesieur, M. R., 1995 Mixing layer Vortices, S. I. Green(ed), Fluid Vortices, pp. 35-63.

[59]- Lesieur, 1987 Turbulence in Fluids, 2nd Edition, Kluwer Acad. Publishers.

[60]- Leslie and Quarini, 1979 The Application of Turbulent Theory to the Formation of Subgrid Modelling Procedures, J. Fluid Mech., v.91, pp. 65-91.

[61]- Lilly, D. K., 1967 The Representation of Small-Scale Turbulence in Numerical Simulation Experiments, Proc. IBM Sci. Comput. Symp. Environ. Sci., IBM Data Process. Div., White Plain, N.Y. pp. 195-210.

[62]- Lin, P. and Pratt, D. T., 1987 Numerical Simulation of a Plane Turbulent Mixing Layer, with Applications to Isothermal, Rapid Reactions, AIAA Pap. 87-0224.

[63]- Mansour, N. N., 1985, A Hybrid Vortex-in-Cell Finite Difference Method for shear Layer Computations, AIAA Paper, 85-0372

[64]- Mansour, N. N., Ferziger, J. H. and Reynolds, W. C., 1978 Large Eddy Simulation of a Turbulent Mixing Layer, Rep. TF-11, Thermophysics Div. Dept. Mech. Engng., Stanford University, Stanford, California.

[65]- Meng, J. C. S. and Thomson, J. A., 1978 Numerical Studies of Some Non-linear

Hydrodynamic Problems by Discrete Vortex Elements Methods, J. Fluid Mechanics, v.84, pp. 433-453.

[66]- Metcalfe, R. W., Orszag, Brachet, Menon and Riley, 1987 Secondary Instability of a Temporally Growing Mixing Layer, J. Fluid Mechanics, v.184, pp. 207-243.

[67]- Milane, R. and Nourazar, S., 1997, Large-Eddy Simulation of Mixing Layer using Vortex Method: Effect of Subgrid-Scale Model on Early Development, Mechanics Research Communications, v. 24, No. 2, pp. 215-221.

[68]- Milane, R. and Nourazar, S., 1995, On the Turbulent Diffusion Velocity in Mixing Layer Simulated using the Vortex Method and the Subgrid Scale Vorticity Model, Mechanics Research Communication, v.22, No. 4, pp. 327-333.

[69]- Mulhearn, P. J. and Luxton, R. E., 1975 The Development of Turbulent Structure in a Uniform Shear Flow, J. Fluid Mech., v.68, pp. 577-590.

[70]- Muller, A. and Gyr, A., 1986, On the Vortex Formation in the Mixing Layer Behind Dunes, J. Hydraul. Res., v.24, pp. 369-375.

[71]- Nakamura, Y., Leonard A., and Spalart, P., 1982 Vortex Simulation of an Invicid Shear Layer, AIAA Pap. 82-0948.

[72]- Neto, A. S., Grand, D., Metais, O. and Lesieur, M., 1993, Numerical Investigation of the Coherent Vortices in Turbulence Behind a Backward-Facing Step, J. Fluid Mech., v.256, pp.1-25.

[73]- Ng, K. K. and Ghoniem, A. F., 1985 Numerical Simulation of a Confined Shear Layer, 10th Int. Colloquium on the Dynamics of Explosions and Reactive Systems, CA. Aug. 4-9.

[74]- Ogami, Y. and Akamatsu, T., 1991 Viscous Flow Simulation Using the Discrete Vortex Model- The Diffusion Velocity Method, Computers and Fluids, v.19, pp. 433-441.

[75]- Orszag, S.A. and Patterson,G. S., 1972 Numerical Simulation of Three Dimensional Homogeneous Isotropic Turbulence, Phys. Rev. Letters, 28, 76.

[76]- Oster, D. and Wygnanski, I., 1982 The forced Mixing Layer Between Parallel Streams, J. Fluid Mech., 123, pp. 91-130.

[77]- Phillips, O. M., 1969 Shear flow Turbulence, Ann. Rev. Fluid Mech., v.1, pp. 245-264.

[78]- Rai, M. M. and Moin, P., 1989 Direct Simulation of Turbulent Flow Using Finite Difference Schemes. AIAA Pap. 89-0369.

[79]- Riley, J. J., Metcalfe, R.W. and Orszag, S. A., 1986 Direct Numerical Simulation of Chemically Reacting Turbulent Mixing Layers, Phys. of Fluids, v.29(2), pp. 406-422.

[80]- Rogallo, R., 1981 Numerical Experiments in Homogeneous Turbulence, NASA Technical Memo. 81315.

[81]- Rogallo, R. and Moin, P., 1984 Numerical Simulation of Turbulent Flows, Ann. Rev. Fluid Mech., 16, pp. 99-137.

[82]- Rogers, M. M. and Moin, P., 1987 The Structure of Vorticity Field in Homogeneous Turbulent Flows, J. Fluid Mech., v.176, pp. 33-66.

[83]- Rohr, J. J., Itsweire, E. C., Helland, K. N. and Van-Atta, C. W., 1988 An Investigation of the Growth of Turbulence in a Uniform Mean Shear Flow, J. Fluid Mech., v.187, pp. 1-33.

[84]- Rose, W. G., 1966 Results of an Attempt to Generate a Homogeneous Turbulent Shear Flow, J. Fluid Mech., v. 25, pp. 97-120.

[85]- Rosenhead, L., 1931 The Formation of Vortices From Surface of Discontinuity, Proc. Roy. Soc., Series A, v.134, pp. 170-192.

[86]- Saffman, P. G., 1981 Dynamics of Vorticity, J. Fluid Mech., v.106, pp. 49-58.

[87]- Sarpkaya, E., 1994, Advances in Applied Mathematics, v.31, pp. 113-247.

[88]- Schlichting, H., 1968 Boundary Layer Theory, McGrow Hill.

[89]- Shaanan, S., Ferziger, J. H. and Reynolds, W. C., 1975 Numerical Simulation of Turbulence in Presence of Shear, Dept. Mech. Engng. Rep. TF-6, Stanford Univ., Stanford, California.

[90]- Shirani, E., Ferziger, J. H. and Reynolds, W. C., 1981 Mixing of a Passive Scalar in Isotropic and Sheared Homogeneous Turbulence, Dept. Mech. Engng., Rep. TF-15, Stanford University, Stanford, California.

[91]- Smagorinski, J., 1963 General Circulation Experiment with the Primitive Equations I, The Basic Experiment, Mon. Wether Rev. 91, pp. 99-164.

[92]- Souza, F., 1993 Experiments in Highly Sheared Nearly Homogeneous Turbulence, M.Sc. Thesis, Dept. Mech. Engng., Univ. Ottawa, Ottawa, Canada.

[93]- Tavoularis, S., 1985 Asymptotic Laws for Transversely Homogeneous Turbulent Shear Flows. Phys. Fluids, 28(3), pp. 999-1001.

[94]- Tavoularis, S. and Corrsin, S., 1981-a Experiments in Nearly Homogeneous Turbulent Shear Flow with a Uniform Mean Temperature Gradient. Part 1. J. Fluid Mech., v. 104, pp. 311-347.

[95]- Tavoularis, S. and Corrsin, S., 1981-b Experiments in Nearly Homogeneous Turbulent Shear Flow with a Uniform Mean Temperature Gradient. Part 2. J. Fluid Mech., v. 104, pp. 349-367

[96]- Tavoularis, S. and Karnik, U., 1989 Further Experiments on the Evolution of Turbulent Stresses and Scales in Uniformly Sheared Turbulence, J. Fluid Mech., v.204, pp. 457-478.

[97]- Tavoularis, S., 1999, Private Communications.

[98]- Tennekes, H. and Lumley, J. L. , 1977 A First Course in Turbulence, MIT Press, Cambridge, Mass.

[99]- Wang, S. S., 1977 Grid-Insensitive Computer Simulation of the Kelvin-Helmholtz Instability and Shear Flow Turbulence, Ph.D. Thesis, Stanford Univ., Inst. for Plasma Res., Stanford, Rep. No. 710.

[100]- Wilcox, D. C., 1993 Turbulent Modelling for CFD, DCW Industries, La Canada, CA.

[101]- Yanenko, N. N., 1971 The Methods of Fractional Steps, Springer Verlag.

[102]- Zawadzki, I. and Aref, H., 1991 Mixing During Vortex Ring Collision, Phys. Fluids A3(5).

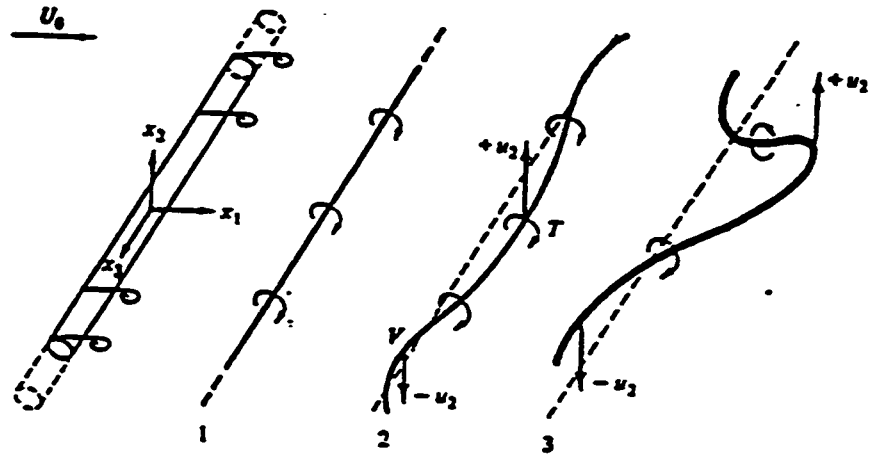

Figure 2.1. Deformation of vortex filaments in a shear layer (Hinze, 1975 page 560).

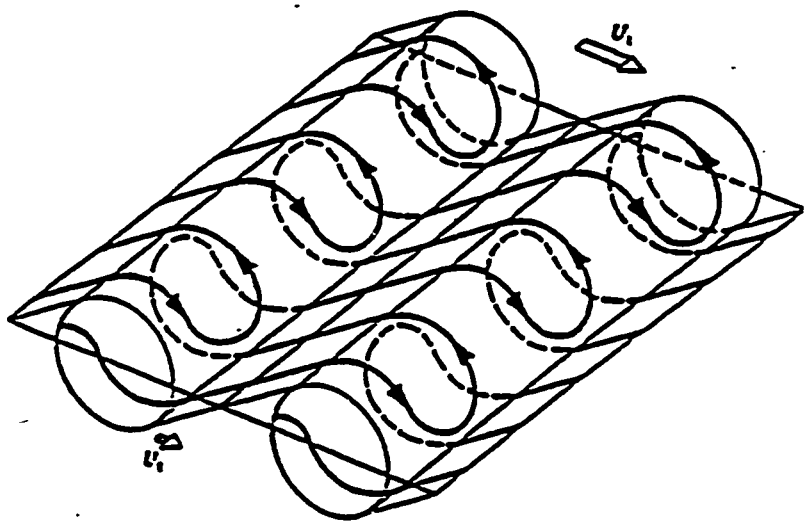

Figure 2.2. Schematic representation of longitudinal hairpins in a mixing layer. Experiment done by Bernal and Roshko (1986)

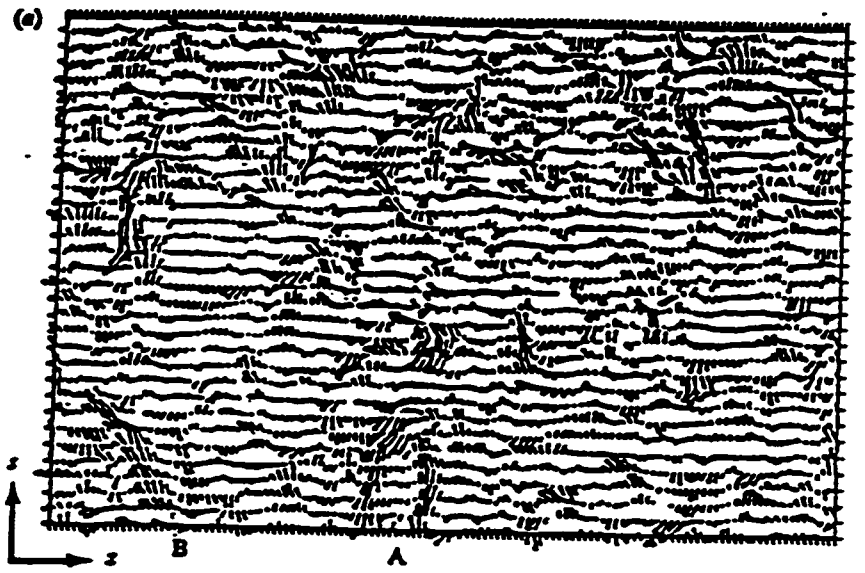

Figure 2.3. Hairpin vortices in a uniformly sheared flow (Rogers and Moin, 1987).

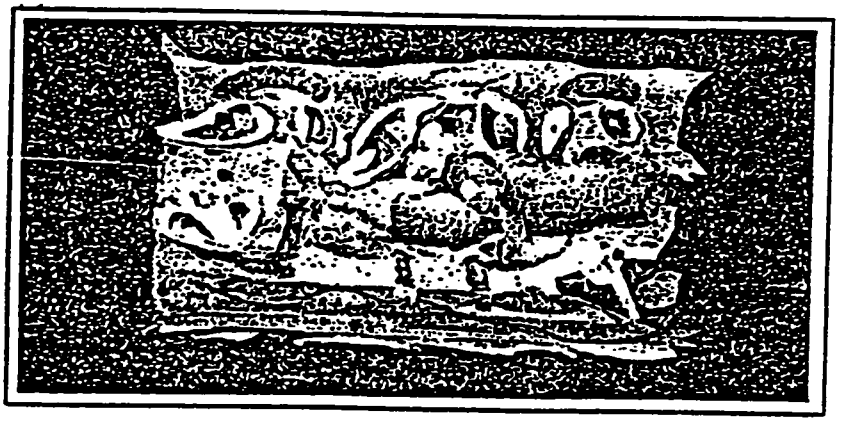

Figure 2.4. Longitudinal hairpin vortices strained behind a backward-facing step. (Neto et. al.1993, J. Fluid Mechanics)

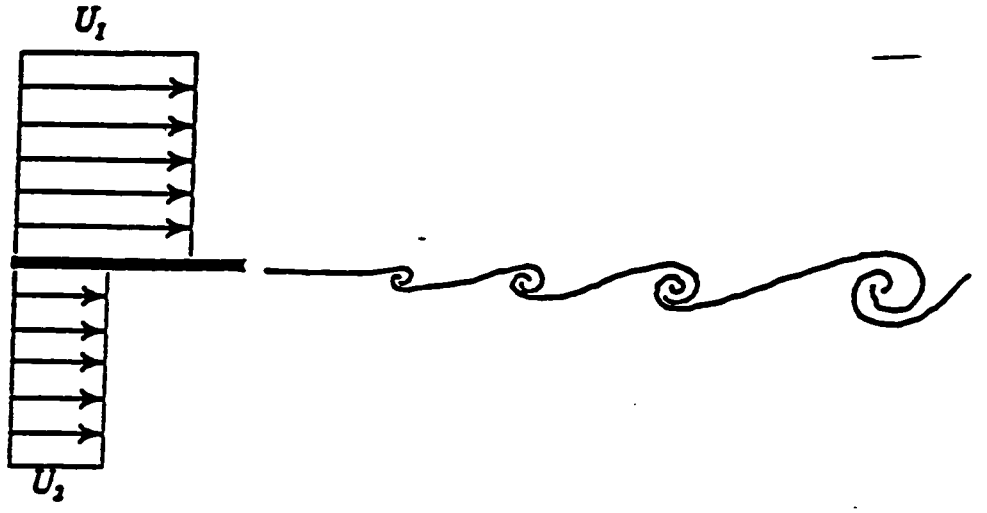

Figure 4.1-a Schematic of a typical plane mixing layer

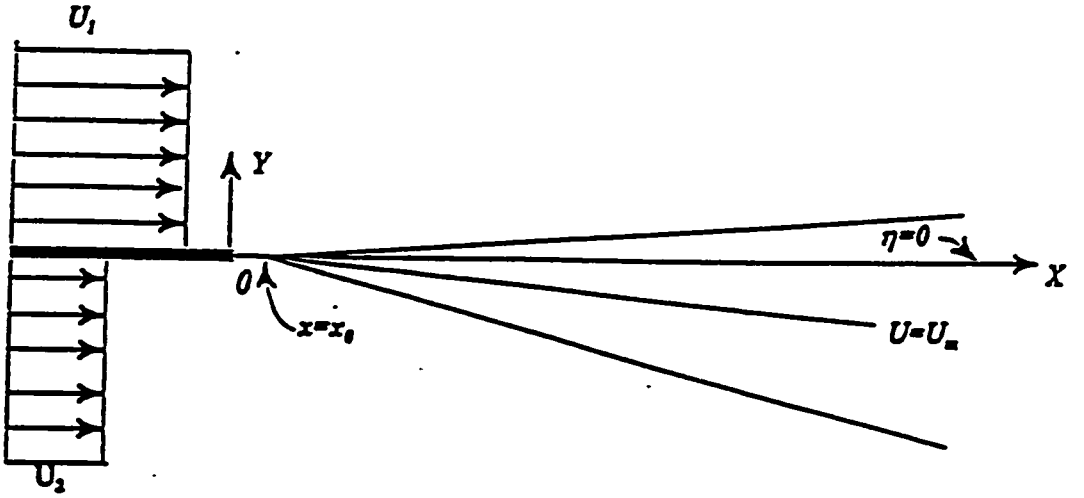

Figure 4.1-b Diagram showing the virtual origin of mixing layer

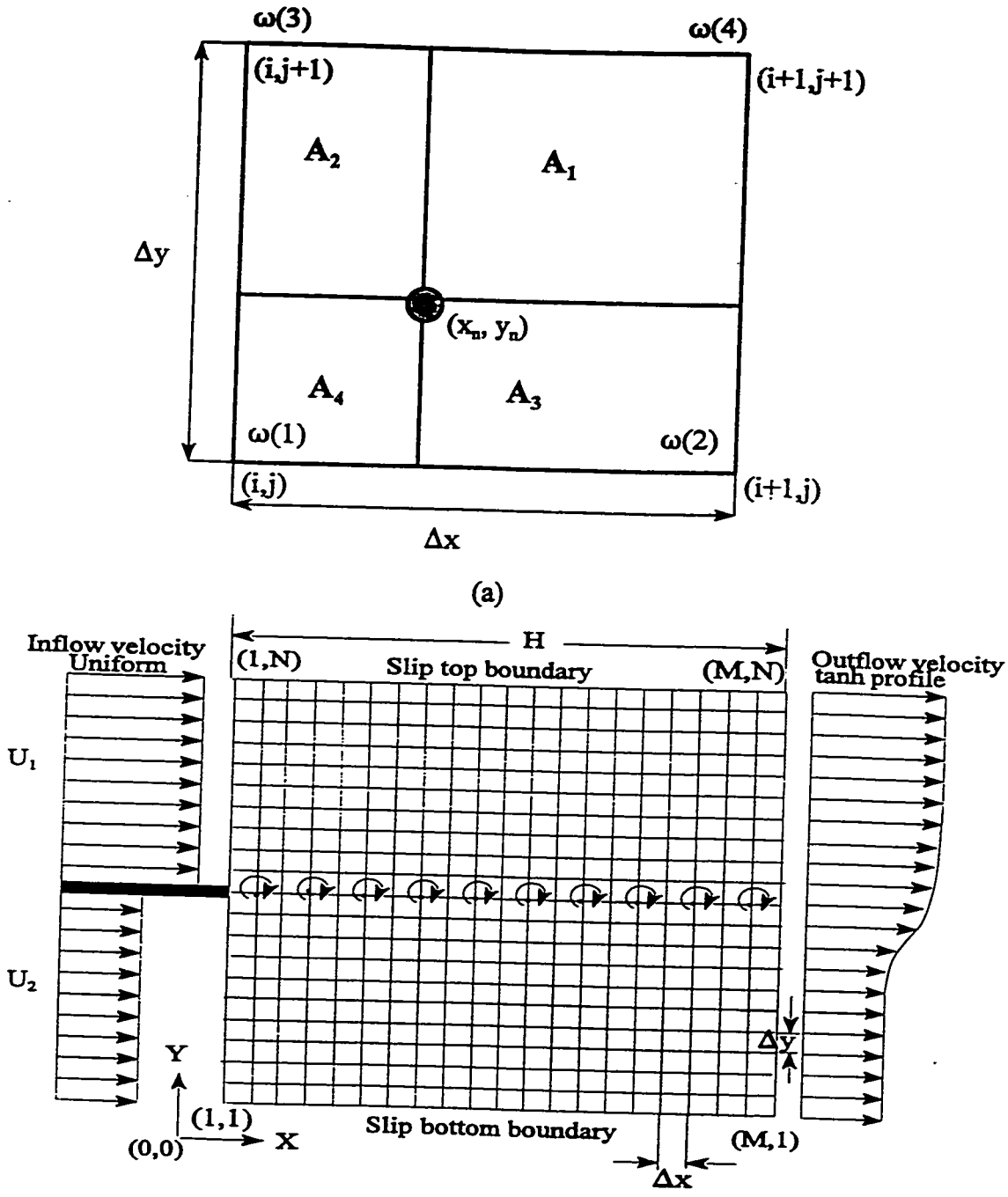

Figure 4.2. (a) Two dimensional area-weighting scheme in the VIC method; (b) Computational domain, rectangular grid, initial position of the vortices, and boundary conditions.

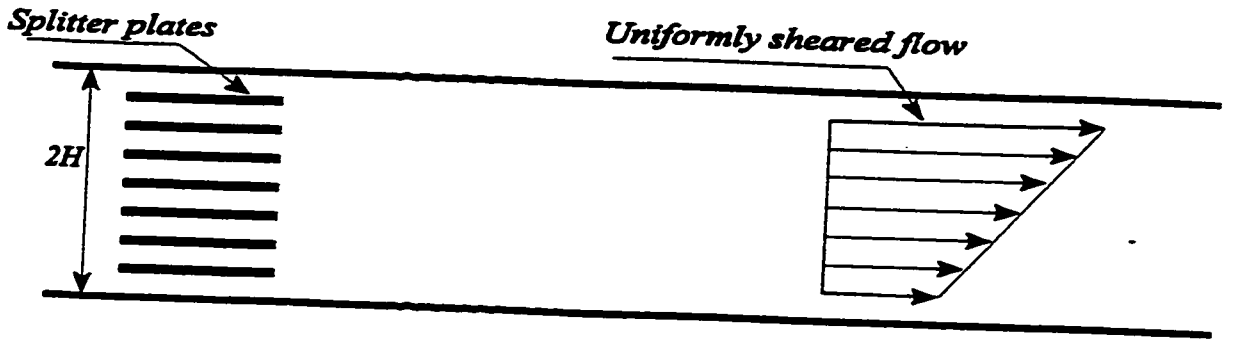

Figure 4.3. Schematic diagram showing the shear generator and velocity profile for a uniformly sheared flow.

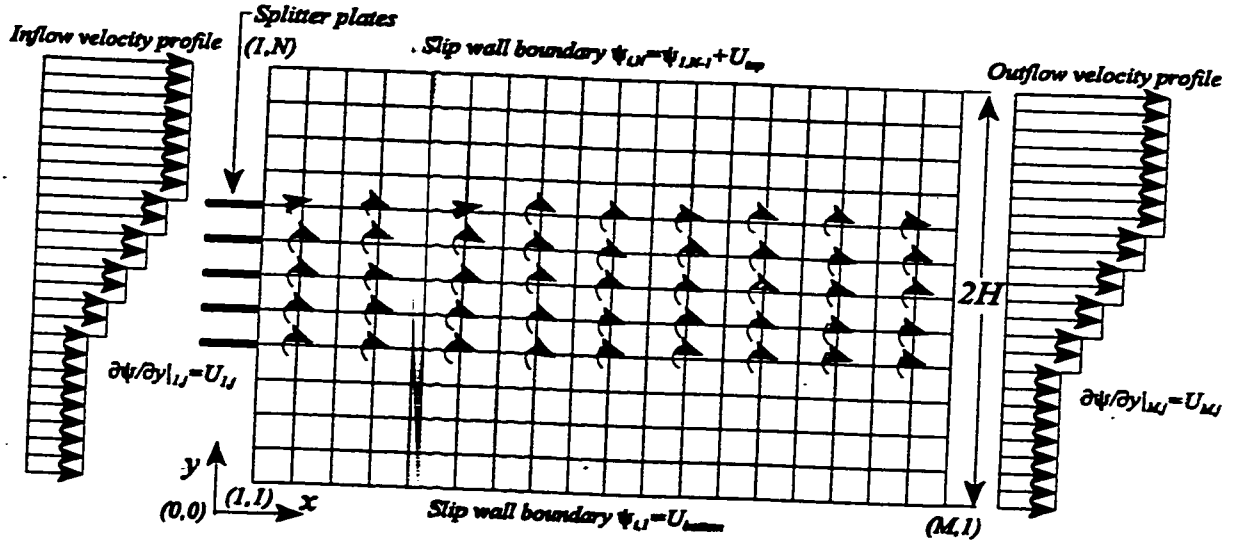

Figure 4.4 Mesh system and boundary conditions used for simulation of a uniformly sheared flow.

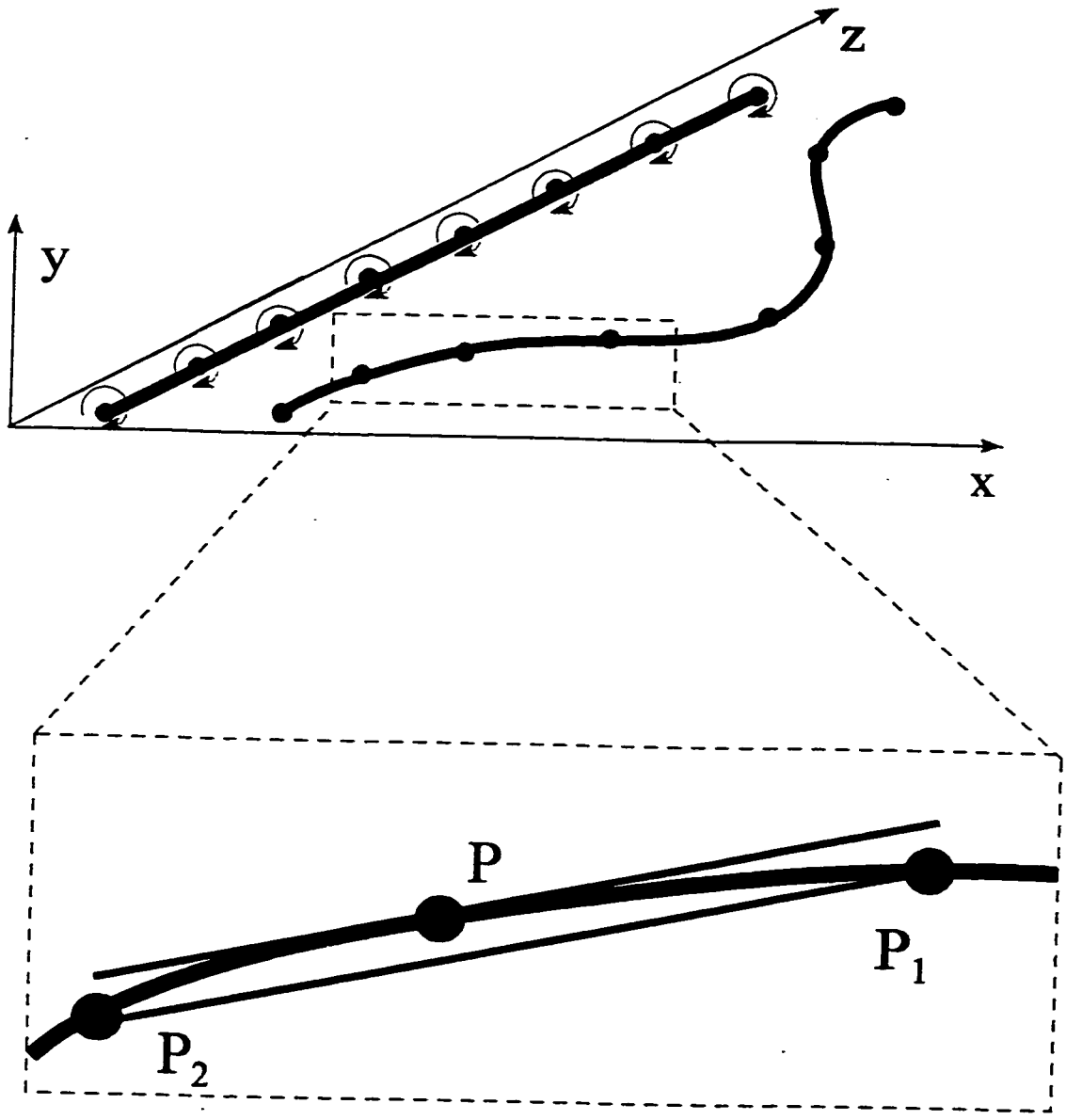

Figure 4.5. A schematic configuration showing the vortex filaments and a model for determining the direction of the circulation vector of each element.

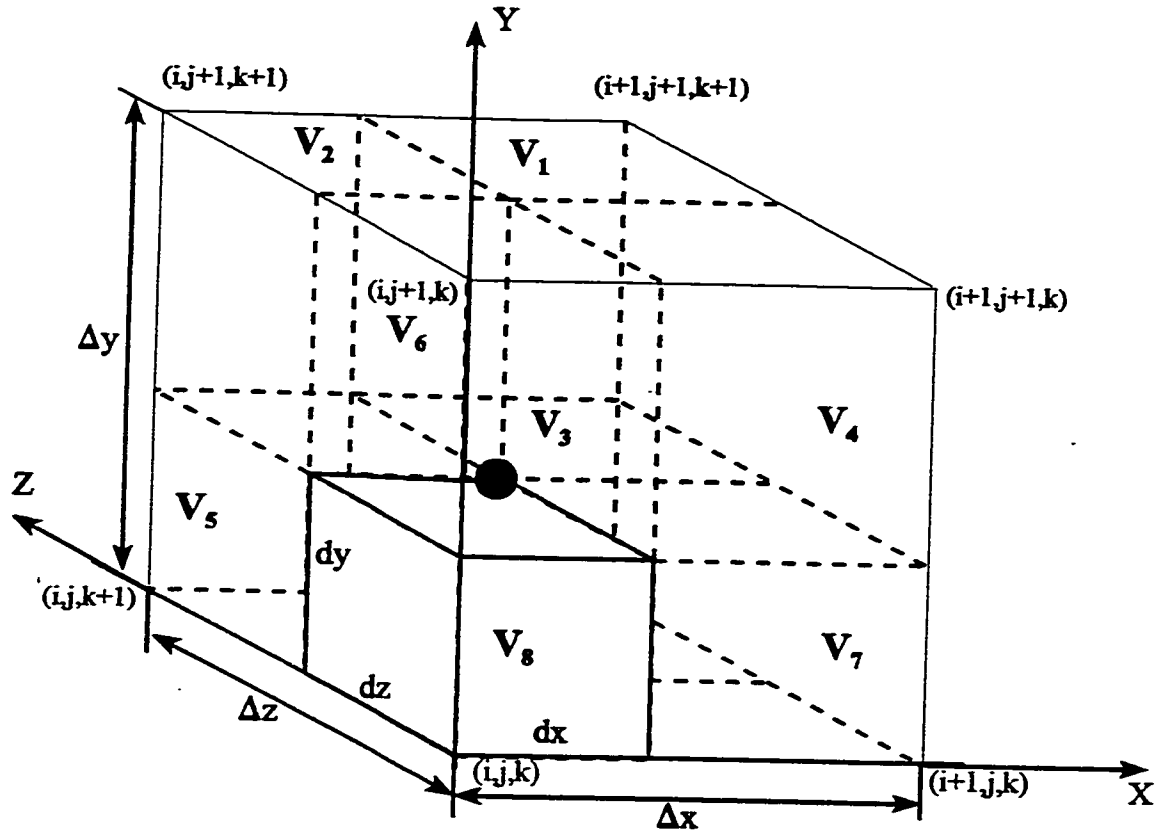

Figure 4.6 Volume weighting scheme for three-dimensional VIC method.

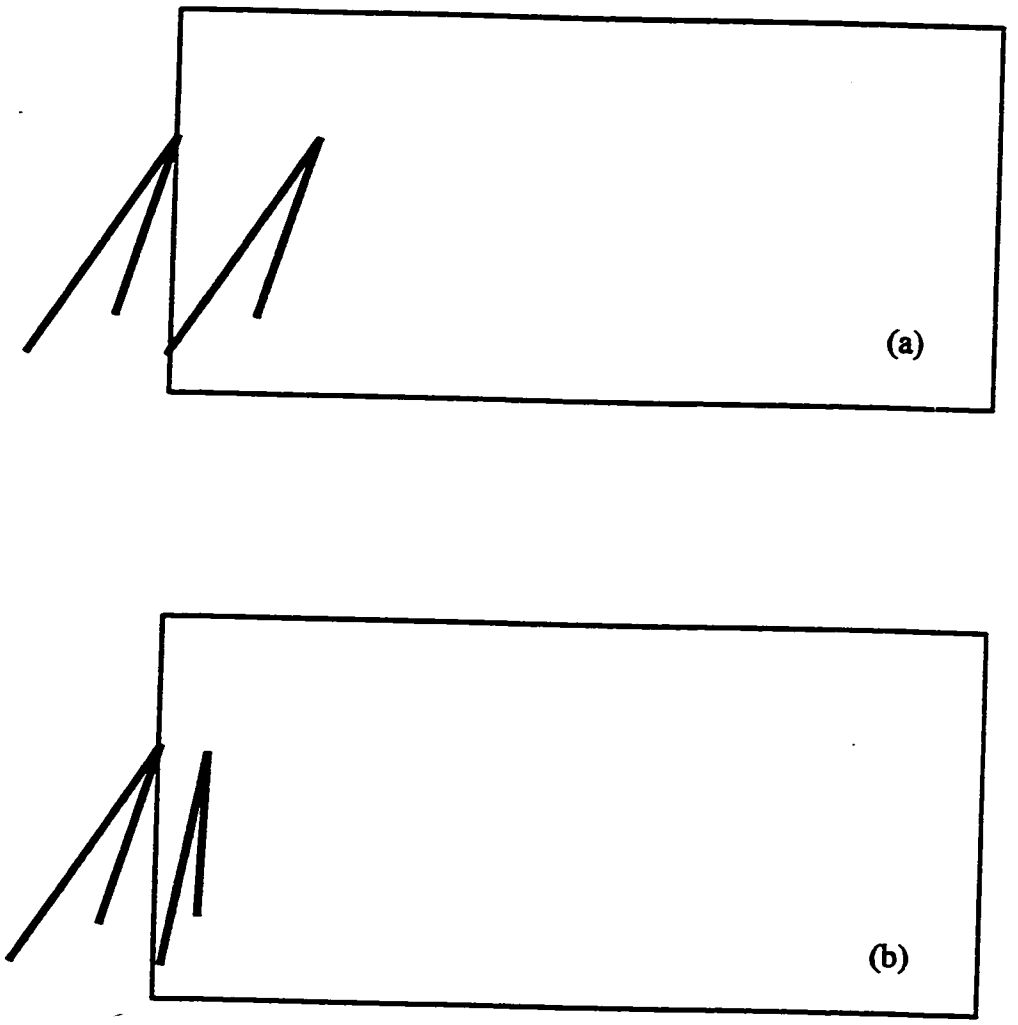

Figure 4.7. Schematic configurations showing the effect of the reshaping on the filaments as they enter to the computational box
(a) Without reshaping (b) With reshaping

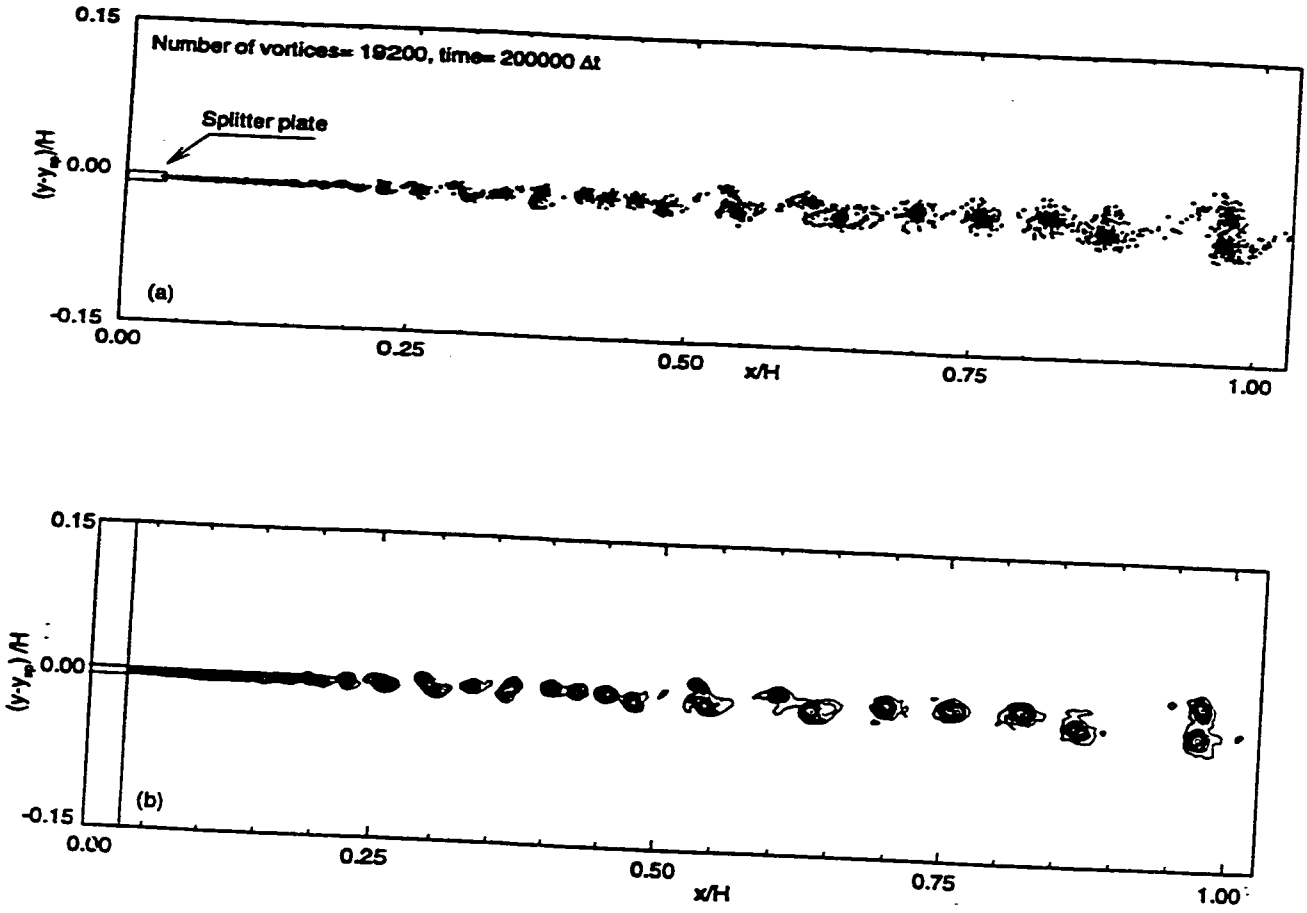

Figure 5.1. (a) Streakline of vortices, and (b) vorticity contours for the base run using 19200 vortices, at time= 200000Δt.

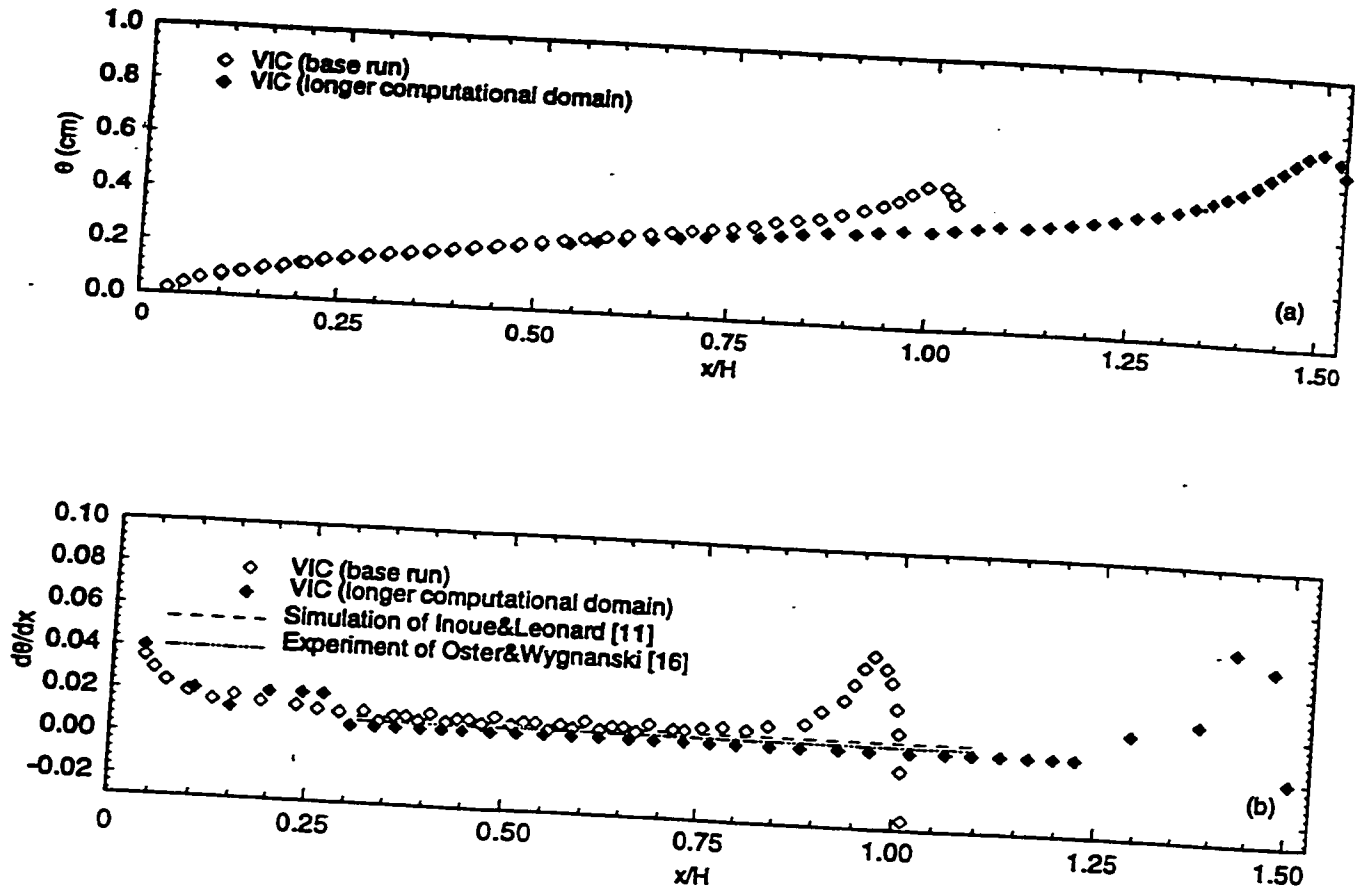

Figure 5.2. (a) Momentum thickness (θ), and (b) momentum thickness growth rate ($d\theta/dx$) versus x/H.

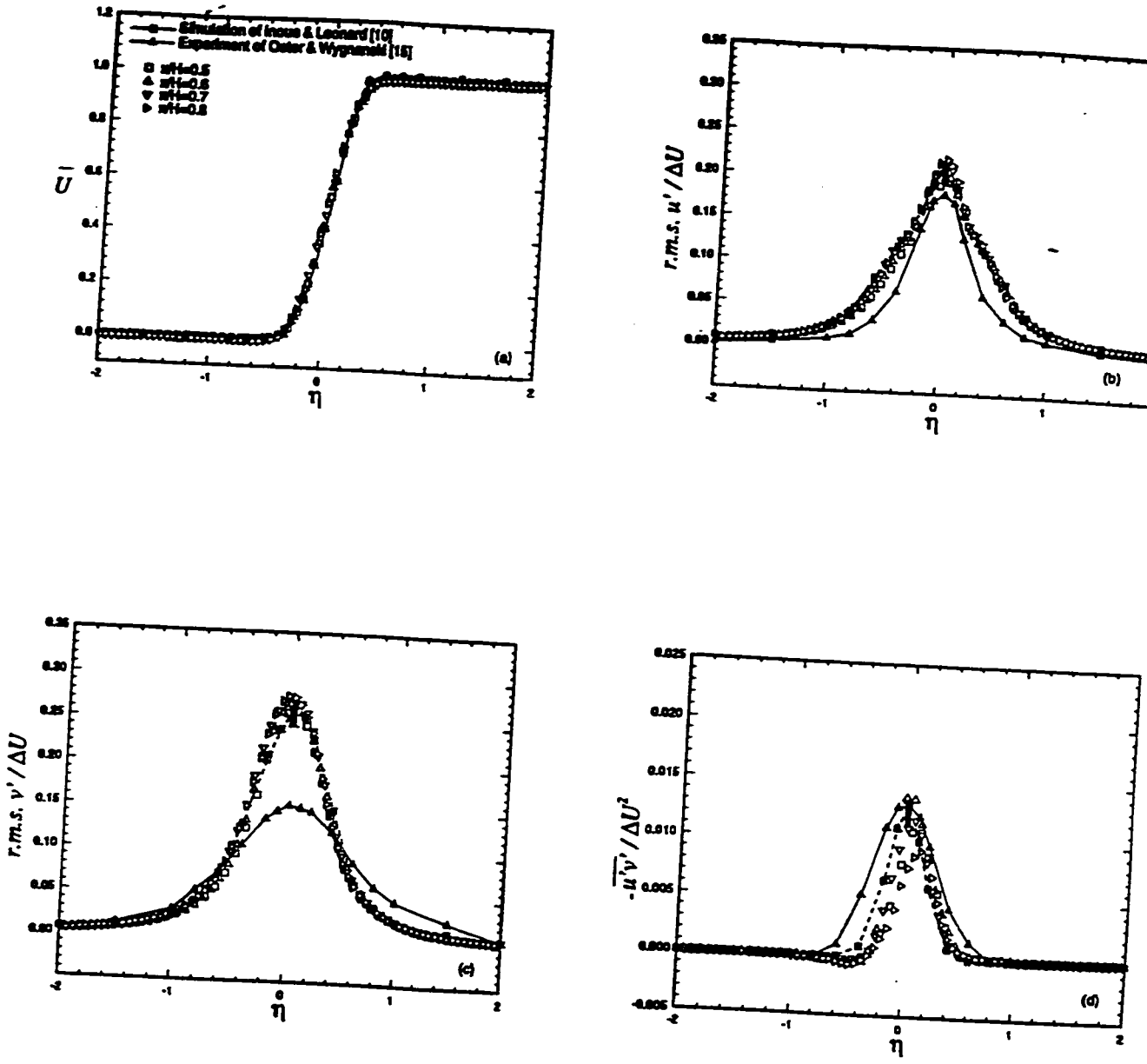

Figure 5.3. Profiles of normalized Reynolds stresses. The vertical bars represent the spread of the maximum values of the Reynolds stresses (Inoue and Leonard, 1987)

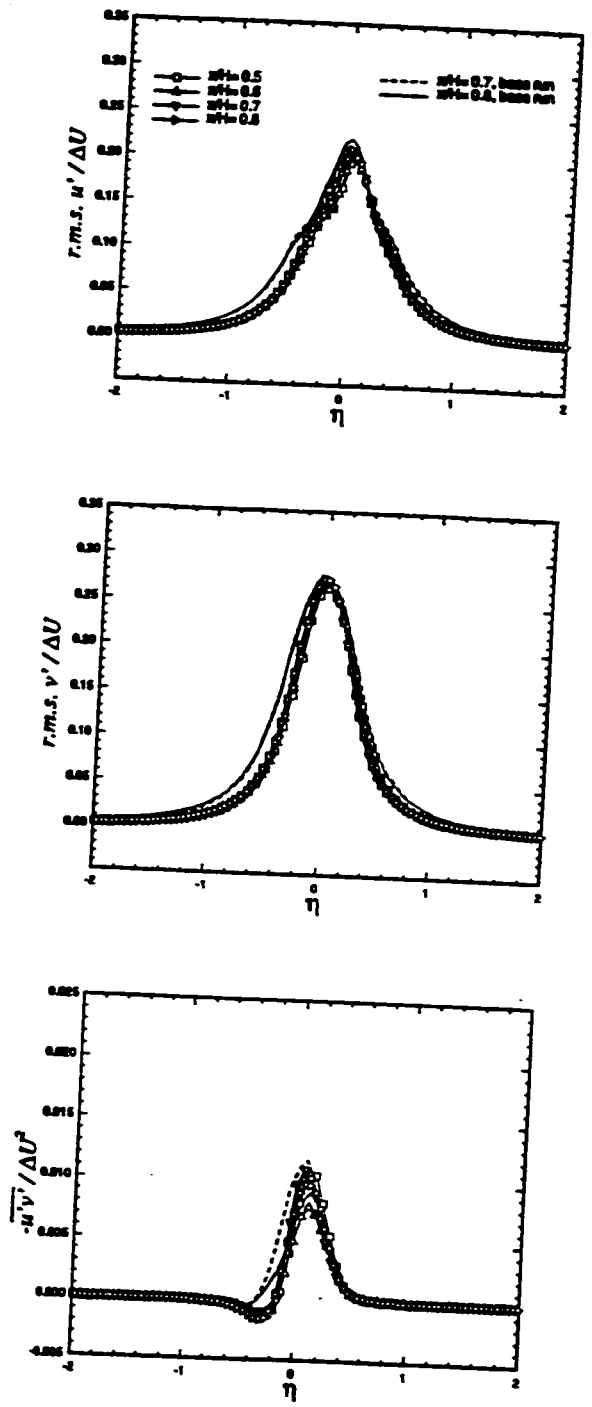

Figure 5.4. Profiles of normalized (a) r.m.s. longitudinal, (b) r.m.s. lateral and (c) Reynolds shear stress for a simulation using 9600 vortices, compared with the base run with 19200 vortices.

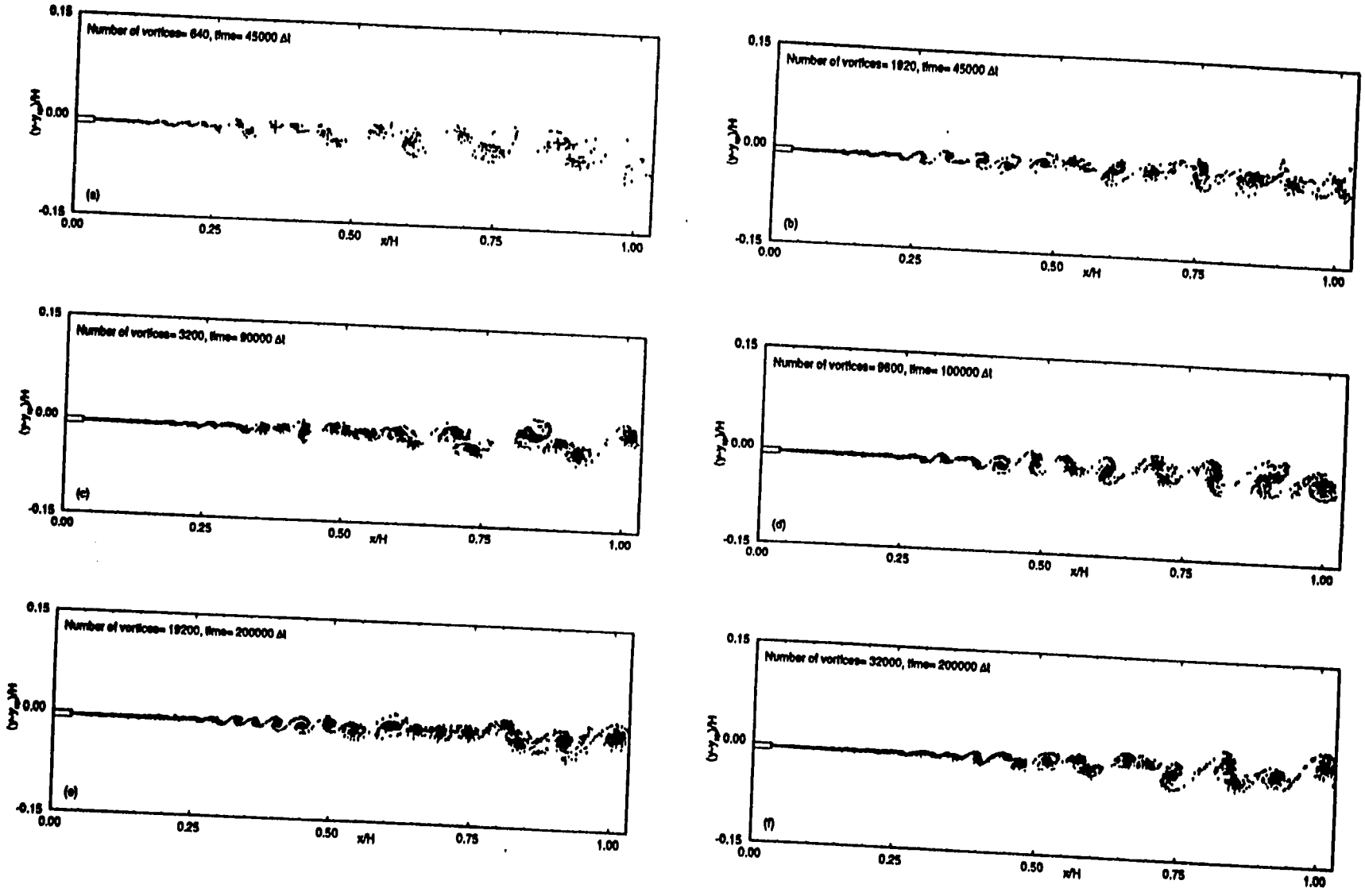

Figure 5.5. Streakline of vortices using (a) 640, (b) 1920, (c) 3200, (d) 9600, (e) 19200 and (f)32000 vortices

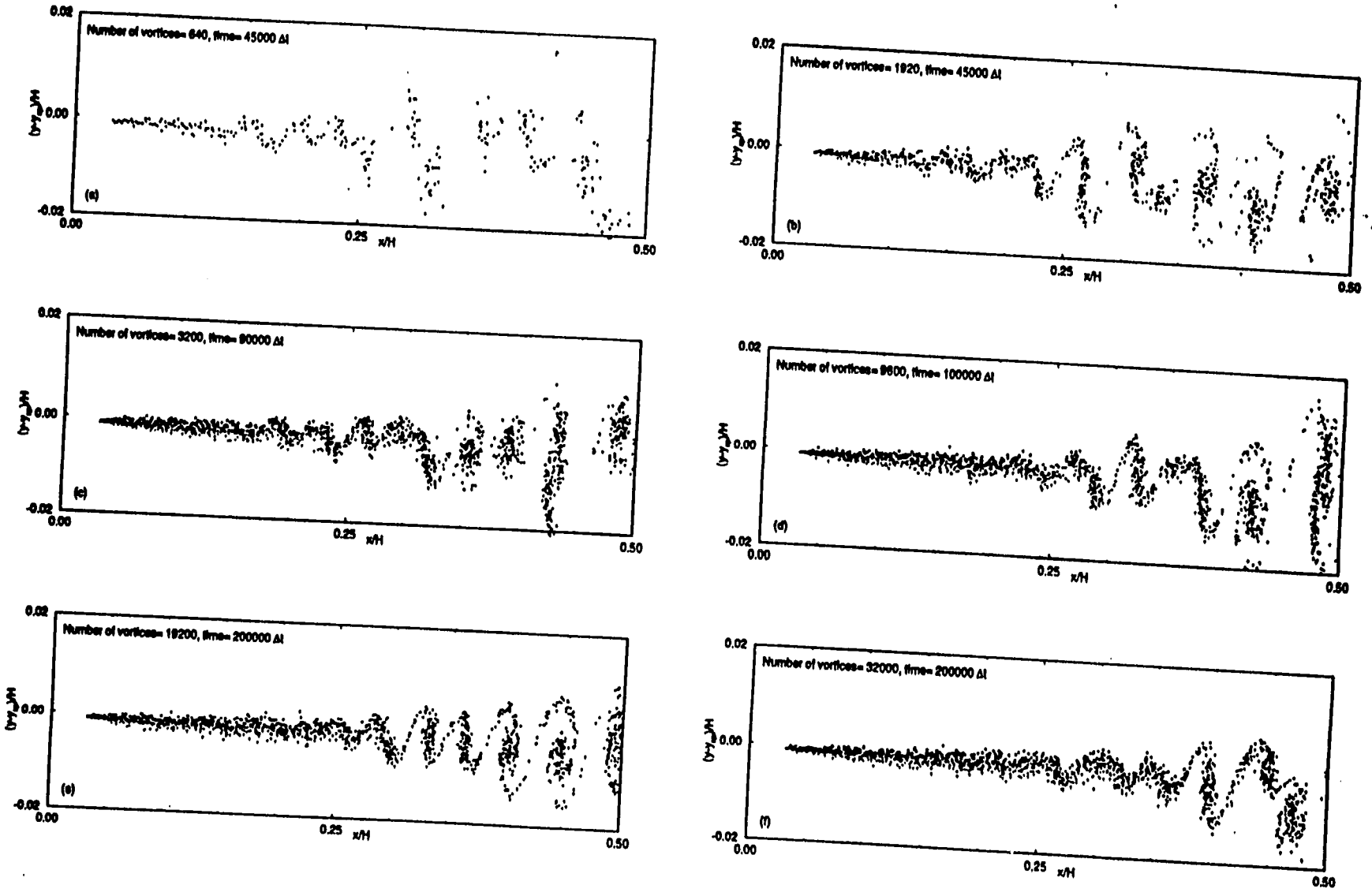

Figure 5.6. Magnified graphs of streakline of vortices shown in figure 5.5-a to f.

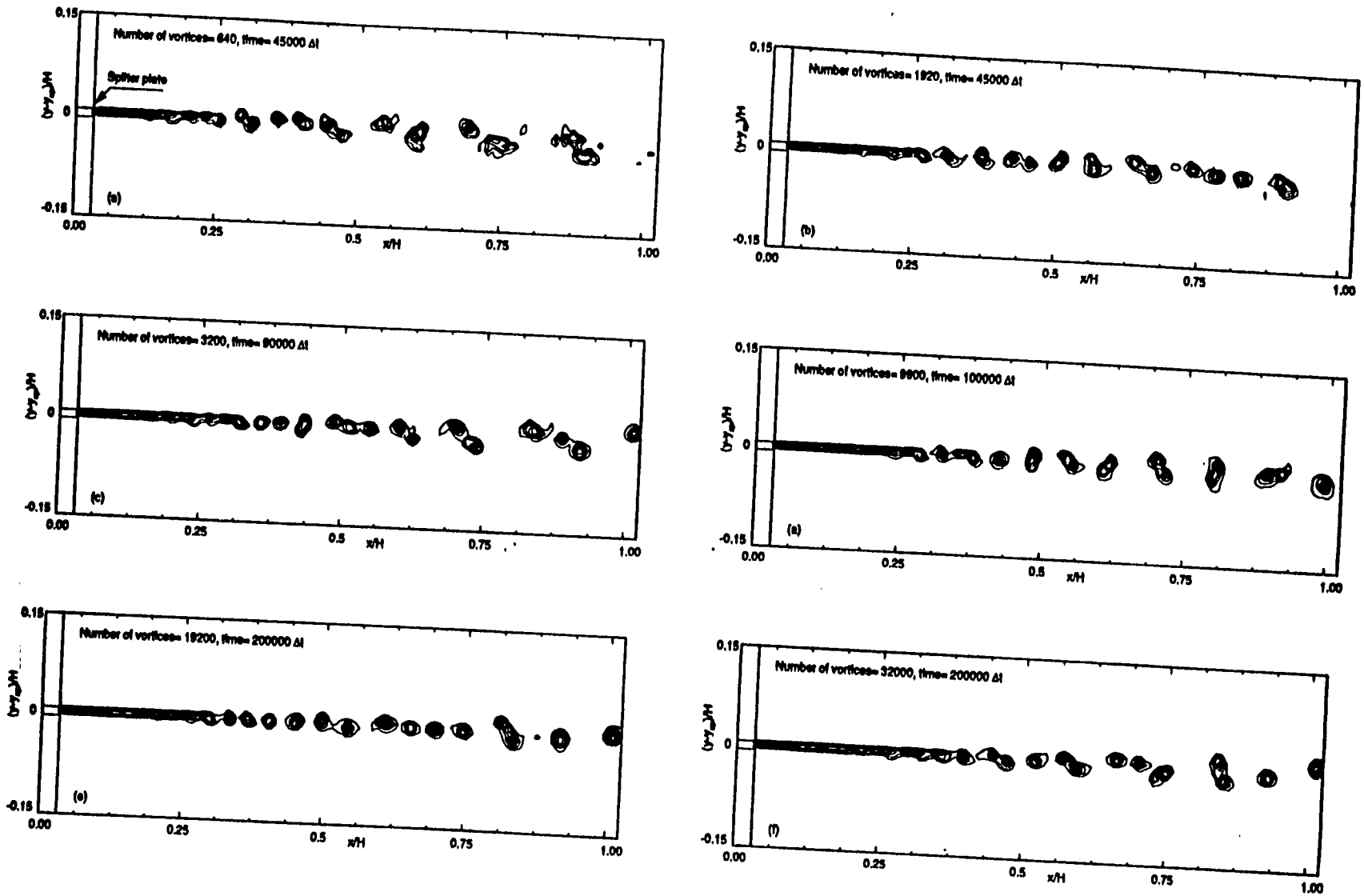

Figure 5.7. Contour-plot of vorticity for simulations using (a) 640, (b) 1920, (c) 3200, (d) 9600, (e) 19200, and (f) 32000 vortices

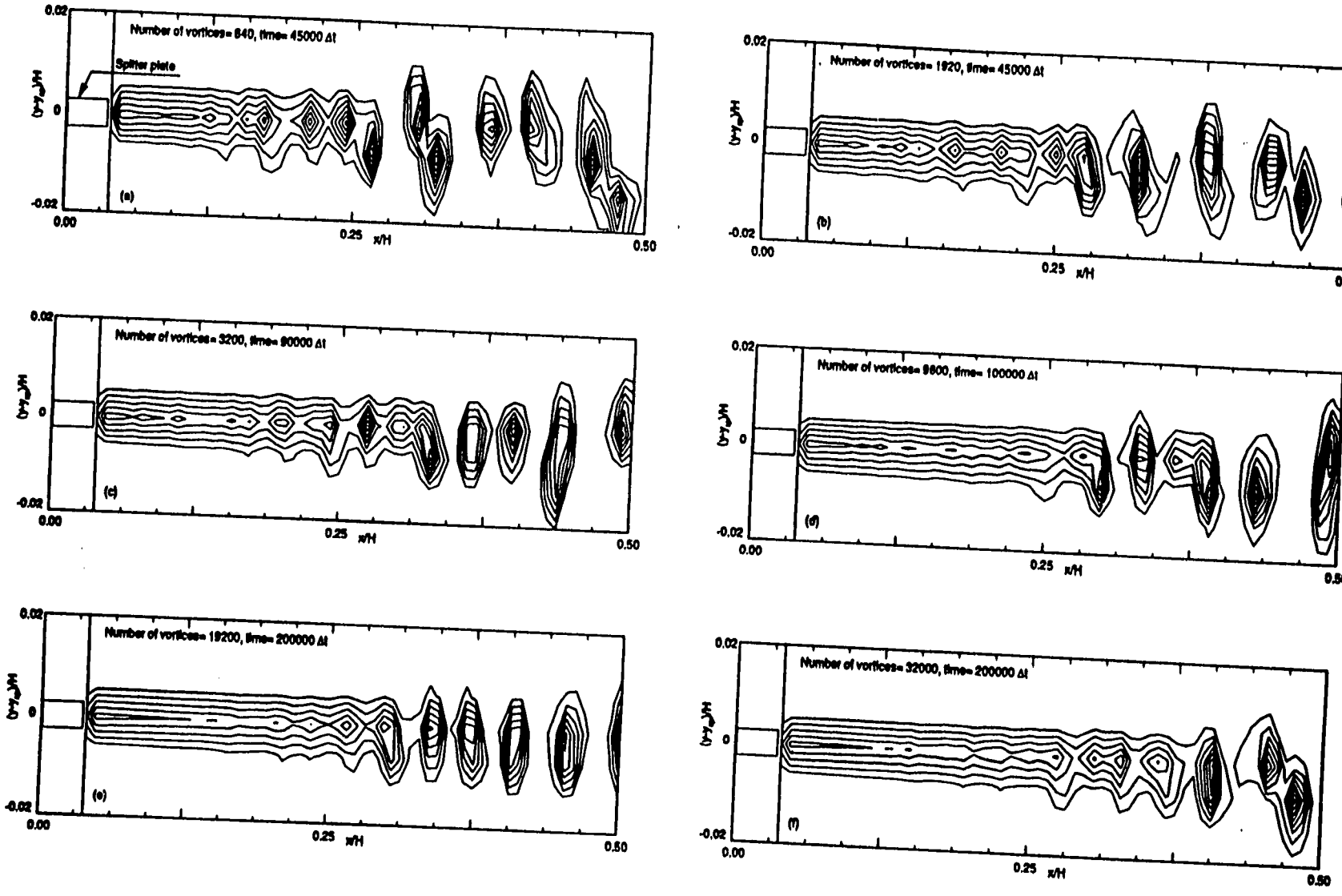

Figure 5.8. Magnified graphs of contour-plot of vorticity shown in figure 5.7-a to f.

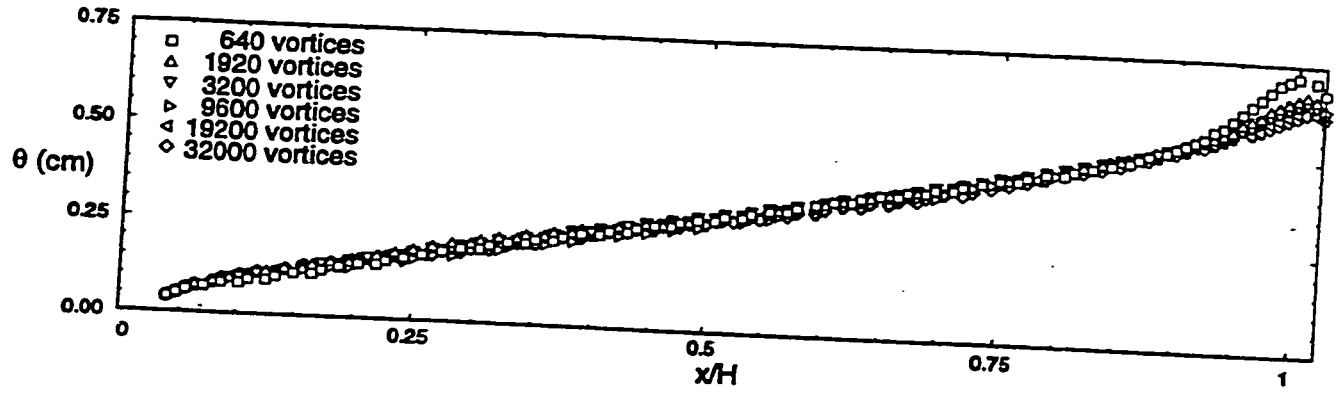

Figure 5.9. Downstream growth of momentum thickness illustrating the effect of the number of vortices.

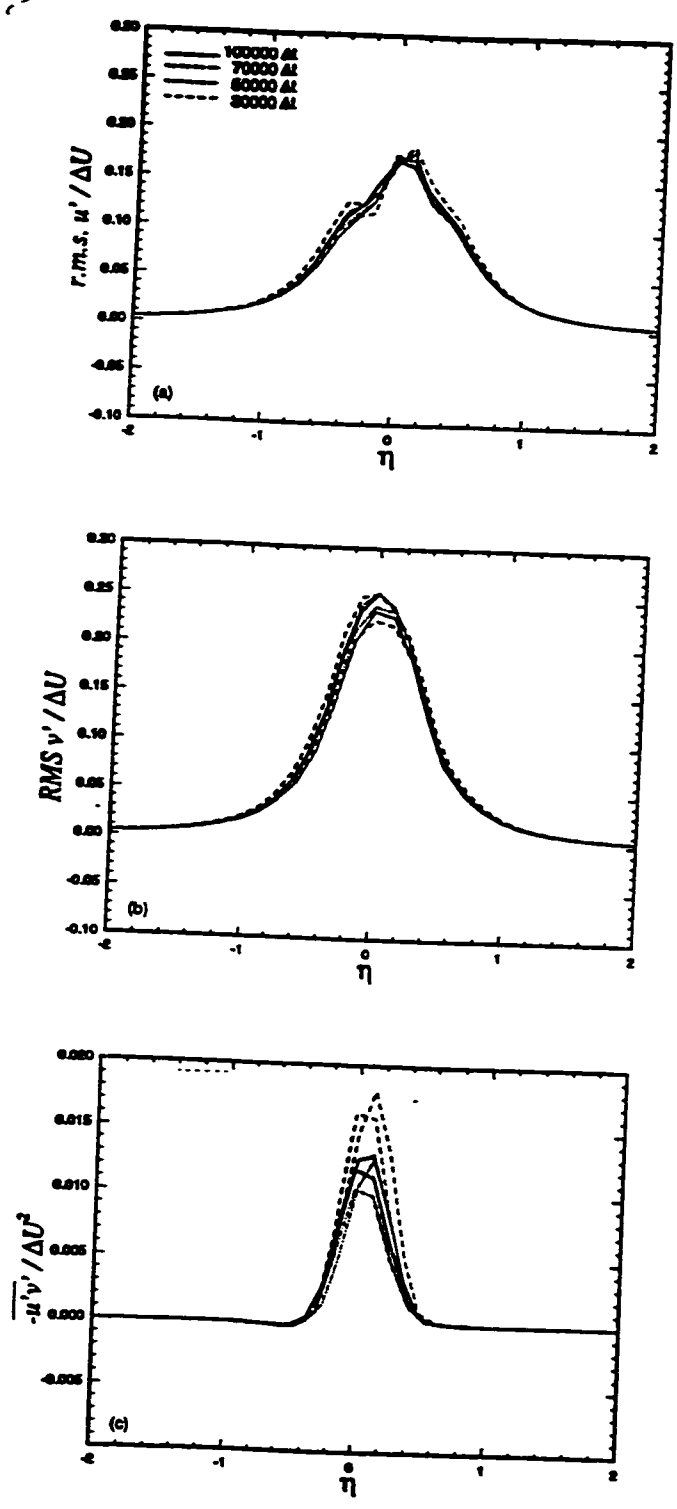

Figure 5.10. Profiles of normalized (a) r.m.s. u', (b) r.m.s. v', and (c) Reynolds shear stress, showing the effect of time averaging on downstream growth of Reynolds stresses.

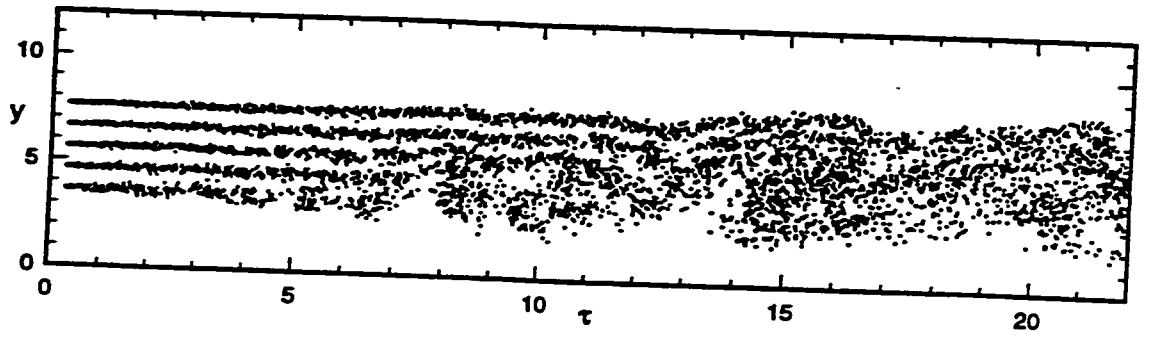

(a)

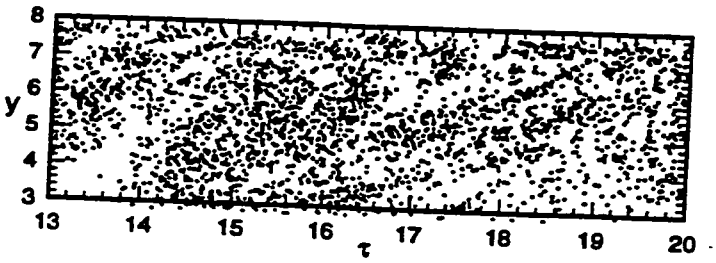

(b)

Figure 5.11. Downstream development of streakline of vortices for Uc=237.5 cm/s and dU/dy=75s^{-1}.

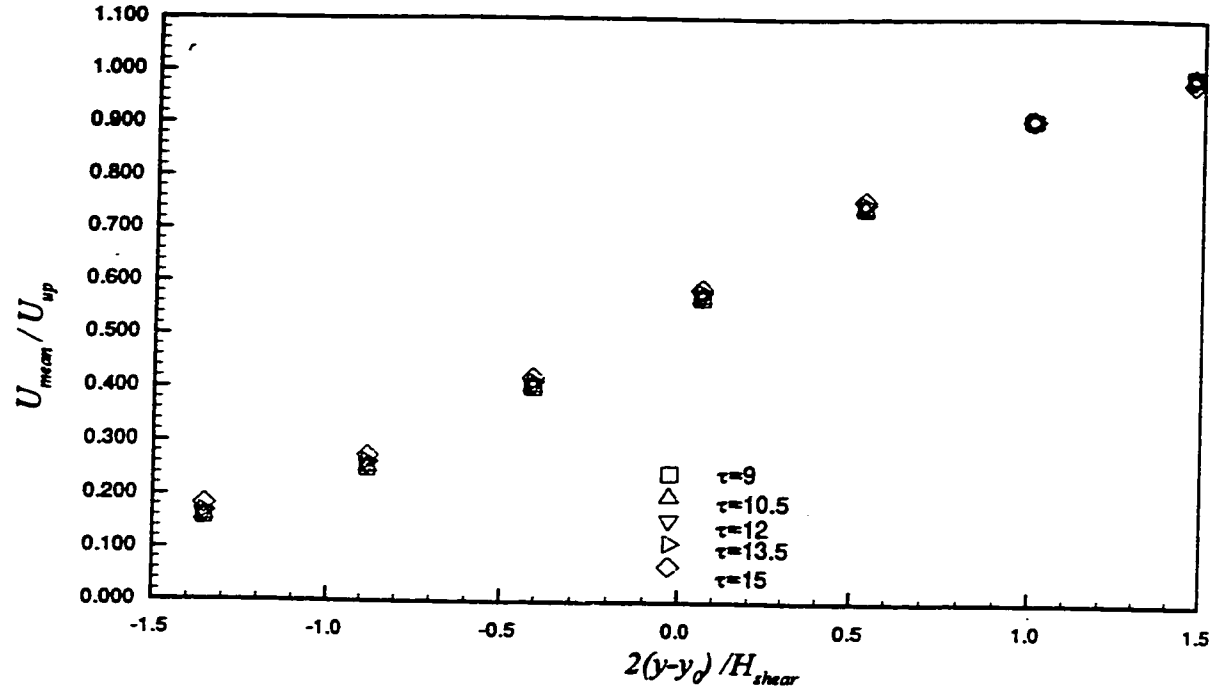

Figure 5.12. Normalized mean velocity profile at several downstream stations for Uc=237.5 cm/s and dU/dy=75 s^{-1}

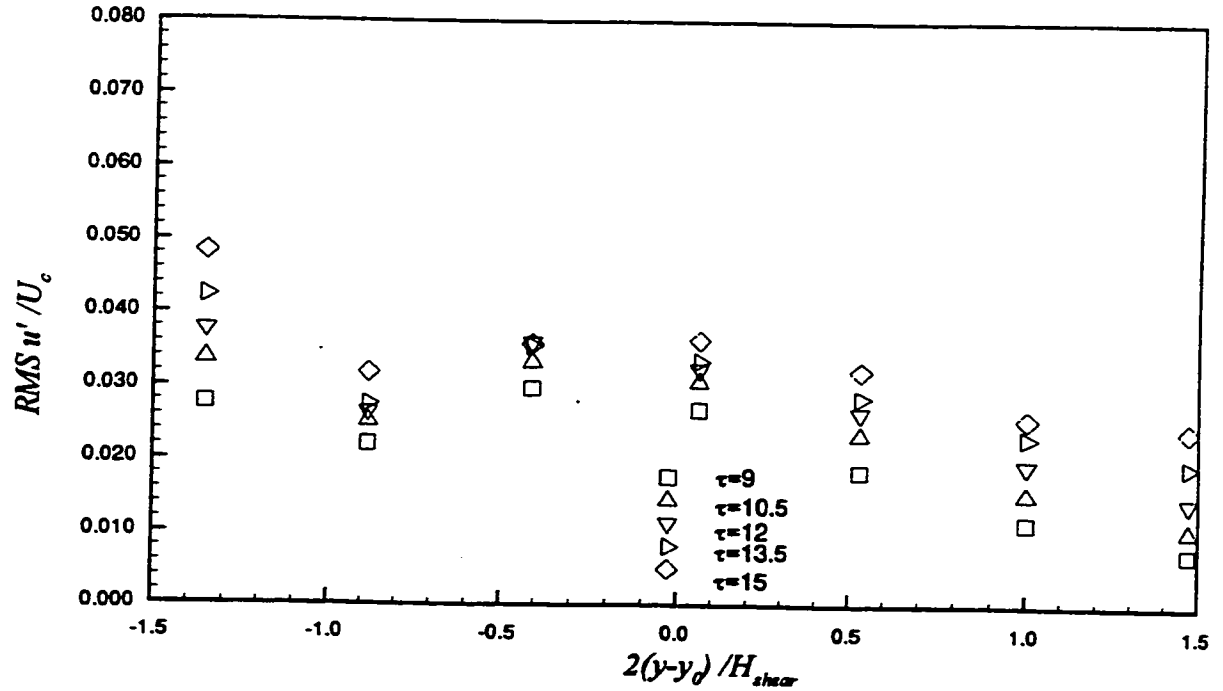

Figure 5.13. Normalized profiles of r.m.s. u' at several downstream stations for Uc=237.5 cm/s and dU/dy=75

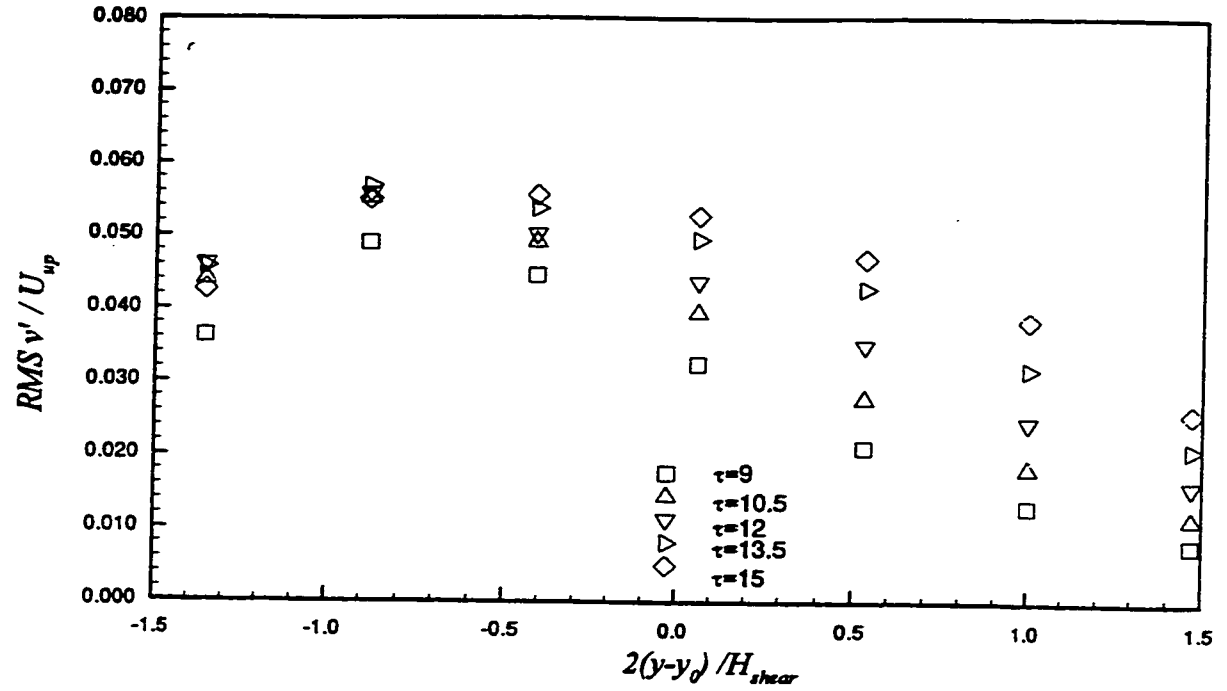

Figure 5.14. Normalized profiles of r.m.s. v' at several downstream stations for Uc=237.5 cm/s and dU/dy=75 s^{-1}

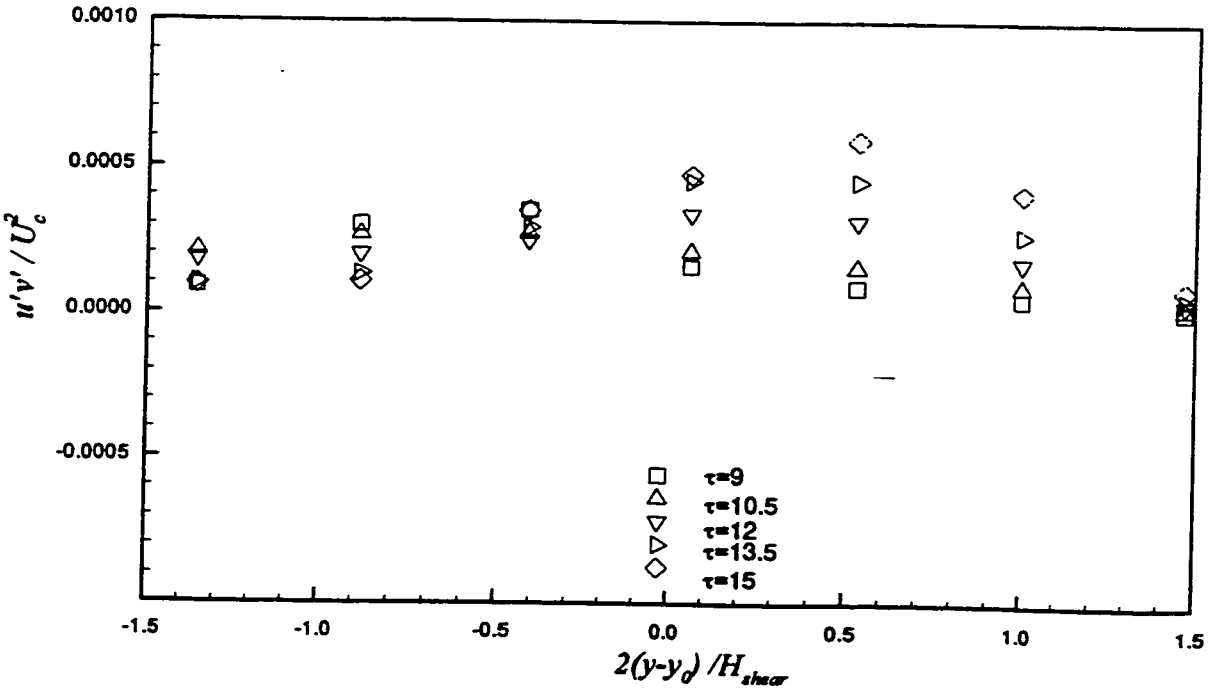

Figure 5.15. Normalized profiles of Reynolds shear stress at several downstream stations for Uc=237.5 cm/s and dU/dy=75

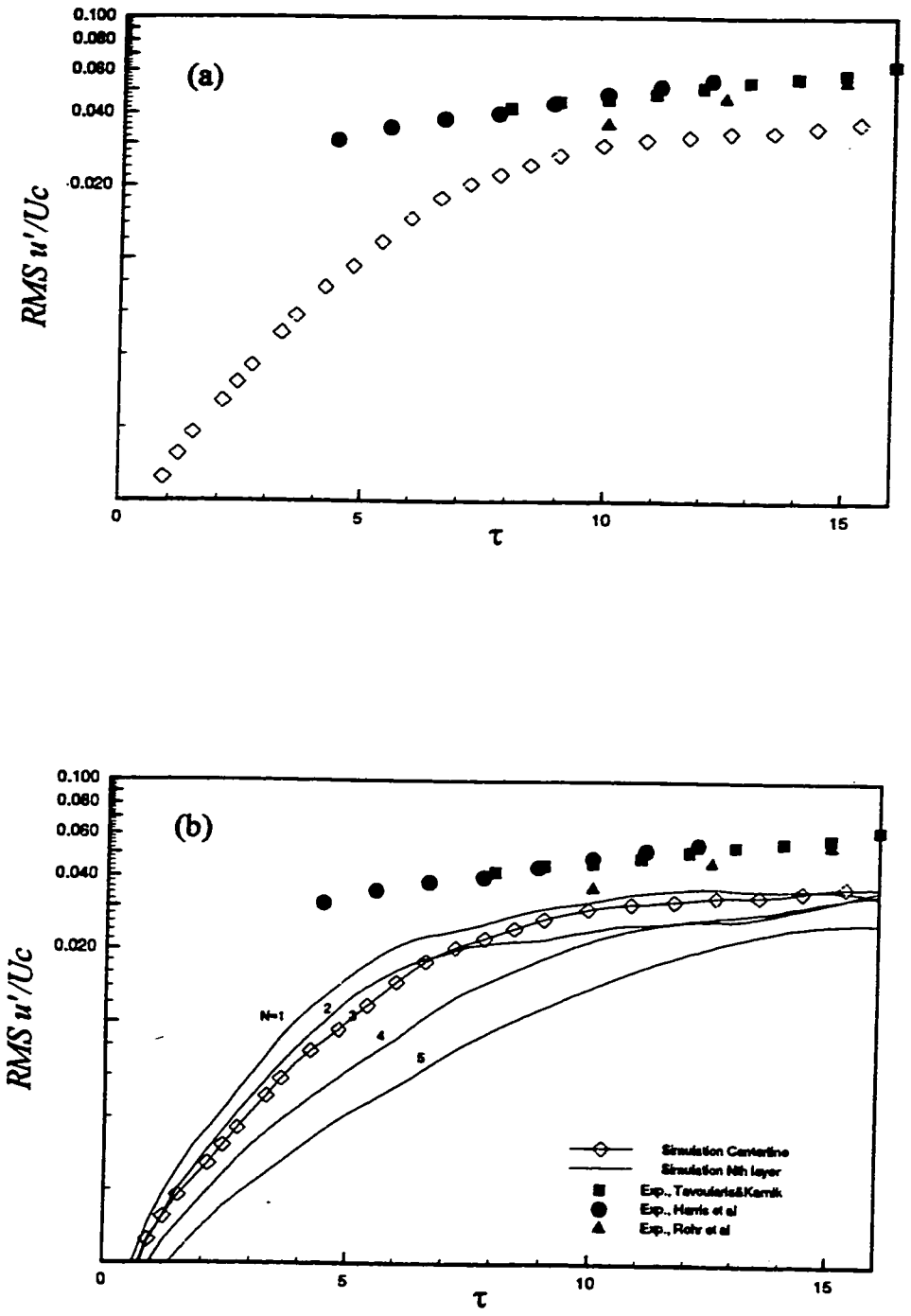

Figure 5.16. Downstream growth of r.m.s. u' versus non-dimensional time for Uc=237.5 cm/s and dU/dy=75; (a) centerline layer; (b) all layers.

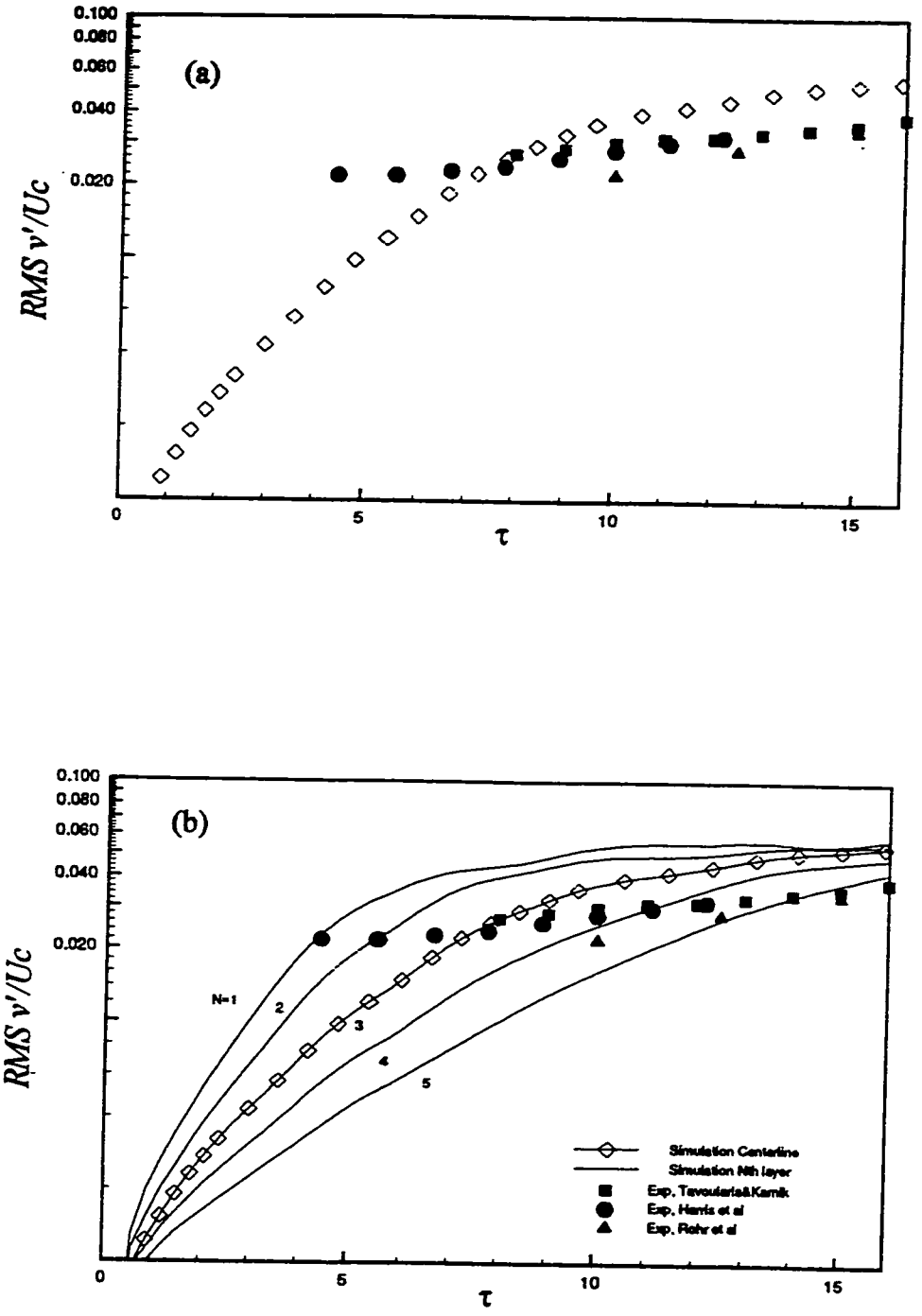

Figure 5.17. Downstream growth of r.m.s. v' versus non-dimensional time for Uc=237.5 cm/s and dU/dy=75; (a) centerline layer; (b) all layers.

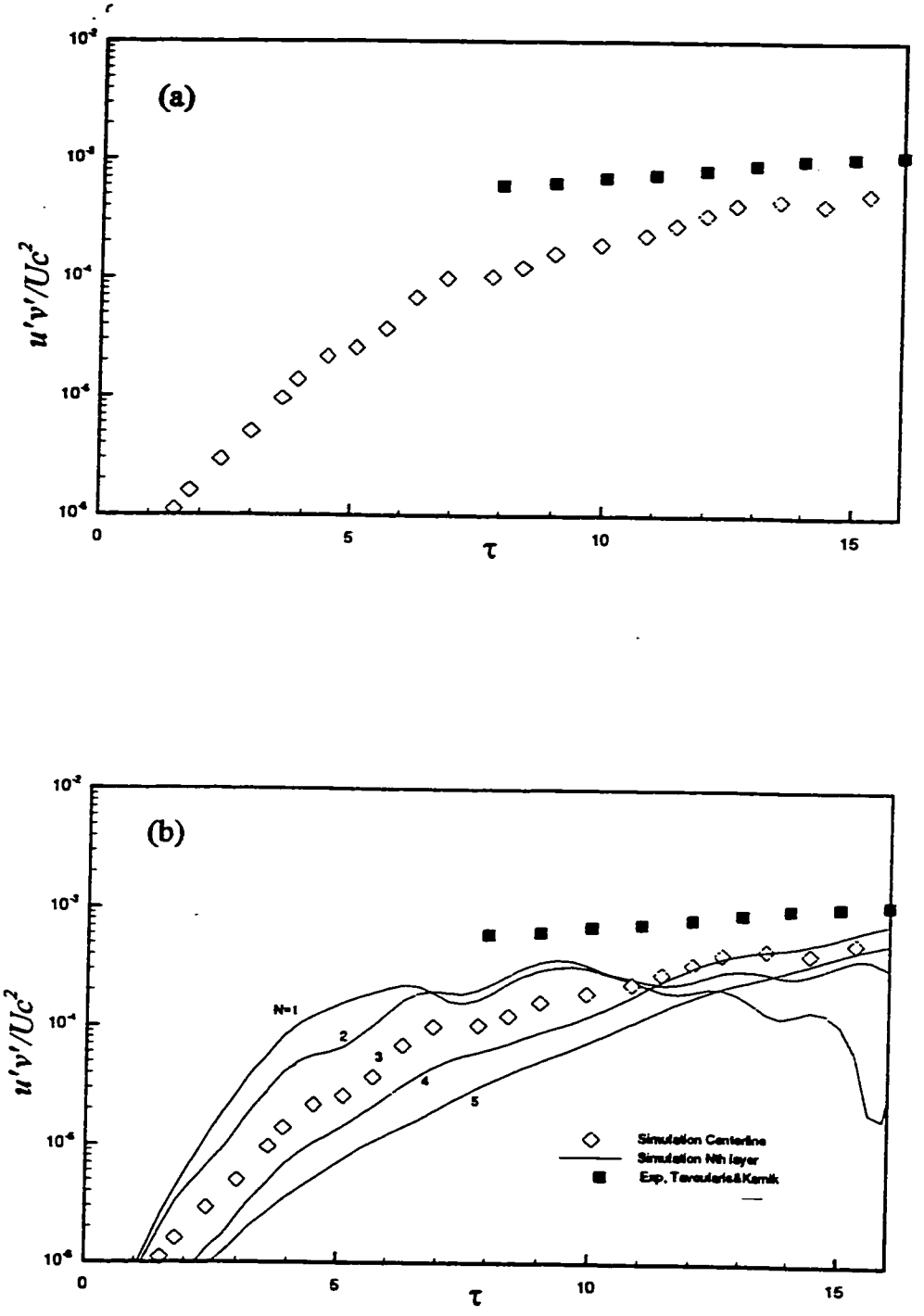

Figure 5.18. Downstream growth of Reynolds shear stress versus non-dimensional time for Uc=237.5 cm/s and dU/dy=75; (a) centerline layer; (b) all layers.

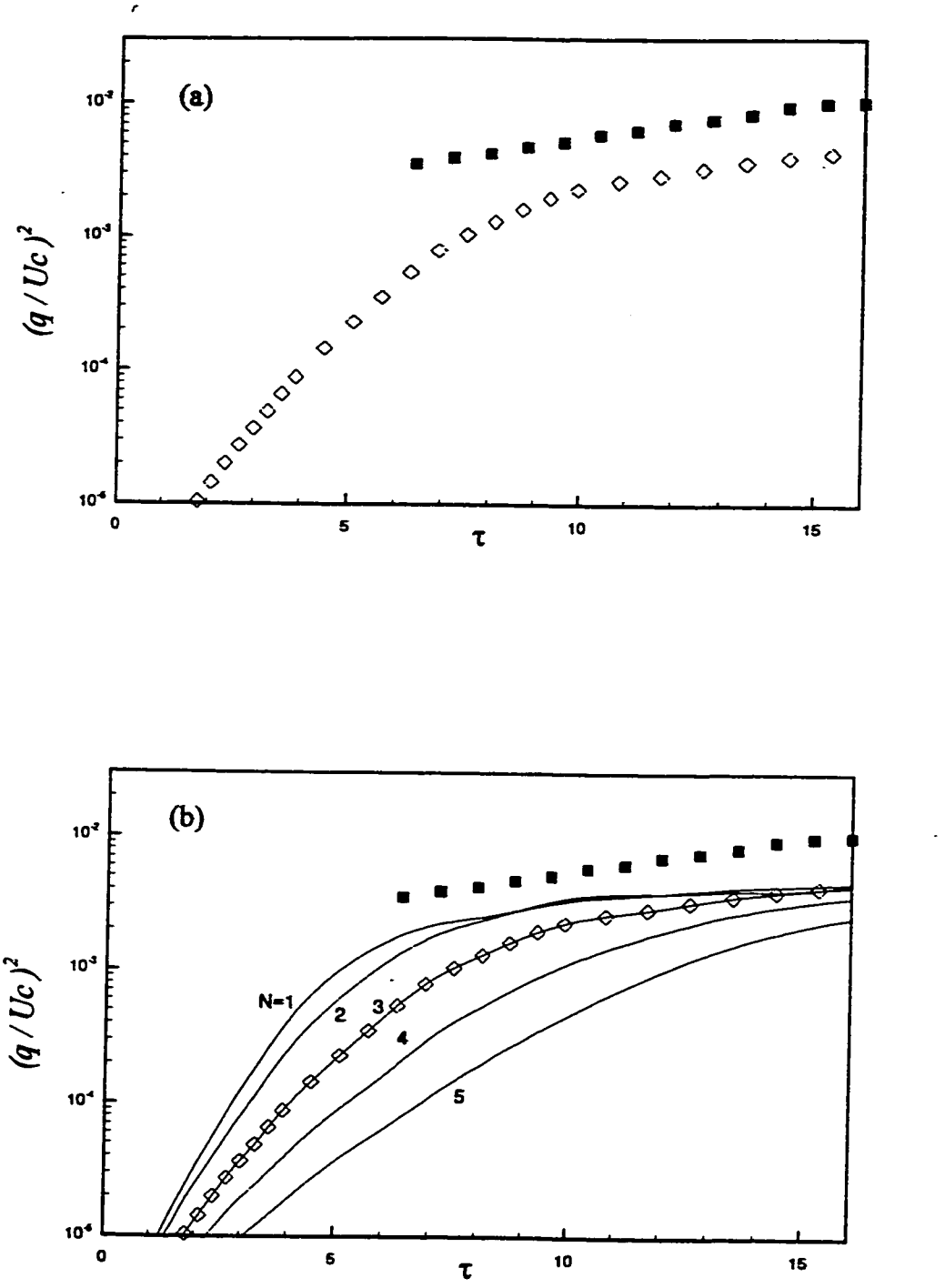

Figure 5.19. Downstream growth of turbulent kinetic energy versus non-dimensional time for Uc=237.5 cm/s and dU/dy=75; (a) centerline layer; (b) all layers.

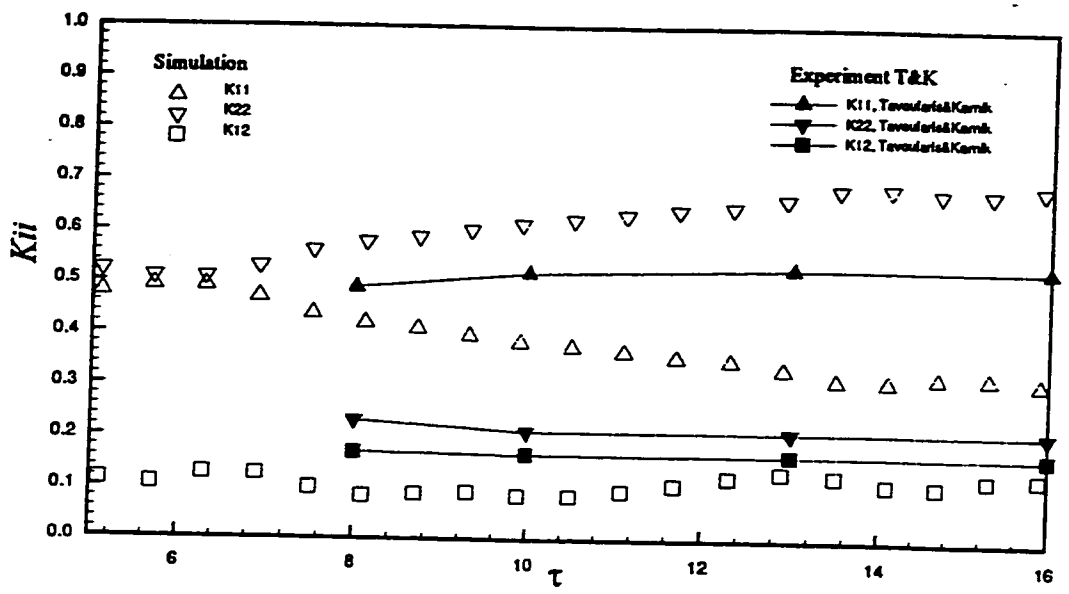

Figure 5.20. Component energy ratios versus non-dimensional time for Uc=237.5 m/s and dU/dy=75 s^{-1}

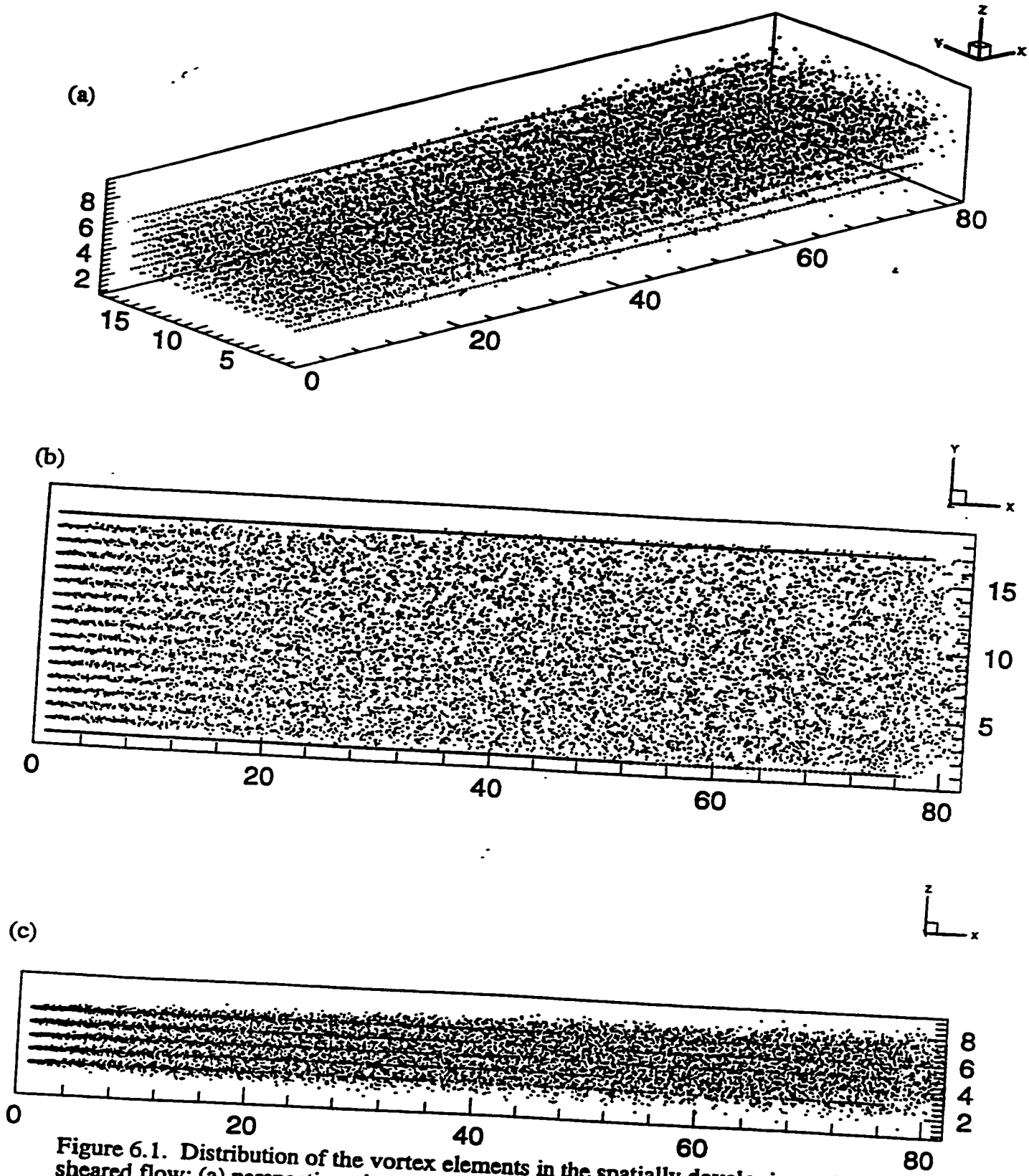

Figure 6.1. Distribution of the vortex elements in the spatially developing uniformly sheared flow; (a) perspective view; (b) top view; (c) side view.

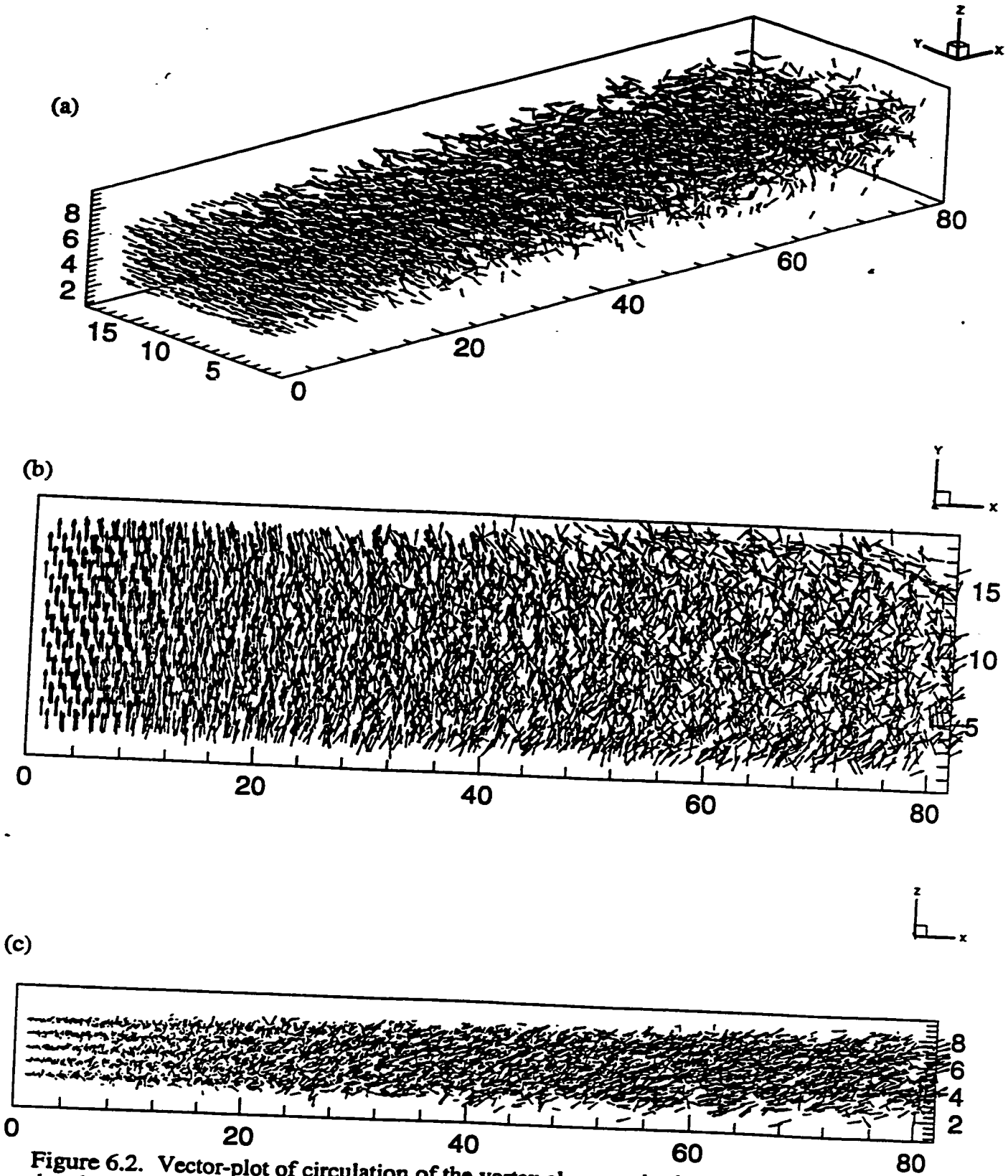

Figure 6.2. Vector-plot of circulation of the vortex elements in the spatially developing uniformly sheared flow; (a) perspective view; (b) top view; (c) side view.

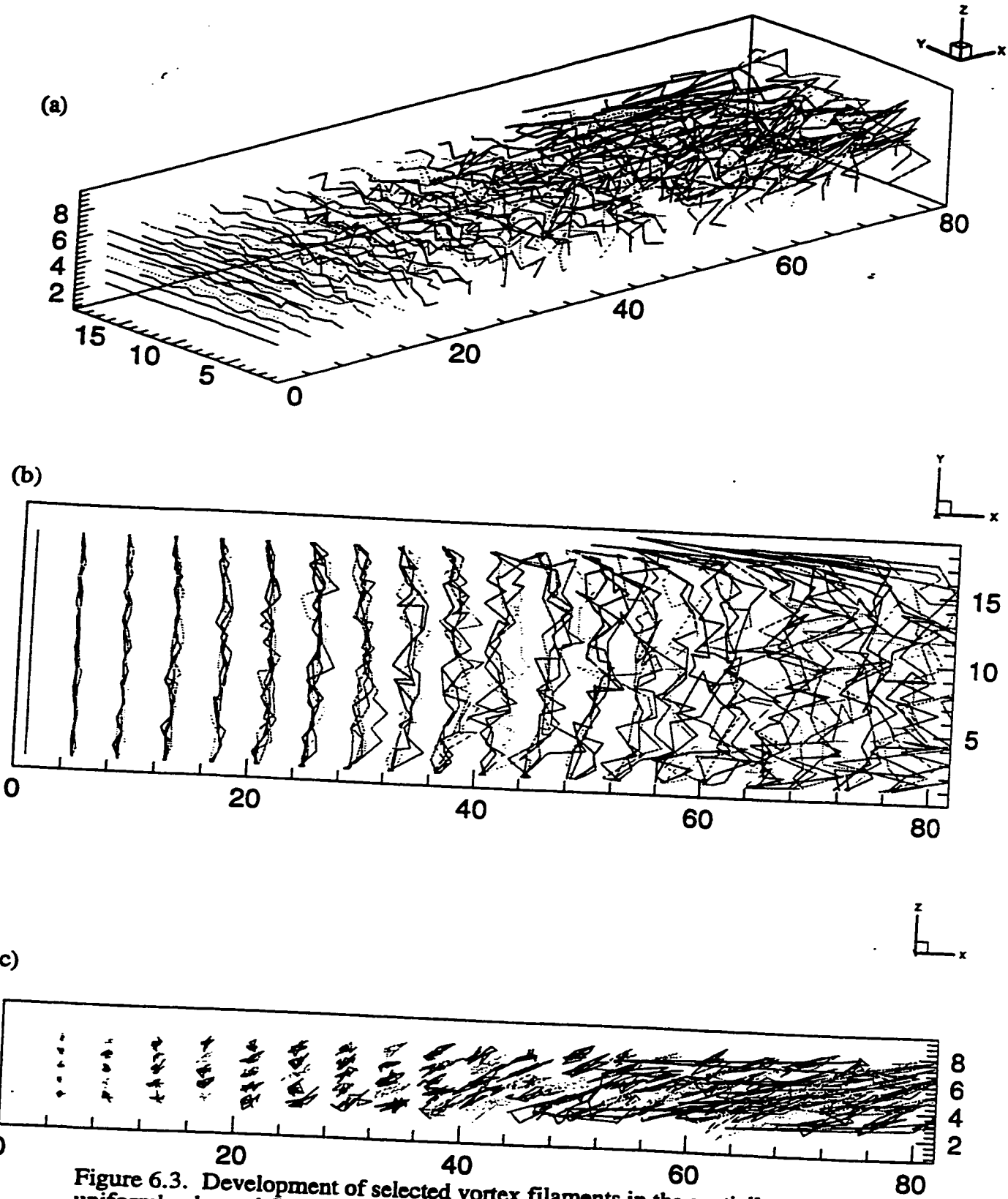

Figure 6.3. Development of selected vortex filaments in the spatially developing uniformly sheared flow; (a) perspective; (b) top view; (c) side view.

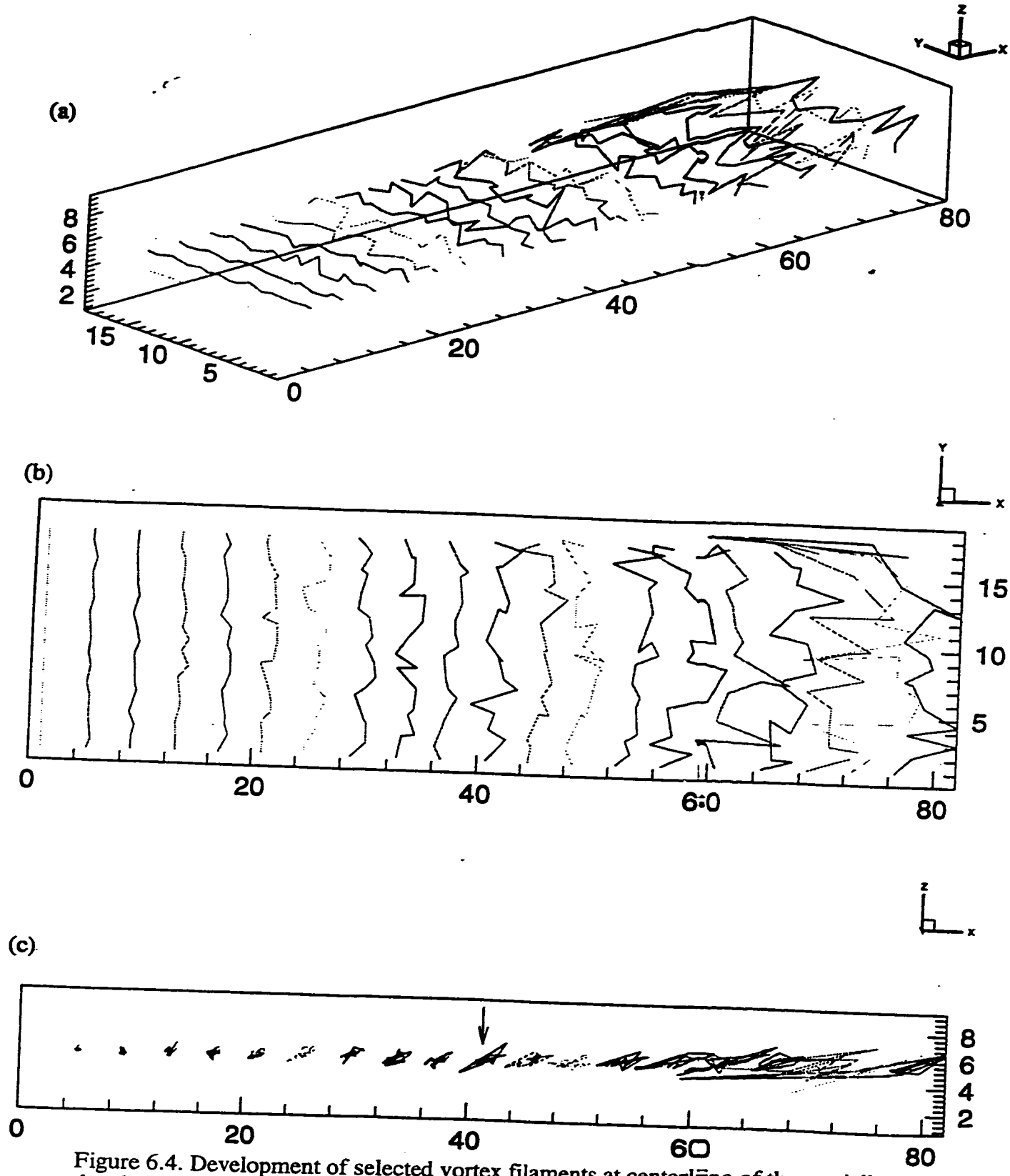

Figure 6.4. Development of selected vortex filaments at centerline of the spatially developing uniformly sheared flow. Different line patterns are used to facilitate the comparison. (a) perspective; (b) top view; (c) side view.

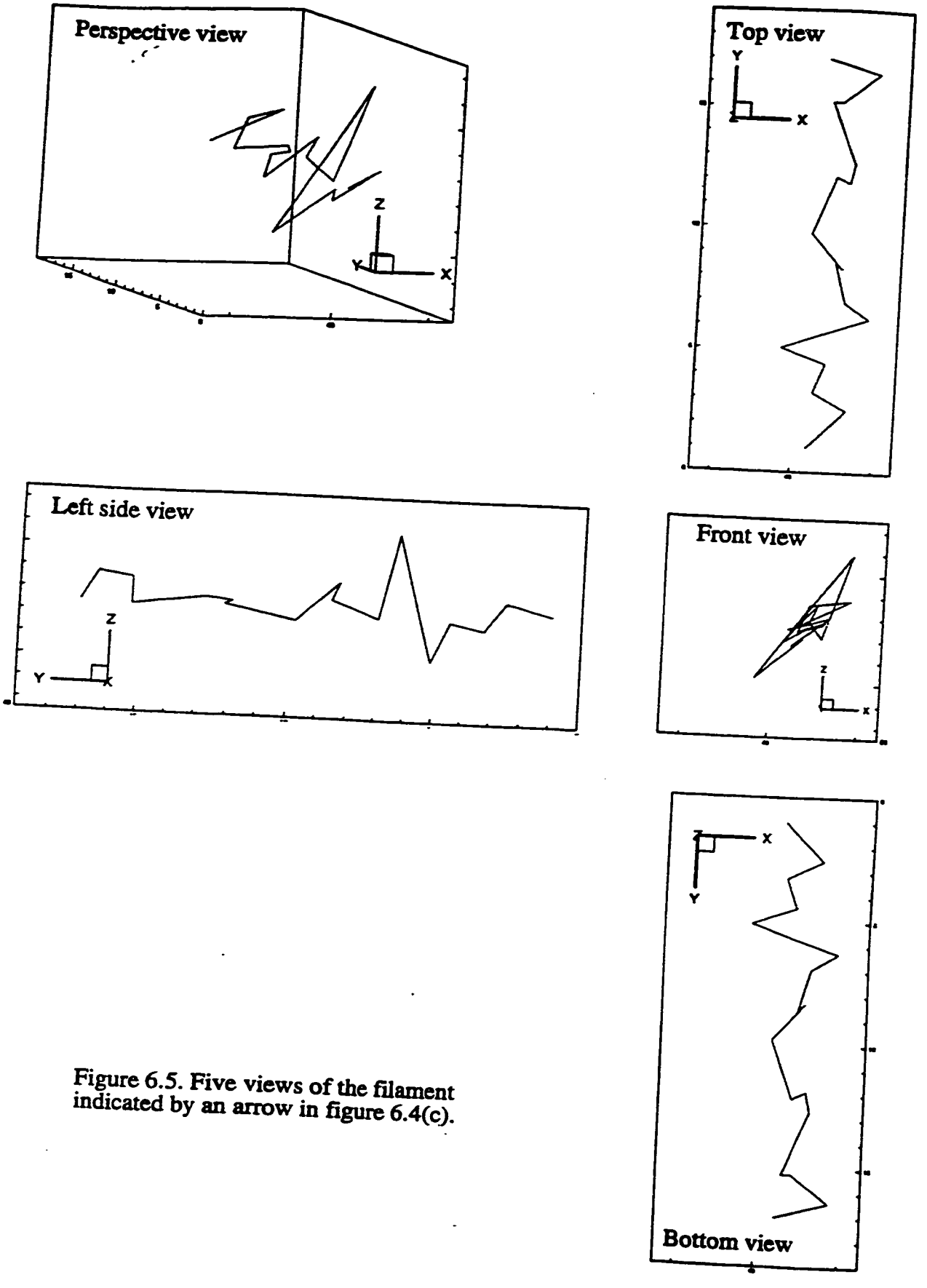

Figure 6.5. Five views of the filament indicated by an arrow in figure 6.4(c).

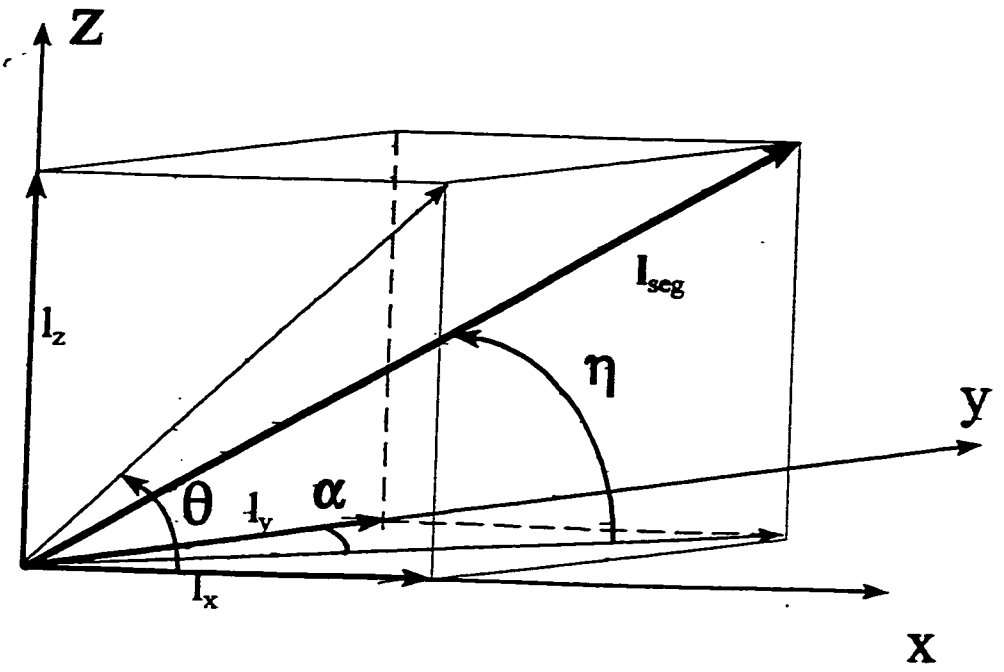

Figure 6.6. Coordinate system used to define the angles α, η and θ of segments of filaments.

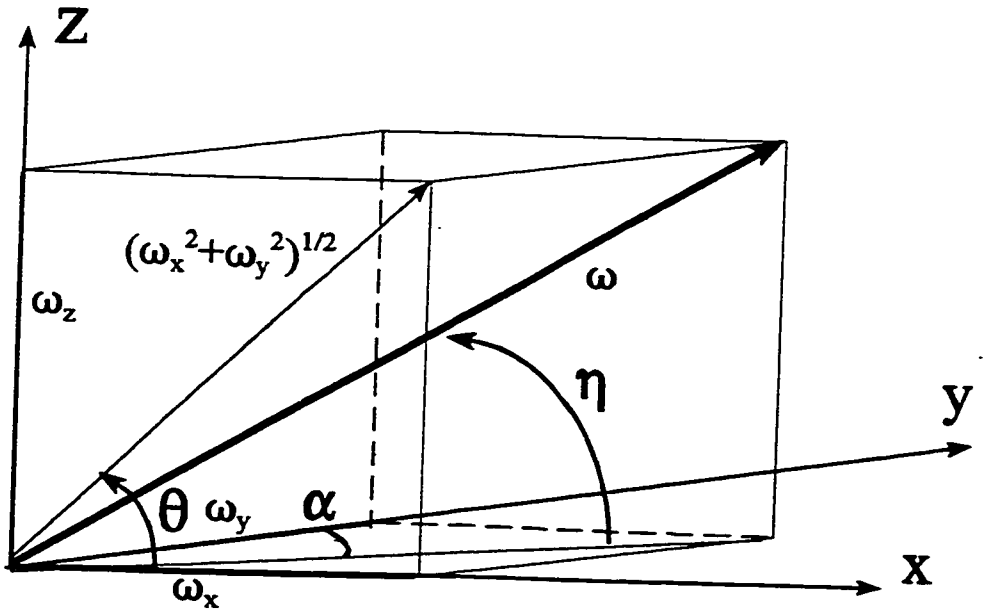

Figure 6.7. Coordinate system used to define angles α, η and θ of a vorticity vector.

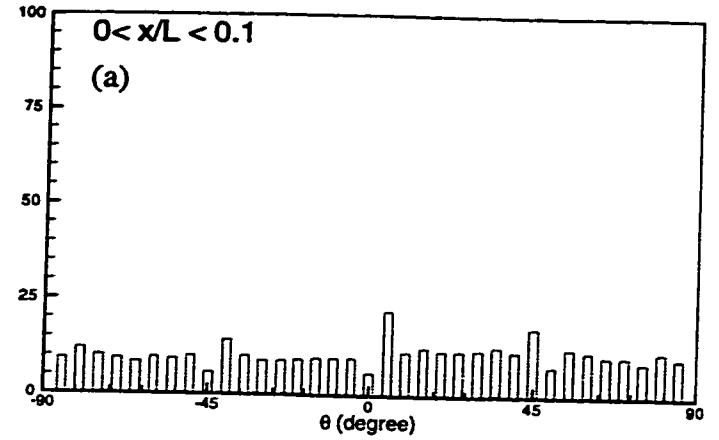

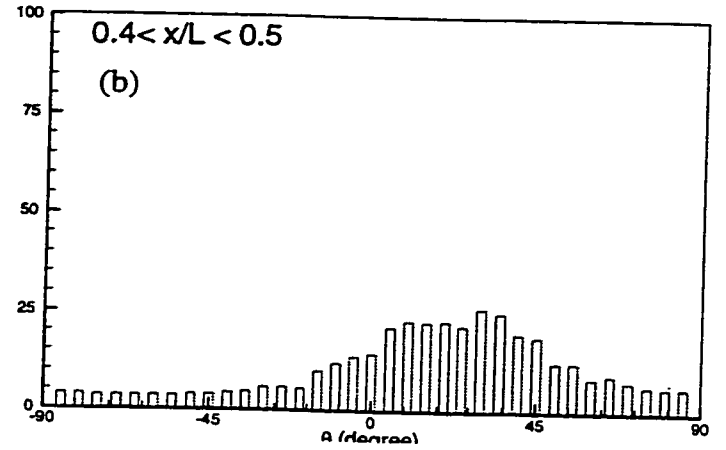

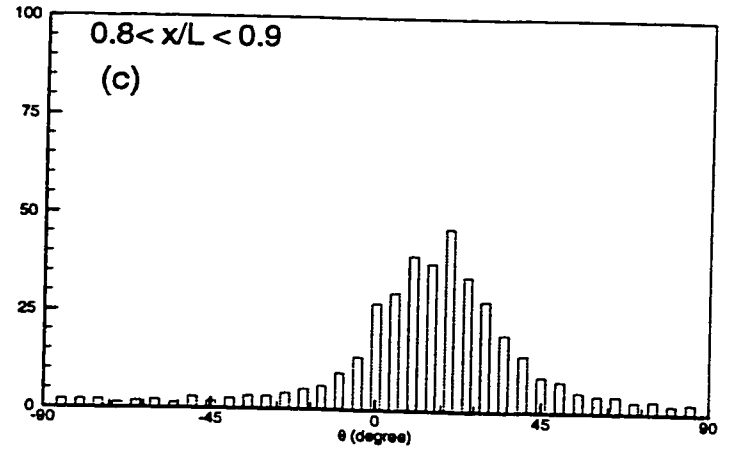

Figure 6.8(a-c). Histograms of the inclination angle(θ) of the vortex filaments with xy-plane for spatially growing uniform shear. Histograms are normalized by the ratio of the length of the segment to the length of the filament that the segment belongs to.

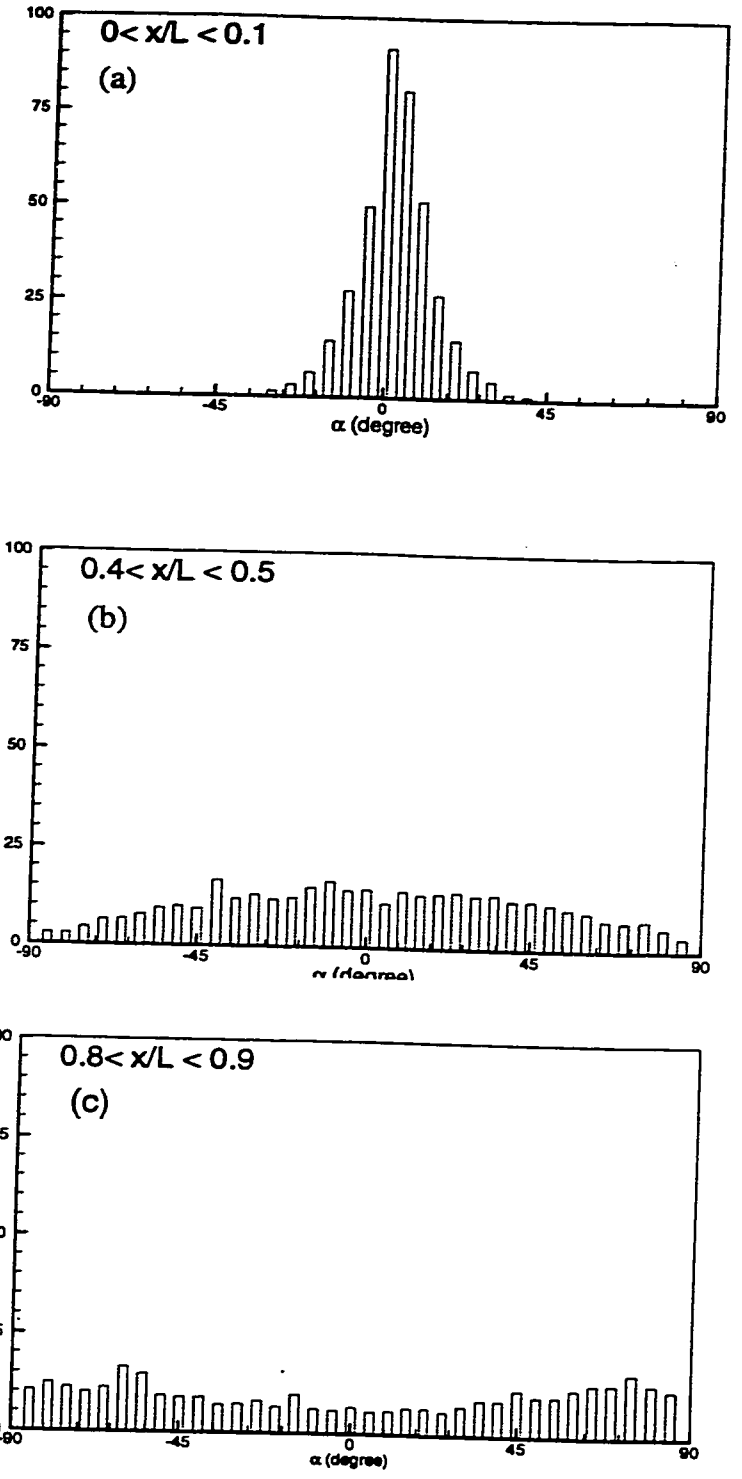

Figure 6.9(a-c). Histograms of the inclination angle(α) of the vortex filaments with yz-plane for spatially growing uniform shear flow. Histograms are normalized by the ratio of the length of the segment to the length of the filament that the segment belongs to.

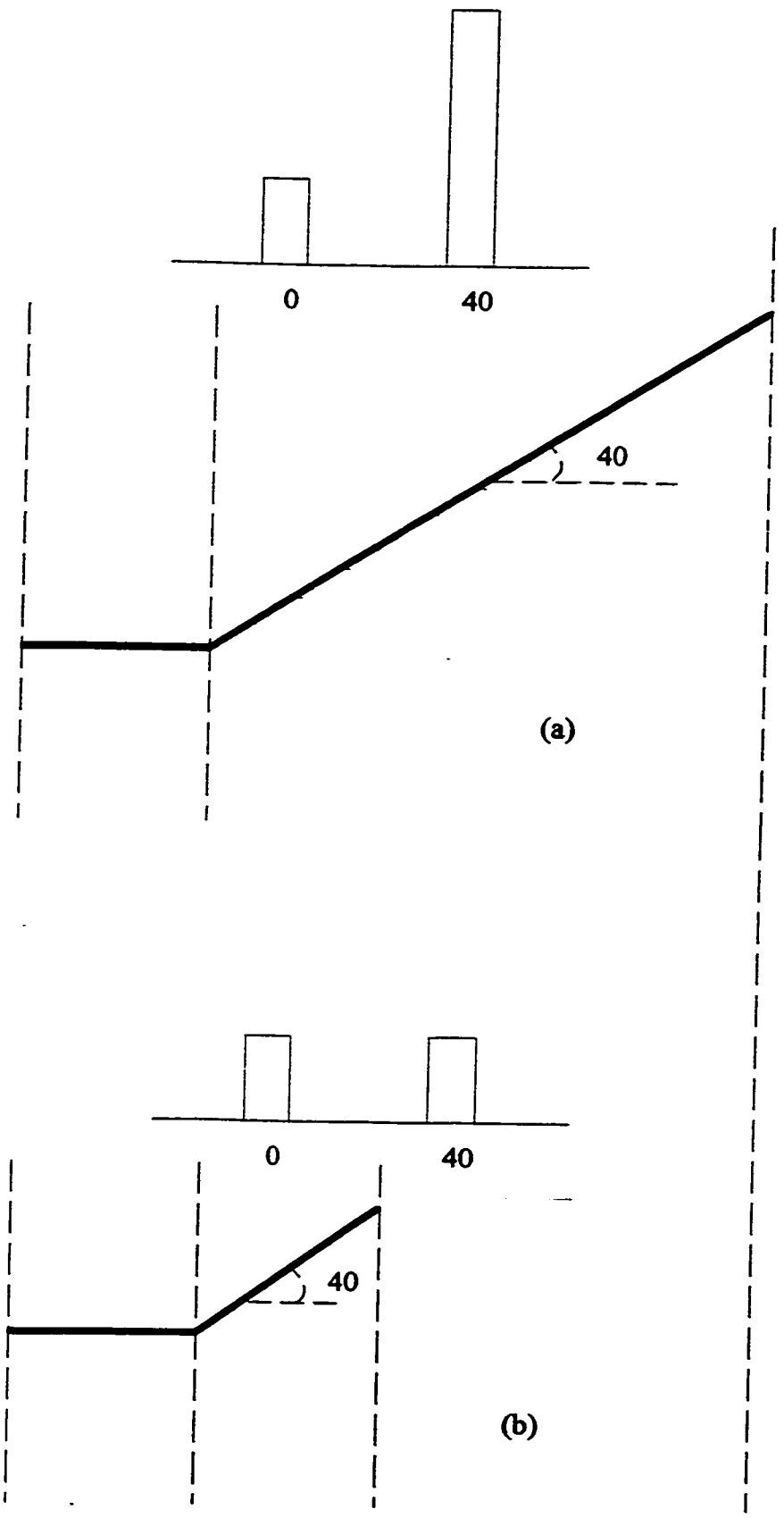

Figure 6.10. A simplified graph showing two elements and the effect of their length on the histogram.

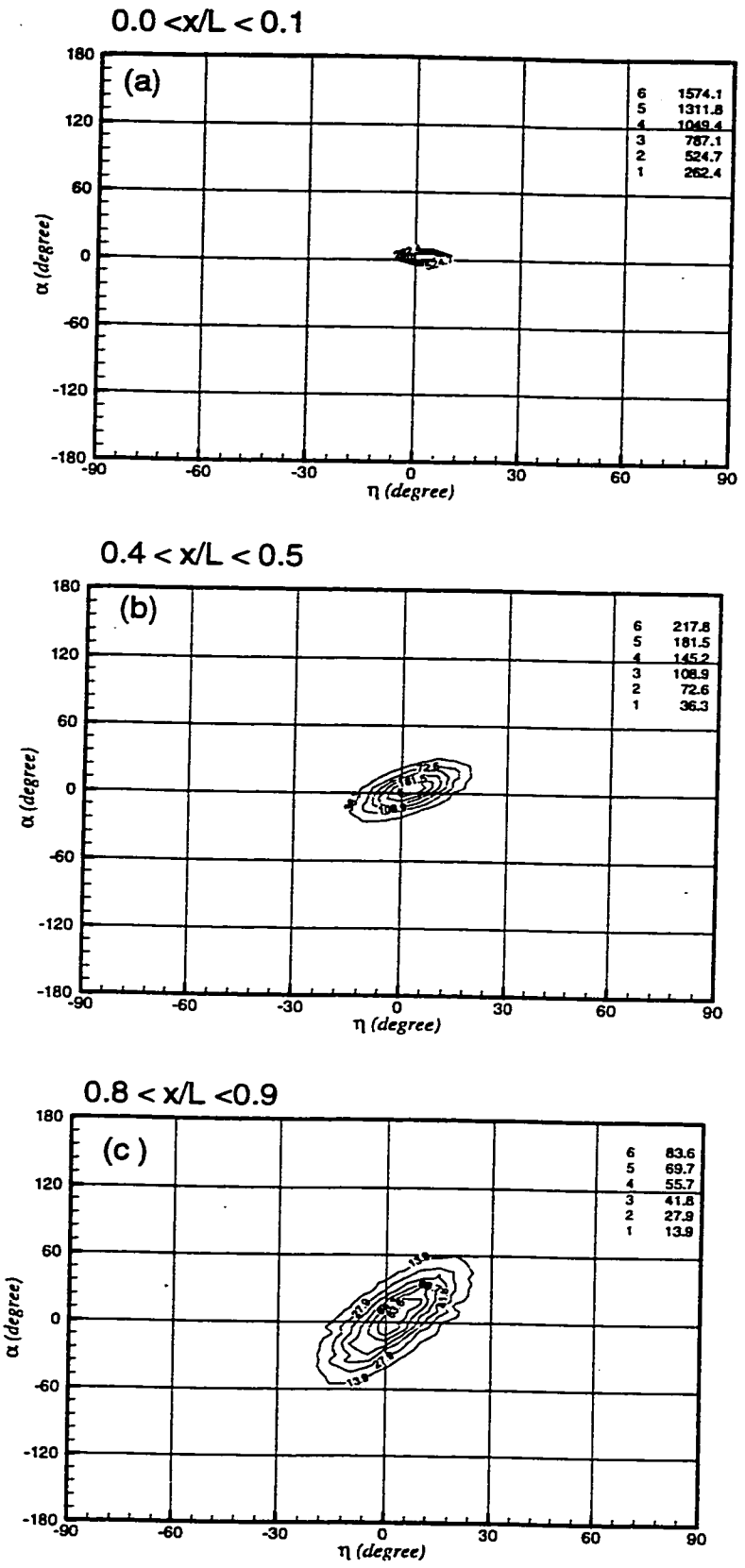

Figure 6.11(a-c). Two-angle probability distribution function of the angles of the vorticity vectors with xy-plane (η) and with yz-plane (α).

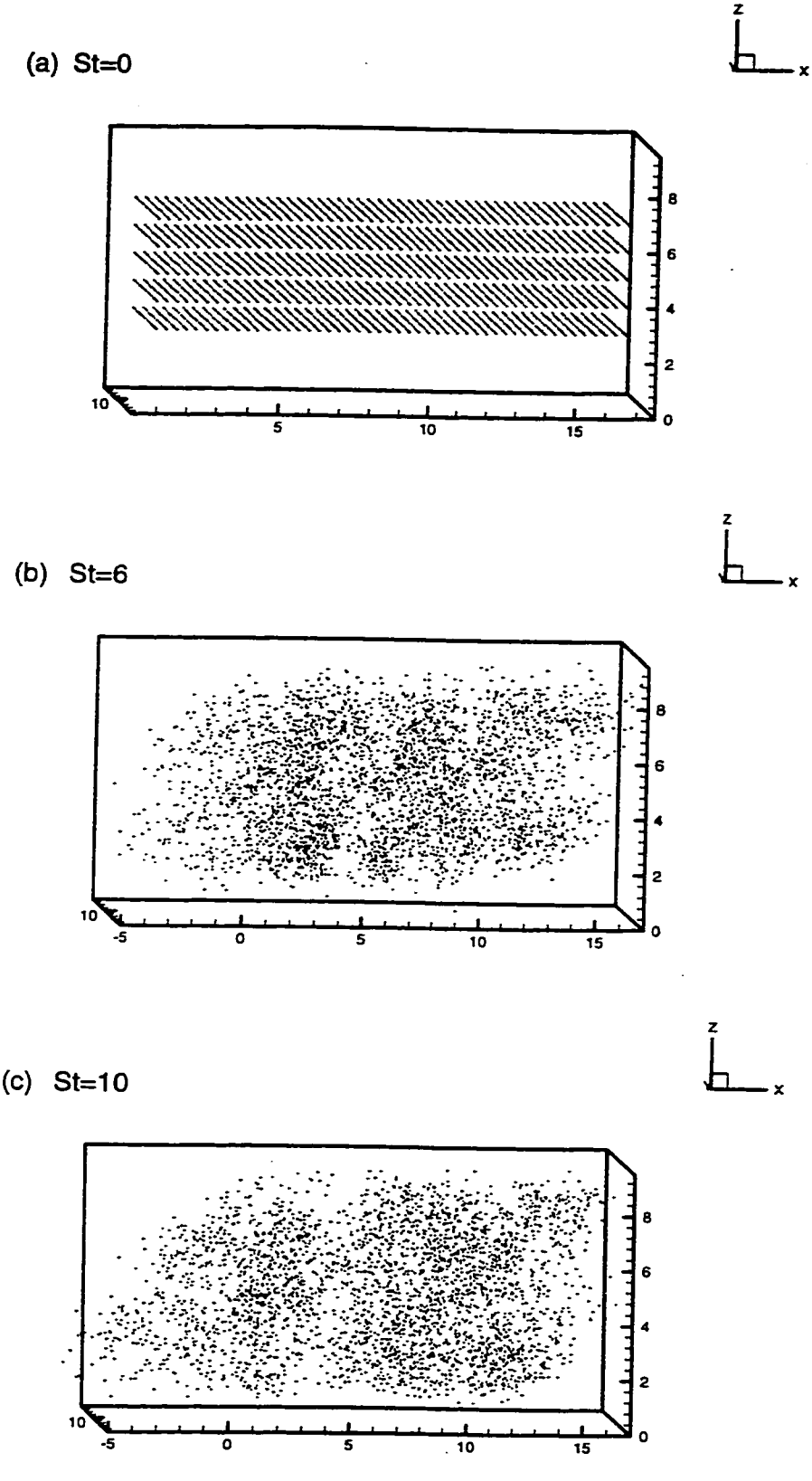

Figure 6.12. Side view at 10 degree angle with y-axis of the distribution of the vortex elements in quasi-temporally growing uniformly sheared flow; (a) St=0; (b) St=6; (c) St=10.

(a) St=0

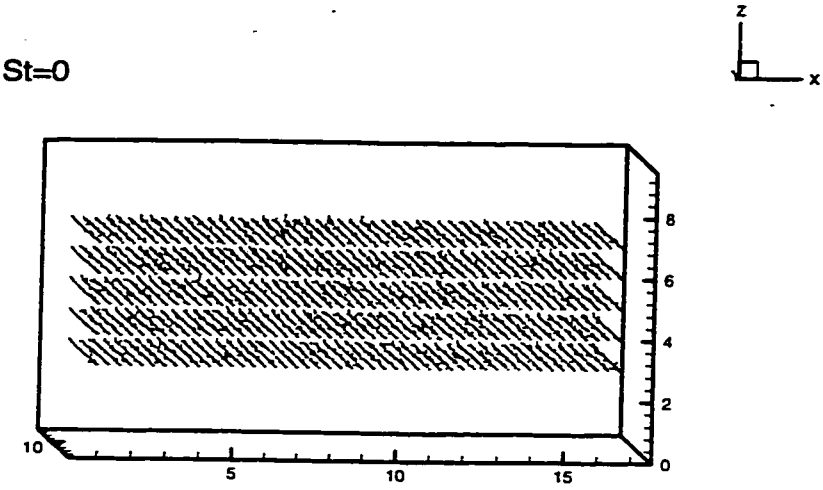

(b) St=6

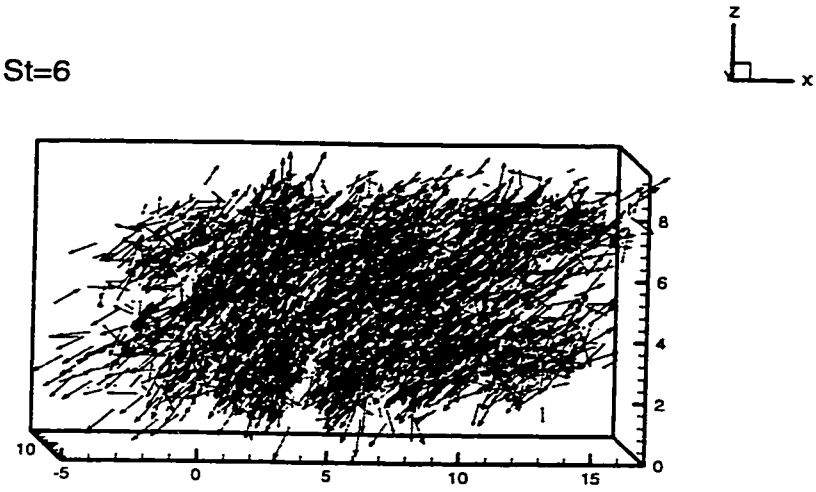

(c) St=10

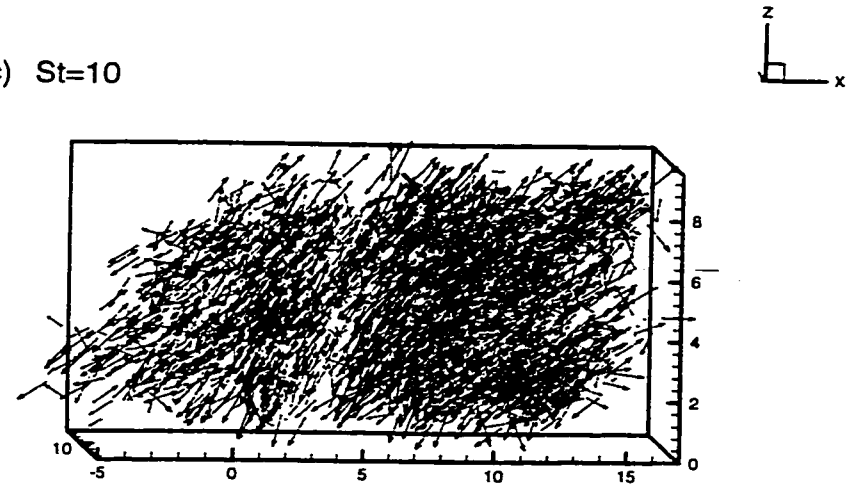

Figure 6.13. Side views at 10 degree angle with y-axis of the vector-plots of circulation of vortex elements in quasi-temporally growing uniformly sheared flow. (a) St=0; (b) St=6; (c) St=10.

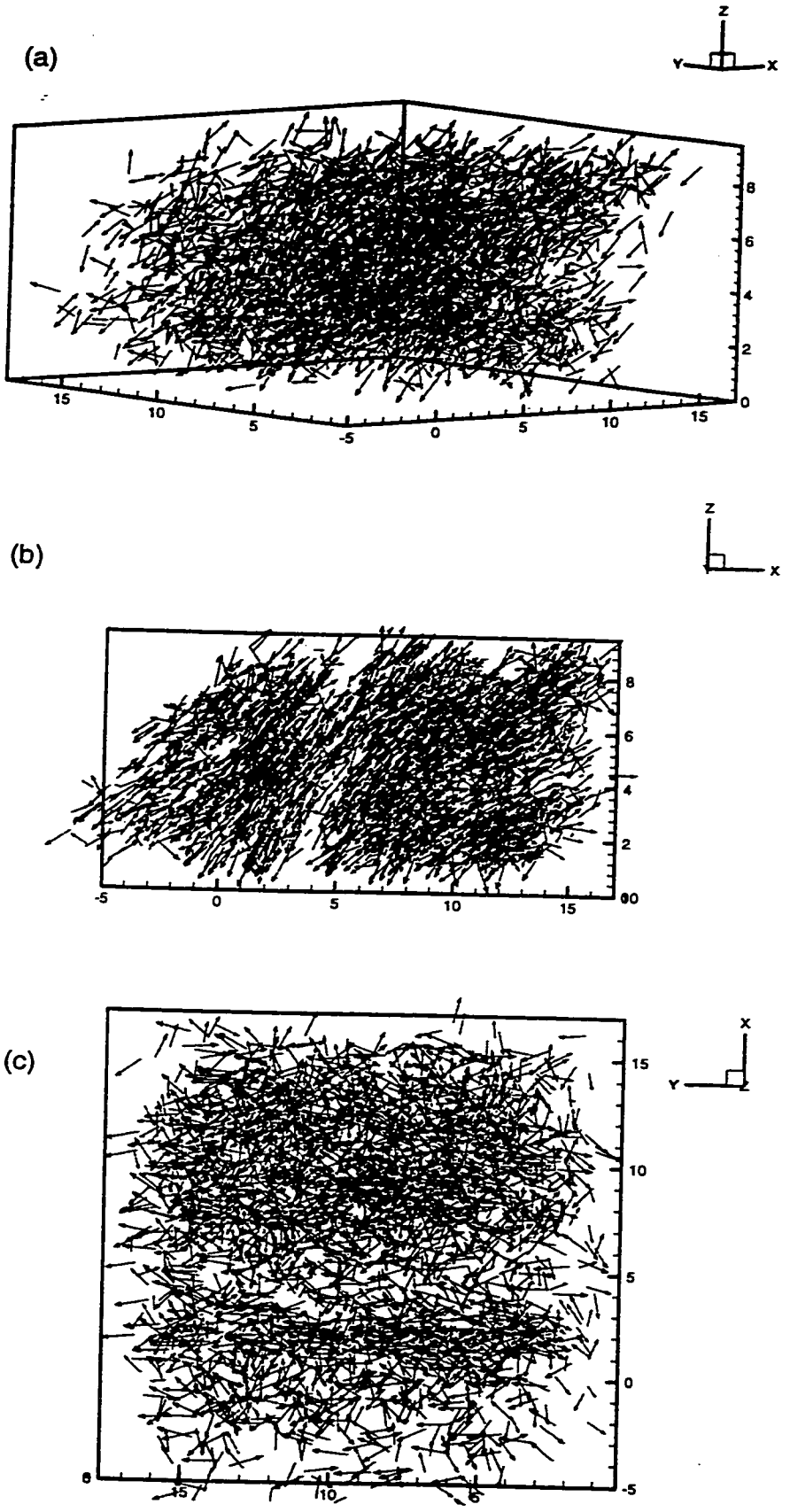

Figure 6.14. Vector-plots of the circulation vectors of vortex elements at dimensionless time St=10; (a) perspective view; (b) side view; (c) top view.

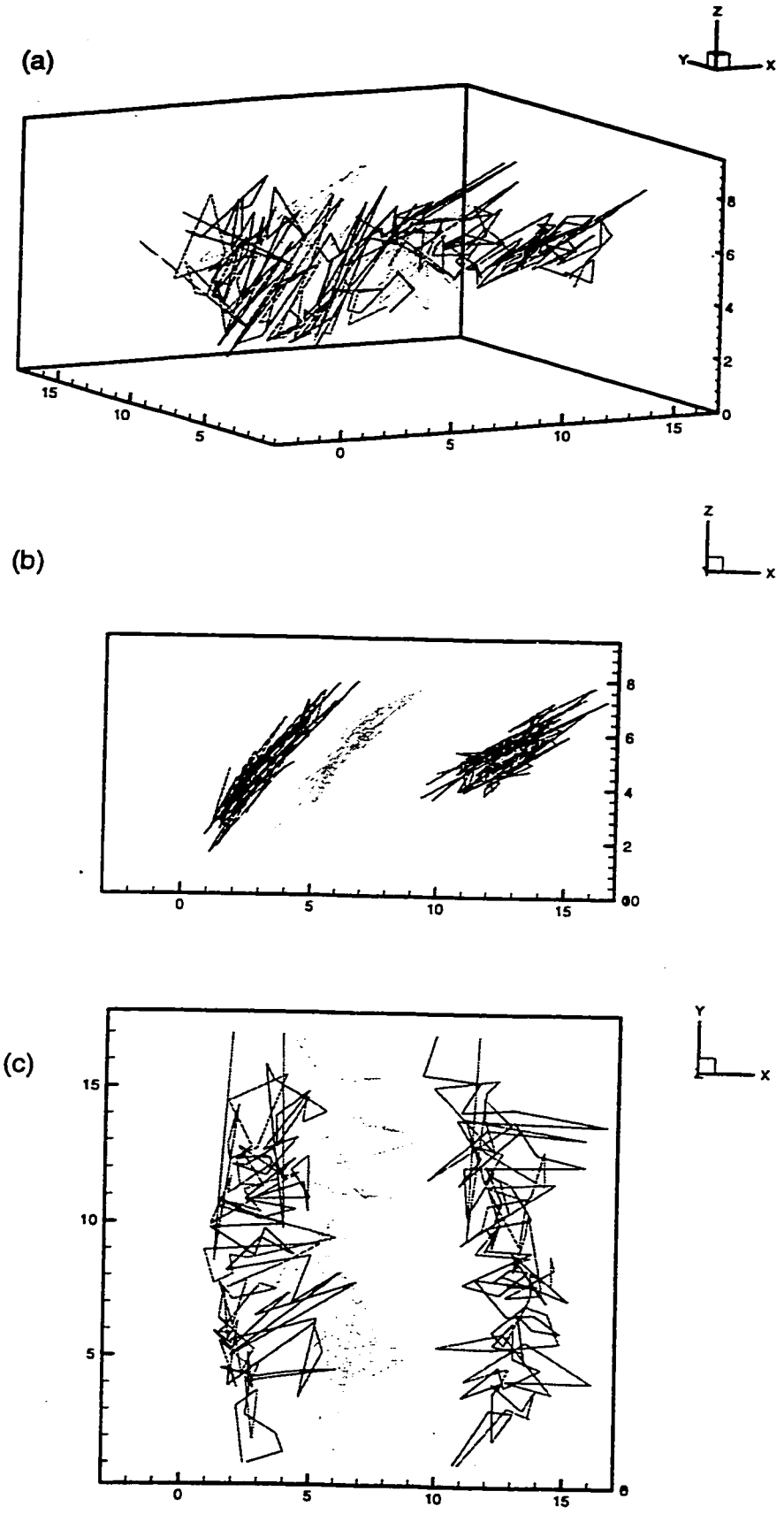

Figure 6.15. Selected vortex filaments at centerline layer, at dimensionless time St=10; (a) perspective view; (b) side view; (c) top view.

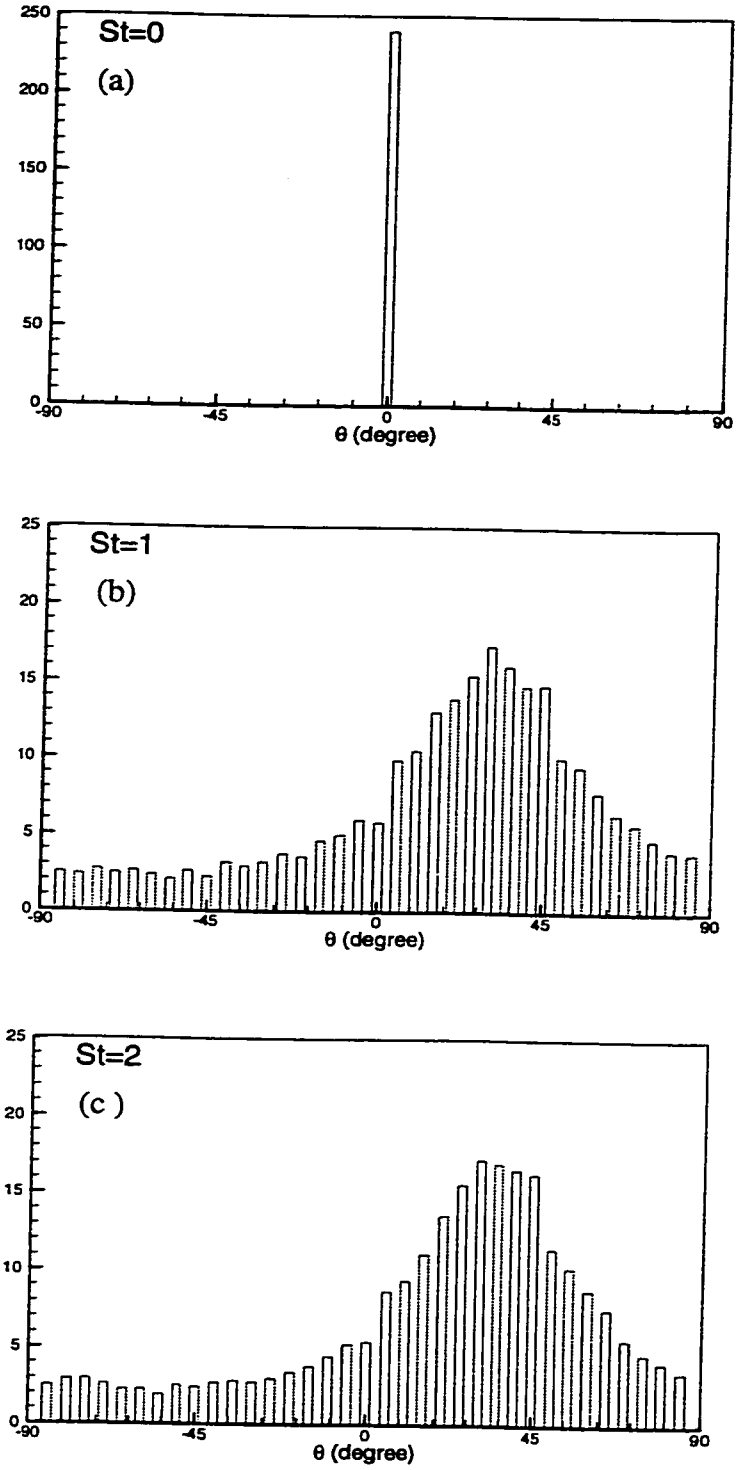

Figure 6.16. Histograms of the inclination angle of the vortex filaments(θ) with xy-plane for temporally growing uniform shear. Histograms are normalized by the ratio of the length of the segment to the length of the filament that the segment belongs to. (a) St=0; (b) St=1; (c) St=2; (d) St=4; (e) St=6; (f) St=10.

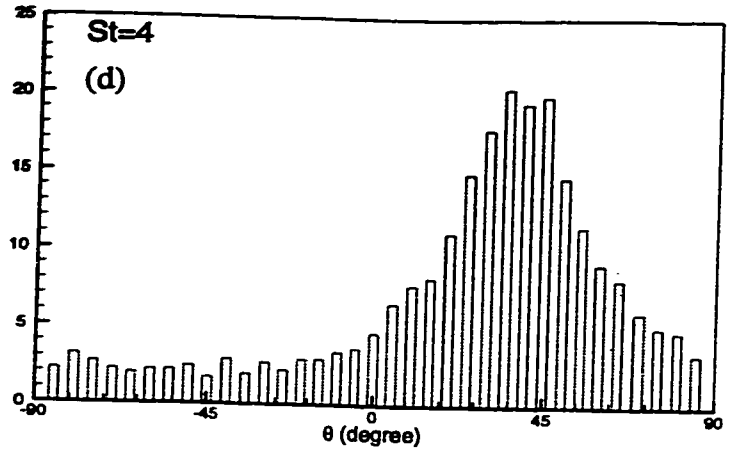

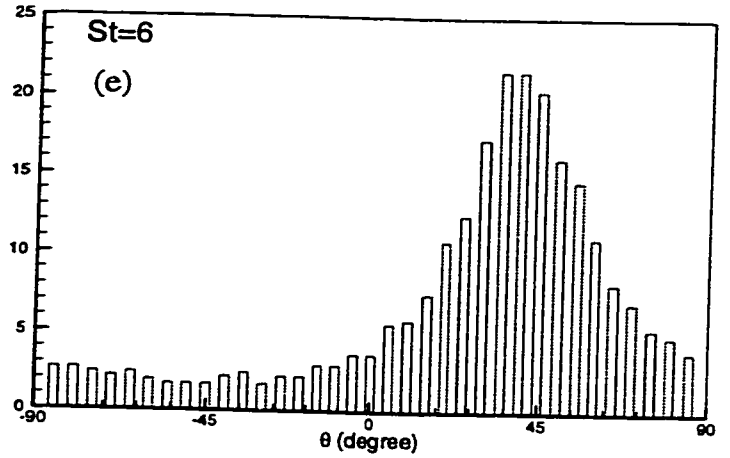

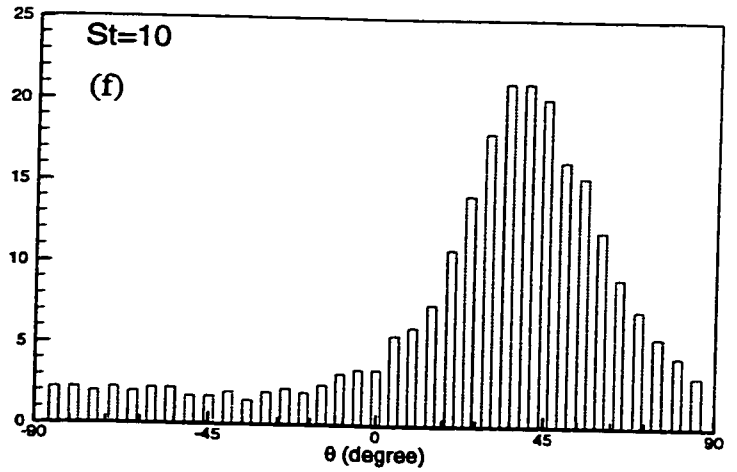

For caption see page 186

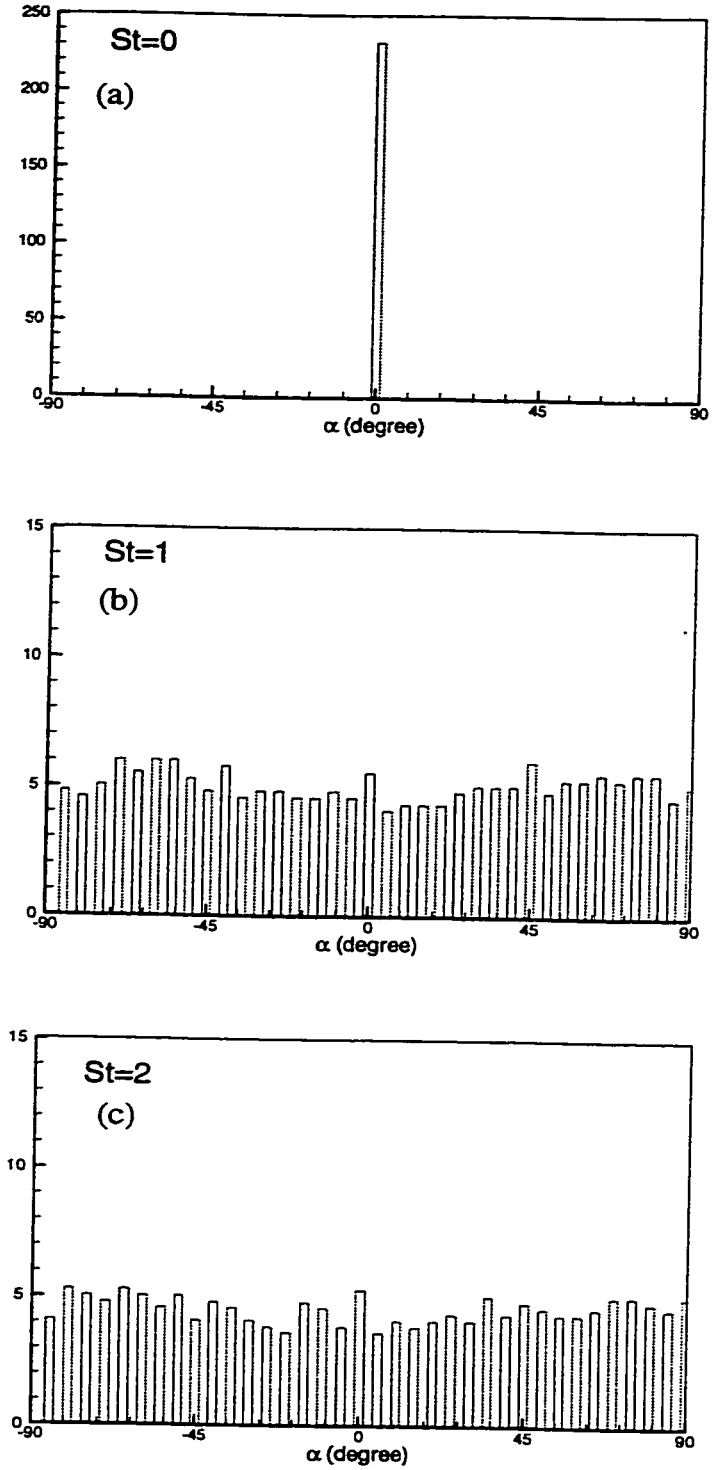

Figure 6.17. Histograms of the inclination angle of the vortex filaments with spanwise direction(α) for temporally growing uniform shear. Histograms are normalized by the ratio of the length of the segment to the length of the filament that the segment belongs to. (a) St=0; (b) St=1; (c) St=2; (d) St=4; (e) St=6; (f) St=10.

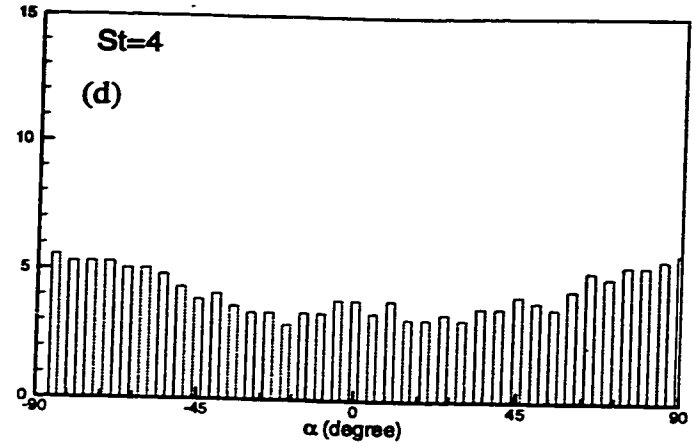

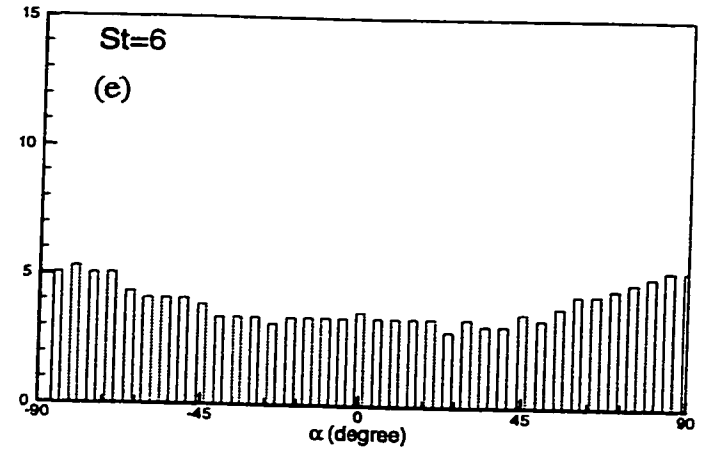

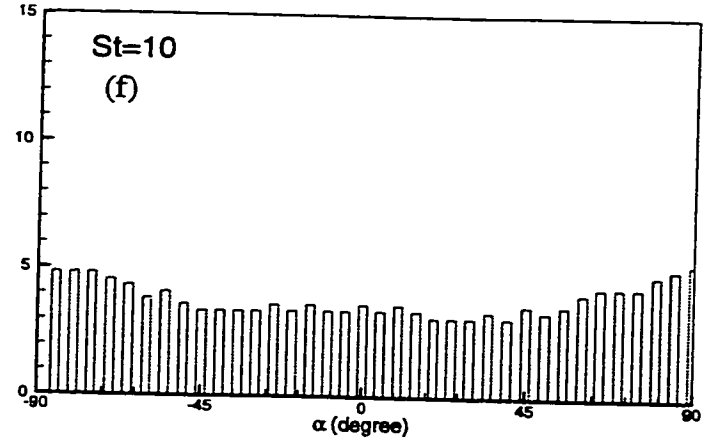

For caption see page 188

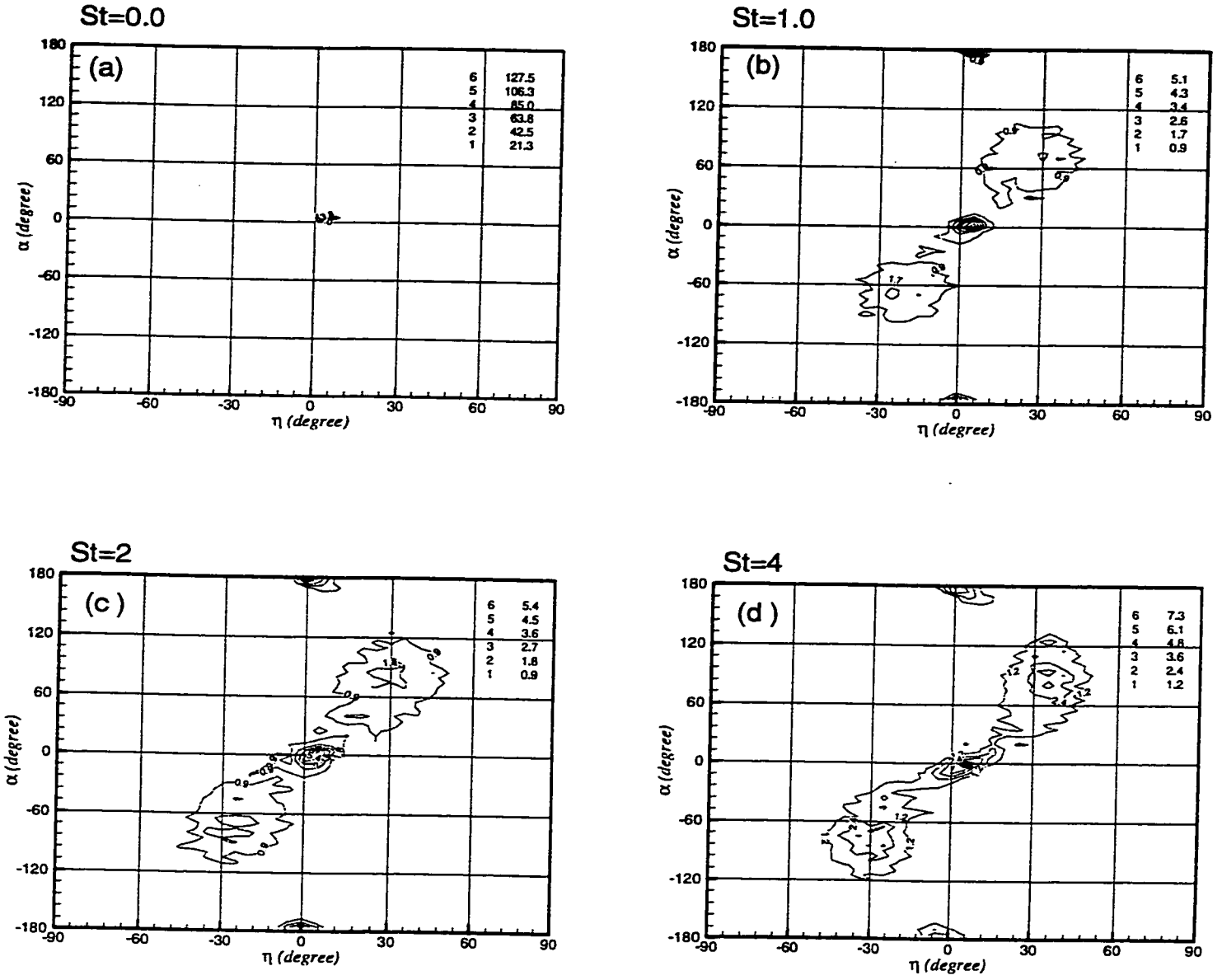

Figure 6.18. Two-angle probability distribution function of the filaments angles with xy-plane (η) and with spanwise direction (α). (a) St=0; (b) St=1; (c) St=2; (d) St=4; (e) St=6; (f) St=10.

St=6

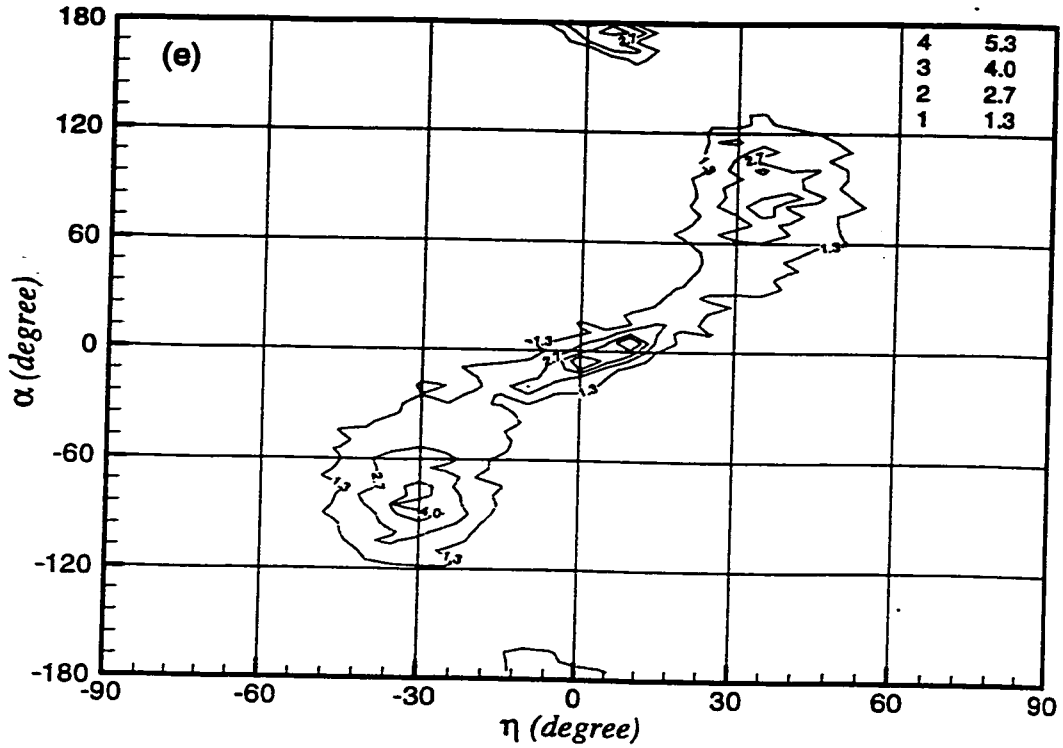

St=10

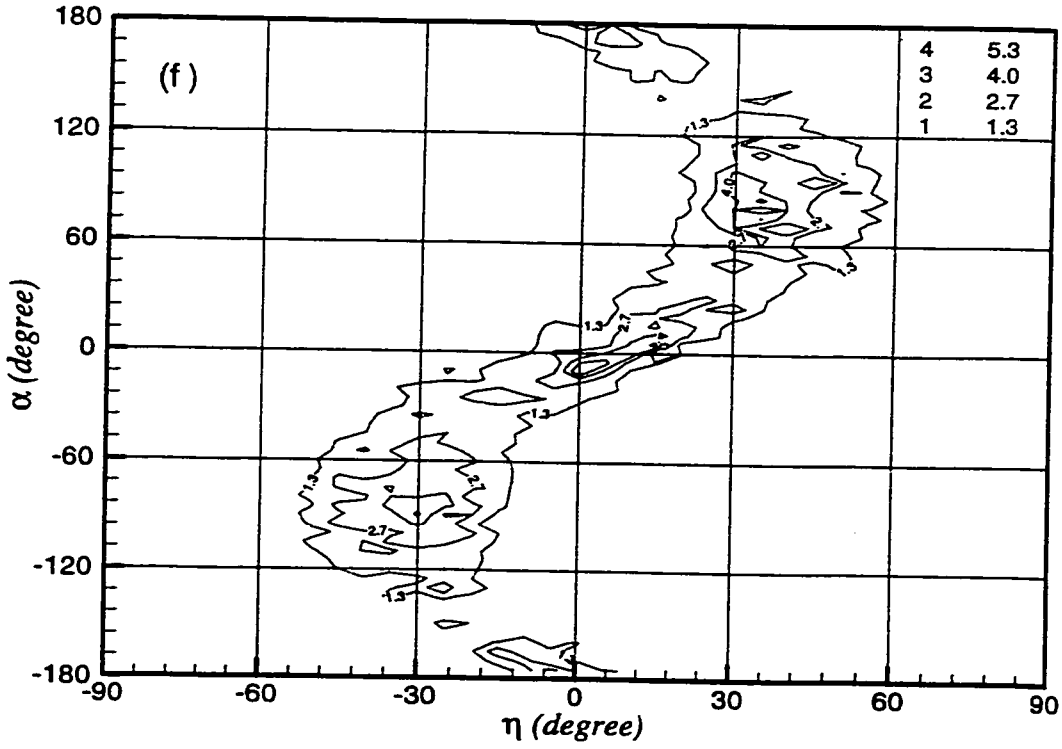

For caption see page 190

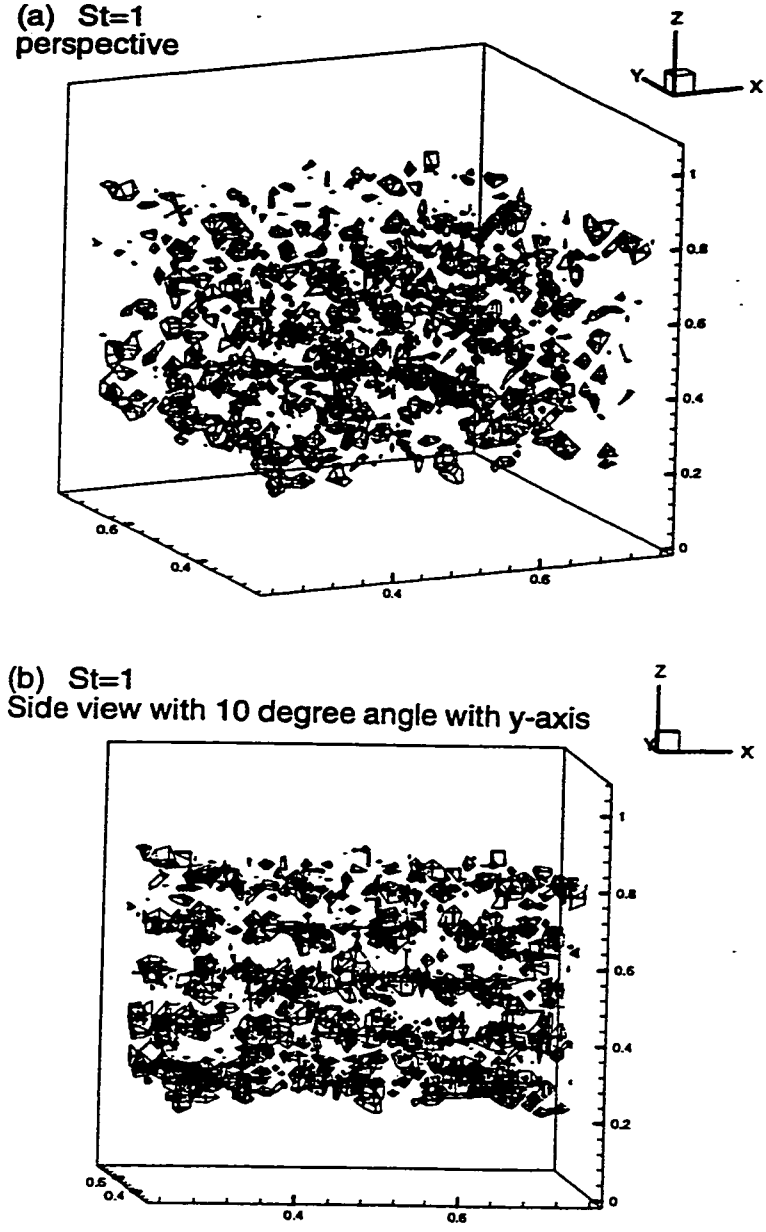

Figure 6.19. Iso-surfaces of magnitude of vorticity at the grid points; (a,b) at St=1, ω=12S, (c,d) at St=10, ω=7S

(c) St=10
Perspective

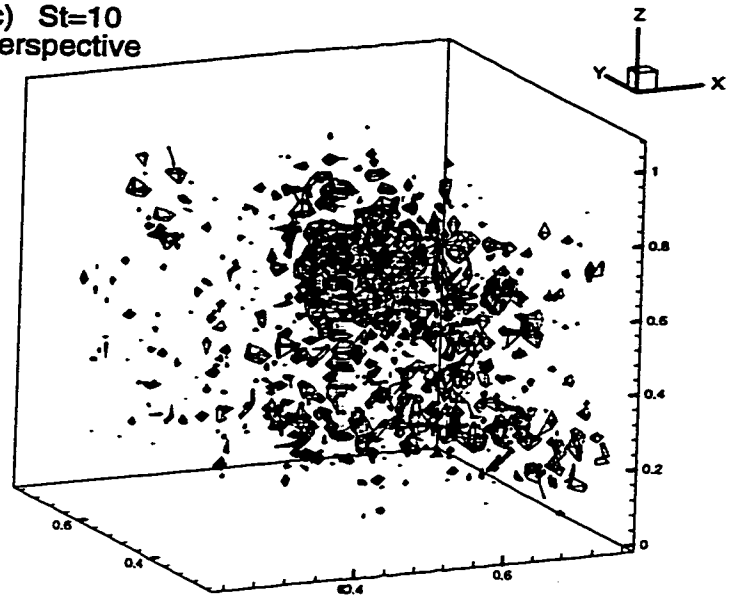

(d) St=10
Side view with 10 degree angle with y-axis

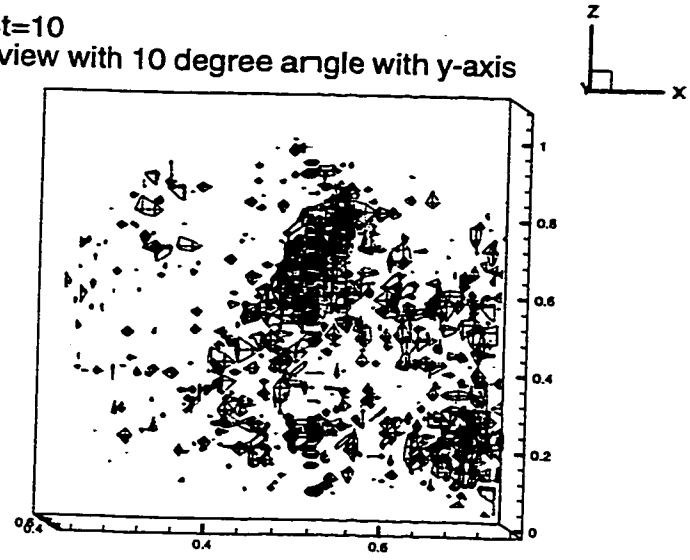

For caption see the previous page

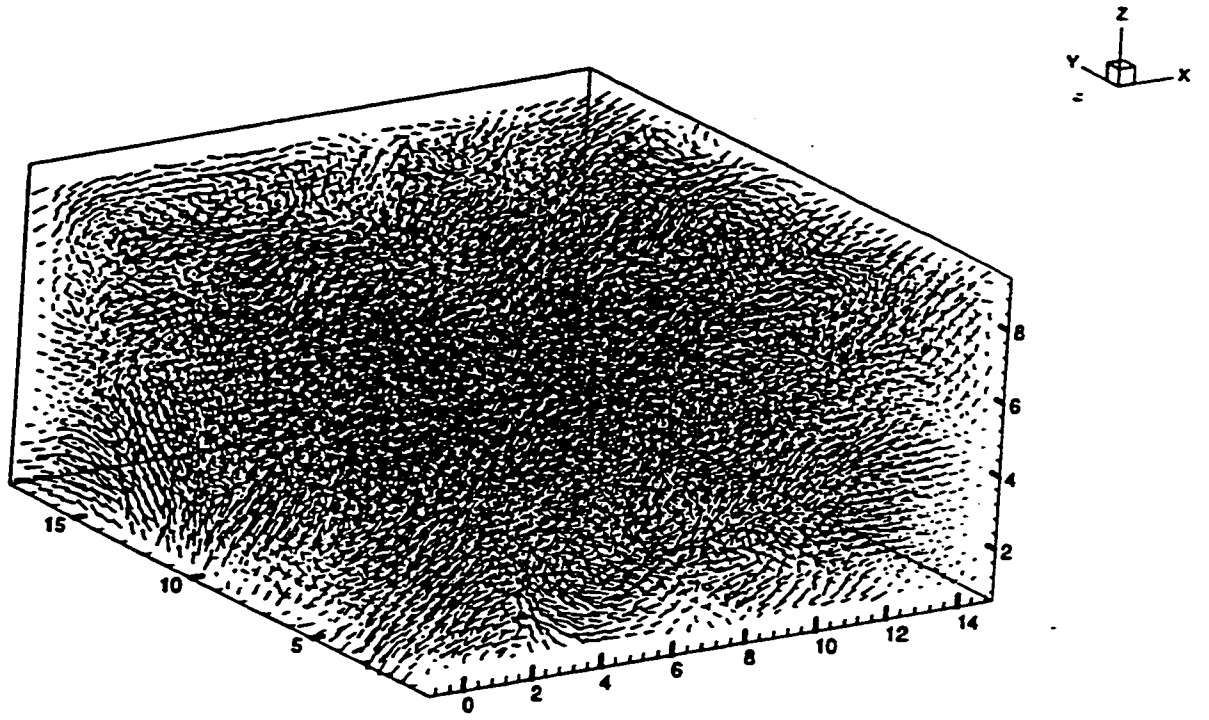

Figure 6.20 Perspective view of vorticity vectors of the filaments interpolated at the nodal points for quasi-temporal shear flow at St=10.

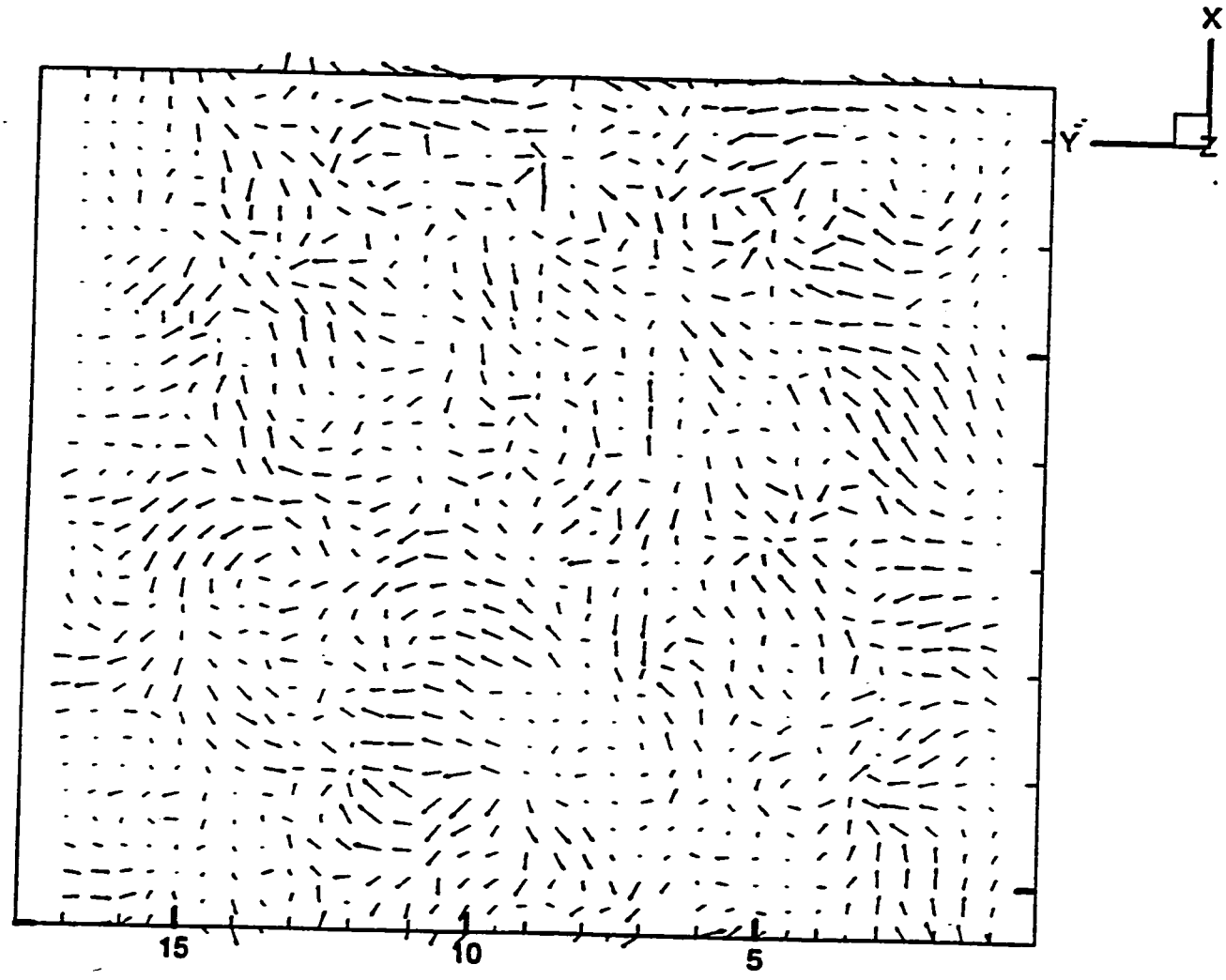

Figure 6.21. Vector plot of vorticity vectors on a plane at 0. degree angle with xy-plane.

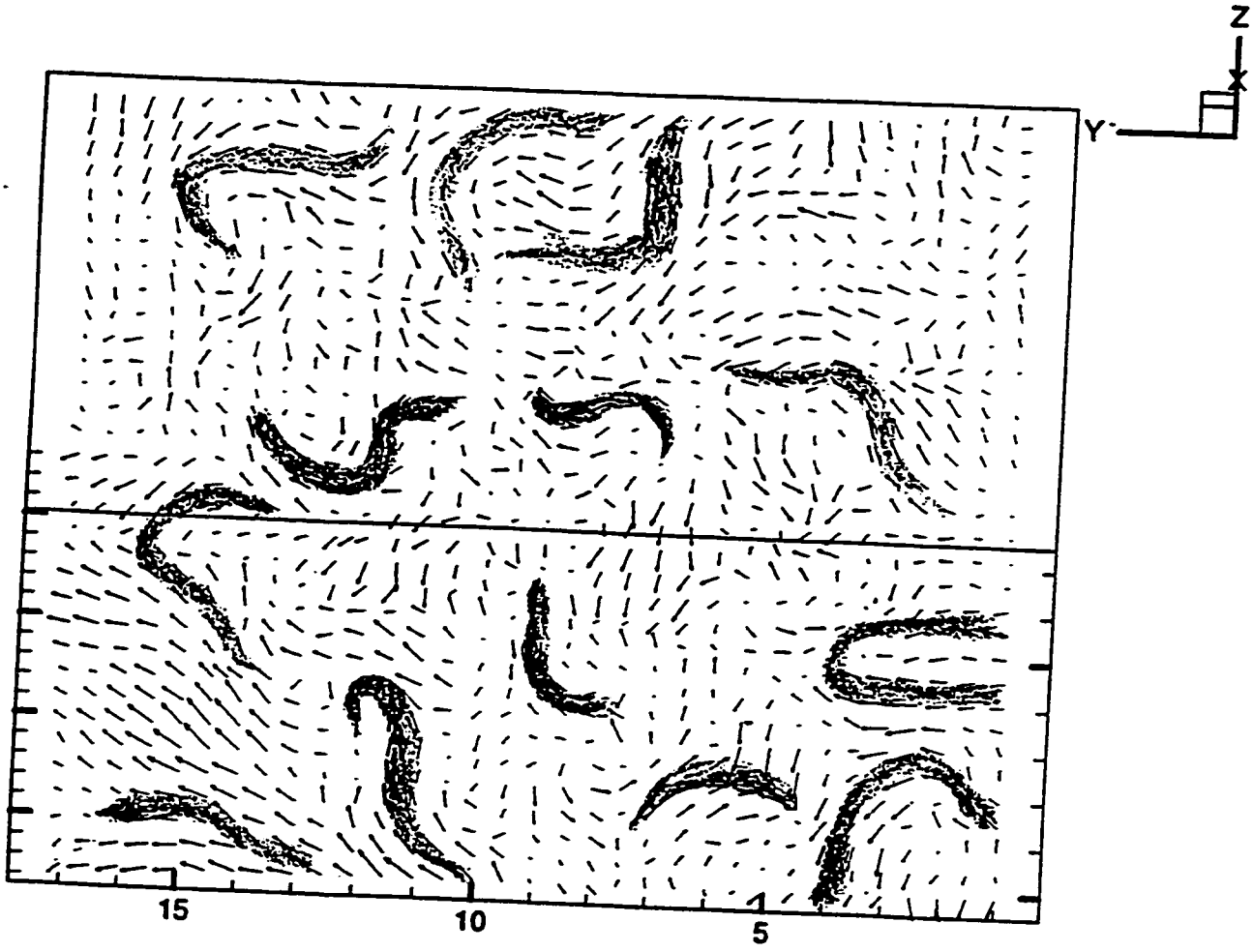

Figure 6.22 Vector-plot of vorticity vectors on a plane with 26.6 degree angle with xy-plane.

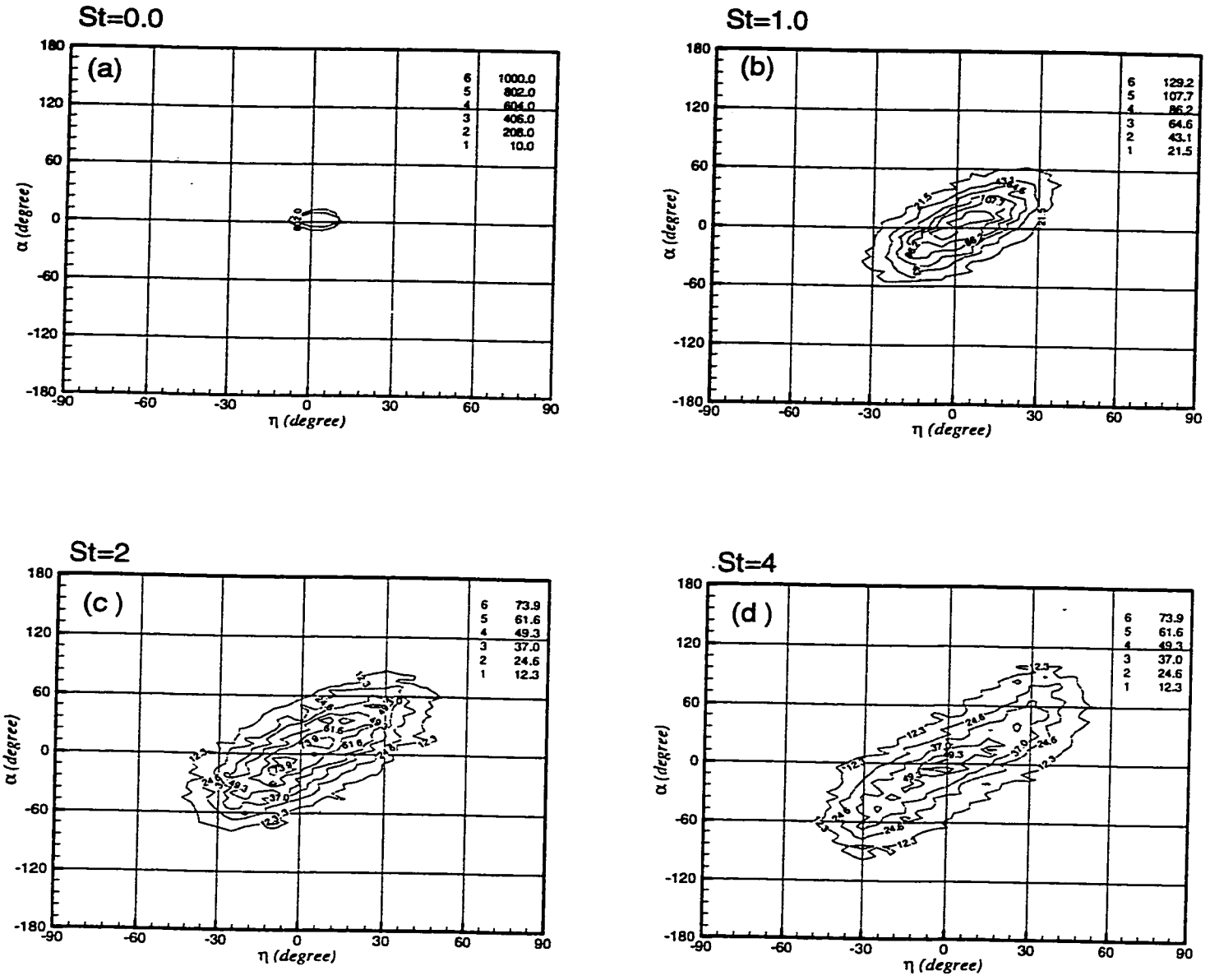

Figure 6.23. Two-angle probability distribution function of the vorticity vectors with xy-plane (η) and with spanwise direction (α). (a) St=0; (b) St=1; (c) St=2; (d) St=4; (e) St=6; (f) St=10.

St=6

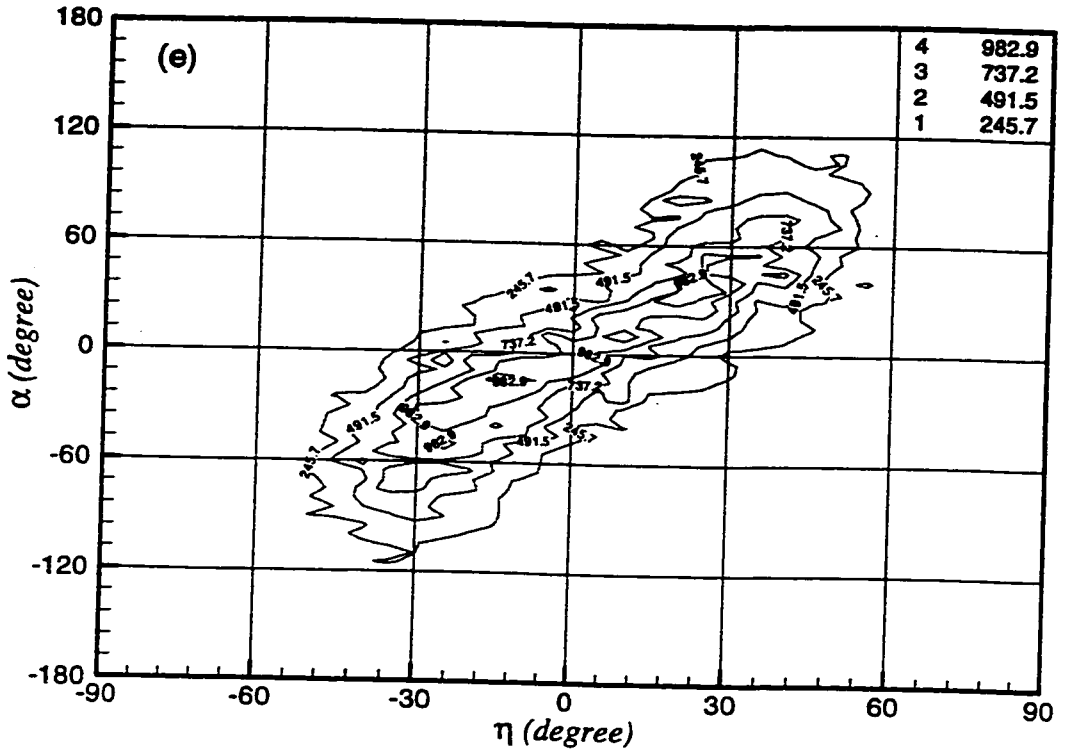

St=10

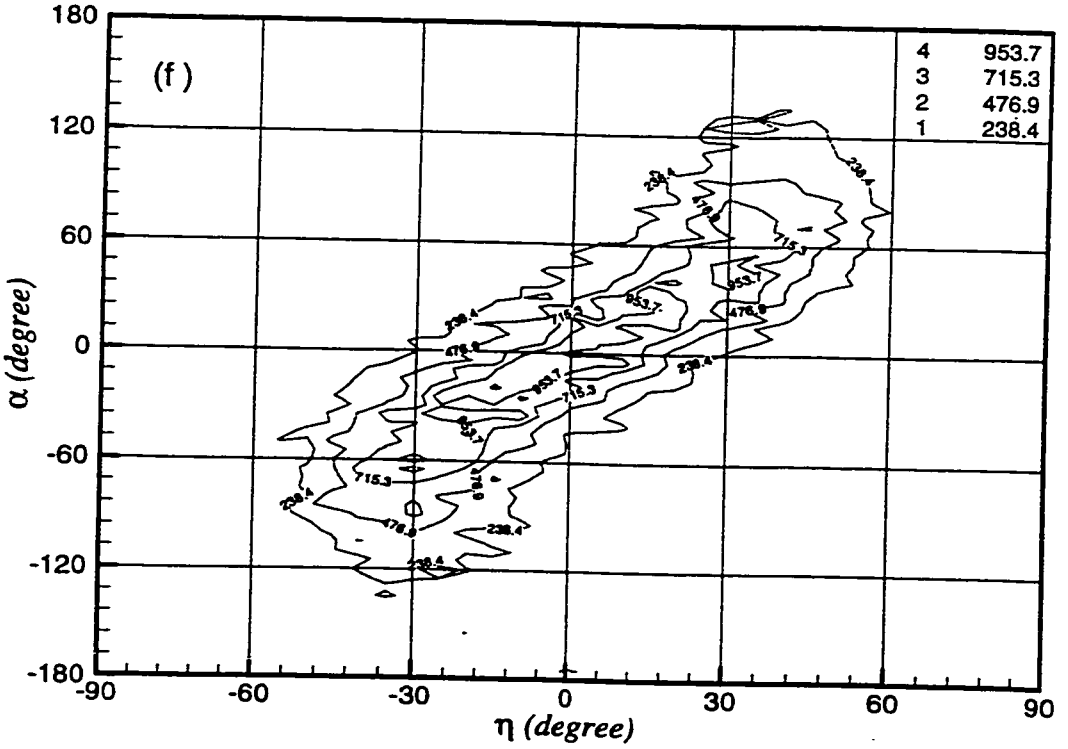

For caption see page 197

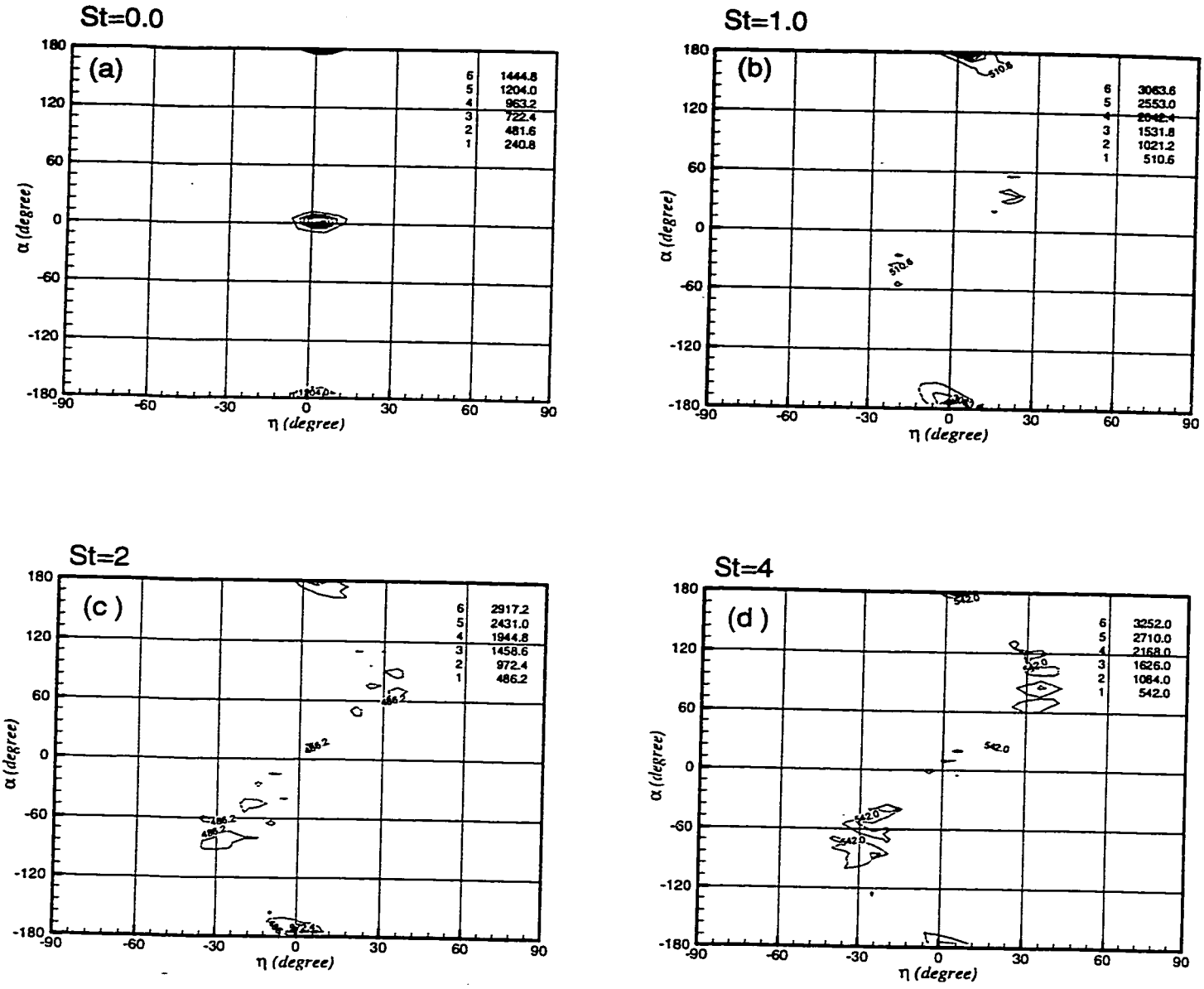

Figure 6.24. Two-angle probability distribution function of the fluctuating vorticity vectors with xy-plane (η) and with spanwise direction (α). (a) St=0; (b) St=1; (c) St=2; (d) St=4; (e) St=6; (f) St=10.

St=6

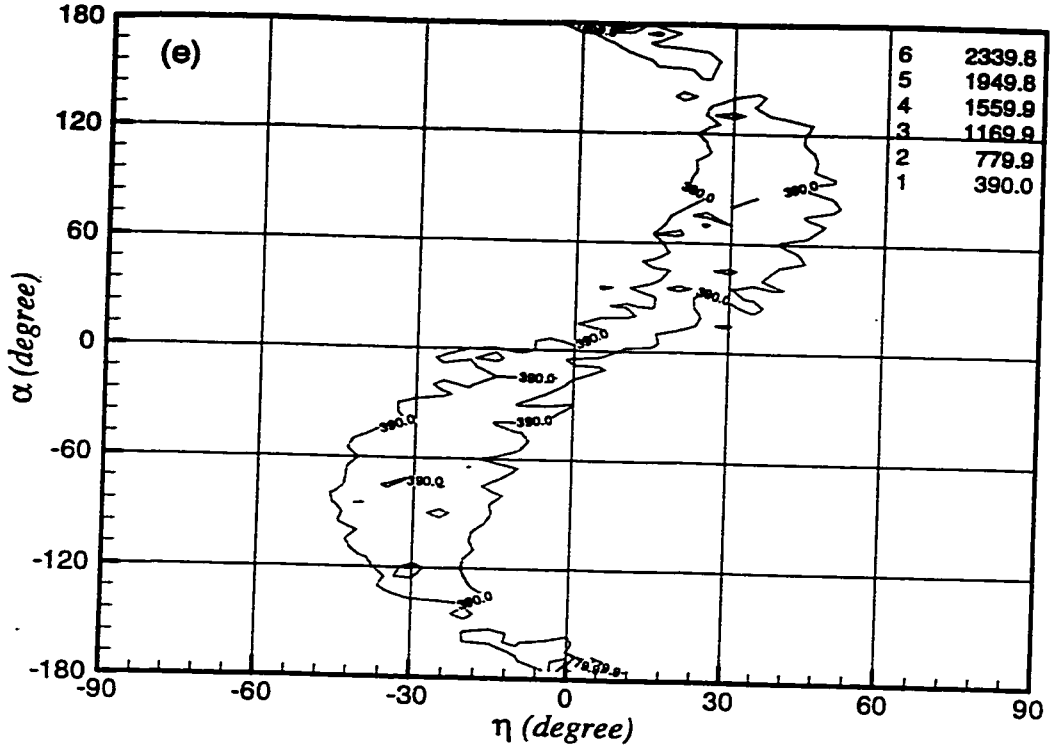

St=10

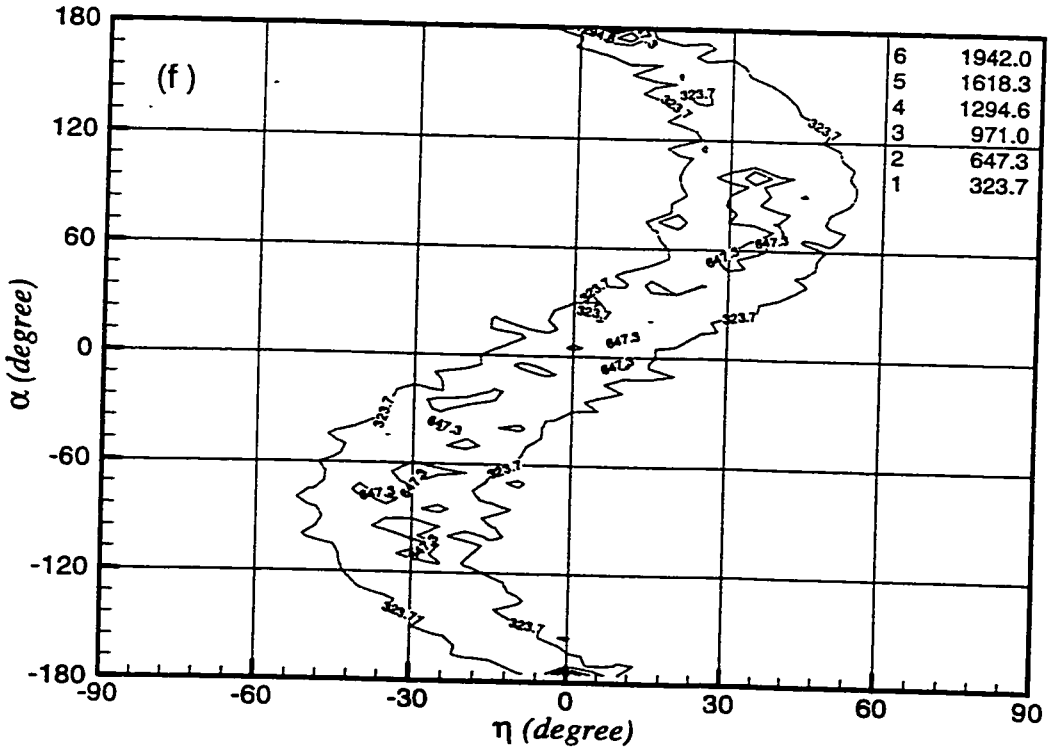

For caption see page 199

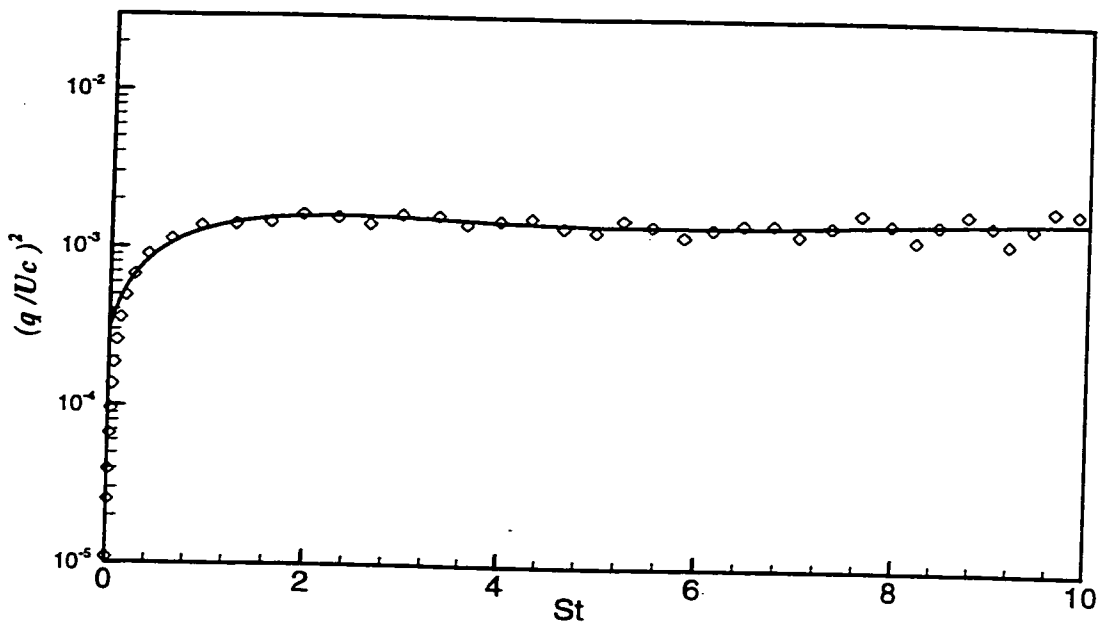

Figure 6.25. Growth rate of turbulent kinetic energy in the three-dimensional simulation of uniformly sheared flow.

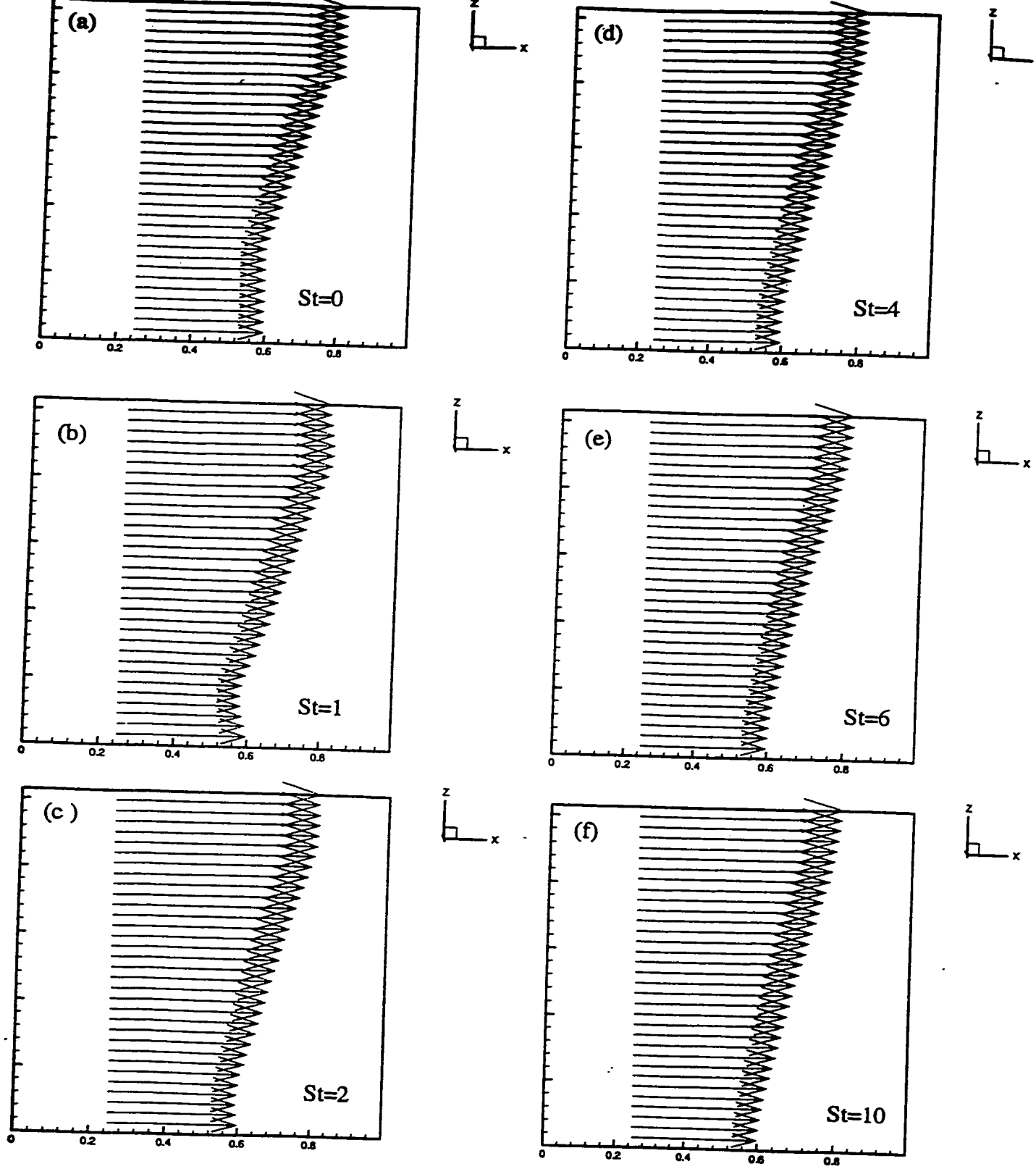

Figure 6.26. Mean velocity profiles at several dimensionless times.

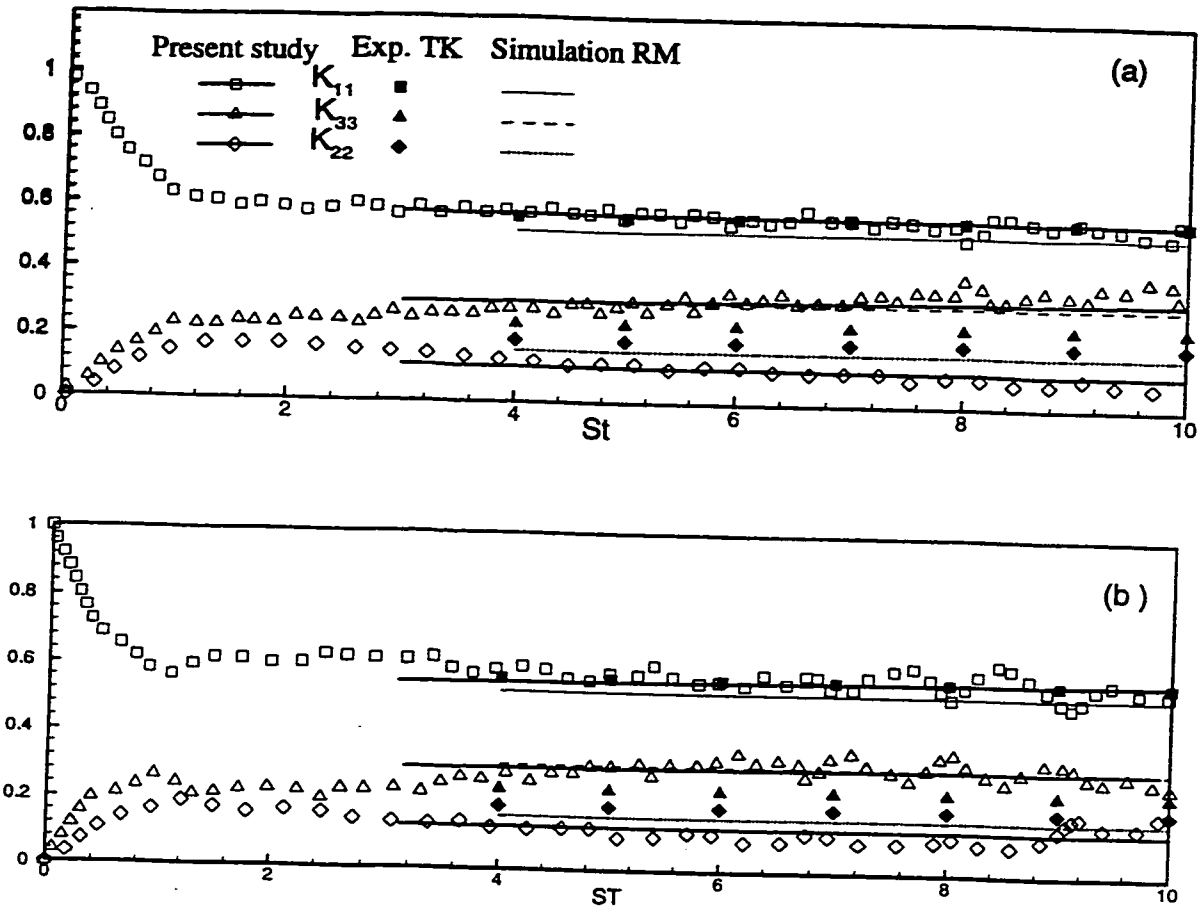

Figure 6.27. Component energy ratios for quasi-temporal shear flow; (a) grid size 0.25 cm and 1200 filaments; (b) grid size 0.125 cm and 2400 filaments.

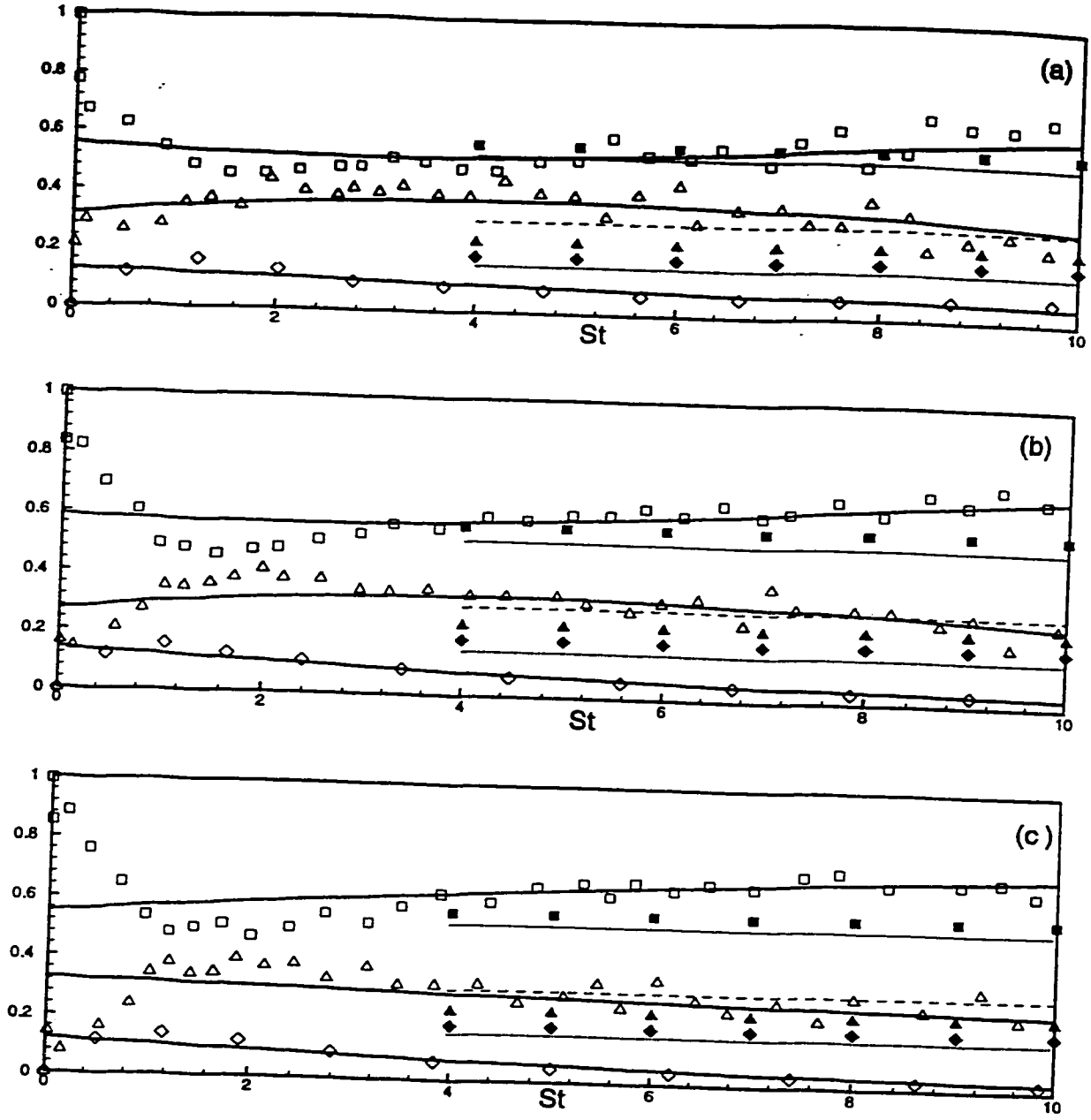

Figure 6.28. Component energy ratios for a quasi-temporal shear flow using grid size 0.5 cm. (a) using 640 vortex filaments; (b) using 1200 vortex filaments; (c) using 2400 vortex filaments. See figure 6.27 for the legend.

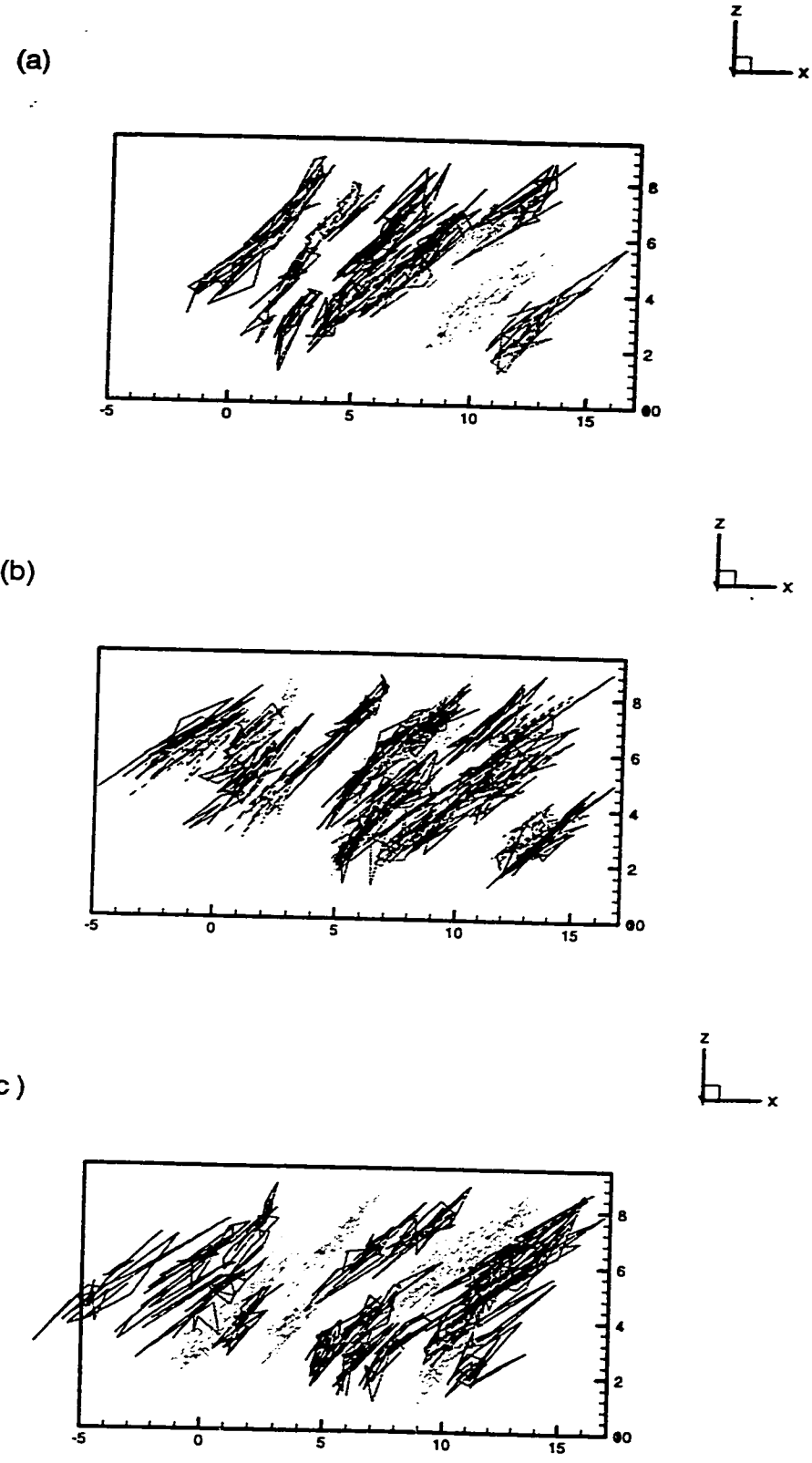

Figure 6.29. Side views of selected of the vortex filaments in quasi-temporally growing uniformly sheared flow at dimensionless time St=10, using (a) 640 filaments, (b) 1200 filaments and (c) 2400 filaments.

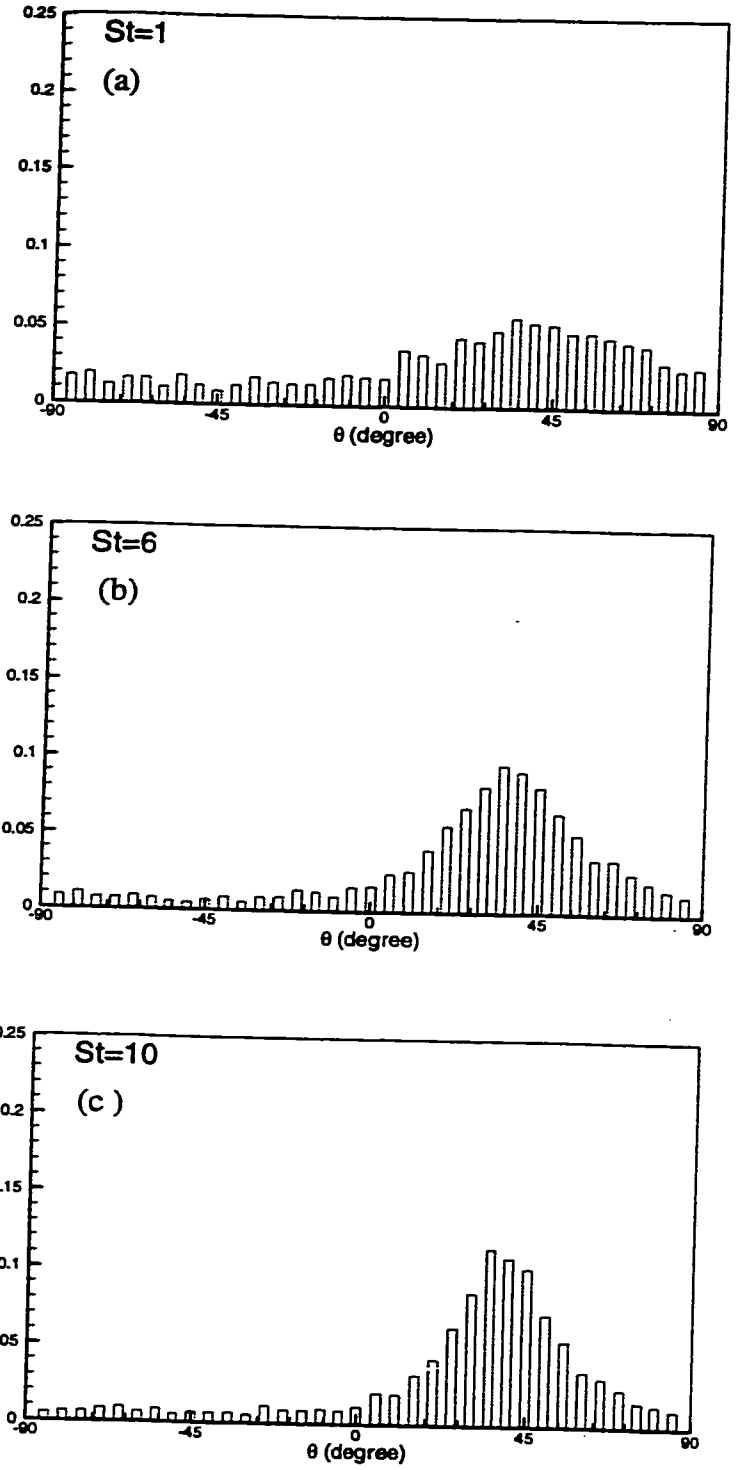

Figure 6.30. Histograms of the inclination angle of the vortex filaments(θ) for temporally growing uniform shear. Figures a, b and c show the angle of the filaments (θ), with xy-plane for the simulation using 640 vortex filaments at St=1, 6 and 10 repectively. Histograms are normalized by the ratio of the length of the segment to the length of the filament that the segment belongs to.

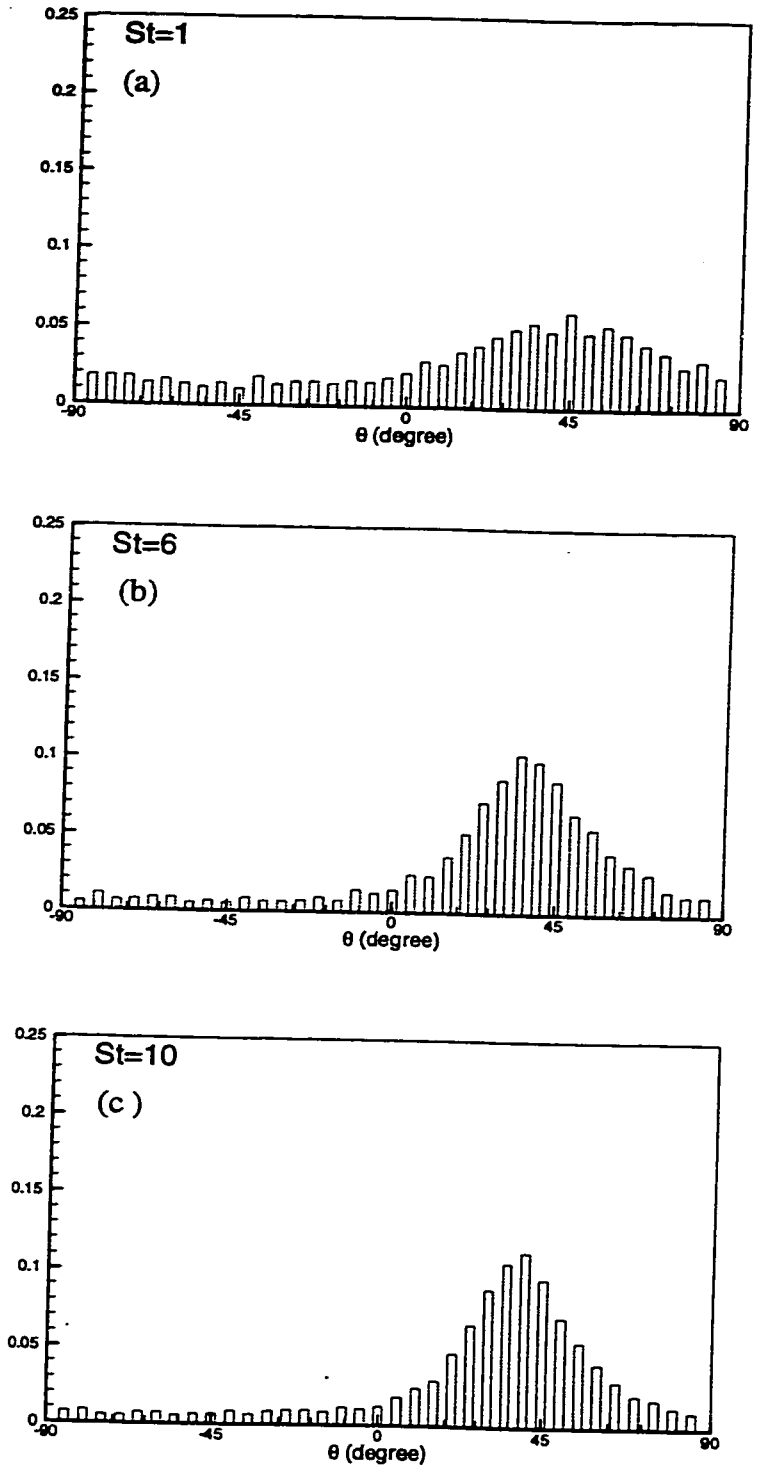

Figure 6.31. Histograms of the inclination angle of the vortex filaments(θ) for temporally growing uniform shear. Figures a, b and c show the angle of the filaments (θ), with xy-plane for the simulation using 1200 vortex filaments at St=1, 6 and 10 repectively. Histograms are normalized by the ratio of the length of the segment to the length of the filament that the segment belongs to.

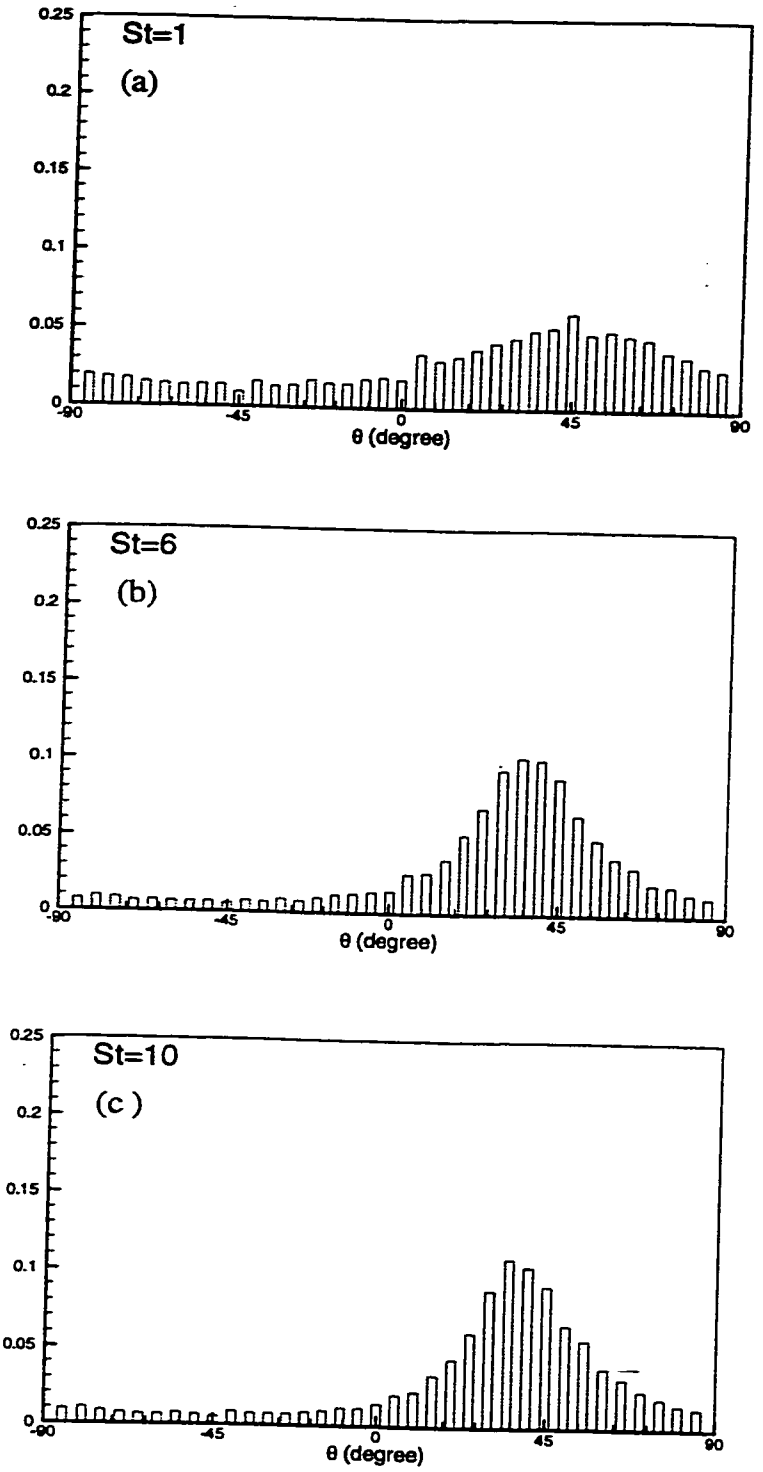

Figure 6.32. Histograms of inclination angle(θ), of the vortex filaments for temporally growing uniform shear. Figures a, b and c show the angle of the filaments (θ), with xy-plane for the simulation using 2400 vortex filaments at St=1, 6 and 10 repectively. Histograms are normalized by the ratio of the length of the segment to the length of the filament that the segment belongs to.

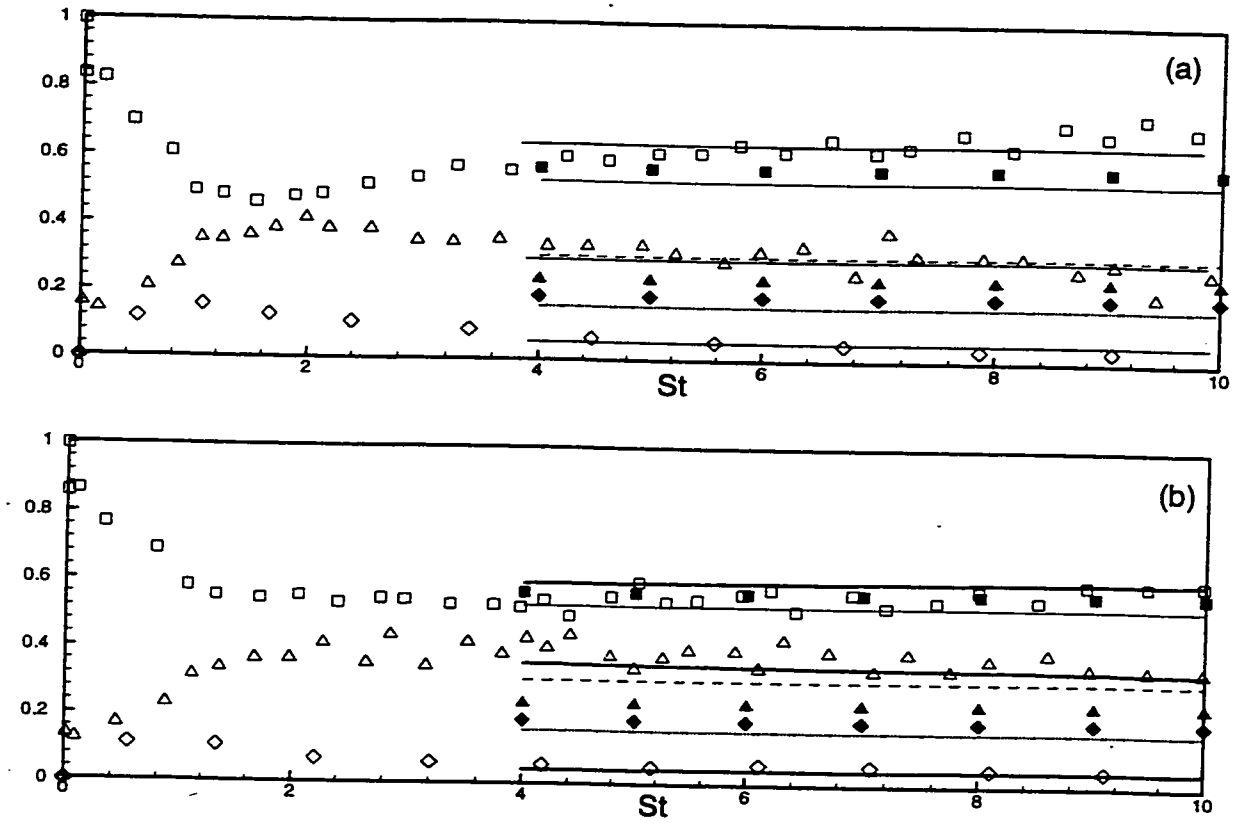

Figure 6.33. Component energy ratios for quasi-temporal shear flow using grid size 0.5 cm× 0.5 cm× 0.5 cm. and 1200 vortex filaments; a) 32 segments per filament(one per grid), b) 64 segments per filament(two per grid). See figure 6.27 for legend.